Title
On the Evolution of Massive Galaxies

Author
Shapiro, Kristen Leah

Publication Date
2010

Peer reviewed|Thesis/dissertation

On the Evolution of Massive Galaxies

by

Kristen Leah Shapiro

A dissertation submitted in partial satisfaction of the
requirements for the degree of
Doctor of Philosophy

in

Astrophysics

in the

Graduate Division
of the
University of California, Berkeley

Committee in charge:
Reinhard Genzel, Chair
Leo Blitz
Steven Boggs
Marc Davis

Spring 2010

On the Evolution of Massive Galaxies

Abstract

On the Evolution of Massive Galaxies

by

Kristen Leah Shapiro
Doctor of Philosophy in Astrophysics

University of California, Berkeley

Reinhard Genzel, Chair

Galaxies, as the fundamental building blocks of the Universe, are the critical link between the overall evolution of the Universe and the assembly of small-scale structures, such as stars and planets, within it. Unfortunately, the formation and evolution of galaxies remains poorly understood, due to the incredible complexity of the physics that governs these processes. To study and constrain these processes, a particularly useful galaxy population are bulge-dominated galaxies such as elliptical and large spiral galaxies, which together are the most massive and most evolved components of the local Universe. In the present day, these galaxies are dominated by old stars; however, their histories likely include an epoch of powerful star formation and rapid growth of their supermassive black holes.

Progress in understanding the evolution of massive galaxies can therefore proceed on two fronts – 1) observations of their formation *in situ* in the early Universe, and 2) detailed studies of the fossil relics of this process in the local Universe – with the ultimate goal being to link progenitors and descendants. A key epoch for such investigations is 10 billion years ago, the most active period in the Universe's history, at which time the vast majority of stellar material in galaxies was assembled. Recent comparisons of the observed properties of galaxy populations across cosmic time have shown that the dominant star-forming galaxy population at these early times were the probable ancestors of present-day massive (bulge-dominated spiral and elliptical) galaxies. The obvious direction for current and future research is therefore to probe the detailed evolution with time of the properties and sub-structures that define this local galaxy population.

This goal has guided my dissertation research, as described in the following pages. Using photometric, spectroscopic, and integral-field observations at optical through mid-infrared wavelengths, I have studied both star-forming galaxies in the early Universe and their present-day descendants. Specifically, this thesis explores the dynamical, star-forming, and black hole properties of galaxies 10 billion years ago and shows that these young galaxies must be assembled via a rapid but steady influx of gas from the surrounding cosmic structure. The resulting large quantity of gas in these galaxies causes super-large star-forming gas clouds to form, and the dynamical interactions of these clouds control the evolution of the galaxies' supermassive black holes and internal sub-structures, producing the bulges and globular

cluster populations observed in the present day. Studies of the resulting local massive galaxy population, also presented herein, confirm that such successive minor dynamical disturbances were important to the assembly of these bulge-dominated galaxies and their supermassive black holes. In the pages of this thesis, an exciting link is emerging in which many observed properties of local galaxies can be explained by the dramatic internal processes occurring in galaxies 10 billion years ago, during the era of the most rapid galaxy assembly.

For my parents

Contents

List of Figures

List of Tables

Acknowledgments

It is a pleasure to acknowledge and thank the amazing people in my life who have made this thesis possible.

Of these, I owe my deepest gratitude to my research advisor, Reinhard Genzel, who has provided me with unlimited guidance and support throughout my graduate career. I cannot thank him enough for sharing his passion for scientific inquiry, for giving me fascinating research problems and working with me to solve them, for teaching me to become an independent researcher, and for providing me with numerous extraordinary opportunities. I will always be grateful to Reinhard for allowing me to learn from him, and I consider myself exceptionally fortunate to have been his student. Above all this, however, I am most appreciative of our wonderful friendship, both in and out of the office, and I will fondly recall and very much miss our daily trips to Strada to drink "hot water" and discuss science, our hikes through the Alps with the "mountain lions," and dozens of fun and delicious dinners.

My sincere thanks also extend to Tim de Zeeuw, an excellent mentor who has continued to advise me over seven years, four countries, and nine time zones. By taking a chance on a undergraduate from a small liberal arts college and introducing her to the world of research, Tim provided me with an incredible start to my career. In the subsequent years, he has remained an endless source of support in my life, and I feel very blessed to have found such a special mentor and friend.

The past six years have given me the opportunity to work with colleagues who make our joint research efforts interesting, challenging, and very pleasant. I am especially appreciative of Linda Tacconi, whose encouragement and support have been so important to me. She has advised me on everything from scientific questions to career decisions to day-to-day issues like grocery shopping in Garching, and she has, on several occasions, graciously opened her home to me. Jesús Falcón Barroso deserves special mention as a fantastic collaborator, who makes work visits fun and unwieldy projects manageable. Numerous other members of the two collaborations in which I participate – the Infrared Group at MPE and the SAURON team – have significantly contributed scientifically and personally to my success, and I apologize for and sincerely regret my inability acknowledge them all individually here.

I also thank my wonderful Berkeley-based colleagues and fellow graduate students. My current and former officemates, including Aaron Parsons, Jeff Silverman, Andrew Wetzel, and Peter Williams, bring a good serving of hummus and humor into my daily life; I have very much enjoyed the amalgam of research questions, commentary on current events, and

inside jokes that characterize our workdays. Julie Comerford is the longest-serving graduate student mentor in history, who has given me advice over the years on everything from coursework to which American Idol contestants will win. Holly Maness and Linda Strubbe, my co-mentor mistresses and close friends, are the ones who keep me sane and make me smile. Many others have continuously brightened my days. In particular, my thanks go to Mo Ganeshalingam for our walks home, John Johnson for recess, Conor Laver for not letting me quit on our Fire Trail runs, Evan Levine for our catch-up dinners, Dexter Stewart for help with nearly everything and for great conversations, my mentor family for cupcakes, and of course my fellow "PLC" members for the whole crazy journey together.

It is an honor for me use this opportunity to also acknowledge the many advisors who have provided me with constant support before and during graduate school. Geoff Marcy embraced his role as my academic advisor; his guidance was always helpful and his enthusiastic encouragement refreshing. I am grateful to my dissertation committee – Leo Blitz, Steve Boggs, and Marc Davis – for their participation in the definition of this thesis during my qualifying exam and for reading and commenting on this final product. I am also deeply appreciative of my undergraduate advisors – Joris Gerssen, Karen Kwitter, Jay Pasachoff, and Roeland van der Marel – for the incredible opportunities that they gave me so early in my career and that have been so instrumental in my subsequent success.

Finally, my thanks go to the dear friends and family who enrich all aspects of my life. To Jasmine, without whom the graduate school experience would have been much lonelier and not nearly as hilarious. To my amazing fiancé Antoine, for his understanding, endless love, and unfailing confidence in me; I cannot wait for our future together. To Lin, who shows me every day that there is nothing so special in this world as a sister. And to my parents, for raising me to become the person I am today, for always helping me grow, and for supporting me throughout my life and my work. Mom and Dad, you are the key to all of my accomplishments, and I dedicate this thesis to you.

Chapter 1

Introduction

1.1 The Study of Astronomy

Of all the physical sciences, astronomy has perhaps the most direct appeal to those among us who seek to understand the existence of our planet and our species. For this reason, astronomy is the oldest natural science; ancient cultures used observations of the night sky to study the seasons, the nature and properties of the Sun and Moon, the motions of planets in the solar system, and the appearance of transient phenomena such as supernovae. Since ancient times, our understanding of the Universe has undergone several revolutions, yet modern progress and unsolved problems in astronomy continue to excite and engage the general public. It can be argued that this interest stems from the basic human desire to know our place in the cosmos.

However, astronomy has practical applications as well. Detailed observations and tracking of small, rocky objects in the Solar System such as asteroids and comets allow us to predict which objects may eventually collide with the Earth. This knowledge may someday help us prepare for and prevent catastrophes on the scale of the one that exterminated the dinosaurs, and it is therefore vital to the safety of our planet and our species. Similarly important are studies of the Sun's weather system, from which energetic ejections can incapacitate space-based communication and defense satellites and can temporarily alter the Earth's upper atmosphere. Because of these vulnerabilities or for other reasons, humans may eventually seek to colonize new planets; in this event, our knowledge of our Solar System and others will prepare us for finding a new home and even, perhaps, neighbors. In the long term, knowledge of our immediate astronomical surroundings may consequently be crucial to the survival of our species. Despite the obvious practical importance of such research topics, this thesis will not address any of them.

Instead, the following pages will focus on the loftier investigation of how galaxies form and evolve. As the fundamental building blocks of the Universe, galaxies are the nurseries inside of which stars, planets, and life are born. The Universe contains roughly 300 billion galaxies, and the average galaxy contains 100 billion stars. Dramatic progress in recent years

has revealed that many of these stars are surrounded by their own planetary systems. The study of galaxies is therefore the study of how the groundwork was laid for all of the stars and planets in the Universe to be created. This sub-field of astronomy has provided and continues to provide insight into the history, fate, and composition of the Universe, as well as the assembly history of matter within it. In other words, an understanding of galaxies is critical to placing ourselves in a cosmic context.

In this chapter, I will elaborate on this concept and provide an introduction to the research described in the following chapters. I begin with an overview of the Universe's history and of the role of galaxy formation within it (§1.2). I then discuss our knowledge of the present-day Universe and its components, as observed in the vicinity of our Galaxy, the Milky Way (§1.3). Afterwards, I move to the more distant Universe and explore our current understanding of the formation history of galaxies (§1.4). I then pause in §1.5 to present the observational methods through which we study galaxies before introducing the goals and results of this thesis in §1.6.

1.2 The Story of the Universe

Once upon 13.7 billion years ago, something went "Bang!" and created our Universe. One possible explanation for this event relies on a property of quantum physics known as Heisenberg's Uncertainty Principle, which states that, at the microscopic level, Nature is capable of only a finite amount of precision. In practice, this means that so-called quantum fluctuations, which occur below Nature's precision limit, are possible. The runaway growth of one such fluctuation may have resulted in our Universe. Likewise, other fluctuations may have produced many other universes, but that is surely a topic for an entirely different thesis. Regardless of the true explanation of the Universe's existence, we do know that, in the beginning, all of the matter and energy in the Universe exploded out from a single location; this event is known as the Big Bang.

1.2.1 The Beginning

This extreme initial concentration of matter in the early Universe caused the Universe to be extremely hot ($\sim 10^{32}$ degrees Celsius). As it grew, the Universe cooled down; its temperature today (-270 degrees Celsius) is only 3 degrees above the absolute minimum achievable temperature. Much of this temperature drop happened during the first half hour of the Universe's existence, and this rapid cooling dictated the evolution of matter within it (see Figure 1.1).

After a very brief period of explosive expansion in the first instant of the Universe's existence, it had already cooled to 10^{28} °C, enabling elementary particles to form. During the first thousandth of a second, these elementary particles (quarks and electrons) were so hot that they raced past each other. In much the same way as the cooling of water slows down water molecules enough that they can stick together and form ice, the cooling of the

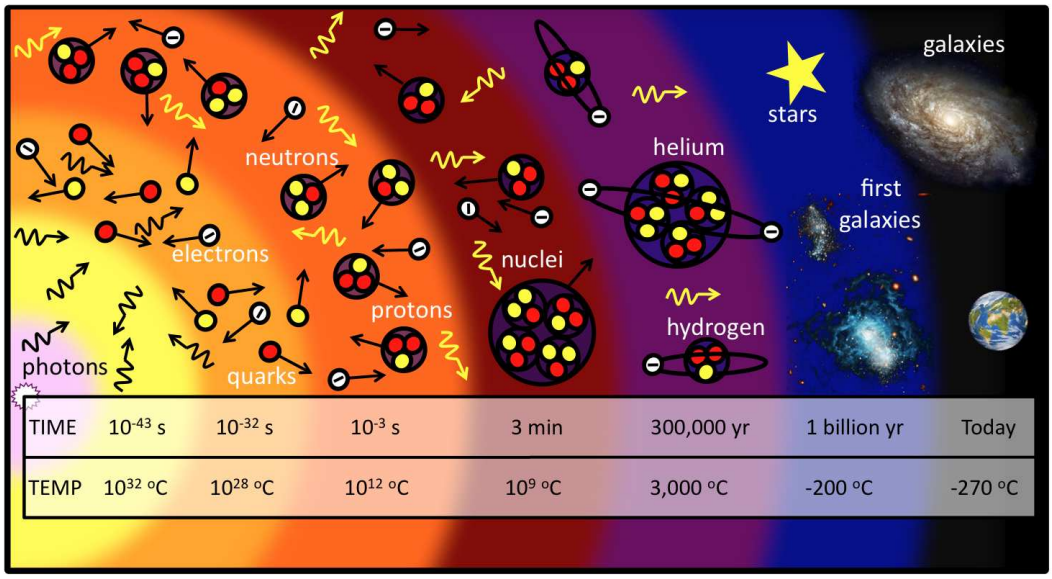

Figure 1.1: Schematic of the history of the Universe. Time since the Big Bang and temperature of the Universe at important epochs are indicated. See text for details. *Image Credit: Adapted from graphic by Ed Gabel, TIME magazine.*

Universe down to 10^{12} °C by the end of the first thousandth of a second allowed quarks to stick together and form protons and neutrons. Likewise, as the Universe cooled below 10^9 °C after the first three minutes, protons and neutrons were able to combine to form hydrogen and helium nuclei. This fusion of hydrogen nuclei into helium nuclei is the fuel that allows stars to burn; unsurprisingly, the centers of stars have temperatures comparable to the Universe in this early epoch. By the time the first half hour had ended, the Universe had settled into a hot primordial soup consisting of atomic nuclei, electrons, and radiation whizzing around and bumping into each other.

The next 300,000 years of the Universe's existence were much less dramatic, as the Universe continued to expand and cool. Since radiation can interact with charged particles (such as electrons and atomic nuclei), the radiation in the primordial soup bounced from one particle to another without ever getting very far (Figure 1.1). If it were possible for us to visit the Universe at this point, we would not be able to see very far, since seeing an object requires light (electromagnetic radiation) to travel uninterrupted from its source to our eyes. In the early Universe, this was not possible; all light travelled only a very short distance before encountering a charged particle and getting deflected from its original path. However, all this changed after 300,000 years, when the Universe's temperature dropped below 3000 °C, at which point electrons and nuclei were cool enough, and therefore moving slowly enough, to bind together into atoms. This transition rapidly changed the Universe from a soup of charged particles into one of neutral atoms, the latter of which interact much less strongly with radiation. Consequently, light became able to travel much further uninterrupted, and the Universe became transparent (Figure 1.1).

Since all of the radiation in the Universe could now travel great distances without encountering charged particles, the light from the final moment of the existence of the charged particle soup can travel uninterrupted through the Universe and could in principle be seen. One could even imagine taking a picture of this first light in every direction and thus mapping its intensity. In fact this has been accomplished, first with the *Cosmic Background Explorer* satellite in 1992 and, more recently and much more clearly, with the *Wilkinson Microwave Anisotropy Probe* in 2001-2008 (Figure 1.2). In 2009, a yet more sophisticated satellite named *Planck* was launched to image this epoch in very fine detail. These data measure the "surface of last scattering," so called because the light comes from the final moment at which radiation scattered off of charged particles in the primordial soup before light became able to travel freely.

1.2.2 The Growth of Structure in the Universe

Figure 1.2 is a picture of the moment of last scattering and shows that the Universe at this point was characterized by small non-uniformities; yellow/red regions are very slightly more dense (equivalent to slightly hotter) than blue/black regions. The fact that the Universe was clumpy at the beginning should not be a surprise to us, since the Universe we observe now is also highly clumpy; matter is concentrated into galaxies with vast, nearly empty space between them. Figure 1.2 is thus a picture of the very small "seeds" of matter concentrations

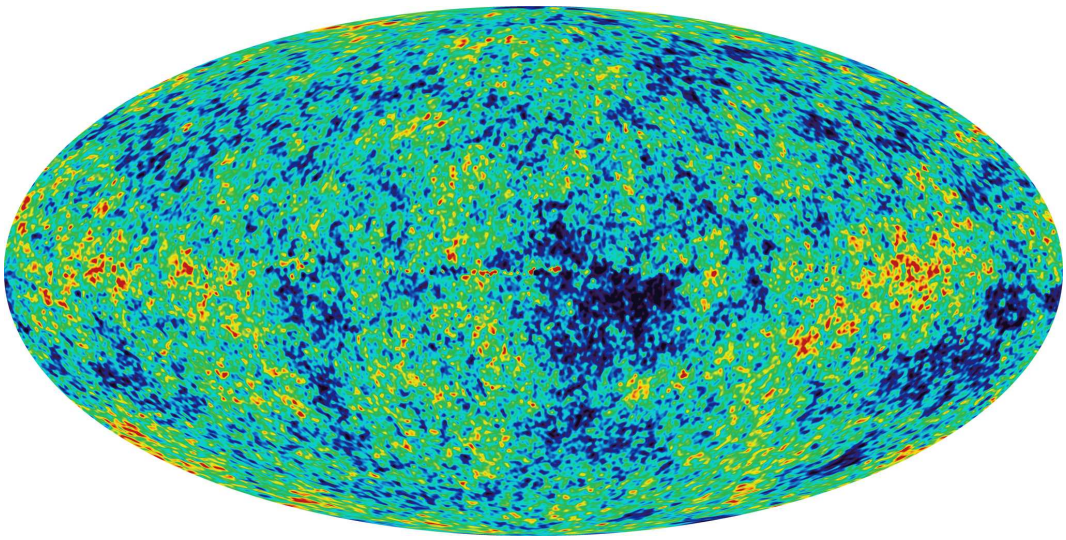

Figure 1.2: Image of the "surface of last scattering" by the *Wilkinson Microwave Anisotropy Probe*. This image is a very precise all-sky temperature map of the Universe from the moment at which protons and electrons combined to form atoms. Yellow/red regions are slightly hotter (by 0.0001 °C) than blue/black regions. This small non-uniformity provides detailed information about the clumpiness (matter concentrations) of the early Universe. (Information about other properties of mass concentrations, such as their relative velocities, is also contained in this map.) *Image Credit: NASA / WMAP Science Team.*

that eventually grew into the large and complex structures observed today. The amplitude of the clumpiness in this figure provides important evidence that much of the Universe ($\sim 60\%$ of all matter) consists of "dark matter," a form of matter that gravitationally attracts all matter but does not interact with light at all (as opposed to protons, electrons, and atoms, the latter of which do interact with light, though much less strongly than charged particles). Because of this property, dark matter was able to begin to cool into concentrations early, while normal matter (protons and electrons) was still being randomly bounced around by collisions with radiation in the primordial soup. The picture in Figure 1.2 is a map of these early dark matter concentrations.

In fact, these concentrations provided the backbone of all the structure in the Universe. To understand this, imagine being a particle in one of the green areas in Figure 1.2. On one side of you is a yellow zone, in which there is slightly more matter and therefore a slightly stronger gravitational pull; on the other side of you is a blue zone, in which there is slightly less matter and therefore a slightly weaker gravitational pull. Clearly, you will fall towards the yellow zone. As this happens over time, the dense yellow clumps become denser and the underdense blue clumps become even more depleted.

Since dark matter experiences only gravity (and does not interact with itself or with light), astronomers find it easier to simulate the evolution of dark matter into ever denser and more massive concentrations over the course of the Universe's history. One of the most massive simulations of this process ever created is called the *Millennium Simulation*, completed in 2005. The gravitational growth of structures according to this simulation is shown in Figure 1.3. The overdense yellow/red regions in Figure 1.2 are represented by light purple and yellow in the color scheme of Figure 1.3; likewise, the underdense blue/black regions in Figure 1.2 translate into dark purple and black in Figure 1.3. In the simulation displayed in Figure 1.3, it is clear that the minor density perturbations in the early Universe (Figure 1.2) grow with time and become much stronger as the Universe evolves.

The bottom panel of Figure 1.3 represents a simulation of the amplitude of structures in the present day Universe. Throughout this simulated universe, multitudes of little yellow dots can be see, as well as several larger yellow regions. The small yellow regions represent the areas in which individual galaxies or small groups of several galaxies will be found, while the larger regions represent the areas in which clusters of hundreds or thousands of galaxies will be found. However, the galaxies themselves are not visible in these images, which represent only the dark matter distribution in the Universe. The dark matter concentrations seen in the images are called "halos" and are the homes in which galaxies reside. The galaxies themselves are made of stars and gas, both of which consist entirely of normal (not dark) matter and therefore can be observed.

1.2.3 The Growth of Galaxies in the Universe

The physics and evolution of normal matter from the primordial soup into galaxies is much more complex than that of dark matter, because normal matter is affected by many phenomena besides gravity. As mentioned above, normal (or "baryonic") matter interacts

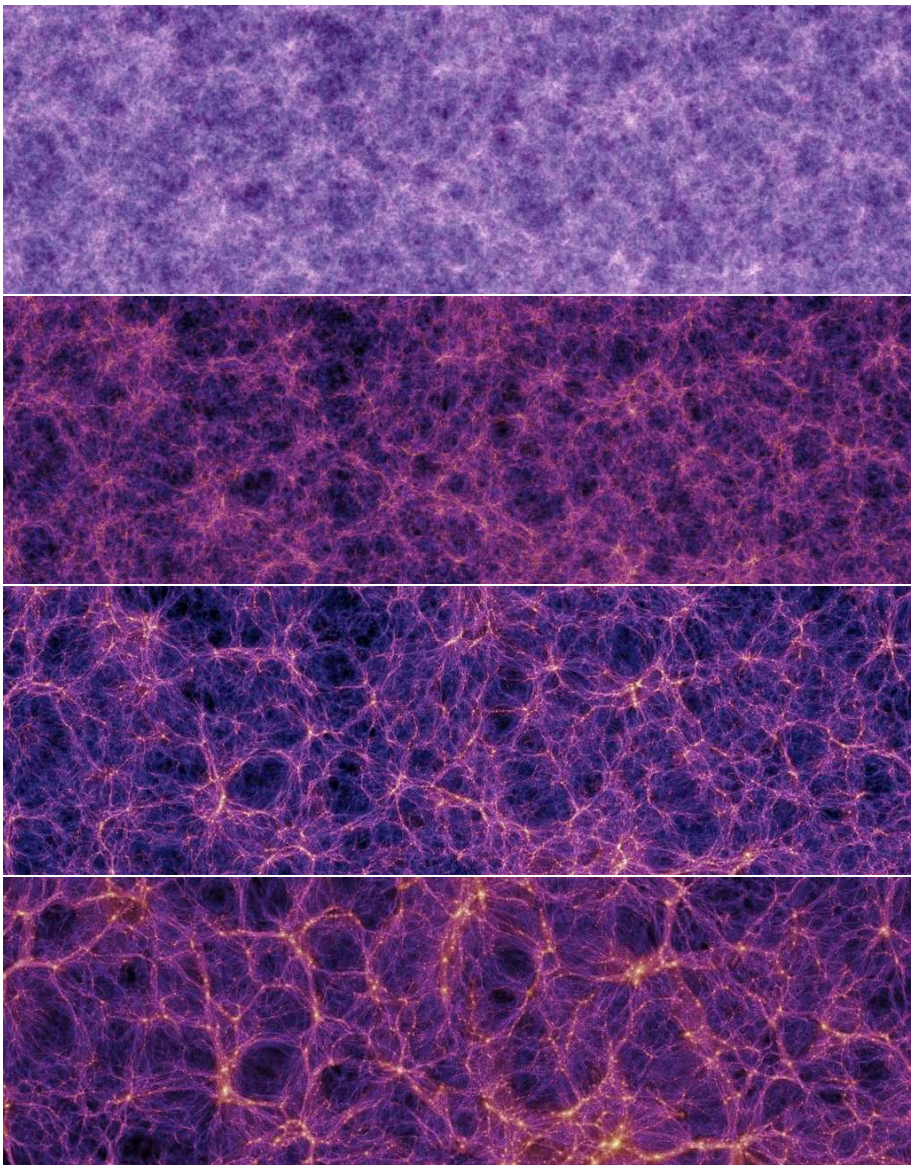

Figure 1.3: Simulated growth of dark matter structures by gravitational attraction of surrounding material over the course of the Universe's history: 210 million years after the Big Bang (*top*), 1 billion years after the Big Bang (*second from top*), 5 billion years after the Big Bang (*second from bottom*), and at present (13.7 billion years after the Big Bang, *bottom*). Light purple / yellow indicates regions of dense matter concentrations, and dark purple / black indicates regions devoid of matter. *Image Credit: Volker Springel.*

with light; atoms can absorb energy from light (excitation, ionization) and re-emit that light (radiation). Additionally, gas in space behaves exactly like a gas on Earth in that its atoms move rapidly and frequently collide with one another. The energy in these encounters is sufficient to excite electrons in the atoms into higher energy levels; to return to their original energy levels, the electrons radiate the extra energy away as light. In this way, energy from the motions of atoms within a gas is converted into radiation and therefore removed from the gas. This process is referred to as dissipation, and dark matter particles, which do not collide with one another or interact with light, have no equivalent behavior.

The structure of galaxies provides an elegant example of the importance of dissipation in shaping dark matter and normal matter structures. If a collection of dark matter particles and gas particles (normal matter) are put into a box, both will fall towards the center of the box under the influence of their mutual gravity. The dark matter particles will feel only this gravity and will therefore minimize their distances from the gravitational center of the system, the center of the box. This will result in a spherical distribution, and indeed dark matter halos around galaxies are known to be roughly spherical (Figure 1.4; true dark matter halos have some angular momentum and are therefore ellipsoids rather than spheres). On the other hand, the gas particles will constantly bump into each other as they fall towards the center of the box, and these encounters will reduce the energy of the gas and allow it to collapse much further. The final distribution of the gas will minimize both the gravitational force and the frequency of collisions experienced by the gas particles. If the majority of the particles were moving in one direction, the minimization is achieved when this motion is shared by all of the gas particles, and the resulting configuration is a small (compared to the dark matter distribution) rotating disk. This is consistent with observations of the gas (and the stars that form out of this gas) in galaxies like the Milky Way (Figure 1.4). The normal matter and dark matter within a galaxy thus have dramatically different distributions.

The different properties of normal matter and dark matter also resulted in very different evolutionary histories. Although the evolution of dark matter can be easily described through gravity alone (Figure 1.3), the evolution of normal matter in the Universe is much more complex. After protons and electrons combined to form atoms (Figure 1.1), the primordial soup separated into light, which could now travel large distances without interacting with matter, and atoms, which were in a gaseous state and were gravitationally attracted to the dark matter structures already in existence (visible in Figure 1.2). This is the point in the Universe's history when the really interesting things began to happen.

Within individual dark matter halos, gas began to accumulate and condense. A first generation of stars was born, which likely were quite different from stars in the present-day Universe, and these stars died quickly in giant explosions. After roughly 1 billion years, the gas in halos further cooled and collapsed into the first galaxies. As with the first stars, this initial generation of galaxies bore little resemblance to present-day galaxies. Once formed, these galaxies embarked on the process of forming stars out of gas and of simultaneously reshaping themselves into the galaxies we observe today. This evolution happened through a combination of processes internal and external to the galaxies. The continuous accumulation of dark matter in dense regions over time (shown in Figure 1.3) implies that the gas contained

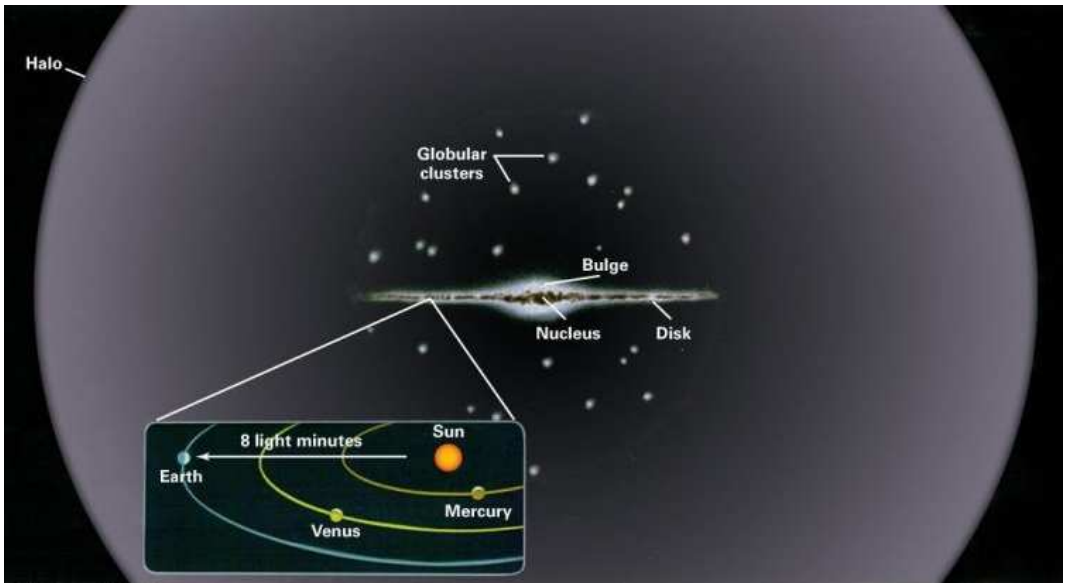

Figure 1.4: Edge-on schematic illustration of the Milky Way Galaxy. The Galaxy is surrounded by an ellipsoidal dark matter halo. Deep inside the halo, the normal matter forms a rotating disk. The Galactic bulge and globular clusters (which live in the sparse "stellar halo") are all composed of normal matter, as is the Solar System, shown here at its location in the Galactic disk. *Image Credit: Thomson Higher Education.*

Figure 1.5: Images of an open (*left*) and globular (*right*) cluster, both in the our Galaxy. *Image Credit: ESO, NASA Hubble Heritage Team.*

in infalling dark matter structures interacted with galaxies already in the dense regions through accretion and galaxy merger events (see §1.3.3).

As galaxies in the Universe grew, they converted their gas into stars rapidly. Additionally, they developed supermassive black holes in their centers and continued to feed these black holes with gas. For the next 2 billion years, this star formation and black hole feeding became increasingly powerful as galaxies continued to grow within the growing dark matter structures shown in Figure 1.3. Eventually, however, galaxies that initially consisted only of gas began to exhaust this gas, which by then had already been converted into stars and larger black holes. As the fraction of galaxies' masses in the gaseous state decreased, this depletion of fuel for star formation and black hole growth became a more important influence on the galaxies than the continued accretion of matter. This occurred roughly 3 billion years after the Big Bang, and the remaining 10 billion years of the Universe's history were characterized by decreasing rates of star formation and black hole growth (see §1.4.2). Galaxies in the present-day Universe are consequently much less active than those 3 billion years after the Big Bang and indeed are "fossil relics" of this earlier epoch of rapid galaxy evolution; I elaborate on this theme in the following sections.

While our understanding of the evolution of galaxies is rather complete in the broad sense outlined here, the formation of a galaxy within a dark matter halo is in fact an extraordinarily complex process. Much of what we know about the evolution of normal matter (gas, galaxies, etc.) in the Universe is observed rather than simulated, because the physics that govern its evolution is far too complicated to be modeled accurately. The answer to the fundamental question of galaxy evolution - what happens inside dark matter halos to turn gas into the galaxies we observe today? - will therefore need to come from observations and from the inferences we can make from these observations. Making progress towards this answer is the general goal of this thesis. In §1.6, I describe my specific goals in detail.

1.3 The Local Population of Galaxies

In order to provide additional context to the above question of how gas in the early Universe is converted in present-day galaxies, I now present an overview of the properties of present-day galaxies.

1.3.1 The Milky Way

Let's begin at home. The Earth is one of eight planets and a number of minor Solar System bodies (including Pluto, sadly) that orbit our Sun. The Sun, in turn, is a very ordinary, middle-aged star among approximately 100 billion stars in the rotating disk of the Milky Way Galaxy. This disk is visible in the edge-on (side) view of the Galaxy in Figure 1.4, with stars represented in white. Within this disk is a much thinner disk, darkened because of the large concentration of dust in it. In the Universe, dust (small collections of molecules floating around in space) and gas (single molecules floating around in space) always occur

together; the dust lane seen in this image of the Milky Way therefore indicates the presence of a very thin gas disk. It is the gas in this disk that is condensing to form young stars. If we could look at the Milky Way from above (which is impossible, since the Sun is embedded within the Milky Way), we would see spiral arms in the Galaxy disk, and these spiral arms are the regions in which the gas is most condensed and consequently in which the formation rate of young stars is highest. This process has been occurring for roughly 10 billion years, so stars in the Galactic disk have a range of ages from 0 to 10 billion years. For comparison, our Sun is 5 billion years old, and the Earth is only slightly younger, having formed out of the debris surrounding the Sun shortly after the Sun's formation.

Surrounding the disk, or "thin disk," of the Galaxy is a much less populous "thick disk" (not depicted in Figure 1.4). The thick disk is so called because it has a larger vertical extent than the very concentrated thin disk. As depicted in Figure 1.4, the concentration of gas and dust in the center of the thin disk implies that there very little gas in the thick disk, and this absence of fuel in turn implies that there should be no star formation in the thick disk. This is indeed the case and has been for quick some time; all of the stars in the thick disk are 10-12 billion years old. The thick disk stars are similar in age to those of the Galactic bulge, the spherical stellar concentration at the center of the Galaxy around which the disk is rotating. As in the thick disk, the paucity of gas in the bulge is largely responsible for the low rate of star formation and the corresponding dearth of young stars. This is in contrast to appearances in Figure 1.4, in which the dust lane appears to strengthen towards the Galatic bulge. This is actually a projection effect; in the edge-on image, we're looking directly through the thin disk, and all of its associated gas, to see the bulge. In other words, the dust that we see projected onto the bulge lies between us (the observers) and the gas-poor bulge, in the intervening thin disk. This is exactly how the Galactic bulge appears when viewed from Earth, from whose position inside the thin disk the Galaxy is viewed edge-on.

Moving outwards, the Galactic disk and bulge are surrounded by small population of spherically distributed stars in the so called "stellar halo." In Figure 1.4, these stars are concentrated in the inner (dark grey) regions of the full dark matter halo, close to the Galaxy. These stars have very old ages ($>$ 12 billion years) and, as such, are older than the vast majority of stars in the Galaxy. The stars in the stellar halo must therefore have been formed prior to those in the main galaxy body, even the bulge and thick disk, and must have existed thereafter in an absence of gas and revived star formation. For this reason, the stellar halo can provide insight into galaxy formation in the very early Universe, before the main components of galaxies were assembled. While the stellar halo is therefore a rich and interesting research topic, the "pre-galaxy" epoch it probes is outside the scope of this thesis, which instead focuses on the assembly of the major components of galaxies: their bulges and disks.

Finally, Figure 1.4 also illustrates the presence of a number of globular clusters, old stellar systems that are distributed throughout the stellar halo as well as in the region of the bulge and thick disk. In Chapter 6, I explore the properties of globular cluster systems in depth and relate these structures to other components in galaxies. For the moment, I

suffice with an illustration of the special nature of these systems in Figure 1.5. The left image is an example of an open cluster, a loose affiliation of 10-1000 stars that is formed in the thin disk of the Milky Way. In contrast, the right image of a globular cluster illustrates the incredibly dense nature of these collections of up to 1,000,000 stars. Since we do not observe globular clusters being formed today in the Milky Way, the conditions of the gas that formed these remarkable systems must have been quite different from those that exist in our Galaxy currently. I return to this point in Chapter 6.

1.3.2 Nearby Galaxies

The components of a galaxy outlined here are by no means unique to the Milky Way; the Milky Way is an average spiral galaxy whose properties are not so different from the population as a whole. However, there are other types of galaxies besides spirals, all of which can be seen in the immediate surroundings of the Galaxy. Continuing our outward journey then, the next structure of interest is the Local Group, a loose collection of several tens of galaxies. As shown in Figure 1.6, this Group consists of our Milky Way, a slightly larger spiral galaxy known as Andromeda, a smaller spiral galaxy known as the Triangulum, and many very small "irregular" galaxies orbiting the spiral galaxies. Of the members of the Local Group, Andromeda can be seen on very dark nights as a smudge in the sky and is easily viewed with a small telescope. The two most massive irregular galaxies near the Milky Way, seen to the lower right of the Galaxy this diagram, are the Large and Small Magellenic Clouds. Both can easily be viewed from the Southern Hemisphere; their appearance is similar to that of the "Milky Way," the swath of stars that stretches across the night sky and that is actually a view through the thin disk of our Galaxy. The Magellenic Clouds can be readily identified by their similar appearance but large distance in the sky (and in reality) from the band of the Milky Way.

Irregular galaxies, so named for their lack of defining structures such as obvious disks or bulges, are quite different from spiral galaxies. Most noticeably, they are 10-1000 times less massive than spiral galaxies and correspondingly smaller. Closer examination shows that their appearance is also very lumpy and that this lumpiness corresponds to large concentrations of stars. These concentrations also contain significant amounts of gas, which itself is forming additional young stars. Indeed, the large mass fractions of gas in irregular galaxies (several times higher than in spiral galaxies) means that irregular galaxies are more vigorously star-forming and consequently have stellar populations that are, on average, younger than in their spiral cousins. As a class, irregular galaxies are quite interesting. These galaxies probe the physics of star and galaxy formation in different environments than in spiral galaxies; their interactions with larger galaxies in the Local Group teach us about the structure and evolution of galaxies and of the Group as a whole; and their gaseous and smaller state can serve as useful analog for larger galaxies at the beginning of the Universe, in the early stages of their formation. This analogy, however, must be used with care, since the Local Group is a markedly different environment than the early Universe. I now turn away from irregular galaxies for the remainder of this thesis and instead focus on larger spiral and

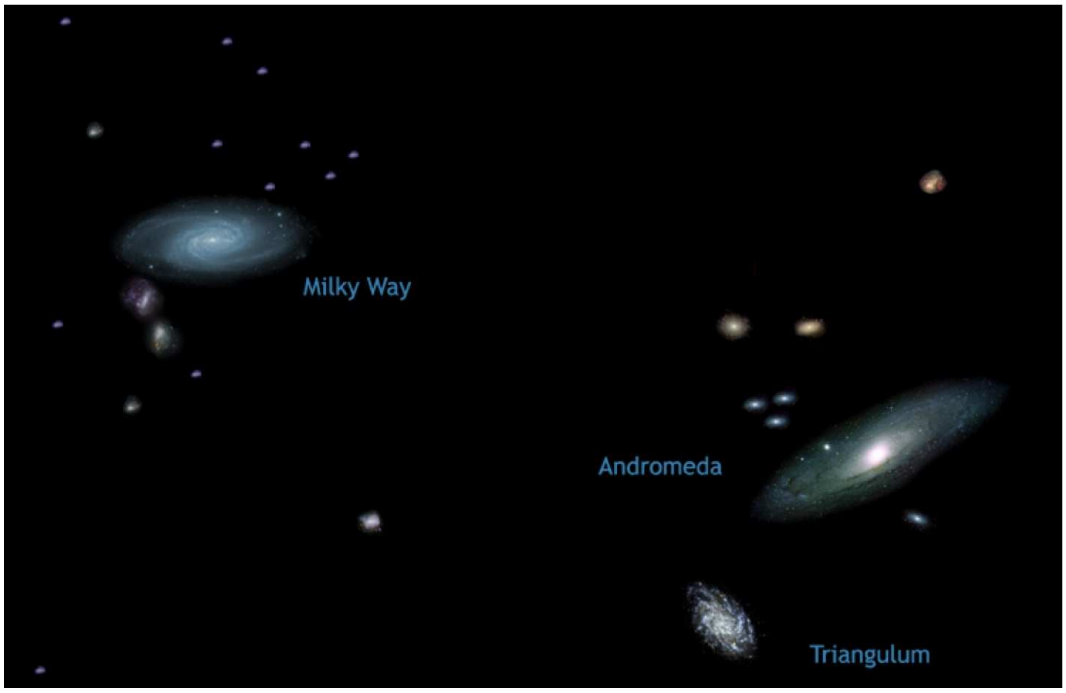

Figure 1.6: Representation of the galaxies in the Local Group, including three spiral galaxies (the Milky Way, Andromeda, and the Triangulum) and roughly 30 irregular galaxies, including the Milky Way's nearest neighbors, the Large and Small Magellenic Clouds. *Image Credit: NASA.*

Figure 1.7: Images of the center (*left*) and entirety (*right*) of the Virgo Cluster. Although this cluster has roughly the same diameter as the Local Group, it contains over 1000 galaxies. In the right image, nearly all of the points visible are in fact galaxies. Although the Virgo Cluster contains all types of galaxies, including the spiral galaxies visible as thin disks in the left image, it is dominated by elliptical galaxies, which appear diffuse and roughly spherical in images. *Image Credit: Rainer Zmaritsch, Matt BenDaniel.*

elliptical galaxies, which contain the bulk of the mass in the Universe.

To find the nearest sizable group of elliptical galaxies, we must travel a distance of approximately 15 times the diameter of the Local Group, arriving at the Virgo Cluster. Figure 1.7 shows the center of the Virgo Cluster (left), which is dominated by very massive elliptical galaxies, easily identified by their diffuse and elliptical appearance. However, this cluster in fact contains roughly 1000 galaxies, as seen in the right panel of the figure, many of which are also elliptical galaxies. Although elliptical galaxies also occur outside of dense, galaxy cluster environments, the occurrence rate of these typically more massive galaxies compared to spiral galaxies increases dramatically in galaxy clusters.

Before discussing why it might be that elliptical galaxies are found more frequently in clusters, I gather some clues from the left panel of Figure 1.7. In the two largest systems in the image, both of which are elliptical galaxies, the characteristic dust features that trace gas (as in Figure 1.4) are not visible. As one might expect, this is due to the paucity of gas in these galaxies; the traditional understanding of elliptical galaxies is that they completely lack gas and thus star formation activity. In recent years, very sensitive observations of elliptical galaxies have shown that they do in fact contain very small (by mass fraction) amounts of gas and star formation, and we explore this further in Chapter 5. However, these new results do not change the long-standing conclusions that elliptical galaxies lack significant star formation and therefore consist primarily of very old stars. In this regard, as well as in their general shape and other properties, elliptical galaxies turn out to be very closely related to the bulges of spiral galaxies.

In fact, as shown in Figure 1.8, there is a smooth transition in galaxy types from more massive elliptical galaxies (left) to less massive spiral galaxies (right) galaxies. Moving from the left to the right in this diagram, the importance of the old, spherical bulge relative to the star-forming disk clearly decreases. Likewise, the relative gas content and resulting star formation activity in galaxies increases to the right in this diagram. The galaxies that occur at the junction between the old elliptical and star-forming spiral regimes are known as "lenticular" galaxies; these systems consist of massive bulges surrounded by smooth disks (without spiral arms) that lack star formation. In recent years, it has become increasingly clear that this scheme, laid out by Edwin Hubble nearly 100 years ago, encapsulates very deep physics on the spiral galaxy half of the diagram and that the prominence of the bulge versus that of the disk is an important driver, and reflection, of a galaxy's evolution. His success on the left side of the diagram was less impressive; it is now known that elliptical galaxies in fact divide into only two classes: one that is strictly dominated by a bulge (called "boxy" or "slow-rotating" ellipticals) and another that contains a low-mass, gas-poor disk rotating around the large bulge (called "disky" or "fast-rotating" ellipticals). Moreover, this latter class appears to be very closely related to lenticular galaxies, blurring the division between ellipticals and lenticulars. Consequently, many studies of the properties and evolutionary histories of these galaxies (as in Chapter 5) include both ellipticals and lenticulars, lumping them together as "early-type" galaxies. This is in contrast to spiral galaxies, which are referred to collectively as "late-type" galaxies. As with so much of the nomenclature in astronomy, these names are arbitrary, are maintained for historical reasons, and have no

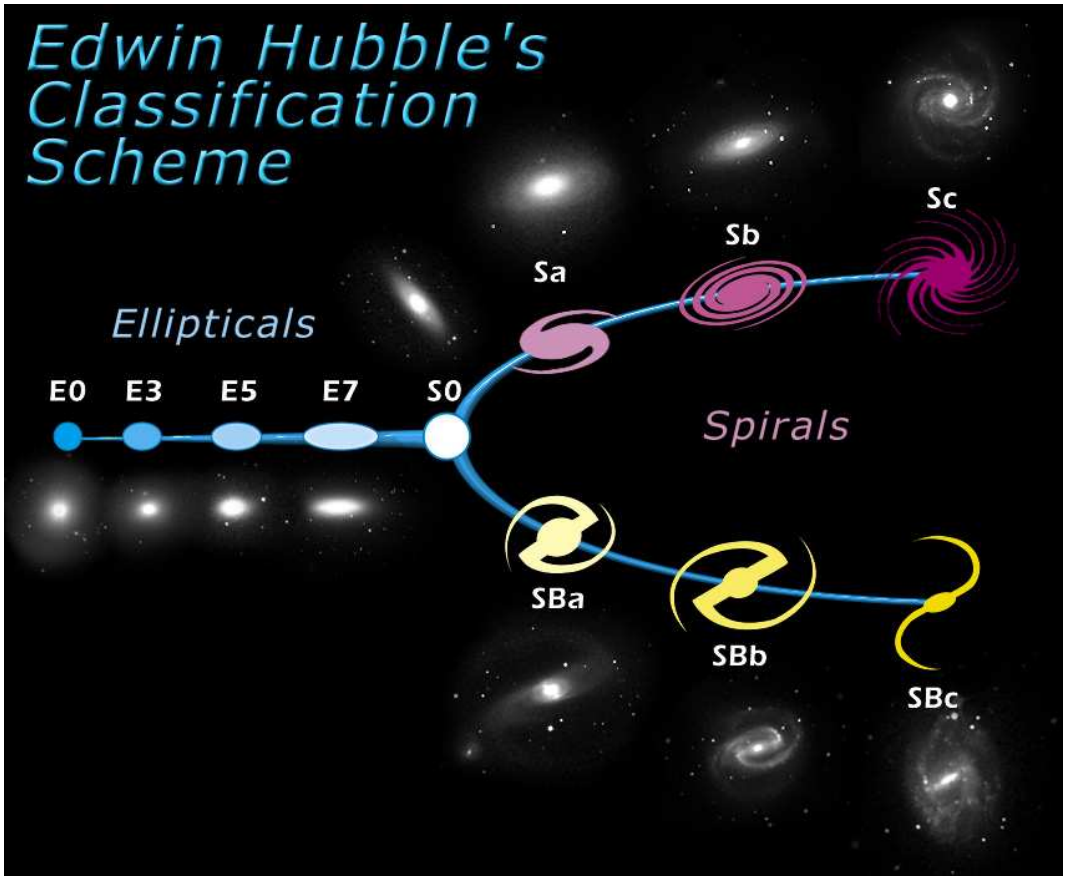

Figure 1.8: The original galaxy classification scheme (also known as the "Hubble Tuning Fork" because of its shape), created by Edwin Hubble in 1926. The properties of galaxies along the Hubble sequence are shown both schematically and with images of representative galaxies for each morphological type. The "early-type" galaxies on the left of the sequence, ellipticals (E0-E7) and lenticulars (S0), are smooth, bulge-dominated systems. The "late-type" galaxies on the right are spirals and divide into two categories: those with straight features called bars emerging from the bulge (SBa-SBc), and those without bars (Sa-Sc). Along the spiral sequence, moving towards later types, bulges become less important and spiral structure becomes more pronounced. As a result, the disk-dominated latest-type spiral galaxies tend to have the highest gas fractions and the highest fractions of young stars. These galaxies are also generally less massive than the early-type spirals and the ellipticals. Modern versions of the Hubble sequence sometimes also include irregular galaxies, whose disorderly structure, high gas fractions, young stellar populations, and low masses place them to the right of the latest-type spirals. *Image Credit: SDSS.*

relation to actual physics.

1.3.3 The Formation of Bulges and Elliptical Galaxies

In § 1.2, I showed that a rotating disk is a natural configuration for gas in a dark matter halo, and it is therefore, in principle, very easy to imagine how the disks of spiral galaxies might form. On the other hand, the formation of elliptical galaxies and of the bulges in spiral galaxies requires more thought, since these configurations are extreme departures from an original disk-like morphology. A clue to how this might occur can be found in on the right side of the left panel of Figure 1.7, in which a close pair of galaxies appears to be surrounded by wisps of material indicative of an exchange of matter as the two galaxies interact. In fact, galaxy mergers such as this one have been shown to be capable of completely rearranging the internal structure of galaxies and redirecting the orbits of stars from a rotating disk into a spherical configuration. Since galaxy interactions will happen much more frequently inside a dense galaxy cluster, the observed larger population of elliptical galaxies in clusters is a logical result. Such mergers are one avenue through which bulges and elliptical galaxies can be formed but are by no means the only one. For example, another mechanism of galaxy transformation using only internal processes to redistribute the matter inside galaxies has received increasing attention in recent years, and I explore this alternative mechanism in greater detail in Chapter 6.

Figure 1.9 illustrates galaxy interactions and accretion of external gas; these are the ways in which galaxies are observed to grow and evolve. Galaxy interactions come in two flavors: major and minor mergers. Major mergers are defined as galaxy collisions between two galaxies of nearly equal mass. Quantitatively, if the less massive of the two galaxies is at least 1/3 the mass of the more massive galaxy (i.e. their mass ratio is <3:1), then the collision is a major merger (top panel in Figure 1.9), and it will redistribute the majority of the galaxies' mass. If the less massive of the two galaxies is between 1/3 and 1/10 the mass of the more massive galaxy (i.e. their mass ratio is 10:1 – 3:1), the event is a minor merger (middle panel of Figure 1.9), and the matter distribution will be less dramatic. The degree of matter distribution also depends on the amount of gas in the merging galaxies; "gas-rich," or "wet," mergers occur between two spiral galaxies and include additional star formation during the merger, and "gas-poor," or "dry," mergers involve two elliptical galaxies and no additional star formation. Finally, galaxies can also grow through the accretion of surrounding gas (bottom panel of Figure 1.9). When a galaxy is at the intersection of filaments in the cosmic structure (see Figure 1.3), this gas can flow in along the filaments in several highly concentrated streams; Chapter 2 discusses the importance of this mode of accretion in the early Universe. In the present-day Universe, however, the intersections of filaments correspond to large galaxy clusters; individual galaxies live inside the filaments and are consequently accreting their gas from all directions. This phenomenon is directly observed in the Milky Way, for which Figure 1.9 shows an isotropic distribution of the inflowing gas. The relative importance of accretion, minor mergers, and major mergers to the growth of galaxies and bulges in the general galaxy population remains a topic of intense

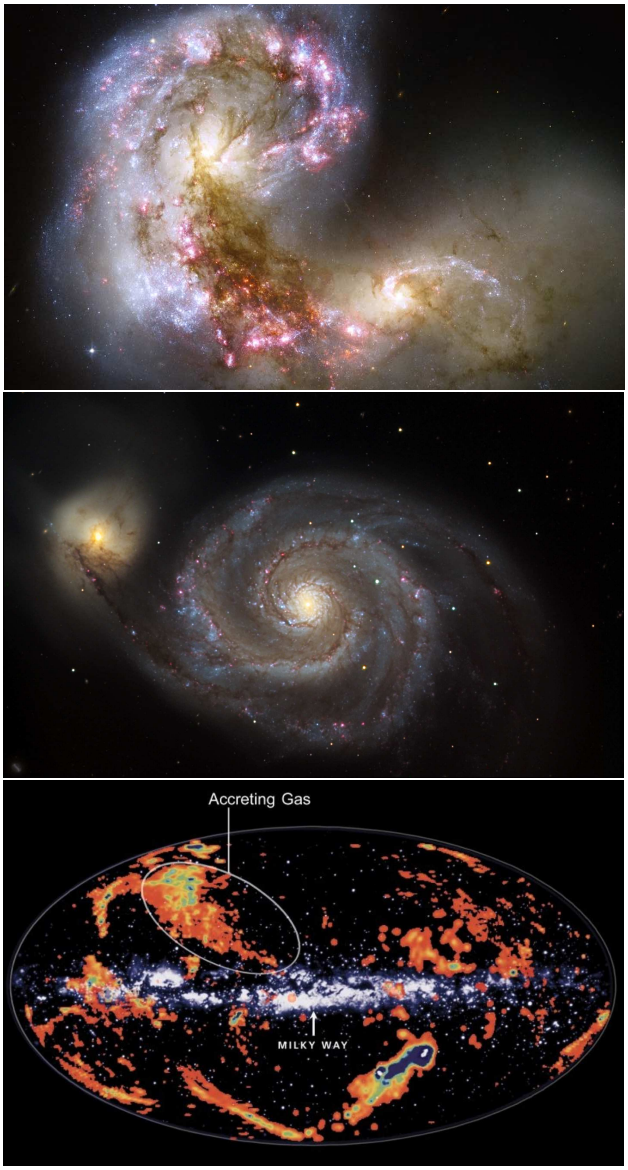

Figure 1.9: Examples of galaxy growth and evolution through a major merger (*top*), a minor merger (*middle*), and gas accretion (*bottom*). The major merger shown here is a system known as the Antennae and consists of a dramatic collision between two spiral galaxies. The minor merger is the spiral galaxy M51 and its lenticular companion. Gas accretion is shown in the Milky Way, in which sensitive observations of cold gas (*false colors blue through red*) detect its inward motion onto the plane of the Galaxy (*white*). *Image Credit: NASA / ESA / Hubble Heritage Team, Jon and Byran Rolfe / Adam Block / NOAO /AURA / NSF, B. Wakker/NASA.*

research, and a general consensus has yet to emerge.

Finally, when considering the formation of bulges and elliptical galaxies, one must account not just for the change in shape of the system but also the change in gas content and star-forming properties. The formative event converts star-forming spirals into bulges and ellipticals, whose persistent lack of gas over many billions years makes their stellar populations very old. How this is accomplished via the loss, removal, or exhaustion of a galaxy's gas is a major topic of current research. One solution that has received a great deal of recent attention involves the supermassive black holes that are known to reside in the centers of bulges. During a merger or internal process that is redistributing a galaxy's stars, the galaxy's gas content will also be rearranged and, in particular, driven to the galaxy center. Such a large amount of rapidly condensed gas has been observed to cause a powerful and spectacular burst of star formation. Some of this gas also falls into the supermassive black hole and creates a so-called Active Galactic Nuclei (AGN), in which the strong gravitational effects of the black hole on the infalling gas cause it to radiate intensely. It has been suggested that this AGN radiation is so strong that, when it encounters the gas in the remainder of the galaxy, it forces this gas out of the galaxy. This complete evacuation of star-forming material leaves behind a gas-free galaxy that has, during the merger, been rearranged into a bulge-like shape. This solution is an appealing explanation of the gas-poor nature of early-type galaxies; however, it remains unconfirmed by observational evidence.

As demonstrated in the preceding few paragraphs, there are major questions remaining in our understanding of how galaxies, especially bulges and elliptical galaxies, are formed. In this thesis, I seek to address some of these questions and to augment our understanding of the formation and evolutionary process that control the growth of massive galaxies, which I define as bulge-dominated spiral (Sa and SBa in Figure 1.8), lenticular (S0), and elliptical (E0-E7) galaxies.

In this endeavor, much can be learned about galaxy formation from present-day galaxies, whose properties reflect the events that occurred during their long ($>$ 10-12 billion years) formation histories. Studying galaxy formation using these galaxies is, in this way, a bit like archaeology. As in archaeology, the best fossils are obtained from objects that have undergone very little evolution since their formation; archaeologists take advantage of dry regions that have had minimal rain, plant growth, and erosion, and astronomers take advantage of gas-poor structures that have experienced minimal star formation. These structures are bulges and elliptical galaxies, which are nearly pristine fossil records of their formation histories, and, if properly excavated, they can teach us much about how galaxies were assembled. I present one example of such an analysis in Chapter 4. However, with great care, one can also gain significant insight from galaxies and regions in galaxies that are still experiencing star formation, for example by tracing the history of the star formation activity through the resulting relics of different ages. In Chapter 5, I use such an analysis to probe small amounts of star formation in massive galaxies and to make inferences about their assembly histories.

1.4 Galaxies in the Distant Universe

Obviously, it would be even better to study galaxies directly *during* their formation and assembly; this amounts to the archaeological equivalent of hanging out in Mesopotamia or ancient China at the dawn of civilization. In this sense, astronomy is kinder than archaeology, because the Universe gives us this opportunity. However, there is a catch: we can only do it from a great distance, as if the ancient Chinese culture still existed on Earth but we had to study it without leaving California.

1.4.1 Distances and Redshift

This astronomical trick is a result of the law that absolutely no signal can travel faster than the speed of light. This includes radio signals, microwaves, heat, and ultraviolet radiation, all of which are actually the same phenomenon as visible light. It takes light 1.3 seconds to travel from the Earth to the Moon, so if an astronaut on the Moon is talking on the phone (via radio signals, as NASA talks to astronauts) to her husband on Earth, there will be an irritating delay in which he has to wait 1.3 seconds for her to hear his question and another 1.3 seconds for her answer to reach him. We therefore say that the Moon is 1.3 light-seconds away.

Now let's put our intrepid astronaut in a spaceship orbiting our nearest star, Alpha Centauri. (We'll let her bring her husband along for this more ambitious journey.) Alpha Centauri is 4.4 light-years away from our Solar System, which means it takes everything in the Universe (including the spaceship) *at least* 4.4 years to travel between Alpha Centauri and Earth. Let's say that once our astronaut and her husband have reached Alpha Centauri, they have a baby, which would be a rather irresponsible thing to do in space. They then set up a webcam for their parents on Earth to watch their grandson grow up. Since the signal from the spaceship moves at the speed of light, by the time the grandparents get to see images of the newborn baby for the first time, he is already 4.4 years old. By the time the grandparents get to see him at 4.4 years old, he is already almost 9 years old. Because of the great distances between the baby and the grandparents, they will forever be incapable of seeing him as he is right now.

In much the same way, when we look at the Andromeda Galaxy, at a distance of 2.5 million light-years (or 7.8 kiloparsecs, where 1 parsec (pc) is 3.26 light-years), we are actually seeing it *as it was* 2.5 million years ago. And this is the nearest spiral galaxy to the Milky Way! The remainder of the galaxy population is more distant, so their light takes longer to travel towards earth. When we view increasingly distant objects, we are therefore viewing them further and further back in history. One might imagine that if we could find objects that are over 10 billion light-years away, we could actually *watch* galaxy formation unfold 10 billion years ago, during the epoch of the most rapid star formation activity in galaxies in the history of the Universe (§1.2). In fact, this is exactly what we do, and I will present observations of galaxies in the early Universe in Chapters 2 and 3. The great distances of these objects mean that they appear very faint, but the demanding observations needed to

study these galaxies produce incredibly rewarding results.

In addition to traveling great distances over many billions of years to reach Earth, the light from distant galaxies also gets "stretched" as it travels through an ever-expanding Universe (Figure 1.10). In other words, the wavelength of the light waves increases. Since red light has a longer wavelength than blue light, this effect is referred to as "redshifting;" the increasing wavelength corresponds to the light is becoming more red. Due to the fact that the Universe is expanding at the same rate everywhere, light that travels to Earth from two galaxies at the same distance from Earth but in different directions will undergo the same amount of redshifting; astronomers can therefore use the so-called "cosmological redshift" of the light to measure and quantify the distance to a galaxy. Galaxies with a higher redshift are observed with light that spent more time traveling longer distances through the expanding Universe. "High-redshift" galaxies thus probe earlier epochs in the Universe's history. Of particular relevance to this thesis is the fact that a distance of 10 billion light-years corresponds to a redshift (z) of approximately 2, written as $z \sim 2$. Redshifts of $3-4$ probe even earlier into the Universe's history, and the earliest known galaxies are found at redshifts of $8-10$.

1.4.2 Galaxy Evolution over Cosmic Time

Using the tool of redshift, I now quantify my statement from §1.2 that star formation and black hole activity peaked 10 billion years ago, or 3 billion years after the Big Bang, at $z \sim 2$. This is shown in Figure 1.11, in which the total star formation rate and black hole activity in the Universe are plotted over a wide range of distances and thus a wide range of look-back times and of redshifts. The prominent peak in these quantities at $z \sim 2$ corresponds to the assembly of the majority of mass in galaxies and especially in massive galaxies.

The star formation rates in individual galaxies in the distant, early Universe must therefore have been significantly larger than what we observe in star-forming galaxies today. Moreover, the peak in this activity 10 billion years ago is a close match to the observed ages of stars in elliptical galaxies and bulges, and there is ever-increasing evidence that $z \sim 2$ is indeed the era in which the majority of stars in elliptical galaxies and bulges were formed. This creates an interesting scenario; while today star formation is restricted to galaxies with lower masses (spirals and irregulars), star formation 10 billion years ago was much more powerful and was taking place in galaxies destined to become elliptical galaxies and bulges in spiral galaxies. Figure 1.11 shows that a similar phenomenon was happening to the supermassive black holes in the centers of these galaxies. These two effects are known collectively as "downsizing," because the most massive structures in the Universe underwent much more powerful star formation and AGN activity earlier than less massive structures.

The phenomenon of downsizing encapsulates the observational result that galaxy assembly was much more interesting in the early Universe than it is today, especially at $z \sim 2$. Assembly processes such as gas accretion and the resulting star formation and black hole growth were happening quite rapidly and producing huge numbers of young stars and grow-

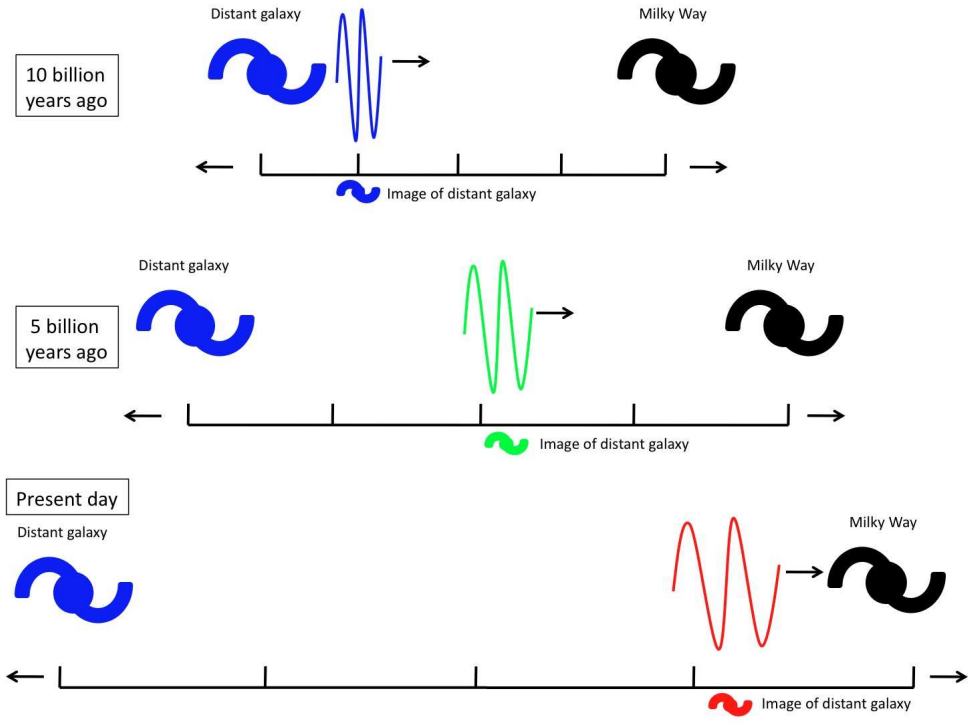

Figure 1.10: Schematic of cosmological redshifting of light from a galaxy 10 billion light-years away from the Milky Way as the light travels towards us. Ten billion years in the past (*top*), the distant galaxy (*blue*) is emitting light carrying an image of the galaxy as it is (*small blue image under the light wave*). As that light travels towards us (*middle*), the wave gets stretched with the expansion of space in the Universe (*expanding ruler*); halway along its journey, the light is somewhat longer, and the image of the galaxy it's carrying would be visible at green wavelengths. When the light finally reaches us (*bottom*), the continued growth of the Universe has stretched the light even further, and we observe the distant galaxy only when looking at red wavelengths. The light we observe is therefore an image of the galaxy as it was 10 billion years ago, shifted into longer (red) wavelengths.

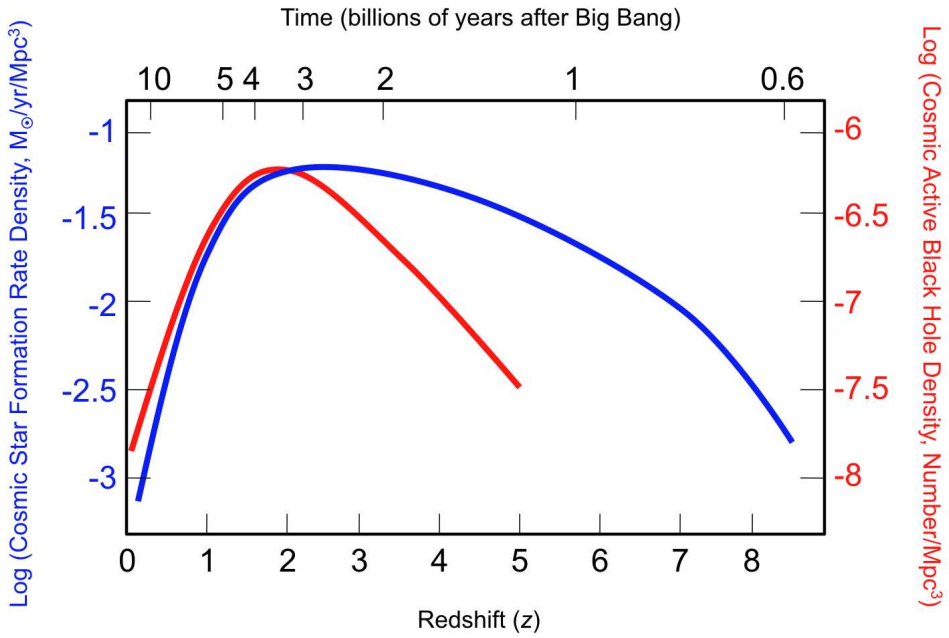

Figure 1.11: Evolution of the rate of star formation (*blue*) and black hole activity (*red*) during the Universe's history. Both are given as densities: the total star formation rate and the number of active black holes per volume, where this volume (1 Mpc^3) is large enough to contain a number of galaxies. The maximum of both densities marks the epoch of the most rapid galaxy evolution in Universe; this occurs between 2 and 4 billion years after the Big Bang (*top axis on left plot*), corresponding to $z \sim 2$. *Image Credit: Adapted from data of Silverman et al. (2005) and Bouwens & Illingworth (2006).*

ing supermassive black holes. The processes that were driving this rapid evolution are of great interest, since the majority of the mass in the Universe was assembled into stars and galaxies during this time.

The obvious questions are then: What was driving this explosion in galaxy evolution at $z \sim 2$? What was so different in the early Universe that made activity in galaxies so much more dramatic 10 billion years ago than it is today? The answer, given already in §1.2, is gas. In the beginning of the Universe, all of the normal matter was in gas (as opposed to in stars). As galaxies grew and accreted their surrounding material, the vast majority of this material was in gaseous form and could therefore immediately contribute to heightened star formation and AGN activity. The downturn in activity in Figure 1.11 towards lower redshifts marks a change in this bountiful growth, caused at least in part by the conversion of a significant fraction of the Universe's gas into stars and the resulting inability of gas-depleted accreting material to fuel new star formation in the growing host galaxy.

This description of galaxy evolution is significantly limited by the fact that it consists of only very general conclusions, reached by averaging over large volumes of space containing many galaxies. The details of galaxy formation and assembly need to be understood to the level of the processes that affect *individual* galaxies. In particular, a complete picture of galaxy evolution requires knowledge of how galaxies in the Universe accrete their gas, how star formation and black hole growth are fueled inside these galaxies, and how these galaxies assemble the major components observed in galaxies in the local (present-day) Universe. In Chapters 2, 3, and 6, I present work done for this dissertation that makes progress in addressing these questions.

1.5 How We Study Galaxies

In the subsequent section (§1.6), I continue the above discussion and describe in detail the content of this thesis and its contributions to our understanding of galaxy evolution. However, since the work I present in this thesis is based on observations, I digress briefly in this section to describe the techniques through which we study galaxies.

1.5.1 The Unique Challenge of Astronomy

Section 1.4 began with the analogy of a historian in California trying to study ancient China. As illustrated in §1.4.1, if China were 3000 light-years away, Californians in the present day would observe the Chinese culture of 3000 years ago. However, when viewed from California, China appears very small and very faint (forgetting for a moment about the curvature of the Earth, which places China well over the horizon). Moreover, our observing location in California only lets us see China from a single angle; if a mountain in Japan happens to block our view of a particularly interesting Chinese city, there's nothing we can do about it.

Such is the fate of astronomers. In exchange for privileged access to the Universe

throughout its history, we are rooted to a single location in the Universe and are limited entirely by what we can *see*. If something is blocked from our view or is oriented at an unfortunate angle, we are helpless. As natural scientists, this makes astronomers rather unique. Physics, chemists, and biologists can alter and repeat experiments to explore a confusing result; they can make measurements from every angle to understand the three-dimensional properties of their experiment; and they can use all of their senses and a variety of tools to measure the different properties (weight, temperature, speed, composition, etc) of objects under study. Astronomers, on the other hand, have only one experiment, the existence of the Universe, which cannot be re-run; we must study this experiment from only a single perspective, our view of the Universe from Earth; and we can make no measurements other than observing the light emitted by the objects we hope to study.

As a result of this predicament, astronomers have developed sophisticated methods of observing, recording, and interpreting light emitted by objects elsewhere in the Universe. In the remainder of this section, I present three such methods and the ways in which these techniques can be used to probe galaxy formation and evolution.

1.5.2 Photometry

The simplest way to record the appearance of an object for future use and inspection is to take a picture. In astronomy, this is accomplished by attaching a camera to the eyepiece of a telescope and opening the shutter for an extended amount of time; this technique is referred to "photometry." The technology available for photometry of visible light (also called optical light) has evolved alongside everyday camera technology from photographic plates, whose recording and processing was analogous to 35mm film, to powerful versions of the same electronic chips (charge-coupled devices, or CCDs), found today in digital cameras.

The oldest of the photometric techniques, imaging at optical wavelengths, has been exceptionally fruitful. A single-color picture of a galaxy (akin to a black-and-white photograph) contains direct information about the size and shape of the galaxy. Additionally, the image quantifies the amount of light coming from the galaxy, which is a proxy for the number of stars in the system and therefore also for its total mass. Photometry can provide even more leverage if images are taken through multiple color filters; for example, a red filter will let only the galaxy's red light pass and be recorded by the camera, while a blue filter will permit only the galaxy's blue light be imaged. Images through three filters (typically red, green, and blue) can then be combined to create "true color images." One common use of such data is an analysis of the colors of the stars. The light from a young stellar population will be dominated by short-lived massive stars, which emit strongly in blue wavelengths, while the light from an older population will be dominated by long-lived less massive stars, which emit the vast majority of their light at redder wavelengths. These effects can be seen clearly in Figure 1.5, in which the true color image of the young open cluster appears blue and that of the old globular cluster appears red. Likewise, the left panel of Figure 1.7 illustrates that elliptical galaxies are red and thus have old stars, while the somewhat younger spiral galaxies in the image have bluer colors.

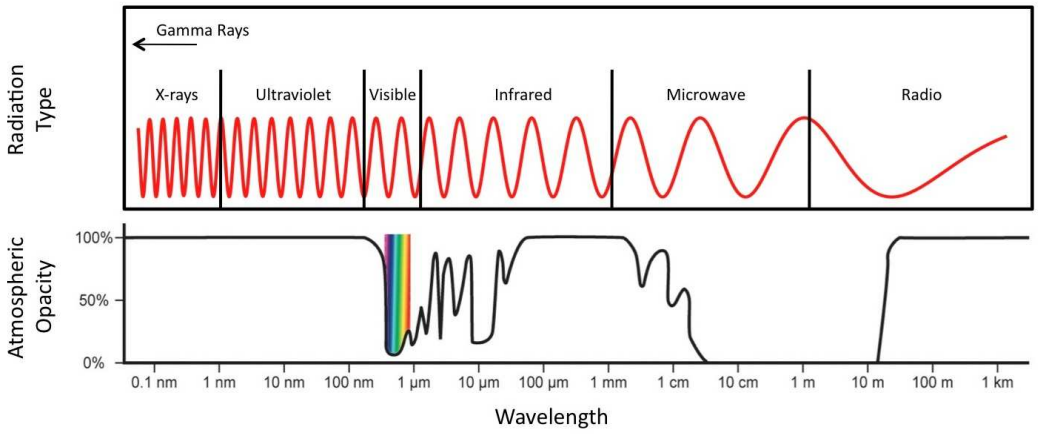

Figure 1.12: The electromagnetic spectrum (*top*), ranging from the shortest wavelength light (gamma rays and X-rays) to the longest wavelength light (microwaves and radio waves). The shortest visible wavelengths are purple; light with shorter wavelengths falls in the ultraviolet regime. The longest visible wavelengths are red; light with longer wavelengths falls in the infrared regime. Shorter wavelengths corresponds to higher frequency and therefore higher energy in individual packets of light, called photons. The Earth's atmosphere is necessarily almost entirely opaque to all high energy radiation (*bottom*), since this radiation is harmful to life. Everyday experience supports this fact with intuition, since the small amount of ultraviolet radiation from the Sun that penetrates the atmosphere causes sunburns and long-term skin damage. At longer wavelengths, the atmosphere is transparent to major portions of the electromagnetic spectrum, allowing ground-based astronomy at visible, parts of the infrared, microwave, and radio wavelengths. Those wavelengths not accessible from the ground can only be studied with space-based observatories in orbit outside the Earth's atmosphere. *Image Credit: Adapted from graphic created by NASA.*

In the past 50 years, advances in detector technology have enabled astronomers to reach beyond the visible spectrum and perform photometry in other wavelength regimes. Figure 1.12 is a schematic of the entire spectrum of light, called the electromagnetic spectrum, of which visible light is only a very small part. The lower panel of this figure illustrates the obscuration of much of the spectrum by the Earth's atmosphere; intense radiation at these wavelengths is very harmful to life. Progress in the space program, resulting in a number of astronomical satellites outside the atmosphere, has made observations at these wavelengths possible and in this way has opened up the full electromagnetic spectrum for investigation. This is critical to the study of astronomical phenomena, since each wavelength regime provides unique insight, as explicitly shown in Figure 1.13 and described in the following paragraphs.

Beginning at the left of Figure 1.12, the most energetic radiation in the Universe is that with the shortest wavelengths, gamma rays and X-rays. This form of radiation is produced primarily by AGN, the active supermassive black holes in the centers of galaxies. X-ray observations are useful measurements of the rate at which black holes are growing, which is a probe of their host galaxies' evolutionary phase. Additionally, X-ray radiation is emitted by the hottest gas in galaxies, revealing regions of energetic events. In Figure 1.13, the X-ray radiation in blue traces a galaxy's central AGN (bright point in galaxy center) as well as the large-scale wisps of very hot gas associated with this activity.

At slightly longer wavelengths is ultraviolet (UV) light; an important source of this very blue radiation are massive stars, as described above. Because these stars are short-lived, ultraviolet radiation probes only regions in galaxies with young stellar populations and therefore with on-going star formation. Photometric measurements of a galaxy's brightness in the ultraviolet is consequently capable of measuring its recent star formation history as well as the spatial distribution of star formation within the galaxy. Since probing the star formation history of a galaxy is equivalent to probing the assembly of its stellar structures from gas, this is central to understanding its evolution. However, photometry in the ultraviolet has a significant short-coming; ultraviolet radiation is highly susceptible to absorption by dust. As a result, much of the ultraviolet light created in a galaxy will be absorbed by that galaxy's dust and will never reach observers on Earth.

Moving through visible wavelengths (described above) and beyond, the regime with longer (more red) wavelengths than visible light is the infrared (IR). A great deal of information is available at these wavelengths. In particular, "near-infrared" (closest to visible) light interacts much less strongly with dust than ultraviolet and visible light, implying that photometry at these wavelengths will penetrate very dusty regions (such as the dust lane visible in optical emission in Figure 1.13). Since stars are born in clouds of gas and dust, near-infrared images are windows into stellar birthplaces. At still longer wavelengths, radiation from the dust grains themselves is visible. These grains are heated by the ultraviolet light they absorb, and they reprocess and re-emit this energy in the form of infrared radiation. As will be discussed in Chapter 5, certain "mid-infrared" wavelengths are excellent tracers of the distribution of low-level star formation in galaxies. "Far-infrared" radiation is also a superb probe of the total star-forming activity of a galaxy, and the sensitivity of the

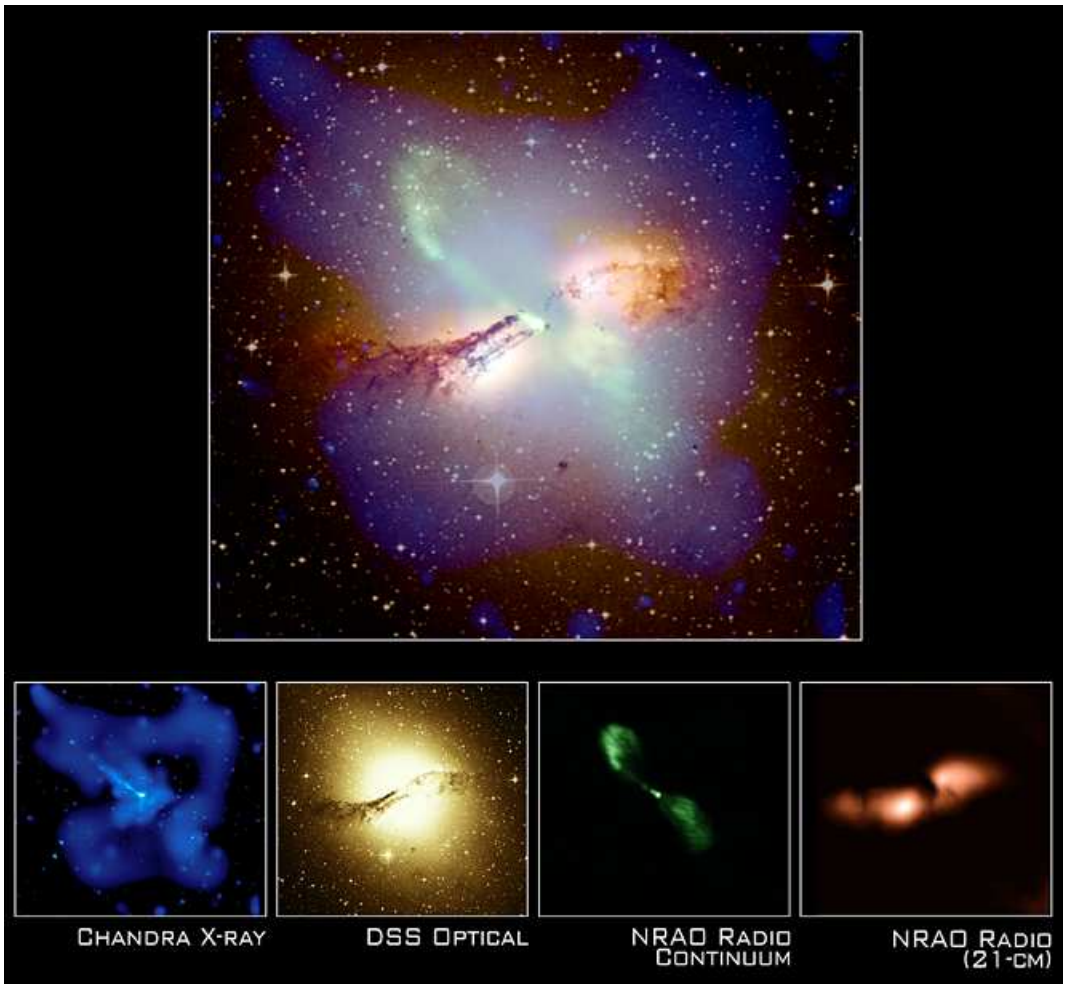

Figure 1.13: Example of observations at different wavelengths tracing diverse astrophysical phenomena within a single system, in this case the galaxy Centaurus A. The central active black hole (*bright point in the galaxy center*) emits primarily at X-ray wavelengths, as does the large-scale hot gas (*wispy structure*); both are observed by the *Chandra X-ray Observatory* (*blue*). The distribution of stars (*spherical distribution*) and dust (*dark horizontal region*) are probed by visible light in the *Digitized Sky Survey* image (*yellow*). Emission from cold gas is traced by light with a wavelength of 21 cm in the radio regime (*red*) by instruments at the *National Radio Astronomy Observatory* and reveals the link between cold gas and dust. Finally, radio emission at all other wavelengths (*green*) reveals the central black hole as well as the powerful twin jets of material ejected as a by-product of accretion onto the black hole. The composite image (*top*) combines information from all wavelengths and enables a detailed study of the interplay of diverse phenomena that would not otherwise be possible. *Image Credit: NASA, NRAO, SDSS.*

recently launched *Herschel Space Observatory* in the far-infrared is now allowing us to make such observations at high redshift. High-redshift observations in the infrared are particularly interesting for another reason; as one looks deeper into the Universe's past, the light from early galaxies is increasingly redshifted. At $z \sim 2$, the era on which half of this thesis focuses, the visible light from galaxies is already shifted into the near-infrared. In order to study galaxies at ever earlier epochs in the Universe's history, we will have to look at ever longer wavelengths.

Beyond the infrared is the microwave regime, at which wavelengths the most famous astronomical result is the image of the surface of last scattering shown in Figure 1.2. The information contained in this image has been instrumental in shaping our understanding of the composition of the Universe and of the laws of physics that govern its evolution. More immediately relevant to the study of galaxies is microwave emission from gas molecules in dense clouds. By imaging the distribution of such molecules as carbon monoxide (CO), we can learn about the distribution and mass of very cold gas clouds in galaxies, and we can study the relationship of this gas to the formation of new stars.

Finally, the longest wavelengths are radio waves, the regime in which radio, television, and cellular phone signals are broadcast on Earth. At these wavelengths, gas atoms, rather than gas molecules, radiate strongly. The most prominent such radiation is from atomic hydrogen, written in chemical notation as HI, because hydrogen is the most abundant element in the Universe. The atomic gas visible at radio wavelengths traces the distribution and mass of the large-scale gas reservoirs of galaxies; this gas is not in the dense state associated with star formation but rather is a diffuse component of galaxies, often with very different properties than the star-forming molecular gas. In Figure 1.13, this emission, identified by its wavelength of 21 cm, is shown in red and illustrates the close spatial correspondence of gas and dust. Another phenomenon that can be imaged at radio wavelengths, through emission from very energetic electrons, are supermassive black holes and the powerful, large-scale outflows driven by their accretion. As gas flows rapidly towards the black hole, this motion paradoxically fuels massive outflows of some of the accreting material. Figure 1.13 shows the AGN (central point) and its spectacular radio jets in green.

This figure provides a dramatic illustration of the strong variation with wavelength of galaxy properties accessible to observations. Clearly, a great deal of information can be obtained with a full sampling of the intensity of a galaxy's light at all wavelengths. Such data are collectively known as a galaxy's "spectral energy distribution." As shown in Figure 1.14, this distribution is complex and has many features throughout the ultraviolet (wavelength $< 0.4\mu$m), visible (wavelength $= 0.4 - 0.8\mu$m), and infrared (wavelength $> 0.8\mu$m). The detailed shape of this distribution, as sampled fairly coarsely through filters (several examples of infrared filters are shown), provides a global picture of the galaxy, including its star formation rate, stellar ages, total stellar mass, gas mass, and presence of an AGN. In Chapters 4 and 5 of this thesis, I will consequently combine observations of nearby galaxies at many wavelengths in order to gain additional insight into their evolution.

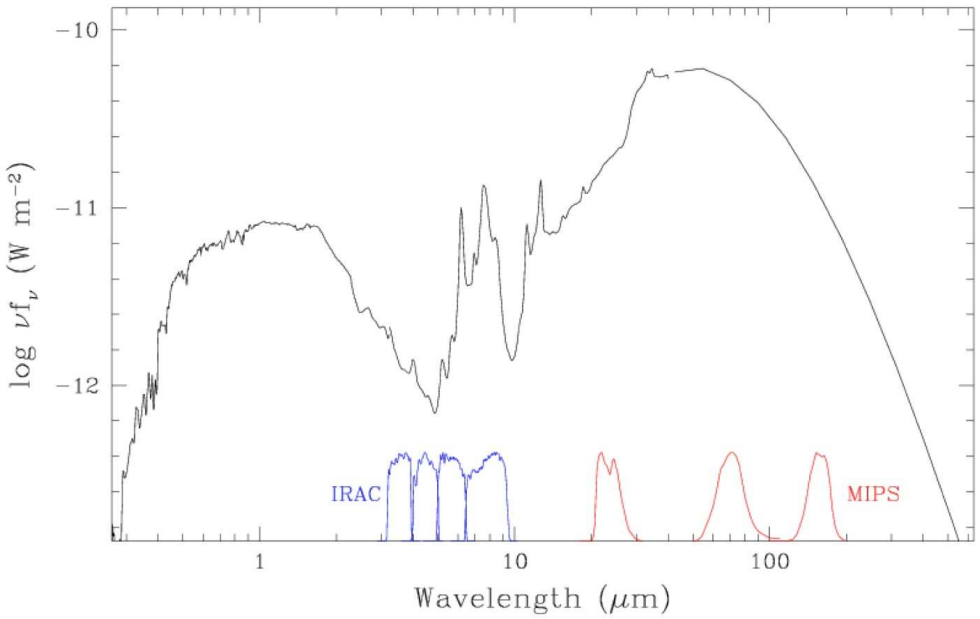

Figure 1.14: The intensity of light emitted as a function of wavelength, the so-called spectral energy distribution, in a typical star-forming galaxy. The energy generated by star formation in this galaxy is radiated nearly equally in the visible through near-infrared (wavelength $= 0.4 - 1.2\mu$m) and far-infrared (wavelength $= 30 - 200\mu$m, also known as sub-millimeter) regimes. The first peak, in the visible, is due to radiation directly from young stars, and the second peak, in the far-infrared, is due to radiation from dust grains, which have been heated by the ultraviolet light from young stars and have reprocessed and re-emitted this light at infrared wavelengths. The complex emission properties seen at $6 - 8\mu$m are due to a specific type of dust grain, also heated by young stars. When observing this radiation through broad wavelength bands, as shown for the photometers available on the *Spitzer Space Telescope* (*blue and red*), all of the complex spectral structure over the included wavelengths is compressed into a single measurement of the galaxy's intensity. In the longest wavelength band on the IRAC instrument (*rightmost blue line*), for example, the spectral intensity at $7.5 - 10\mu$m is summed to produce only a single measurement of intensity, without spectral information. Using multiple bands, as shown here, allows an observer to probe a galaxy's spectral energy distribution very coarsely, in this case with 7 data points, one for each waveband. *Image Credit: SINGS Team.*

1.5.3 Spectroscopy

As seen in Figure 1.14, photometry through filters (shown in blue and red) creates images by sampling a large range in wavelengths. The result of this "broad-band imaging" is that no information is gained about the complex small-scale spectral features in the spectral energy distribution. For example, the prominent features at $6 - 8\mu$m are covered by only a single broad-band filter; the light at all of the wavelengths covered by this filter will be added and only the total intensity will be recorded. In photometry, all of the spectral information, including the location, width, and amplitude of different spectral features, is lost.

Spectroscopy, another important tool in astronomy, overcomes this limitation by dispersing broad-band light through a prism in order to study spectral features, i.e. the variations in the intensity of light at different wavelengths. With spectroscopy, the spectral lines generated by atoms and molecules can be probed. Figure 1.15 illustrates the basic concept. Light originating in the centers of stars is a continuous spectrum, with the intensity of light varying smoothly with wavelength (top panel of this figure). If the light passes through a cooler cloud of gas, the atoms and molecules in that gas will absorb certain wavelengths of light in order for their electrons to transition to higher energy levels. An observer for whom the cool gas is in front of a warmer star will therefore see an absorption spectrum with light at these specific wavelengths removed (middle panel of the figure). Of particular relevance to this thesis is the fact that the outer layers of stars are actually cooler than their inner layers, in which a continuous spectrum of light is generated. Consequently, all stellar spectra contain absorption features from their own atmospheres; these "stellar absorption lines" are studied in Chapters 4 and 5.

Returning to the absorbing gas cloud in Figure 1.15, the wavelengths absorbed by atoms in the cloud will be re-emitted by these atoms as their electrons transition back down to their original energy levels. This light will be emitted in all directions, so any observer for whom the gas and star are not directly in line will see only the gas cloud (with the star off to one side). In this scenario, the gas cloud is then hotter than the empty space behind it, and the gas cloud will appear to the observer as in the bottom panel in the figure. This gas will be emitting light at exactly the wavelengths it absorbed from the star, and an emission line spectrum will be visible. The information contained in gas emission lines is used extensively in Chapters 2-5 of this thesis. Dust emission lines are also important to the analysis of Chapter 5; however, emission from dust grains differs slightly than that from gas atoms and molecules. While many important gas emission lines occur at exactly the same wavelengths as the absorbed light, dust reprocesses incident light and emits it at completely different wavelengths. As described in the previous section, dust is a powerful absorber of ultraviolet light, which it converts and re-emits as infrared radiation with new spectral features.

Each molecule, atom, and ion has its own unique spectral signature. As a result, the absorption spectrum of a star tells us directly about the composition of the outer layers of the star. This information is retained in the galaxy spectrum, which is a cumulative spectrum of many stars, and several important stellar absorption features are visible in the $0.4 - 1\mu$m range in Figure 1.14. The relative depths of these features contain information

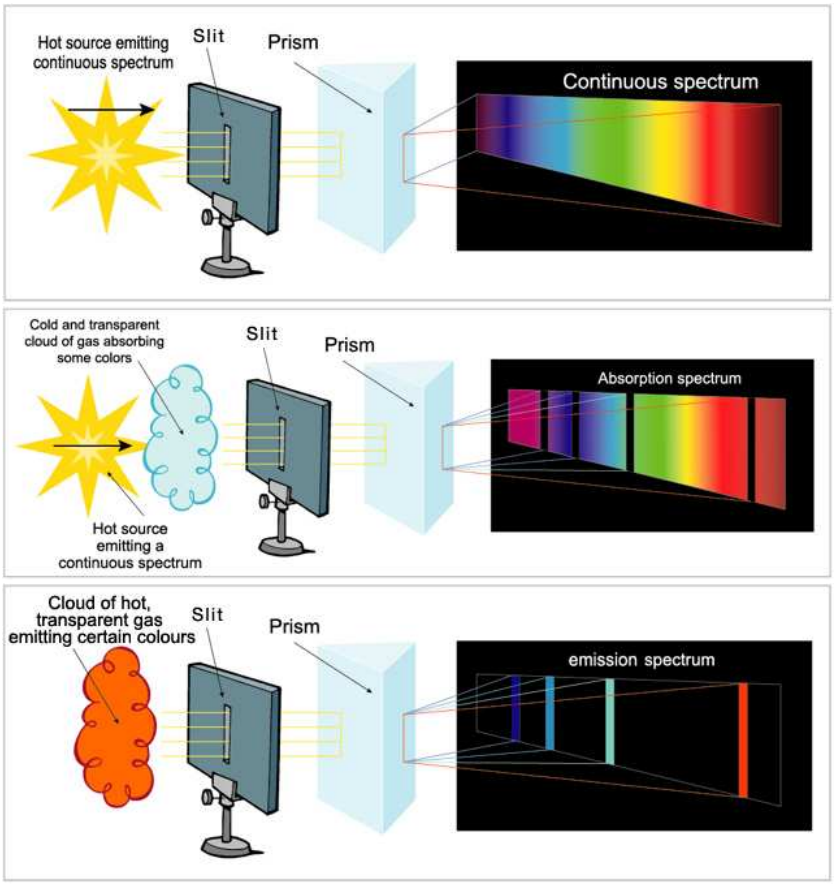

Figure 1.15: The different types of spectra. Stars emit light at all wavelengths, with the peak intensity occurring in the ultraviolet through near-infrared regime (Figure 1.14). A prism will split the "white light" into its different spectral components, revealing light at all wavelengths (*top*). When "white light," or a continuous spectrum, from a star passes through a cloud of gas colder than the star, the gas atoms will absorb the wavelengths of light that allow their electrons to transition to higher energy levels. The observer will then see an absorption spectrum, with those specific wavelengths removed (*middle*). An observer looking at the cloud from a perspective without the star directly behind it will see a cloud that is hotter than the object behind it (empty space) and that is re-emitting the absorbed light. The resulting emission spectrum will contain only light at specific wavelengths (*bottom*). *Image Credit: Virtual Museum of Canada.*

about the ages and chemical enrichment of the galaxy's stellar population. In addition to the absorption features, the spectrum in Figure 1.14 has emission features from gas and dust, the most prominent of these being a dust emission feature at $6 - 8\mu$m. This emission originates in diffuse dust, and the relative strengths of these features provide insight into the composition of the dust as well as its temperature and density. Such spectral signatures are the source of much of our knowledge of the gas and dust in a galaxy, which are collectively referred to as the "interstellar medium."

In addition to revealing the composition of stars and the interstellar medium in a galaxy, absorption and emission features in galaxy spectra can be used to trace large-scale motions. For example, if all of the gas in a galaxy is being ejected from the system, the gas will be moving towards an observer, while the stars will remain stationary. The motion of the gas will induce a shift in the wavelengths of emission features away from their expected positions, and measuring this wavelength difference directly measures the velocity of the outflowing gas. Shifts in line positions can also be used to measure motions of stars and gas within a galaxy. If, as in Figure 1.15, an observer places a slit on the sky and observes a galaxy through this slit, he can measure the spectrum at one end of the slit (i.e. one side of the galaxy) and compare it to that from the other end. If the galaxy is rotating, this will be evident in a relative shift in spectral features between the two spectra. On one side of the galaxy, stars and gas will be moving towards the observer and their lines will be shifted towards blue wavelengths, and on the other side, they will be moving away from him, and their lines will be shifted towards red wavelengths. The wavelength difference between these two sides is a direct measurement of the speed of internal rotation in the galaxy. Such "longslit" spectra, taken with the *Hubble Space Telescope*, are used in Chapter 4 to probe gas motions in the center of a galaxy.

1.5.4 Integral-Field Spectroscopy

The above techniques, photometry and spectroscopy, are very valuable tools in studying galaxies. With photometry, the two-dimesional appearance of a galaxy on the sky reveals much about the galaxy's evolutionary history. Spectroscopy complements this information with detailed information about the motion and composition of the galaxy's stars and gas. However, as discussed above, traditional spectrographs in the ultraviolet, optical, and infrared operate in "longslit" mode, which provides spectra along only one dimension on the sky. As a result, one can measure *either* the two-dimensional appearance of galaxy *or* its spectrum. It would be ideal, of course, to measure spectral information at every location in a galaxy in order to probe the two-dimensional motions and compositional variations within the galaxy.

The technique of integral-field spectroscopy was developed to do exactly that. This technique combines photometry and spectroscopy in order to record a spectrum at every point across two dimensions, as illustrated in Figure 1.16. The integral-field unit (IFU) in this diagram operates by "slicing" the on-sky image of a galaxy into a number of one-dimensional images: a series of slits divides the galaxy in the vertical (y) direction, and

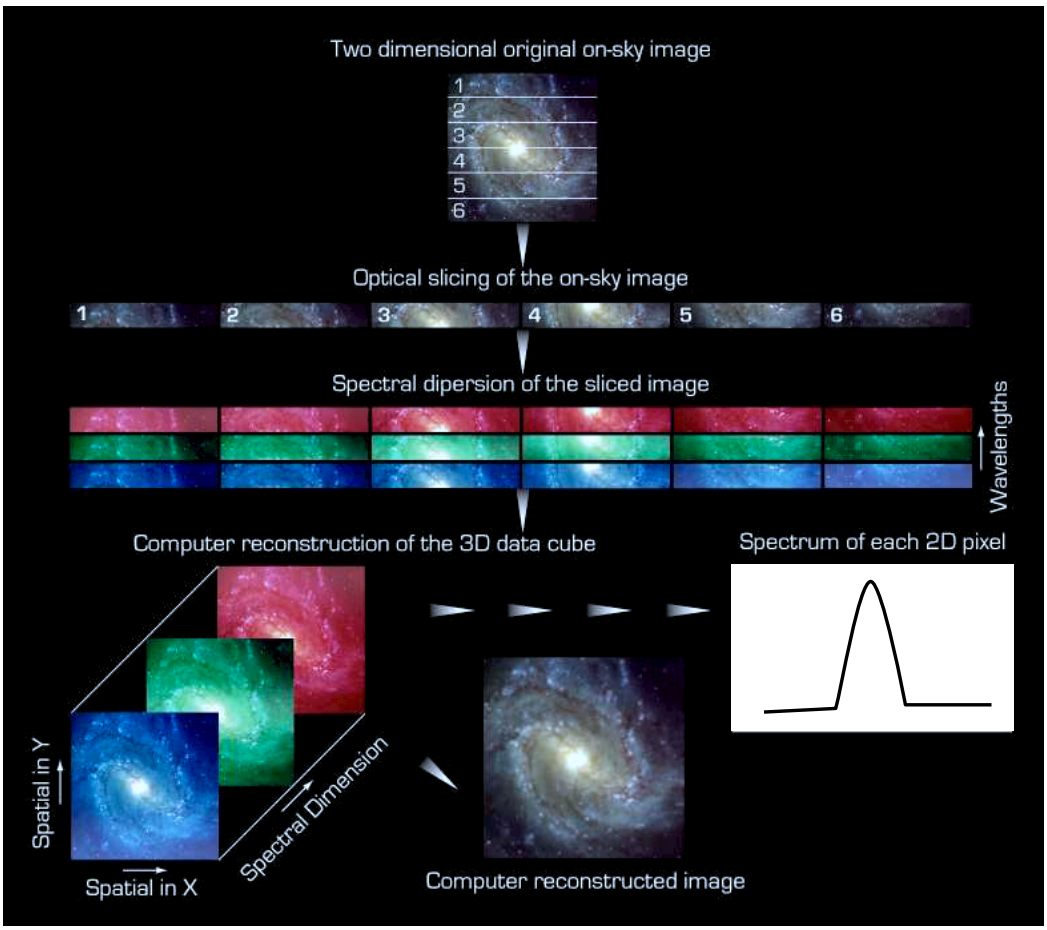

Figure 1.16: Schematic of the technique of integral-field spectroscopy. When the two-dimensional galaxy image on the sky reaches an integral-field unit behind a telescope, the light is first "sliced" via a complex set of mirrors into horizontal cuts through the galaxy. Each resulting one-dimensional image is sent through a prism that disperses the light spectrally. For each horizontal cut, there is then a two-dimensional image of the galaxy intensity along the horizontal direction and spectral direction. This information is recorded on a digital camera in the integral-field unit. Computer reprocessing of the observations recombines the different cuts through the galaxy to produce a datacube containing two dimensions of spatial information and one of spectral information. For each spatial pixel, the full spectral information of the galaxy is available (*lower right*) and for each wavelength, the full two-dimensional spatial information is available (*lower left*). Summing the datacube in the wavelength direction reproduces the original galaxy image and color (i.e. spectral) information (*lower center*). *Image Credit: Modified from original graphic by ESO.*

each slit contains spatial information along the horizontal (x) direction. The slits are then placed end-to-end and sent through a prism to extract spectral information, producing data containing one dimension of spatial information (x) and one dimension of spectral information (called λ) for each slit. The data is recorded in this form on a CCD, and the slits are later recombined digitally to recover the vertical information (y). The resulting "datacube" has three dimensions: two spatial (x and y) and one spectral. This datacube can be summed along the spectral axis to reconstruct the original two-dimesional image (lower center of Figure 1.16) or the spectrum from every spatial location can be studied (lower right of Figure 1.16).

The integral-field technique can be achieved through several implementations, all of which have their own strengths and limitations. Figure 1.17 compares the two techniques relevant to this thesis. The image slicer technique, shown at the bottom, is diagrammed in detail in Figure 1.16; a very precise set of mirrors directs the galaxy light into end-to-end slits, which are then sent through a prism. The SINFONI IFU, on the Very Large Telescope (VLT) in Chile, operates on this principle, and data from this instrument are discussed in Chapters 2 and 3. The success of SINFONI has shown the image slicer technique to have minimal light losses and consequently to be very sensitive to faint objects. This success, however, requires exquisite precision in manufacturing the tiny mirrors used to redirect the galaxy light into the slit configuration.

Alternatively, the lenslet technique, shown at the top of Figure 1.17, focuses the galaxy light through a grid of pupils. When the light from each pupil is spectrally dispersed through a prism, the resulting spectra are angled with respect to one another. As a result of the close stacking of the spectra on the CCD, the light from one spectrum may "spill over" into the adjacent spectra and mix information from separate regions of a galaxy. When corrected during data analysis, this effect can be largely removed; this is more easily accomplished for some lenslet IFUs than for others. Data obtained from the SAURON lenslet IFU, on the William Herschel Telescope (WHT) in the Canary Islands, has produced very high-quality results, as presented in Chapters 4 and 5. In this case, the lenslet IFU is a success.

As indicated above, integral-field spectroscopy is the primary technology used to obtain data for this thesis. With SAURON, I have studied the optical spectroscopic properties of nearby elliptical galaxies; the IFU data provide information on stellar populations and motions (from stellar absorption lines) and gas composition and motions (from gas emission lines). With SINFONI, I have studied the spectroscopic properties of galaxies at $z \sim 2$ in the near-infrared, into which wavelength range their optical light is redshifted. We therefore say that we are studying the "rest-frame" optical spectra. In these distant and faint galaxies, the stellar absorption features are too faint to observe, so we measure gas emission lines properties, which probe the composition and kinematics of the gas in these young galaxies.

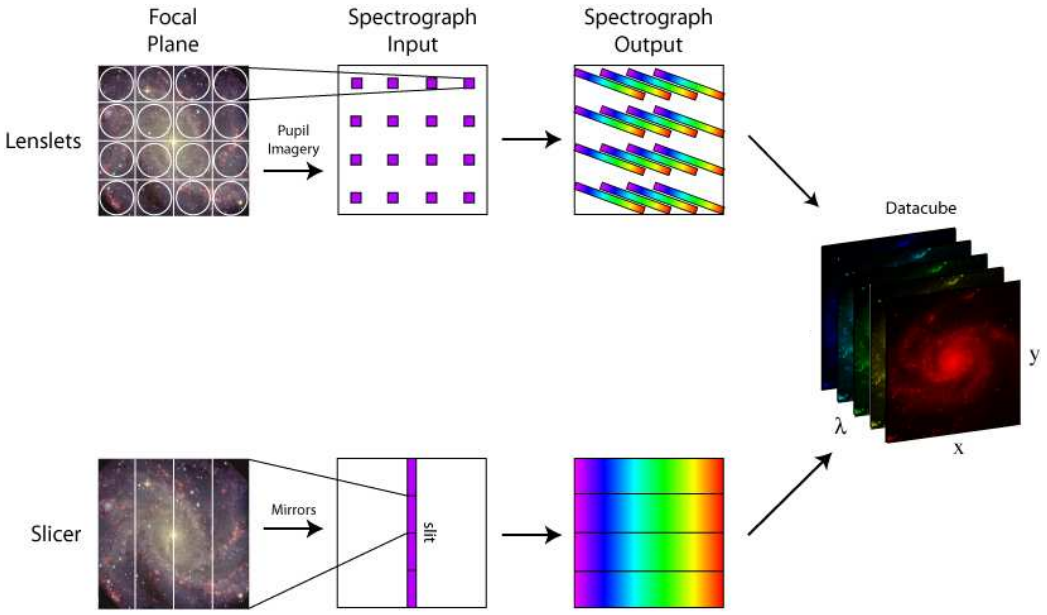

Figure 1.17: The two integral-field techniques used in this thesis. *Top:* In the lenslet technique, a mask of pupils inside the IFU focuses light from different parts of the galaxy through a grid of holes. The light from each pupil is sent through a prism, and the resulting spectra are stacked diagonally on the digital camera, where the observation is recorded. *Bottom:* In the slicer or slitlet technique, also shown in Figure 1.16, small slits placed across the galaxy image direct the light into a single one-dimensional "image" of the galaxy via a complex mirror inside the IFU. This slit of light is sent through a prism, and the resulting side-by-side spectra are recorded on the digital camera. In both cases, post-processing in a computer (*final image on right*) enables the observer to reconstruct the two-dimensional image of the galaxy, with spectral information (λ) available at every spatial position (x and y). *Image Credit: Adapted from graphic by Mark Westmoquette.*

1.6 This Thesis

The above introduction to my dissertation has briefly outlined our present understanding of the history of the Universe, the assembly of the dark matter halos that host galaxies, the nature of galaxies in the local Universe, and the global picture of galaxy evolution across cosmic time. Specifically, I have introduced early-type (elliptical and lenticular) galaxies, which are the most massive and most evolved components of the local Universe and are therefore important test sites for understanding the growth of galaxies. In the past, these galaxies likely hosted much more powerful star formation and nuclear activity than is found in present-day assembling (spiral) galaxies, a phenomenon known as "downsizing." However, these galaxies have long since ceased such violent activity and have red colors associated with their aging stellar populations.

As alluded to in previous sections, several important questions about the evolution of massive galaxies remain unanswered:

- How does the growth of dark matter halos over the Universe's history affect the growth of galaxies within them?
- What happens inside dark matter halos to convert gas into galaxies?
- How do star formation and black hole growth proceed within galaxies?
- What processes control the assembly of structures within galaxies?

This thesis is a very small part of a large on-going effort to address these questions. The approach taken here is to use detailed studies of the processes operating in individual galaxies in order to probe the physics responsible for the observed characteristics and evolution of the overall galaxy population. This is accomplished with a composite method, in which both the *in situ* formation of massive galaxies in the distant Universe and their fossil record in the local Universe are studied. This approach allows me to begin to link emerging knowledge from both regimes into a description of galaxy evolution across cosmic time. To conclude this introduction, I therefore give an overview of the progress made in this direction by my dissertation.

1.6.1 Massive Galaxies in the Distant Universe

My thesis work on the *in situ* formation of massive galaxies 10 billion years ago, at $z \sim 2$, was completed in collaboration with the "SINS" team, who have used integral-field spectroscopy with SINFONI to carry out the first large integral-field survey of the dominant star-forming galaxy population at this redshift. The resulting data yield two-dimensional maps of the composition and internal motions of the gas in these young galaxies.

One of the most surprising results from this survey is the discovery at $z \sim 2$ (an era in which major mergers were assumed to dominate galaxy evolution) of Milky Way-size galaxies whose kinematics (internal motions) are qualitatively consistent with undisturbed

regular rotation. To interpret this result, I created a quantitative scheme through which the kinematics of a galaxy could be linked to its dynamical state (i.e. undergoing a major merger or undisturbed). As calibrators for this technique, I drew on a diverse sample of local galaxies, which I simulated as they would be observed with SINFONI at $z \sim 2$. Using measurements of the rotational velocity of the gas as a function of its location in the galaxy, I created a criterion that quantifies the level of dynamical disturbance in a galaxy and therefore identifies galaxies undergoing major mergers. When implemented on $z \sim 2$ galaxies from our SINS survey, this technique confirmed that the majority of these galaxies have not undergone recent major mergers. This result has important implications for our understanding of how galaxies acquire gas in an epoch of the Universe's history previously thought to be dominated by major mergers. In particular, this was one of the first indications that smooth and rapid transport of gas into dark matter halos from the surrounding filamentary structures (see Figure 1.3) may be important to galaxy assembly at high redshift. This work is described in detail in Chapter 2 and was originally published in Shapiro et al. (2008).

Rapid gas accumulation in galaxies at high redshift fuels high star formation rates, and reasonable extrapolation would suggest that other gas-driven processes, such as black hole growth and large-scale gas outflows, may occur with equal intensity. I therefore searched for faint signatures of these processes in the unique SINS data set. Such a probe required coaddition of all of the spectra from all of the observed galaxies into a single, much more precise spectrum; doing so revealed a very faint emission line with a much larger spectral width than the primary gas emission lines. The observed feature can be interpreted as a sign of either of two phenomena: 1) a signature of powerful galactic-scale outflows driven by the explosions of young stars (supernovae) and therefore by star formation, or 2) a tracer of the unique energetics of gas in the vicinity of growing supermassive black holes. In the first scenario, the observed brightness and spectral properties of the line imply mass outflow from $z \sim 2$ galaxies at rates comparable to the rate of star formation. In the second scenario, the black holes in galaxies at $z \sim 2$ are estimated to be ten times smaller relative to their host galaxy than those observed in the local Universe, suggesting a delayed assembly of supermassive black holes with respect to the galaxies they inhabit. Differentiating between these two processes is an obvious goal that will be possible with next-generation observational facilities. This work is described in Chapter 3 and was originally published in Shapiro et al. (2009).

In addition to the work performed in the context of this thesis, the SINS team has compared the properties of $z \sim 2$ Milky Way-sized star-forming galaxies to local Milky Way-sized star-forming galaxies; the results indicate that gas is converted into stars via the same processes in both regimes but that the higher percentage of gas in galaxies at $z \sim 2$ (§1.4) enhances their star formation rates significantly with respect to their local counterparts. Moreover, this gas has substantial effects on the distribution of matter within the galaxy. The SINS project has shown that the large amount of gas in star-forming galaxies at $z \sim 2$ causes them to be dominated by star-forming regions that are 1000 times larger than those in local galaxies. These unique features may be one of the keys to linking galaxies at $z \sim 2$ to their local descendants (§1.6.3).

1.6.2 Massive Galaxies in the Local Universe

Complementary to the *in situ* study of the formation of massive galaxies, my dissertation also probes the relics of galaxy assembly, local bulge-dominated galaxies. This was done in collaboration with the "SAURON" team, named for the integral-field unit it has employed to create two-dimensional maps of the motions and composition of stars and gas in a representative sample of local massive (elliptical, lenticular, and bulge-dominated spiral) galaxies.

The unprecedented detail achieved in the SAURON and auxiliary data sets is such that even studies of individual galaxies can provide important insights into the assembly of massive galaxies and their substructures. In my thesis, I have investigated gas and stellar motions in the local elliptical galaxy NGC 3379 in order to constrain the mass and formation history of its central supermassive black hole. Using dynamical models of the stellar and gas motions in the vicinity of the black hole, I obtained two independent measurements of the black hole mass and found good agreement between the two, suggesting both methodologies are sound. Additionally, I compared these models to theoretical predictions for different galaxy and black hole formation scenarios; the results indicated that the observed properties of NGC 3379 cannot be straightforwardly explained if the galaxy and its black hole were created in a single major merger. Instead, NGC 3379 may have been assembled through multiple, and perhaps less dramatic, merger events. This work is described in Chapter 4 and was originally published in Shapiro et al. (2006).

Studying the full SAURON galaxy sample provides additional leverage on the formation of the local massive galaxy population. I have therefore combined the full suite of SAURON stellar and gas two-dimensional maps made at optical wavelengths with mid-infrared photometry taken with the *Spitzer Space Telescope*. As described in §1.5.2, imaging in the mid-infrared is an excellent tracer of star formation; I used this capability to identify very low-level star formation in these evolved red galaxies. In the sub-sample of SAURON galaxies with small amounts of star formation, I isolated two distinct modes operating in massive, bulge-dominated galaxies. In the first mode, star formation is a large-scale process occurring throughout the galaxy, and the responsible gas clearly originated outside the galaxy, suggesting that these galaxies are in the final stages of minor mergers. In the second mode, star formation is confined to a central disk or ring, and the very old stellar populations outside of this region imply that these galaxies have experienced a recent rejuvenation of star formation. A comparison to other massive galaxies further suggests that this process may eventually occur in a majority of these galaxies. This work is described in Chapter 5 and was originally published in Shapiro et al. (2010b).

In addition to the work performed in the context of this thesis, the SAURON team has studied the stellar and gas properties of the full SAURON sample in detail and has used these data to further constrain the evolutionary history of massive galaxies. In particular, it is becoming clear that most massive galaxies, including those classified as ellipticals, in fact contain rotating disks, and these disks are not observed in optical images as a result of the large sizes of their host galaxies' bulges and the small percentage of the galaxies'

mass contained in the disks. The work in Chapters 4 and 5 is part of a growing body of evidence that favors minor mergers, rather than the much more dramatic major mergers, as the most important assembly mechanisms for such galaxies. The emerging solid foundation of knowledge about the formation history of local massive galaxies is therefore ripe for combination with our developing understanding of their early Universe predecessors.

1.6.3 Linking Galaxy Evolution across Cosmic Time

The most powerful way to probe galaxy formation is through the synergy of studies at high and low redshift. The SINS team has recently made important strides in this direction, most fundamentally by establishing a solid connection via theoretical simulations between the dominant star-forming population at $z \sim 2$ and local massive galaxies. Moreover, the super-large star-forming regions (1000 times more massive than in local star-forming galaxies) observed inside star-forming galaxies at $z \sim 2$ have been found to be dynamically important entities that migrate to their host galaxies' centers and form bulges, thereby beginning the transition from large, rotating, star-forming galaxies to bulge-dominated systems. This process produces structures that mimic those expected from multiple minor mergers, and it may in fact be responsible for some properties of local massive galaxies often attributed to those mergers.

I have focused part of my dissertation work in this direction and have linked other structures observed in local massive galaxies with their counterparts in star-forming galaxies at $z \sim 2$. In particular, an examination of the super-large star-forming regions in $z \sim 2$ galaxies revealed that these objects could be the formation sites of one of the globular cluster populations. With the assumption that star formation in super-large star-forming regions proceeds as a scaled-up version of local star formation in normal-sized star-forming regions, I predicted the numbers and masses of globular clusters that would be produced. These properties, in addition to the chemical composition, the spatial distribution, the motions, and the expected evolution of super-large star-forming regions, match very well with observational constraints on globular cluster properties in the local Universe, confirming the plausibility of this link. This work is described in Chapter 6 and was originally published in Shapiro et al. (2010a).

Such connections between galaxy populations across cosmic time enables us to directly track the formation and evolution of local galaxies, the fundamental building blocks of the local Universe. The outlook for the field is very bright; these early results will be developed into a complete picture of galaxy evolution via observations with next-generation facilities and via additional insights. In Chapter 7, I provide some concluding comments and a brief discussion of directions for exciting future progress.

Chapter 2

Kinemetry of SINS High-Redshift Star-Forming Galaxies: Distinguishing Rotating Disks from Major Mergers

Abstract

We present a simple set of kinematic criteria that can distinguish between galaxies dominated by ordered rotational motion and those involved in major merger events. Our criteria are based on the dynamics of the warm ionized gas (as traced by Hα) within galaxies, making this analysis accessible to high-redshift systems, whose kinematics are primarily traceable through emission features. Using the method of kinemetry (developed by Krajnović and coworkers), we quantify asymmetries in both the velocity and velocity dispersion maps of the warm gas, and the resulting criteria enable us to empirically differentiate between non-merging and merging systems at high redshift. We apply these criteria to 11 of our best-studied rest-frame UV/optical-selected $z \sim 2$ galaxies for which we have near-infrared integral field spectroscopic data from SINFONI on the VLT. Of these 11 systems, we find that $> 50\%$ have kinematics consistent with a single rotating disk interpretation, while the remaining systems are more likely undergoing major mergers. This result, combined with the short formation timescales of these systems, provides evidence that rapid, smooth accretion of gas plays a significant role in galaxy formation at high redshift.

2.1 Introduction

In recent years, deep observations of galaxies at $z \sim 2-3$ have provided detailed insight into the growth of structure and galaxy evolution in the early Universe. High-resolution broad-band imaging and long-slit spectroscopic surveys have shown the population at this redshift to be rapidly evolving and diverse. This is a reflection of the significant growth of

galaxies that occurs at this epoch; at $z \sim 2$, both the cosmic star formation rate and the luminous quasar space density are at their peak (e.g. Fan et al. 2001; Chapman et al. 2005; Hopkins & Beacom 2006). Correspondingly, the stellar mass density in galaxies increases from $\sim 15\%$ its current value at $z \sim 3$ to $50-75\%$ its current value at $z \sim 1$ (e.g. Dickinson et al. 2003; Fontana et al. 2003; Rudnick et al. 2003, 2006), making this the era when much of the assembly of massive galaxies occurs. Systems at this redshift consequently show a wide range in properties, with nuclear activities varying from negligible to active to powerful QSOs, star formation rates varying from less than 1 $M_\odot$ yr^{-1} (e.g. passively evolving BzK-selected objects and quiescent DRGs; Cimatti et al. 2004; Daddi et al. 2005; Labbé et al. 2005; Kriek et al. 2006; Wuyts et al. 2007) to over 10^3 $M_\odot$ yr^{-1} in sub-mm-selected galaxies (SMGs; e.g. Blain et al. 2002; Smail et al. 2002; Tacconi et al. 2006), and correspondingly large variations in morphology, stellar populations, excitation properties, and dust content (e.g. Reddy et al. 2005; Papovich et al. 2006; Kriek et al. 2007).

Furthermore, the resolving power of 8-10m class telescopes and of millimeter interferometric arrays reveals velocity gradients within many of these systems (Erb et al. 2003; Genzel et al. 2003). By coupling such telescopes with high-resolution integral field spectrographs, we are now able, for the first time, to resolve the dynamic structures and internal processes at work within massive galaxies during their critical stages of evolution (Förster Schreiber et al. 2006; Genzel et al. 2006; Wright et al. 2007; Law et al. 2007, see also e.g. Flores et al. 2004; Puech et al. 2006; Swinbank et al. 2006). With surveys of the spatially-resolved kinematics of various high-z populations (Bouché et al. 2007), we can now begin to understand the forces driving such rapid and intense evolution as well as the role of secular evolution and major mergers in these processes.

Differentiating between systems in ordered rotation and those undergoing major merger events has significant ramifications in understanding the evolution of both the baryons and the underlying dark matter distributions. Kinematic measurements of a system's baryonic component, combined with basic assumptions about the morphology of the system, enables a detailed probe of the mass and angular momentum of dark matter halos at $z \sim 2$ and of the interaction between these halos and their baryons (Förster Schreiber et al. 2006; Bouché et al. 2007). Additionally, the baryons themselves can also constrain formation and evolution scenarios, by probing whether the active star formation seen in these objects is triggered by major mergers (e.g. Hopkins et al. 2006) or by smooth accretion (Birnboim et al. 2007). In several well-resolved systems at $z \sim 2$, the young age of the stellar population ($\sim 500-1000$ Myr), when combined with the high star formation rate (up to ~ 200 $M_\odot$ yr^{-1}), suggests extremely rapid (< 1 Gyr) formation (Förster Schreiber et al. 2006; Genzel et al. 2006). This is most surprising since the dynamics of these systems qualitatively appear to be consistent with no recent major merger events, thus indicating a rapid and intense, but still smooth, mass accretion mechanism.

However, a quantitative and definitive understanding of the structure of these high-z systems is complicated by the limited spatial resolution attainable at this redshift and the lower signal-to-noise (S/N) associated with these faint objects. Existing prescriptions for measuring galaxy morphology use surface brightness information and rely solely on char-

acteristics of the broad-band emission (CAS: Conselice 2003; Gini/M20: Lotz et al. 2004; Sérsic fitting: Ravindranath et al. e.g. 2004; Cresci et al. e.g. 2006). At lower redshifts, these techniques have been shown to effectively distinguish disparate populations over a wide range of resolutions and S/N (Lotz et al. 2004). At $z \gtrsim 2$, however, the situation is more complicated, since optical observations probe the rest-frame ultraviolet morphology, which is strongly affected by extinction and by the light from massive stars in star-forming regions. Near-infrared observations, which correspond to rest-frame optical emission at $z \sim 1-4$, are a significant improvement, but high-resolution near-infrared imaging is still quite observationally expensive. To reliably probe the dynamical state of a system, a promising alternative comes from integral-field spectroscopic (IFS) observations, yielding spatially-resolved kinematic information. While this approach is also still observationally expensive, it has the advantage of directly probing the system's dynamics and total enclosed mass.

Given the detailed kinematic information available with such observations, a technique complementary to morphological methods can be developed to fully exploit the measured two-dimensional velocity structure. Existing IFS observations of Hα emission in a few cases at $z \sim 2$ reveal dynamics suggestive of either the "spider diagram" structure found in local disk galaxies or of the complex structures found in mergers (Förster Schreiber et al. 2006). If the observed internal dynamics of the warm gas do in fact reflect those of the system, then it appears possible to distinguish mergers and non-mergers using current data. Indeed, simulated observations with current technology have predicted that the kinematic differences between non-merging and merging systems should be qualitatively visible in IFS data (Law et al. 2006).

In this chapter, we present a scheme for discerning between merging and non-merging galaxies, based on their emission-line kinematic properties and also on the distribution of the stellar continuum intensity, which, with integral-field observations, can be unambiguously separated from the emission lines. We use kinemetry (Krajnović et al. 2006) to quantify asymmetries in the velocity and velocity dispersion maps, enabling us to differentiate a system in regular, ordered rotation from one disturbed by the complex dynamics of a major merger, even at the $\sim$ 4 kpc spatial resolution typical of seeing-limited (FWHM $\sim 0\farcs5$) observations of $z \sim 2$ systems. In §2.2, we describe this method, and in §2.3, we illustrate the power of our technique with a number of template galaxies, drawn from observations of local systems and from simulations (from Daigle et al. 2006; Colina et al. 2005; Naab et al. 2007). We apply this classification scheme to the well-resolved $z \sim 2$ systems from the Spectroscopic Imaging survey in the Near-infrared with SINFONI (SINS; see Förster Schreiber et al. 2006; Genzel et al. 2006; Bouché et al. 2007; Cresci et al. 2009) in §2.4. We discuss the results from this analysis and address the inherent assumptions in our method, including the use of Hα kinematics as a tracer of dynamics at high redshift, in §2.5. Finally, we summarize our conclusions in §2.6.

Throughout this chapter, we compare the two classes of systems that we aim to distinguish: those with recent major merger events (mass ratio $\leq 3:1$) and those without. For simplicity, we refer to these two classes as "mergers" and "disks" respectively, but the obvious caveats of such nomenclature are worth mentioning. Our analyses focus mainly on

the gaseous component in galaxies, which relaxes quickly into a flat, disk-like configuration, e.g. in late-stage mergers (e.g. Barnes & Hernquist 1996; Mihos & Hernquist 1996; Tacconi et al. 1999; Naab et al. 2006). The naming scheme adopted here does not reflect an inability to distinguish late-stage mergers from non-merging systems; in fact, we illustrate in §2.3 that the gas motions in even late-stage mergers are still sufficiently disturbed that they can be clearly identified as such (see also Barnes 2002; Arribas & Colina 2003). In the context of this chapter, these systems are never referred to as "disks," despite their probable geometry; that term is instead reserved for galaxies that show no sign of a recent major merger.

We assume a Λ-dominated cosmology with $H_0 = 70$ km s^{-1} Mpc^{-1}, $\Omega_{\rm m} = 0.3$, and $\Omega_\Lambda = 0.7$. For this cosmology, $1''$ corresponds to ≈ 8.2 kpc at $z = 2.2$.

2.2 Method

To determine whether a particular observed system is a disk or a merger, we use two main criteria: the symmetry of the velocity field of the warm gas, and the symmetry of the velocity dispersion field of the warm gas. An ideal rotating disk in equilibrium is expected to have an ordered velocity field, described by the so-called "spider diagram" structure, and a centrally-peaked velocity dispersion field (Figure 2.1, see also van der Kruit & Allen 1978).

Likewise, such a disk is also expected to have the regular and centrally-peaked continuum distribution characteristic of exponential disks. Indeed, this feature is the basis for low-redshift morphological classification schemes (e.g. Conselice 2003; Lotz et al. 2004; Cresci et al. 2006). However, in our IFS observations, the highest S/N is usually obtained from the Hα emission from the warm, star-forming gas, rather than from the underlying stellar continuum whose light is dispersed over many more spectral pixels. In Förster Schreiber et al. (2006), for example, the emission features have a typical S/N of ~ 25, whereas the stellar continuum is often only detected in a small part of a given system, with typical S/N ≤ 10 in the brightest region. We therefore perform only the simplest analysis of the distribution of the stellar component in these systems, using this information to supplement and inform the detailed analysis possible with the high-S/N emission line velocity and velocity dispersion data.

In our analysis, we do not include constraints based on the intensity distribution of the emission lines. This tracer of the location and power of star-forming regions is often clumpy and asymmetric in even the most kinematically regular disks (Figure 2.1; see also Daigle et al. 2006 for local examples) and, consequently, reveals little about the mass distribution and dynamical state of the system. Rather, it is the kinematics of this gas, and not its spatial distribution, that reflects the dynamical state of the system and therefore forms the basis for our analysis.

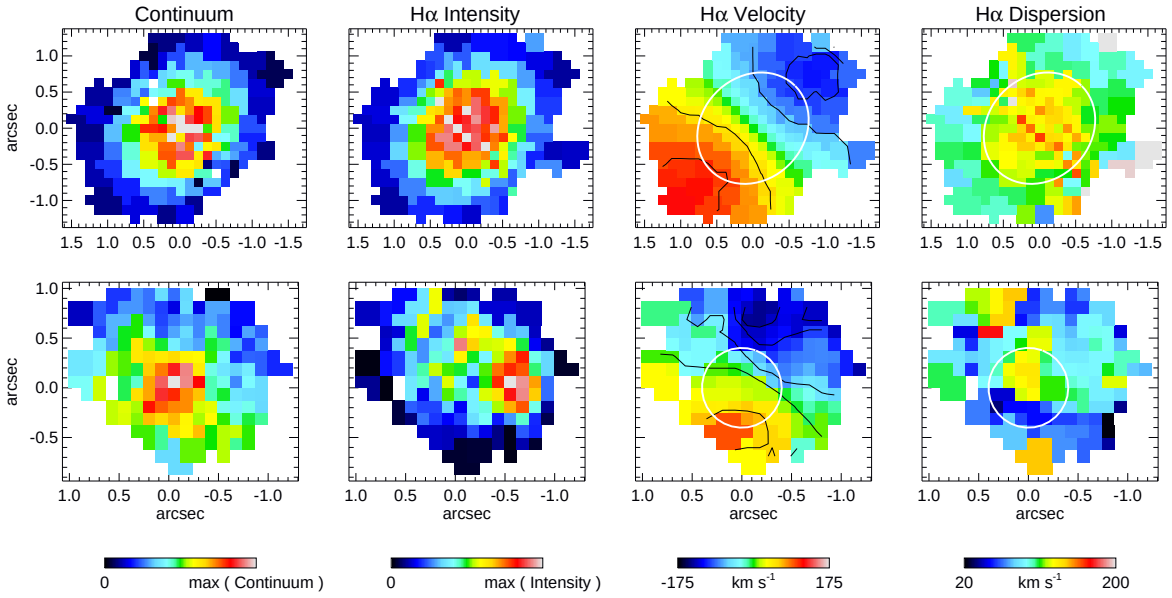

Figure 2.1: *From left to right:* Continuum intensity in rest-frame R-band, intensity of the Hα line emission, and velocity and velocity dispersion of the Hα-emitting component, for a simulated ideal disk (*top*) and for the high-redshift galaxy BzK-6004 observed as part of the SINS program (*bottom*). In the ideal disk, the star formation (Hα intensity) follows the mass distribution (continuum), whereas in the observed $z \sim 2$ system, a significant off-center star-forming region is seen. Overplotted on the velocity maps are isovelocity contours, whose concave curvature on either side of the rotation axis displays the so-called "spider diagram" structure characteristic of rotational motion (van der Kruit & Allen 1978). Also overplotted on the velocity and dispersion maps are sample ellipses from the expansion with kinemetry. Along a kinemetry ellipse in the velocity map, the velocity varies as the cosine of the azimuthal angle. Along an ellipse in the velocity dispersion map, the dispersion is approximately constant with angle.

2.2.1 Quantifying Symmetries with Kinemetry

The symmetries in kinematic fields can be measured via the kinemetry method developed and described in detail by Krajnović et al. (2006). Briefly, kinemetry is an extension of surface photometry to the higher-order moments of the velocity distribution. The procedure operates by first describing the data by a series of concentric ellipses of increasing major axis length, as defined by the system center, position angle, and inclination. The latter two parameters can either be determined a priori and used as inputs or can be measured functions of semi-major axis length as a first step in the kinemetric analysis. Along each ellipse, the moment as a function of angle is then extracted and decomposed into the Fourier series

$$K(\psi) = A_0 + A_1 \sin(\psi) + B_1 \cos(\psi) + \ A_2 \sin(2\psi) + B_2 \cos(2\psi) + \ldots, \tag{2.1}$$

where the radial dependence of all A_n's and B_n's is implicit, since the above expression is for a single kinemetry ellipse. Here, ψ is the azimuthal angle in the plane of the galaxy, measured from the major axis; points along the ellipse are sampled uniformly in ψ and are therefore equidistant if the ellipse is projected on to a circle. The series can be presented as a function of semi-major axis length a and in a more compact way,

$$K(a, \psi) = A_0(a) + \sum_{n=1}^{N} k_n(a) \cos[n(\psi - \phi_n(r))], \tag{2.2}$$

with the amplitude and phase coefficients (k_n, ϕ_n) defined as

$$k_n = \sqrt{A_n^2 + B_n^2} \qquad \text{and} \qquad \phi_n = \arctan\left(\frac{A_n}{B_n}\right). \tag{2.3}$$

The full moment map (i.e. velocity or velocity dispersion) can thus be described by the geometry of the rings and the amplitude of the coefficients k_n (or equivalently, A_n and B_n) of the Fourier terms as a function of semi-major axis length a (Figure 2.2).

To be more specific, the velocity field in an ideal rotating disk is expected to be dominated by the $\cos\psi$ term, since the velocity peaks at the galaxy major axis ($\psi \equiv 0$) and goes to zero along the minor axis ($\psi = \frac{\pi}{2}$, Figure 2.2). The power in the B_1 term therefore represents the circular velocity at each ring a, while power in the other coefficients (normalized to the rotation curve, B_1) represents deviations from circular motion. In local galaxies with very high S/N observations, for example, various coefficients have been shown to identify bars/radial inflow, lopsidedness/warps, multiple components, and spiral structure (Schoenmakers et al. 1997; Wong et al. 2004; Krajnović et al. 2006). In lower S/N data with sparser spatial sampling, these higher-order coefficients will also be affected by the rapid variations along each ring induced by the noise.

The velocity dispersion field, on the other hand, is an even moment of the velocity distribution and, as such, its kinemetric analysis is identical to traditional surface photometry.

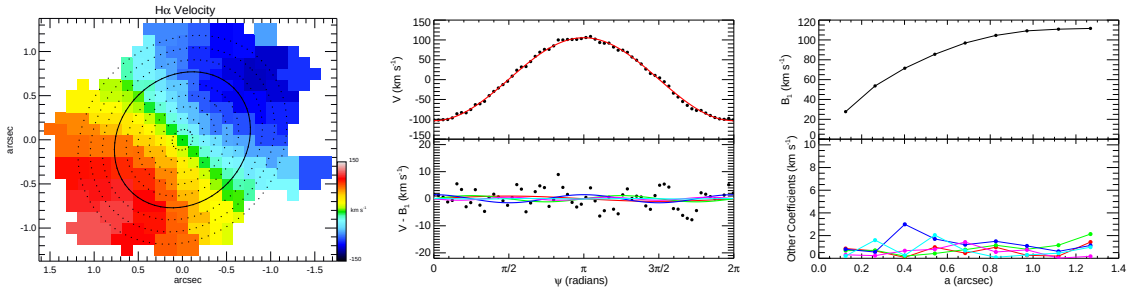

Figure 2.2: *Left:* Velocity field of a toy disk model (see §2.3.2), with kinemetry ellipses overlaid. One ellipse is emphasized with the solid line; the sampling of the rest of the ellipses are shown with the black dots. *Center:* The kinemetry expansion as a function of angle ψ along the solid ellipse. The top panel shows the measured velocities (*black points*) and the fit with the B_1 coefficient (*red*); the bottom panel shows the residuals from this fit (*black points*), and the higher order coefficients measured as a function of ψ (A_1 *in red,* A_2 *green,* B_2 *blue,* A_3 *magenta, and* B_3 *cyan*). *Right:* The kinemetry expansion from the center panel, now shown for all ellipses as a function of semi-major axis length a. The top panel shows B_1 as a function of a; this is the rotation curve. The bottom panel shows the strength of the higher order coefficients (*same colors as above*), all of which are negligible, as would be expected in an ideal disk. In this toy model, deviations from zero in these coefficients reflect the noise in the velocity field.

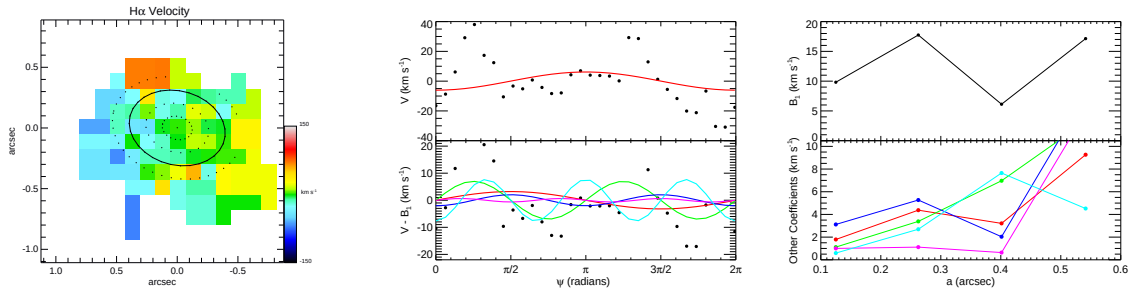

Figure 2.3: Same as Figure 2.2, but for an observed merger (IRAS 15206+3342) simulated at $z \sim 2$ (see §2.3.1). The irregular velocity field (*left*) is not well fit by a $\cos\psi$ term and therefore has significant power in all higher order coefficients (*center*). The combined effects of the lack of power in B_1 from the poor fit to $\cos\psi$ and the power in all other coefficients (*right*) will produce normalized coefficients k_n/B_1 that are much higher than those of a disk (Figure 2.2).

In an ideal rotating disk, the velocity dispersion will be constant along each ring and will decrease between rings of increasing semi-major axis length (Figure 2.1). For this moment of the velocity distribution, the power in the A_0 term as a function of semi-major axis length a will represent the velocity dispersion profile, and all azimuthally varying terms (higher-order kinemetry coefficients) will be zero. In analogy to the case with the velocity field, non-zero A_n's and B_n's can thus identify expected deviations from symmetry, in the form of lopsidedness and boxy/disky iso-velocity dispersion contours, but are also susceptible to variations caused by noise.

2.2.2 Kinemetry of High-Redshift Systems

Kinemetry was originally designed by Krajnović et al. (2006) for use with very high S/N (> 100) stellar kinematic data, as found in observations of bright galaxies in the local Universe. It has also been used to analyze simulated mergers and merger remnants by Jesseit et al. (2007) and Kronberger et al. (2007). To apply this method to the much lower S/N emission line data obtained at $z \sim 2$, the breadth of the analysis must be somewhat restricted. We therefore employ kinemetry in a more limited capacity; rather than using kinemetry to measure and interpret subtle dynamical features of a velocity field, we instead use it to determine the strength of deviations of the observed velocity and dispersion fields from the ideal rotating disk case. This is identical to assuming that any deviations from the ideal case that might occur in a disk (e.g. lopsidedness, warps, spiral structure) induce less power in the higher Fourier coefficients than those caused by the noise and much less than those that occur in a disturbed, merging system (compare Figures 2.2 and 2.3).

The first step in the analysis is locating the center of the system, around which the kinemetry ellipses are constructed. The robustness of this step is critical to the result, since Krajnović et al. (2006) show that an incorrect assumed center induces artificial power in the derived kinemetry coefficients. The primary result of a miscentering are elevated A_2 and B_2, but other coefficients (A_0, A_1, A_3, and B_3) are affected as well. It is therefore important that we use a robust definition of the system center, such that the center of an ideal disk is accurately recovered.

This is a non-trivial task in the clumpy and irregular Hα intensity distribution, the spatial distribution of which corresponds only to regions with enhanced star formation rates, is influenced by extinction, and therefore does not necessarily reflect the intrinsic mass distribution in the system (Figure 2.1). It is also not straightforward to robustly derive the location of the galaxy center from the velocity and velocity dispersion maps themselves (Krajnović, private communication). We therefore take advantage of the continuum distribution, which can be detected in the integral field data at a somewhat lower S/N underneath the emission lines. In general, the continuum surface brightness distribution is distinct from that of the emission line intensity (Figure 2.1, see also examples in local spiral galaxies in Daigle et al. 2006) and has sufficient S/N to differentiate regions of strong continuum emission from those of weaker continuum emission.

At $z \sim 2$, the detected continuum in near-infrared observations corresponds roughly to

rest-frame R-band. Observations at this wavelength therefore typically provide an accurate probe of the stellar distribution, although the effects of extinction have been shown to be significant in some local dusty mergers (Arribas & Colina 2003). While it is difficult to know precisely how large a role extinction plays in the observed R-band continuum distributions of high-z observations, some constraint can be provided from visual analysis of the data themselves. Several systems observed at $z \sim 2$ show a compact bright, central region of continuum emission, which remains single-peaked even at $< 0\farcs5$ (4 kpc) resolution (e.g. Figure 2.1), suggesting that this is an unobscured measure of the stellar (and mass) distribution in these systems.

As such, the continuum surface brightness distribution can be used to locate the center of a system. The natural choice for a galaxy's center is the position of the peak in the continuum intensity, which in an ideal disk also corresponds to the centers of the kinematic fields (Figure 2.1); however, in noisy data, this must be carefully defined. We identify the center of the continuum distribution by using the data in the brightest 25% of the pixels and finding the continuum-intensity-weighted average of their positions. This definition of the system center thus has the added benefit that the center of an early-stage major merging system (with two distinct nuclei) will be directly between the two components and not skewed towards only one of the two mass concentrations.

In high S/N data, the location of the center is the only parameter that must be determined prior to running a kinemetric analysis; the relevant geometric parameters (position angle and inclination) are derived during the kinemetry analysis. However, the lower S/N and coarse spatial sampling of the $z \sim 2$ data (see Figure 2.1) renders kinemetry's radius-by-radius solution for position angle and inclination rather unstable. For these systems, a much more robust solution for these parameters is found by considering the entire velocity field at once and solving for a global position angle and inclination. In nearby spiral galaxies, these quantities are observed to vary slowly throughout the system (Wong et al. 2004), thus making global values for position angle and inclination decent approximations.

To determine the position angle and inclination of a system, we use the known effects of errors in these parameters on the kinemetry coefficients A_n and B_n. Krajnović et al. (2006) demonstrate that, in the kinemetric expansion of a velocity field, a slightly incorrect assumed position angle generates excess power in the A_1, A_3, and B_3 coefficients, while a slightly incorrect assumed inclination affects primarily the B_3 term. However, large errors in these values can produce significant power in other coefficients as well. We therefore use the measured power in all coefficients to derive these parameters.

We solve first for the global position angle by stepping through all possible values, in increments of 3°, and performing a kinemetric expansion of the velocity field at each assumed value. Since this procedure focuses on locating the angle of steepest velocity gradient, the axial ratio of the ellipses (i.e. the inclination of the system) does not affect the results and is therefore held constant at unity, forcing the kinemetry ellipses to be circles. The goodness-of-fit of the assumed position angle is determined as the sum of the squared residuals between the "circular" velocity field (the 2D image reconstructed from only the B_1 term) and the observed velocity field. These residuals reflect the combined powers in the higher coefficients,

which appear as asymmetries in the velocity field. The curve of the goodness-of-fit as a function of position angle is then smoothed by 3 data points (=9°) to eliminate spurious results induced by the noise in the data, and the best-fit position angle is identified as the position angle that minimizes the smoothed curve.

Assuming this position angle, we then solve for the global inclination of the system, again using kinemetric expansion of the velocity field. We test ~ 50 values for the inclination, evenly spaced between axial ratios of 0.1 and 1.0. At every assumed ellipticity, kinemetry is performed, with the position angle held constant at the previously-determined best-fit value and the inclination held constant at the assumed value. The goodness-of-fit is determined as above, using the residuals between the "circular" velocity field and the actual measured values. The minimization of this method therefore finds the inclination that produces the smallest deviations from the circular term. However, since ellipses of similar axial ratios to that measured from the morphology will maximize the kinemetry coverage of the velocity field, and thus minimize the residuals measured near the edges of the system, this process induces a slight bias towards an inclination similar to that of the morphology. In practice, this bias partially mediates the adverse affects of beam smearing, in which the circular beam increases the opening angle of the isovelocity contours of the inclined velocity field. As with the position angle determination, we smooth the goodness-of-fit curve by 3 data points to reduced the impact of the noise in the velocity field, and we find the inclination that minimizes the smoothed residuals curve.

With the position angle and inclination held constant at these best-fit values, we can then perform a robust kinemetric analysis of the low-S/N high-z velocity and velocity dispersion fields. As in Krajnović et al. (2006), kinemetry is carried out to the fifth order terms, A_5 and B_5, which include most of the physical deviations from symmetry in the field but are not overly affected by rapid point-to-point variations induced by noise. Since the kinemetry coefficients are by definition orthogonal, this somewhat arbitrary choice of where to stop the expansion will not alter the measured values of the kinemetry coefficients.

2.2.3 Criteria for Differentiating Disks and Mergers

The main component of the analysis thus consists of running kinemetry, with pre-defined system center, global position angle, and global inclination, on both the velocity and velocity dispersion field of a galaxy. Since the quantity of interest is the deviations of these fields from those of ideal disks, we find the average deviation, defined as the average of the kinemetry coefficients that would be identically zero in a noiseless ideal disk.

For a velocity field in an ideal, rotating disk, the only non-zero kinemetry coefficient ought to be B_1, which we denote here as $B_{1,v}$ to indicate that this is the kinemetry result from the velocity field (Figure 2.2). Information about additional asymmetries are therefore contained in the higher-order terms, $k_{2,v}$ – $k_{5,v}$. Although Krajnović et al. (2006) use only odd kinemetry terms (e.g. k_5) to describe odd moments of the velocity distribution (velocity field), we include both the even and the odd terms in the kinemetry expansion here, since mergers produce extremely disturbed velocity fields, with power in all kinemetry coefficients

(Figure 2.3). In principle, one could also include the $A_{1,v}$ term as a measure of asymmetry, since this term represents any velocity gradients (inflows/outflows) found along the minor axis. In practice, however, we choose not to use the presence of a non-zero $A_{1,v}$ coefficient in the definition of non-ideal disks, since significant radial flows may be the result of such phenomena as outflows related to AGN/starburst winds or inflows induced by bar instabilities (see discussion in §2.5.2), and so do not provide information as to whether a system is undergoing a merger. We therefore compute the average $k_{avg,v} = (k_{2,v} + k_{3,v} + k_{4,v} + k_{5,v})/4$ as a measure of the non-ideal components of a system.

This average deviation $k_{avg,v}$ is normalized to the rotation curve $B_{1,v}$ in order to assess the relative level of deviation, following the prescription of Krajnović et al. (2006). This normalization has the added benefit of accounting for the loss of dynamic range in $k_{avg,v}$ at high redshifts, where the dim outer regions of a galaxy are too faint to be detected. In merging systems, greater radial coverage will correspond to greater detectable deviations from the ideal disk geometry, and it will also correspond to a greater dynamic range in the velocity gradient B_1 (Figure 2.4). By normalizing $k_{avg,v}$ to $B_{1,v}$, then, a system will roughly retain the same amount of detectable asymmetry regardless of the radial extent of the data. We therefore define the asymmetry, or level of deviation from an ideal disk, in the velocity field to be

$$v_{asym} = \left\langle \frac{k_{avg,v}}{B_{1,v}} \right\rangle_r , \tag{2.4}$$

where the average is over all radii (relative to the continuum peak) of the kinemetry ellipses.

For the velocity dispersion field, the only non-zero kinemetry coefficient in an ideal, rotating disk is $A_{0,\sigma}$, which quantifies the velocity dispersion profile. All higher-order coefficients $k_{1,\sigma}$ – $k_{5,\sigma}$ therefore measure any asymmetries in the field. For this moment of the velocity distribution, then, $k_{avg,\sigma} = (k_{1,\sigma} + k_{2,\sigma} + k_{3,\sigma} + k_{4,\sigma} + k_{5,\sigma})/5$ will contain information about the deviations from the ideal case.

Krajnović et al. (2006) note that, when looking at the velocity dispersion of the stellar component, the appropriate normalization for this even moment is the $A_{0,\sigma}$ coefficient. In the stellar case, the $A_{0,\sigma}$ term traces the mass of the system; however, this is not generally true of the velocity dispersion of a gas component, which can also be affected by shocks, especially in the violent environment of a major merger. In the kinemetry of gas kinematics, if there is significant rotation, the potential is often more reliably probed by the rotation curve, $B_{1,v}$. Furthermore, in Figure 2.4, the weakness of using a normalization to $A_{0,\sigma}$ in the presence of varying radial coverage is clear. As with the velocity field deviations $k_{avg,v}$, the velocity dispersion deviations $k_{avg,\sigma}$ become stronger with radius; a loss in radial coverage therefore directly corresponds to a loss in dynamic range in the asymmetries. In contrast, the value of the $A_{0,\sigma}$ circular term remains roughly constant, even when observed with the broader PSF of $z \sim 2$ observations. The value of $k_{avg,\sigma}/A_{0,\sigma}$ consequently decreases significantly for a given system when observations are less sensitive to the outer regions. A more appropriate normalization is the rotation curve of the velocity field, $B_{1,v}$, which is both a more reliable

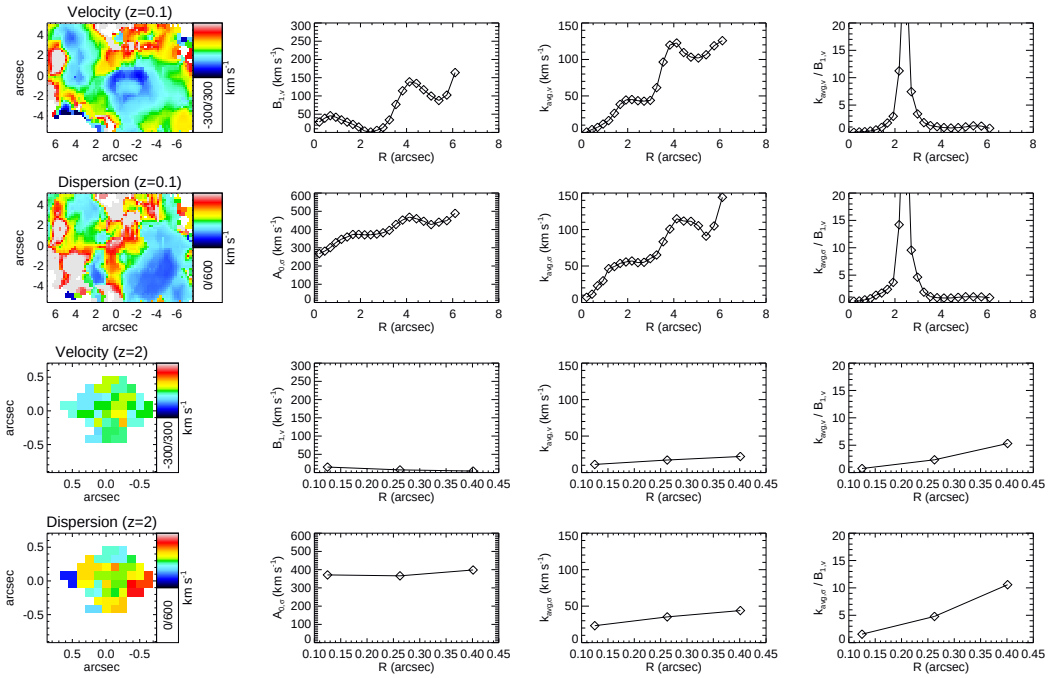

Figure 2.4: *From left to right:* The map of a given velocity moment, followed by the circular term of its kinemetry expansion, the higher order coefficients of the expansion k_{avg}, and the derived asymmetry parameter, all as functions of radius from the system center. This is shown, from top to bottom, for the velocity and velocity dispersion of the $z \sim 0.1$ ULIRG Mrk 273, and for the velocity and velocity dispersion of the simulated version of this system at $z \sim 2$ (see text for details). In the velocity maps, the diminished spatial extent of the high-redshift data corresponds to less resolution of both the rotation curve and the higher order coefficients. On the other hand, the velocity dispersion maps show negligible change in the dispersion profile with changing spatial coverage, while the higher order terms, as with those from the velocity field, lose dynamic range.

measure of the system's mass and responsive to the loss of dynamic range with decreased sensitivity. We therefore define the asymmetry in the velocity dispersion field as

$$\sigma_{asym} = \left\langle \frac{k_{avg,\sigma}}{B_{1,v}} \right\rangle_r , \tag{2.5}$$

where the average over all radii is unaffected by the combination of velocity and velocity dispersion kinemetric coefficients, since the kinemetry ellipses for the two maps are identical by the construction described in §2.2.2.

2.3 Application to Template Galaxies

To assess the capabilities of these criteria, we draw on a sample of observed low-redshift disks and mergers, which are then "observed" as if they were at $z \sim 2$, as well as on a sample of synthetic high-z systems, created from simulations of varying complexity. This set of template galaxies spans a large range in morphology, merging history, nuclear activity, and star-formation rate.

2.3.1 Observed Systems

Our template local galaxies are drawn from two samples: the SINGS spiral galaxy survey ($z \sim 0$; Kennicutt et al. 2003), as observed in Hα by Hernandez et al. (2005); Daigle et al. (2006); Chemin et al. (2006), and the Hα observations of low-z ultraluminous infrared galaxies (ULIRGs, $z \sim 0.1$) of Colina et al. (2005). Together, these data sets provide high-quality local observations of disks and mergers, respectively.

The SINGS galaxies were observed in Hα emission with the FANTOMM Fabry-Perot scanning interferometer (Hernandez et al. 2003). The template galaxies used here were all observed at the 1.6m telescope of the Observatoire du mont Mégantic in Québec, Canada (Hernandez et al. 2005; Daigle et al. 2006; Chemin et al. 2006). The pixel scale of the velocity maps is $1\farcs61$, and the spectral resolution R=12200-20000. From this sample, we use six spiral galaxies (NGC 925, NGC 3198, NGC 4321, NGC 4579, NGC 4725, and NGC 7331), which together span a range of Hubble types, nuclear activity, star formation rates, and distribution of star-forming regions throughout the system.

The ULIRG merger systems were observed in Hα emission and optical continuum with the INTEGRAL fiber-fed integral field system (Arribas et al. 1998), mounted on the 4.2m William Hershel Telescope of the Roque de Los Muchachos Observatory of La Palma, Spain. These data have resolution elements (fibers) of $0\farcs9$ diameter and spectral resolution R=1500 (Colina et al. 2005). From this sample, we use eight mergers (Mrk 273, Arp 220, IRAS 08572+3915, IRAS 12112+0305, IRAS 14348-1447, IRAS 15206+3342, IRAS 15250+3609, and IRAS 17208-0014), which, in analogy with the spiral sample, span a range of merger stage, nuclear activity, star formation rates, and distribution of star-forming regions throughout the system.

For both the disk and merger template galaxies, we simulate observations of these systems as if they were at $z \sim 2$ and were observed with the SINFONI integral field unit (Eisenhauer et al. 2003; Bonnet et al. 2004), on the Very Large Telescope (VLT) at Cerro Paranal, Chile. To artificially "redshift" the template galaxies, we convolve the datacubes to the mean seeing of such observations (FWHM of $0\farcs5 \simeq 4$ kpc; Förster Schreiber et al. 2006 achieved this beam size as typical seeing, while Genzel et al. 2006 used adaptive optics to reach a seeing FWHM of $0\farcs15$) and to the spectral resolution of the instrument (75 km s^{-1} at 2.2μm), interpolate the data onto the larger pixel scale (spatial scale of $0\farcs125 \simeq 1$ kpc; velocity scale of 33 km s^{-1}), account for the cosmological surface brightness dimming, and add Gaussian noise such that the S/N of the resulting datacubes is comparable to that of VLT/SINFONI observations. The Hα kinematics are extracted from these datacubes using the same technique as that of Förster Schreiber et al. (2006) and Bouché et al. (2007) on actual SINFONI observations and are shown in Appendix Figures 2.8 and 2.9.

The resulting sample of observed galaxies thus totals 14; six of local disks and and eight of local mergers, all "redshifted" to $z \sim 2$.

2.3.2 Simulated Systems

Because this naive "redshifting" of local systems cannot truly emulate the proto-galaxy population at $z \sim 2$, in which such phenomena as massive (10^{8-9} M$_\odot$) clumps of star formation affect the structure and kinematics of the systems (Bournaud et al. 2007a), we supplement our template galaxies with synthetic systems of various complexity. For this, we use both toy disk models, in which we have a complete understanding of all aspects of the data, as well as the detailed hydrodynamic cosmological simulations of Naab et al. (2007), from which we can "observe" synthetic systems at $z \sim 2$.

For the toy disk models, we use the modeling routines described in Förster Schreiber et al. (2006), which generate simple models of azimuthally-symmetric rotating disks, parameterized by mass, inclination, scale length, scale height, and isotropic velocity dispersion. Appropriate pixel sizes, beam smearing, spectral resolution, and noise levels are also included in the construction of the toy datacube. We improve on this model by allowing both an azimuthally-symmetric coupled mass and light distribution, and an overlaid light-only distribution (not azimuthally symmetric). The former therefore represents the stellar component of the system, while the latter produces very bright regions corresponding to areas of increased star formation. This addition allows us to generate models that more realistically simulate the clumpy and irregular Hα intensity distribution of systems at $z \sim 2$. We create five models with this technique, all of which have a centrally-peaked and azimuthally-symmetric mass distribution. We vary their light distribution (star-forming regions) as follows: one galaxy is nearly edge-on and is azimuthally symmetric around a centrally-peaked light distribution, one is nearly edge-on with a varying light distribution, one is of intermediate inclination and is azimuthally symmetric around a centrally-peaked light distribution (shown in Figure 2.1), one is of intermediate inclination with a light distribution much more extended on one side of the galaxy, and the last is of intermediate inclination with the light

distribution illuminating only a single side of the galaxy. From these models, we extract the emission line kinematics and continuum intensity by fitting a Gaussian with a constant offset to each spectrum (see Appendix Figure 2.10 for the models and their derived kinematics).

Our cosmologically-simulated models are drawn from Naab et al. (2007). The synthetic $z \sim 2$ systems come from high resolution (10^6 gas particles and 10^6 dark matter particles per halo) SPH simulations of 8 halos with a variety of mass accretion histories. Based on these mass accretion histories, we select time snapshots in which the halos have been evolving without a major merger in recent history or in the near future as well as snapshots in which the halos are visibly in the process of a major merger. For the latter group, these selection criteria essentially require the system to have a double nucleus, separated by $\lesssim 5$ kpc. From the 8 halos, we find 6 snapshots between $z = 1.8$ and $z = 2.8$ in which the systems are unambiguous disks and 4 snapshots between $z = 1.6$ and $z = 3.0$ in which the systems are unambiguous mergers. These 10 snapshots of the model galaxies are "observed" by converting the star-formation rate to Hα emission using the conversion factor from Kennicutt (1998), accounting for cosmological surface brightness dimming, binning to SINFONI-size pixels, convolving the data to the appropriate spatial and spectral resolutions, and adjusting the (Gaussian) noise level such that the S/N in Hα is comparable to that of the SINS observations. The continuum intensity for each system is "observed" through a similar process, using the stellar mass and converting to R-band luminosity with an assumed $M/L_R = 1$, typical for a Kroupa IMF in star-forming systems at this redshift (Fontana et al. 2004). We then rotate the halo to a random inclination, as given by a $\sin(i)$ probability distribution function, and extract the Hα kinematics from the resulting datacube (see Appendix Figures 2.11 and 2.12).

The resulting sample of model galaxies totals 15; five toy disks, six cosmologically simulated disks at $z = 1.8 - 2.8$, and four cosmologically simulated mergers at $z = 1.6 - 3.0$.

2.3.3 Classification

We test the criteria described in §2.2.3 on the 29 template galaxies to determine how well we can differentiate disks and mergers based on warm gas kinematics. For each system, we perform the analysis of §§2.2.2 and 2.2.3 to measure v_{asym} and σ_{asym} for these templates. (The results of the kinemetric analysis are summarized in Appendix Table 2.2 and shown in Appendix Figures 2.8 through 2.12.) Since this method does not lend itself to straightforward error propagation, we use Monte Carlo realizations of the noise in the data to measure the probability distribution functions (PDFs) of the asymmetries in these systems.

For each template system, the Monte Carlo realizations consist of creating 1000 realizations of the moment maps - the continuum intensity, and the emission line intensity, velocity, and velocity dispersion - based on their corresponding error maps. These error maps correspond to the measurement errors of the velocity moments, as derived when fitting the kinematics from the datacubes. For each moment map, we perturb the observed data points by randomizing them, using Gaussian noise parametrized by the measured (1-σ) errors. The new set of maps is then rerun through the entire analysis described in §§2.2.2 and 2.2.3.

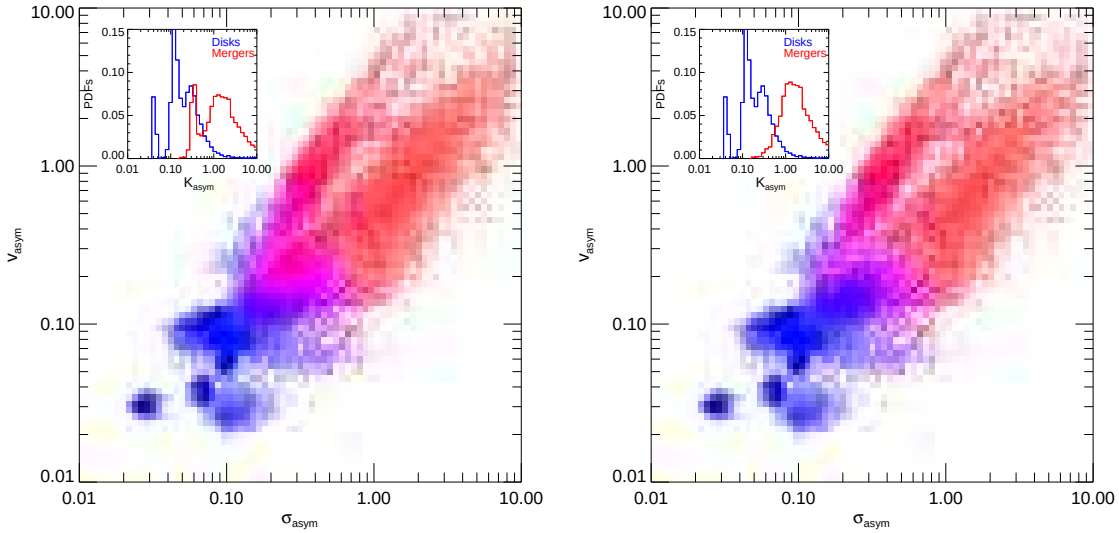

Figure 2.5: Asymmetry measure of the velocity and velocity dispersion fields for all of the template galaxies (*left*) and all of the template galaxies except the obviously misclassified ULIRG, IRAS 12112+0305 (*right*). The probability distributions in this space are shown with shading for the template disks (*blue*) and mergers (*red*), as derived from the Monte Carlo realizations. Inset are the PDFs for the total kinematic asymmetry (K_{asym}) for disk and mergers. The empirical delineation of K_{asym}= 0.5 cleanly separates the two classes, as is especially visible in the right panel.

Figure 2.5 illustrates the resulting v_{asym} and σ_{asym} measurements for the template systems. In this figure, all of the results from the Monte Carlo realizations are plotted, with red shading indicating the resulting PDF of the merger templates and blue shading indicating that of the disk templates. These two classes can be cleanly separated by the empirical delineation of total kinematic asymmetry $K_{asym} = \sqrt{v_{asym}^2 + \sigma_{asym}^2} = 0.5$, as visible in the inset.

The majority of the disks (89%) are located in the lower left (low v_{asym}, low σ_{asym}) of the diagram, with the small deviations from the ideal case ($v_{asym} \equiv 0$, $\sigma_{asym} \equiv 0$) coming from noise, thickness of the disk, and other kinematic features such as warps and multiple components. The mergers, for the most part, show strong deviations from zero in both v_{asym} and σ_{asym} and are located towards the upper right of the plot. However, 20% of merging systems remain indistinguishable from disks. This is largely due to a single ULIRG, IRAS 12112+0305, whose velocity and velocity dispersion fields appear regular at $z \sim 2$ (see Appendix Figure 2.9), although other systems contribute to a lesser extent as well (Figure 2.5). Based on these results, we can roughly estimate the errors in these criteria and can expect to correctly classify $\sim 89\%$ of disks and $\sim 80\%$ of mergers.

Because these conclusions are based on a detailed and complicated analysis (§2.2.2), we tested on several systems how changes in the assumed center, position angle, and inclination would affect the classification of the system as a disk or a merger. We first examined variations in the assigned center and found that, for disks, the classification of a system as such is virtually independent of the center, except in extreme miscenterings when the center is assigned to the very edge of the system. However, the location of the center is more important in the case of mergers with a double nucleus. In these systems, if the center is skewed too far towards one of the two mass concentrations (both of which have some ordered rotational motion), the system can be misclassified as a disk. This reinforces the necessity of choosing the center of mass of the system, via the continuum-intensity-weighted center as described in §2.2.2.

The test of variations in position angle indicated that the classification of a system as a disk or merger is even more robust against changes in this parameter. In the case of disks, these systems maintain their low K_{asym} through extreme variations in position angle, until the position angle is aligned within $\sim 10^{\rm o}$ of the minor axis. In mergers, the position angle has no physical meaning but, by the process described in §2.2.2, has been defined such that it minimizes K_{asym}. As a result, in these systems, all variations in position angle only increase their measured asymmetries, making their classification as mergers even stronger. Finally, variations in inclination were also examined and were shown in nearly all cases to have no effects on the classification of either disks or mergers. These tests of the effects of assumed inclination, position angle, and center on the classification of a system therefore suggest that, even in systems where there remains some uncertainty about the values of these parameters, our method will provide a robust classification with K_{asym}.

2.4 Application to High-Redshift Galaxies

Having tested our criteria on the above template galaxies, we now apply them to the 'unknowns,' the high-z systems observed in the SINS program (Förster Schreiber et al. 2006; Genzel et al. 2006; Bouché et al. 2007; Cresci et al. 2009). Here we examine those galaxies with sufficient spatial resolution and data quality to perform the kinemetric analysis described above. Galaxies that are unresolved, have large errors in the kinematics, or have significantly lower S/N than the majority of the sample are omitted from the present discussion; in future work, we will expand our criteria to include variations in these quantities.

2.4.1 Data

The SINS $z \sim 2$ sample is taken from large photometric samples, in which high-z objects are identified through either their rest-frame ultraviolet color/magnitude (BM/BX criterion: Adelberger et al. 2004; Steidel et al. 2004; Erb et al. 2006c,a), or their rest-frame optical properties (s-BzK: Daddi et al. 2004a,b; Kong et al. 2006, GDDS: Abraham et al. 2004). These selection criteria sample luminous (L $\sim 10^{11-12} L_{\odot}$) galaxies with a range of star formation rates (SFR $\sim 10 - 200$ $M_{\odot}$/yr) and ages (50 Myr - 2Gyr; Erb et al. 2006c; Daddi et al. 2004a,b). From these photometric samples, our selection criteria emphasize somewhat brighter ($<$F(Hα)$>$ of 10^{-16} compared to 6×10^{-17} erg/s/cm^2) systems, with broader line widths ($<v_c>$ of 175 ± 68 compared to 140 km/s) than the average galaxy in the Erb et al. (2006a) sample. Both samples have similar mean dynamical masses.

The SINS galaxies were observed in Hα emission, which at $z \sim 2$ is redshifted to the K-band, with VLT/SINFONI. Approximately R-band continuum emission is visible beneath the strong emission lines. Most of the data have 0.″125 x 0.″250 pixels, sampling a typical PSF FWHM of 0.″5, and have a spectral resolution of $R \sim 4000$. Additionally, a few systems have been observed with adaptive optics, enabling the use of the finer pixel scale of 0.″05 x 0.″10 to sample the typical PSF FWHM of 0.″15. The data analysis is described in Förster Schreiber et al. (2006); here we add the additional step of spatially binning the datacube to a minimum amplitude-to-noise ratio of 5 with the Voronoi binning technique of Cappellari & Copin (2003). This reduces the spatial resolution at the fainter edges of a system, where several spatial elements must be summed, but the amplitude-to-noise requirement ensures a more robust measurement of the kinematics in each bin.

The SINS systems were observed with integration times ranging from 1.5 hours to over 8 hours (Förster Schreiber et al. 2006; Genzel et al. 2006; Bouché et al. 2007; Cresci et al. 2009), which, when coupled with differences between systems, results in a wide range of errors on the kinematic measurements, S/N levels, and number of beams covering the systems. In Figure 2.6, we compare the assumed values for our template galaxies (typical values for the entire sample) to the actual values for individual SINS galaxies (see figure caption for details). For this sample, the most critical and most limiting requirement is that the systems are well resolved, which we define as covered by $\gtrsim 3$ beams, although we also require that the continuum be detected with a significant S/N level and that the kinematic measurements be

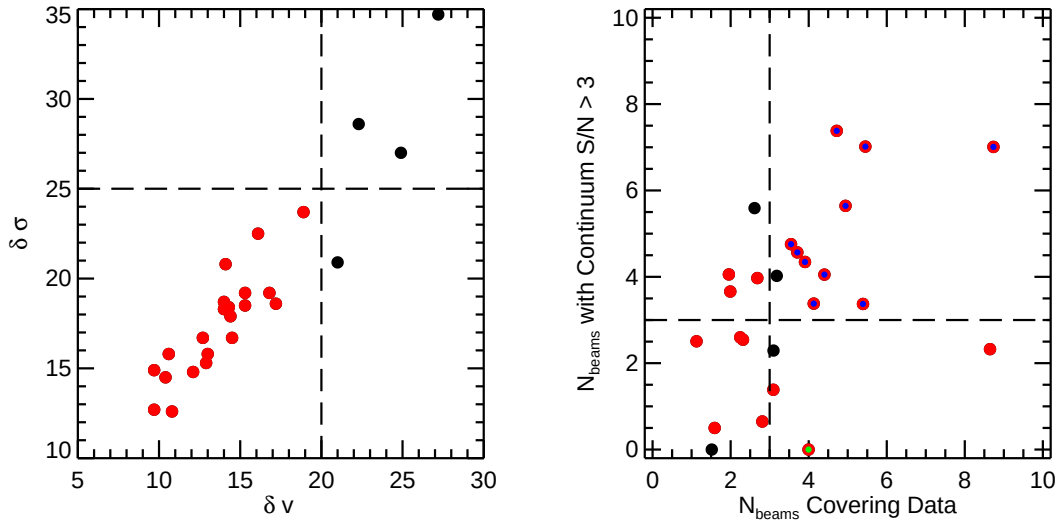

Figure 2.6: *Left:* Comparison of the "redshifted" template galaxies' typical errors in velocity and velocity dispersion (*dashed lines*) with the measured median errors of each of the SINS program galaxies. SINS systems with smaller errors than those of the templates are shown in red. *Right:* The horizontal axis compares the median number of beams covering each system in the template galaxies (*vertical line*) with those of the SINS galaxies. The vertical axis compares the median number of beams covering data with continuum S/N > 3, as used to determine the galaxy centers, in the template galaxies (*horizontal line*) with those of the SINS systems. Red points are the same galaxies shown in red in the left panel; red and blue points are those systems with data of better quality than that of the templates, based on both panels. Only these systems are included in our analysis, with one additional inclusion. We also analyze BzK-15504, shown with the red and green point, which fulfills three of the four data quality requirements but has insufficient S/N in its continuum emission. The lower S/N per pixel is in part due to the finer spatial sampling of this system, which Genzel et al. (2006) observed with the 0.″1 pixel scale. Fortunately, the continuum emission of this system has been observed in deep VLT/NACO imaging with laser guide star adaptive optics, which revealed a distribution consistent with that measured from the SINFONI data. We are therefore confident that the continuum center measured from the SINFONI data does in fact reflect the center of the mass distribution in this system.

Table 2.1: Properties of the High-z Galaxies

Galaxy	z	SFR[a] ($M_\odot$/yr)	M_{dyn}^b (10^{10} $M_\odot$)	$R_{1/2}$ (kpc)	Selection[c]
SSA22a-MD41	2.17	34	4.0	5.8	UV
Q1623-BX528	2.27	28	2.3	6.2	UV
Q2343-BX389	2.17	93	11.0	6.2	UV
Q2343-BX610	2.21	115	10.2	5.4	UV
Q2346-BX482	2.26	69	7.8	6.4	UV
BzK-6004	2.39	157	16.2	6.6	optical
BzK-12556	1.59	38	1.8	5.1	optical
BzK-15504[d]	2.38	101	10.0	5.3	optical
D3a-6397	1.51	65	6.3	7.6	optical
K20-ID7	2.22	84	3.5	4.5	optical
K20-ID8	2.22	42	1.8	5.4	optical
Average	2.12	81	6.8	5.9	–
SINS UV Sample[e]	2.26	60±36	4.1±3.7	4.3±2.1	UV
SINS Optical Sample[f]	2.02	46±49	4.2±4.5	4.7±1.6	optical

[a] As derived from the total Hα flux measured from the SINS data. These values are converted to SFR via the Kennicutt (1998) conversion, with an additional conversion to a Chabrier IMF. Extinction A_V is measured from SED modeling (see Förster Schreiber et al. 2009), and the Calzetti extinction law is used to estimate extinction $A_{H\alpha}$, from which the extinction correction is calculated.

[b] From the measured circular velocity, $R_{1/2}$, and axial ratio of the intensity distribution.

[c] Rest-frame waveband in which the object was identified.

[d] Observed with AO, yielding a PSF FWHM of $0''.15$; all other systems were obtained in seeing-limited mode with a mean PSF FWHM of $0''.5$.

[e] Systems observed in the SINS program that were originally identified with rest-frame UV photometry. Values given are mean and standard deviation of the sample.

[f] Systems observed in the SINS program that were originally identified with rest-frame optical photometry. Half of this sample has $z \sim 2.3$, and half $z \sim 1.5$. Values given are the mean and standard deviation of the sample.

sufficiently precise. Analyzing data that do not meet these standards will adversely affect the spatial sampling of the kinemetry ellipses, their centering, and the precision of the derived asymmetry measures v_{asym} and σ_{asym}; the calibration of our analysis to such lower quality data is outside the scope of this chapter. We find that 11 of the $z \sim 2$ systems have equal or higher quality data than the templates and thus their kinematic asymmetries can be reliably determined. We therefore perform our analysis on only these systems.

The properties of this subsample are listed in Table 2.1 and compared to the average properties of the UV-selected and optically-selected samples observed in the SINS program. In most cases, the star formation rates, dynamical masses, and half-light radii of the objects analyzed here are slightly higher than the mean values for these parameters from the full SINS sample but still within the standard deviations. Since the SINS sample contains a number of spatially unresolved compact objects (Förster Schreiber et al. 2006), these statistics are consistent with the data requirements outlined above, in which only the well resolved (and thus large half-light radius and likely high mass) objects are selected for analysis. It is these resolved objects in which the most progress can be made; for this reason, these systems were also the focus of Förster Schreiber et al. (2006) and Genzel et al. (2006).

In their analyses, Förster Schreiber et al. (2006), Genzel et al. (2006), and Bouché et al. (2007) study the SINS data using the framework of rotating disks. These authors have argued from qualitative examination of the data, along with analysis of the rotation curves and comparison to model disks in several cases, that many of these UV/optical-selected systems are candidate disk galaxies, although they note that a minority do in fact have the disturbed velocity fields expected of mergers. We are now in a position to quantitatively test these conclusions.

2.4.2 Classification

We perform the analysis of §§2.2.2 and 2.2.3 on the SINS systems, with the same 1000 Monte Carlo realizations, as done on the template $z \sim 2$ systems (§2.3.3). In Figure 2.7 we plot the resulting v_{asym} and σ_{asym} measurements for these galaxies. These results confirm the analyses of Förster Schreiber et al. (2006) and Genzel et al. (2006) in that $> 50\%$ (8/11) of galaxies in the SINS subsample studied here are consistent with a rotating disk interpretation (see Appendix Table 2.2 for a list of results for each system). Given the error rate of these criteria, as found with the template systems, this suggests that these results sample a parent population composed of 8.4 disks and 2.6 mergers, such that $89\% \times 8.4 + 20\% \times 2.6 = 8$ systems are observed as disks and $80\% \times 2.6 + 11\% \times 8.4 = 3$ systems are observed as mergers, making the fraction of disks in the subsample of Table 2.1 as high as $8.4/11 = 75\%$. Additionally, we expect that $20\% \times 2.6 \sim 1$ merger will be misclassified as a disk and that $11\% \times 8.4 \sim 1$ disk will be misclassified as a merger.

It is of special interest to specifically investigate the most qualitatively convincing disks in the sample identified by Förster Schreiber et al. (2006, SSA22a–MD41, Q2343–BX389, Q2343–BX610) and Genzel et al. (2006, BzK–15504). We highlight these systems in Figure 2.7 and indeed find that all four are consistent with a rotating disk interpretation. Förster

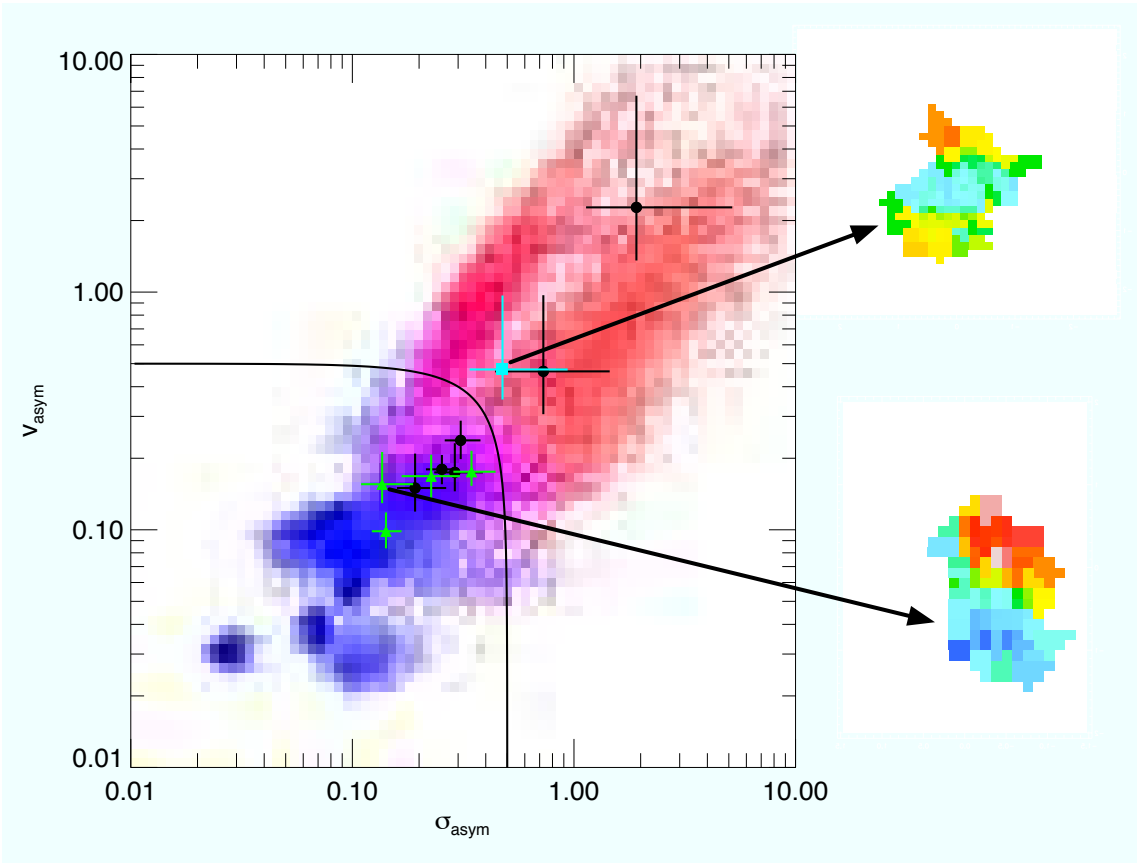

Figure 2.7: Asymmetry measure of the velocity and velocity dispersion fields for the SINS program galaxies that have high enough quality data for such analysis, overplotted on the disk and merger template PDFs from Figure 2.5. The line indicates the division between disks and mergers at $K_{asym} = 0.5$. The probable disks identified by Förster Schreiber et al. (2006) and Genzel et al. (2006) are indicated here as green triangles. The merger identified by Förster Schreiber et al. (2006) is shown with the cyan square. Sample velocity fields of SINS disk-like and merger-like systems are shown at right; the full analysis of the SINS sample is recorded in Appendix Table 2.2 and shown in Appendix Figures 2.13 and 2.14.

Schreiber et al. (2006) also point out that two of their systems that may in fact be mergers; the one such system with sufficient data quality, Q1623–BX528, is identified in Figure 2.7 and is in fact a merger. Our criteria thus make intuitive sense based on visual analysis of the observed velocity and velocity dispersion fields and therefore demonstrates quantitatively the validity of the rotating disk interpretation as applied to the SINS sample.

2.5 Discussion

The efficacy of our dynamical criteria in identifying systems undergoing major mergers and their applicability to the SINS high-z survey is illustrated in §§2.3.3 and 2.4.2; however, there are a number of caveats in this method that merit closer investigation. Here we expand the discussion of §2.4.2 to highlight the impact of this technique on high-z studies of galaxy formation, as well as address the most critical issues with this technique: the ability of the Hα kinematics to reflect the underlying dynamics of a system, and the observational constraints on probing the structure of a distant system in detail.

2.5.1 Implications for Galaxy Formation at High-Redshift

Of the $z \sim 2$ systems analyzed here, we find that 8/11 ($> 50\%$) are consistent with a rotating disk interpretation. These results, coupled with the large stellar and dynamical masses of these systems ($M_{dyn} \sim 10^{10-11}$ M$_\odot$; Table 2.1), quantitatively confirm that massive disks were already in place at this redshift. It furthermore strengthens the conclusions of Förster Schreiber et al. (2006) and Genzel et al. (2006) that the high (up to 100 M$_\odot$ yr^{-1}) star formation rates of these systems are not the consequence of recent violent mergers but rather are happening within disks dominated by ordered rotation.

In the case of a typical massive ($\sim 10^{11}$ M$_\odot$) star-forming galaxy, BzK-15504, which Genzel et al. (2006) studied in detail, modeling of the spectral energy distribution (SED) from broad band photometry was used to measure the stellar mass and age of the system. With the stellar mass M$_* = 8 \times 10^{10}$ M$_\odot$ and the star formation rate of ~ 100 M$_\odot$ yr^{-1} (as measured from Hα), together with the assumption of a constant star formation rate, all the stars in this system could have been formed in ~ 500 Myr (Genzel et al. 2006). This number agrees well with the stellar age measured from the SED fitting ($300 - 800$ Myr), making it likely that this system formed rapidly with continuous star formation (and therefore mass inflow) at its current rate (Genzel et al. 2006). Given that the above analysis (Figure 2.7) indicates that this system has not undergone any recent major merger activity, and given that this system is typical for its population, our results provide new and direct empirical evidence that the smooth accretion mechanism can play an important role in the early stages of the evolution of massive galaxies.

The diagnostic tool described here is critical in expanding our understanding of structure formation and evolution in the early Universe. With current extensive data sets of high-z systems, including broad-band photometry and integral-field kinematic observations, much

can be learned about the stellar populations, star formation processes, and nuclear activity of the galaxies evolving in a critical epoch of the Universe's history. We now add another crucial piece to the study of high-z systems by introducing a method to quantitatively evaluate the dynamical state of a system and therefore to link that system's observed properties with a major merger event or with a more quiescent evolutionary history.

2.5.2 Hα as a Probe of a System's Dynamics

The reliability of using Hα emission to study the structure of a galaxy is, at first glance, rather unclear. The motions of the warm gas are not guaranteed to reflect those of the underlying stellar distribution, since the former component is much more easily disturbed - with gravity or pressure fluctuations - than the more massive, collisionless stars. On the other hand, the dissipative gas component also more efficiently relaxes into a thin disk and could conceivably demonstrate ordered rotational motion while disturbances in the stellar (and mass) distribution persist (e.g. Mihos & Hernquist 1996). These competing effects, together with the ambiguity caused by the limitations of spatial resolution, could conceivably render it difficult to interpret the kinematics of the warm gas as uniquely representing a disk or a merger.

Furthermore, the kinematics of the warm gas are also expected to reflect such phenomena as the large-scale gas flows that feed active nuclei and the powerful galactic winds from AGN/starburst activity, both of which at $z \sim 2$ are thought to play an important role in regulating the star formation history of the Universe. For this reason, we designed our criteria with input from templates that were likely to include as many of these phenomena as possible. Our sample of disks includes a kinematically perturbed system, several barred systems, and two Seyfert galaxies. One of these active systems (NGC 4579) is a barred galaxy in which the radial motion of the gas is clearly visible as a strong velocity gradient along the minor axis (Gonzalez Delgado & Perez 1996; Daigle et al. 2006). We also observe such an inflow in a SINS system, BzK-15504, as described by Genzel et al. (2006). In this system, a strong velocity gradient is also seen along the minor axis, in the form of a high $A_{1,v}$ term, presumably corresponding to the driving of fuel towards a growing bulge with an embedded active nucleus (Genzel et al. 2006). We can nevertheless robustly identify both the "redshifted" NGC 4579 and BzK-15504 as disks, since the kinemetric signature of the inflows is restricted to the $A_{1,v}$ coefficient, which is excluded from our analysis for precisely this reason (and could potentially be used in future work as a tracer of AGN feedback at high redshift). As shown in §2.3.3, this omission does not diminish our ability to detect mergers, since the disturbed velocity fields of such systems also produce power in all the higher-order kinemetry coefficients.

To discount the possibility of contamination by large-scale outflows in the $z \sim 2$ kinematics, we compare with observations of local systems with substantial galactic winds. In general, line emission from these "superwinds" in local starbursting galaxies dominates neither the total Hα surface brightness nor the emission line kinematics along the galaxy major axis (Lehnert & Heckman 1995, 1996a,b). The gas flowing outward along the minor axis

has been shown to contribute only a small fraction of the total Hα luminosity; in even the extreme cases of local infrared-luminous and highly-extincted starburst galaxies, Armus et al. (1990) show that the extended emission-line gas outside of a few kpc from the nucleus accounts for $< 25\%$ of the total Hα emission. In a few cases in our SINS sample, our data reveal a high-velocity outflow component, but this wind contributes $< 10\%$ to the total Hα luminosity of the system. Similar results have been found with integral field data of a $z \sim 2$ SMG by Nesvadba et al. (2007).

For the majority of the SINS $z \sim 2$ systems, then, it is likely that we can rule out possible contamination from superwinds and that we have sufficiently accounted for the affects of large-scale gas inflows. The $z \sim 2$ data are thus more consistent with the scenario in which the emission line kinematics trace dynamical features similar to those of the template galaxies.

This argument suggests that the kinemetric analysis of a system is largely independent of SFR-driven phenomena and therefore of the overall SFR, a fact that is borne out by the data themselves. In local spiral galaxies, where the relatively low SFRs ($\sim 1-10$ M$_\odot$ yr^{-1}) reflect low gas fractions, the dynamics of the warm gas are driven by those of the dominant, rotating stellar component. In contrast, the SINS galaxies, with SFRs characteristic of ULIRGs (up to and exceeding 100 M$_\odot$ yr^{-1}), have significantly higher gas fractions ($f_{gas} \sim 0.4$; Tacconi et al. 2006; Bouché et al. 2007) and consequently a dynamically important dissipative component. The gas in these systems quickly concentrates into massive, powerful star-forming regions, which drive turbulent motion and thus high velocity dispersions in the warm gas. However, the clumps detected in SINS systems have not fatally disrupted the dynamics of their host galaxy; $> 50\%$ of SINS systems display velocity fields consistent with ordered rotation and regular (though elevated) velocity dispersions. Despite orders of magnitude difference in SFR between local spiral galaxies and SINS systems, it appears that the processes governing the Hα kinematics in the two regimes are remarkably similar. This is consistent with results from Bouché et al. (2007), who demonstrated that star formation at high SFR and high redshift is governed by the same physics as in the local Universe. For the purpose of the analysis presented here, then, Hα emission can be effectively employed as a tracer of a system's dynamics for a large range of SFR and redshift.

2.5.3 Continuum Surface Brightness Distribution

One of the unique capabilities of the integral-field data used in our analysis, besides providing spatially resolved kinematics of a system, is separating the emission coming from star-forming regions, as visible in Hα emission, from that of the underlying stellar background, visible in approximately R-band continuum emission. Morphological criteria using the continuum distribution to detect mergers have been implemented at lower redshift by e.g. Conselice (2003) and Lotz et al. (2004) using *HST* data. However, at $z \sim 2$ the stellar distribution is difficult to probe at optical (rest-frame UV and B) wavebands, since this emission can be severely affected by extinction in gas-rich systems (e.g. Colina et al. 2005). It is therefore of interest to examine the rest-frame R-band continuum emission measured

directly in our integral field data.

Unfortunately, these methods require both high S/N and resolution elements smaller than 1 kpc/pixel, which with SINFONI at $z \sim 2$ is attainable only in AO-assisted observations. Since our observations were optimized for the analysis of the line emission properties of the sources and were mostly obtained in seeing-limited mode, we tested several simpler criteria, based on kinemetry of the continuum distribution (which by definition is identical to surface photometry). Any asymmetries in the continuum distribution would likely be due to the presence of multiple mass concentrations, as in an early-stage merger. We find that the systems identified as potential early-stage mergers are, as expected, a subset of those identified as mergers by the kinematic criteria. This result highlights the unique capabilities of directly probing the dynamical properties of high-z systems with integral field observations.

We do not develop further any analysis of the continuum emission in our SINS IFS data, as the low S/N of this emission limits the strength of the conclusions that can be drawn from such analyses. Forthcoming sensitive high-resolution (*HST* and ground-based AO-assisted) imaging of the SINS systems in the near-infrared will provide the necessary resolution and S/N required for the quantitative morphological analyses of broad-band emission (Förster Schreiber et al. in prep). The comparison of such results with those from the kinemetric analysis developed here will provide a valuable further probe into the nature of high-z systems.

2.5.4 Limitations of the Method

For the analysis described here, we designed our template systems to have S/N, resolutions, and spatial extent comparable to typical values of the SINS survey at $z \sim 2$. In §2.4.1, we illustrated that a subsample of 11 SINS observations have higher quality data than the templates and thus have morphologies that can be reliably measured.

For the remainder of the systems, and for systems at other redshifts or measured under different observing conditions, the current criteria cannot be blindly applied. We expect that there will be fundamental data limitations beyond which these criteria cannot distinguish disks from mergers. In future work, we will therefore generalize this methodology to a wide range of S/N, spatial resolutions, and spatial sampling in order to investigate the effectiveness of our criteria for a more complete range of redshifts and observing conditions.

2.6 Conclusions

We present a simple set of kinematic criteria that can be used to distinguish mergers and disks in the SINS survey and in similar observations (i.e. with Keck/OSIRIS). The reliance of our criteria on dynamical information, rather than on surface brightness distributions, takes full advantage of the wealth of information provided with integral field data.

We show, via a large set of template galaxies, that our criteria can reliably distinguish the majority of major mergers (80%) from disks. When applied to the SINS galaxies, this

tool provides quantitative support for the rotating disk / smooth accretion scenario that the interpretation of recent results has suggested (Förster Schreiber et al. 2006; Genzel et al. 2006; Birnboim et al. 2007). In the subset of the SINS systems studied here, we quantitatively show that $> 50\%$ likely have not had a major merger in their recent history to fuel their rapid star formation, providing direct evidence for this scenario.

Looking forward, the differentiating of disks and mergers on a galaxy-by-galaxy basis that is now possible is useful both immediately and in the future with next-generation high-z surveys on 30m class telescopes. As an increasing number of galaxies in the high-redshift Universe are probed with spatially resolved kinematics, the tool presented here can be used to observationally constrain merger fractions, as well as to understand the effect of mergers on star formation rates, nuclear activity, and growth of structure within proto-galaxies.

Acknowledgments

We are very grateful to the entire SINS team, whose input greatly improved the quality of this work. We also thank Carl Heiles for many useful discussions and the anonymous referee for helpful comments.

2.7 Appendix

In this appendix, we present the kinemetric analysis on all template and SINS galaxies. These results are summarized in Table 2.2 and are shown for each system in Figures 2.8 through 2.14.

Table 2.2: Kinemetry Results for the Template and High-z Galaxies

Galaxy	Type	$v_{asym}{}^a$			$\sigma_{asym}{}^a$			Classification
NGC 925	SABd; HII	0.14	0.18	0.25	0.18	0.26	0.37	Disk
NGC 3198	SBc; non-active	0.11	0.14	0.20	0.16	0.21	0.32	Disk
NGC 4321	SABbc; LINER	0.13	0.16	0.21	0.24	0.37	0.61	Disk
NGC 4579	SABb; Seyfert	0.24	0.43	1.11	0.13	0.21	0.47	Disk
NGC 4725	SABab; Seyfert	0.08	0.08	0.10	0.06	0.08	0.11	Disk
NGC 7331	SAb; LINER	0.06	0.07	0.10	0.10	0.23	0.49	Disk
IRAS 08572+3915	ULIRG; HII	0.20	0.42	1.34	0.75	1.58	4.40	Merger
IRAS 12112+0305	ULIRG; LINER	0.18	0.22	0.26	0.22	0.26	0.31	Disk
IRAS 14348-1447	ULIRG; LINER	0.56	0.99	2.47	1.35	2.25	5.02	Merger
IRAS 15206+3342	ULIRG; LINER	0.57	1.07	2.96	0.78	1.57	4.43	Merger
IRAS 15250+3609	ULIRG; LINER	0.17	0.47	2.10	0.56	1.52	6.42	Merger
IRAS 17208-0014	ULIRG; LINER	0.19	0.34	0.95	0.64	1.12	2.92	Merger
Mrk 273	ULIRG; Seyfert	0.55	1.10	3.25	0.96	1.97	5.82	Merger
Arp 220	ULIRG; HII	0.18	0.27	0.51	0.24	0.34	0.64	Merger
Toy Simulation 1	Toy Disk Model	0.03	0.03	0.04	0.10	0.11	0.16	Disk
Toy Simulation 2	Toy Disk Model	0.13	0.15	0.17	0.16	0.20	0.28	Disk
Toy Simulation 3	Toy Disk Model	0.07	0.08	0.09	0.11	0.13	0.16	Disk
Toy Simulation 4	Toy Disk Model	0.03	0.03	0.03	0.03	0.03	0.03	Disk
Toy Simulation 5	Toy Disk Model	0.10	0.10	0.11	0.05	0.07	0.08	Disk
Halo A ($z = 1.80$)	Simulated Disk	0.03	0.04	0.04	0.07	0.07	0.08	Disk
Halo B ($z = 2.00$)	Simulated Disk	0.11	0.12	0.12	0.07	0.09	0.10	Disk
Halo C ($z = 2.75$)	Simulated Disk	0.10	0.13	0.18	0.19	0.24	0.31	Disk
Halo E ($z = 2.75$)	Simulated Disk	0.08	0.10	0.13	0.11	0.13	0.16	Disk
Halo L ($z = 2.00$)	Simulated Disk	0.05	0.06	0.07	0.09	0.10	0.11	Disk
Halo M ($z = 2.50$)	Simulated Disk	0.08	0.09	0.10	0.08	0.09	0.11	Disk

Continued on Next Page...

Table 2.2 – Continued

Galaxy	Type	v_{asym}[a]			σ_{asym}[a]			Classification
Halo C ($z = 2.00$)	Simulated Merger	1.01	1.71	2.84	0.40	0.70	2.22	Merger
Halo E ($z = 1.60$)	Simulated Merger	0.30	0.51	1.28	0.24	0.57	1.59	Merger
Halo Q ($z = 2.75$)	Simulated Merger	0.55	0.82	1.97	0.28	0.42	0.92	Merger
Halo V ($z = 3.00$)	Simulated Merger	0.85	1.43	4.80	0.32	0.46	1.19	Merger
SSA22a-MD41	SINS Galaxy	0.08	0.10	0.12	0.12	0.14	0.17	Disk
Q2343-BX389	SINS Galaxy	0.13	0.16	0.21	0.11	0.14	0.19	Disk
Q2343-BX610	SINS Galaxy	0.14	0.17	0.21	0.17	0.23	0.31	Disk
Q2346-BX482	SINS Galaxy	0.20	0.23	0.29	0.26	0.31	0.38	Disk
BzK-6004	SINS Galaxy	0.15	0.17	0.23	0.23	0.29	0.39	Disk
BzK-15504	SINS Galaxy	0.15	0.18	0.21	0.28	0.34	0.44	Disk
D3a-6397	SINS Galaxy	0.15	0.18	0.21	0.21	0.25	0.30	Disk
K20-ID8	SINS Galaxy	0.12	0.15	0.21	0.16	0.19	0.27	Disk
Q1623-BX528	SINS Galaxy	0.35	0.47	0.97	0.34	0.48	0.94	Merger
BzK-12556	SINS Galaxy	1.36	2.27	6.71	1.13	1.91	5.18	Merger
K20-ID7	SINS Galaxy	0.31	0.46	0.97	0.44	0.73	1.45	Merger

[a]Listed here is the 68% confidence interval, as derived from 1000 Monte Carlo realizations, with the three columns indicating the lower bound on the confidence interval, the median value, and the upper bound on the confidence interval, respectively.

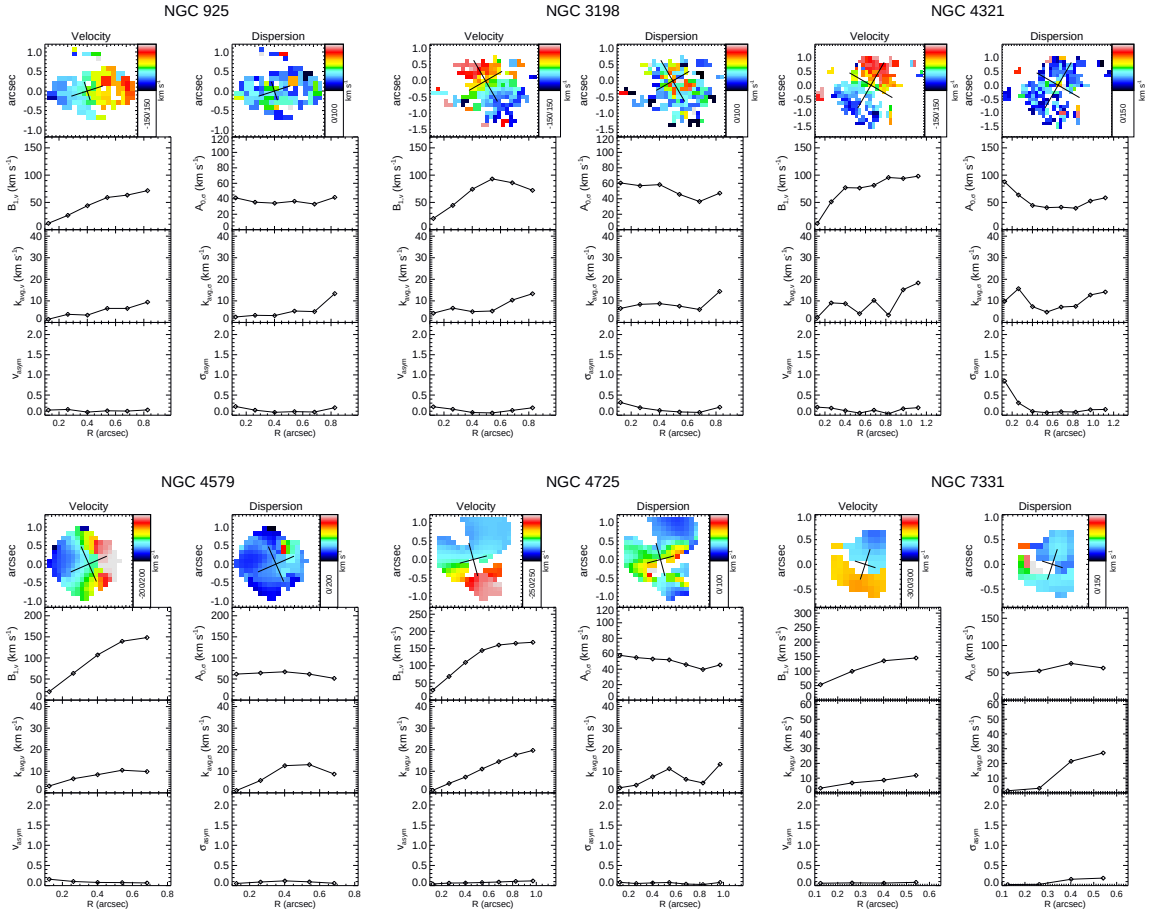

Figure 2.8: Kinemetry of "redshifted" observed template disks at $z \sim 2$. For each system, the velocity and dispersion fields are shown, followed by results from the kinemetric expansion. Overplotted on the velocity and dispersion fields are the major and minor axes of the kinemetry ellipses used in the expansion, centered on the continuum center of the system (see text for definition). Because the analysis described in §§2.2.2 and 2.2.3 does not lend itself to straightforward error propagation, we do not include error bars on these figures. The most reliable measurement of the kinemetry errors comes from the Monte Carlo realizations, whose results are summarized in Table 2.2.

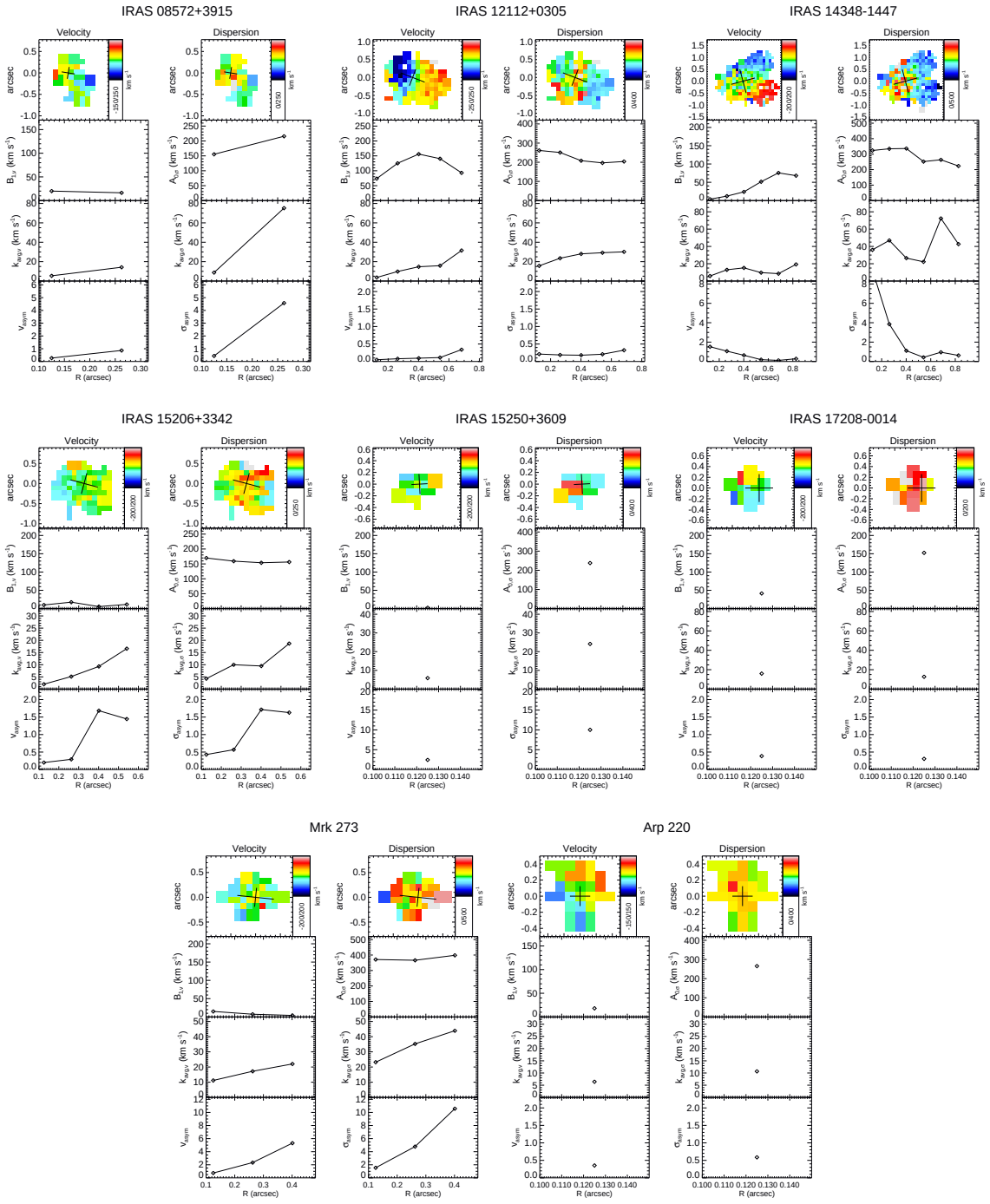

Figure 2.9: Kinemetry of "redshifted" template mergers at $z \sim 2$.

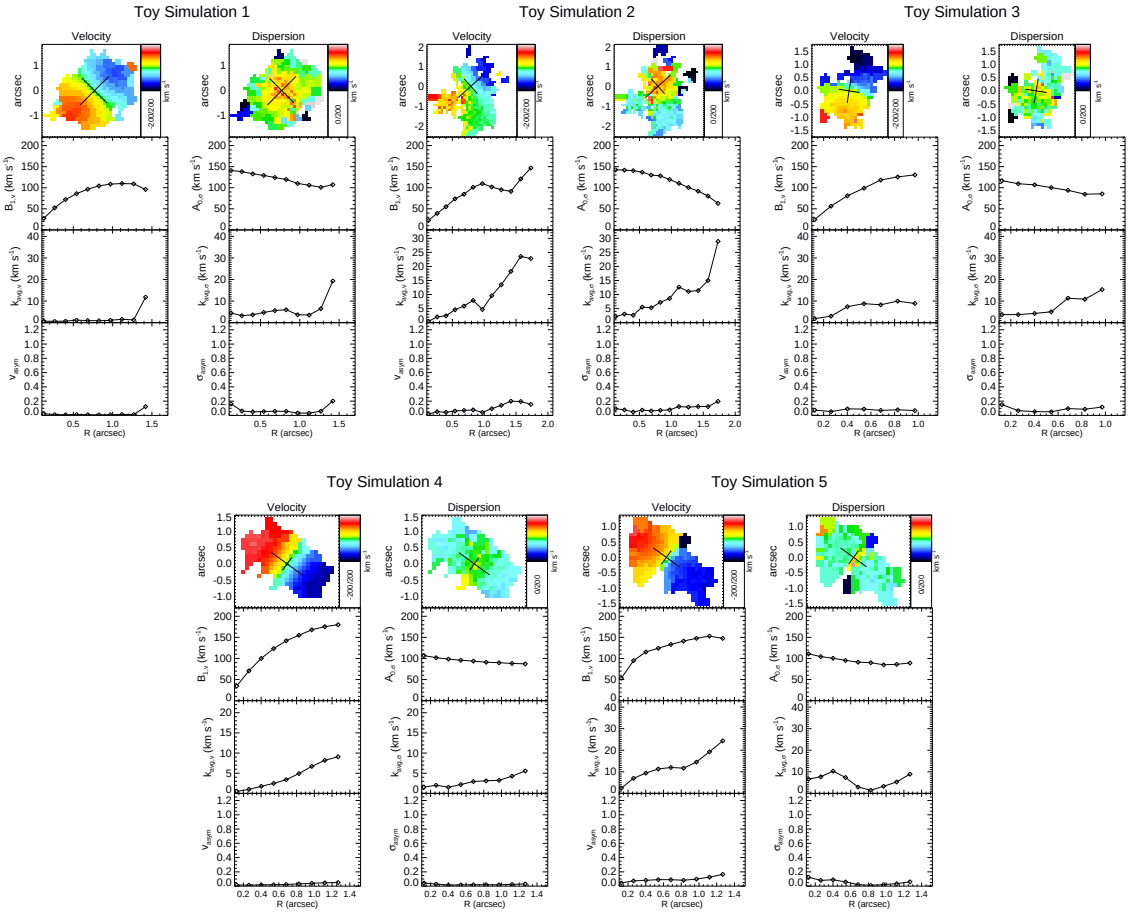

Figure 2.10: Kinemetry of template toy model disks at $z \sim 2$. Simulation 1 is of intermediate inclination with a centrally-peaked azimuthally-symmetric light distribution. Simulation 2 is of intermediate inclination and has a light distribution much more extended on one side of the galaxy. Simulation 3 is of intermediate inclination, with the light distribution illuminating only one side of the galaxy. Simulation 4 is nearly edge-on with a centrally-peaked, azimuthally-symmetric light distribution. Simulation 5 is nearly edge-on with a varying light distribution.

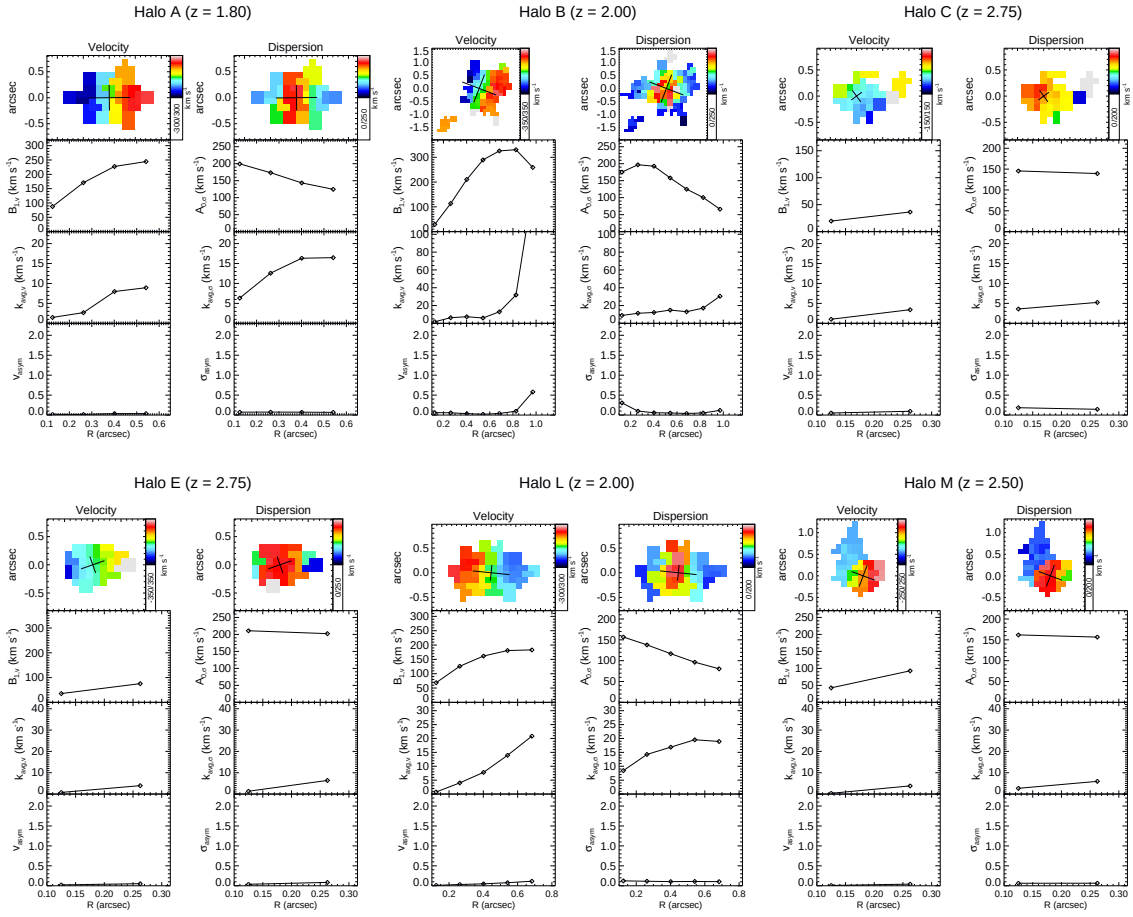

Figure 2.11: Kinemetry of cosmologically-simulated disks at $z \sim 2$. The halo lettering is taken from Naab et al. (2007), who describe the evolution of Halos A, C, and E in detail. The snapshots at specific redshifts were selected such that the halos are accreting smoothly, with no major mergers, at this point in their histories.

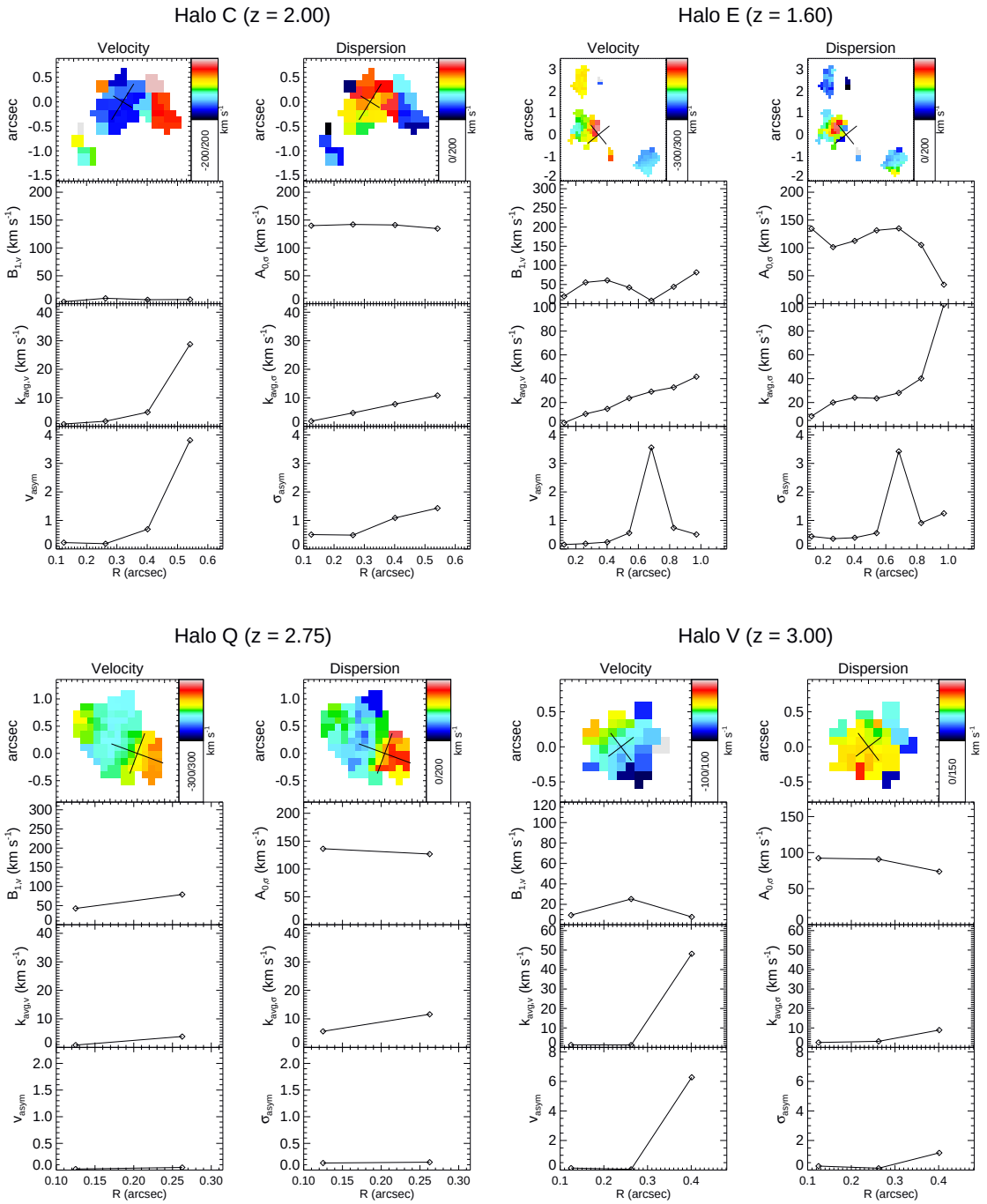

Figure 2.12: Kinemetry of cosmologically-simulated mergers at $z \sim 2$. The halo lettering is taken from Naab et al. (2007), who describe the evolution of Halos A, C, and E in detail. The snapshots at specific redshifts were selected such that the halos are undergoing major mergers at this point in their histories.

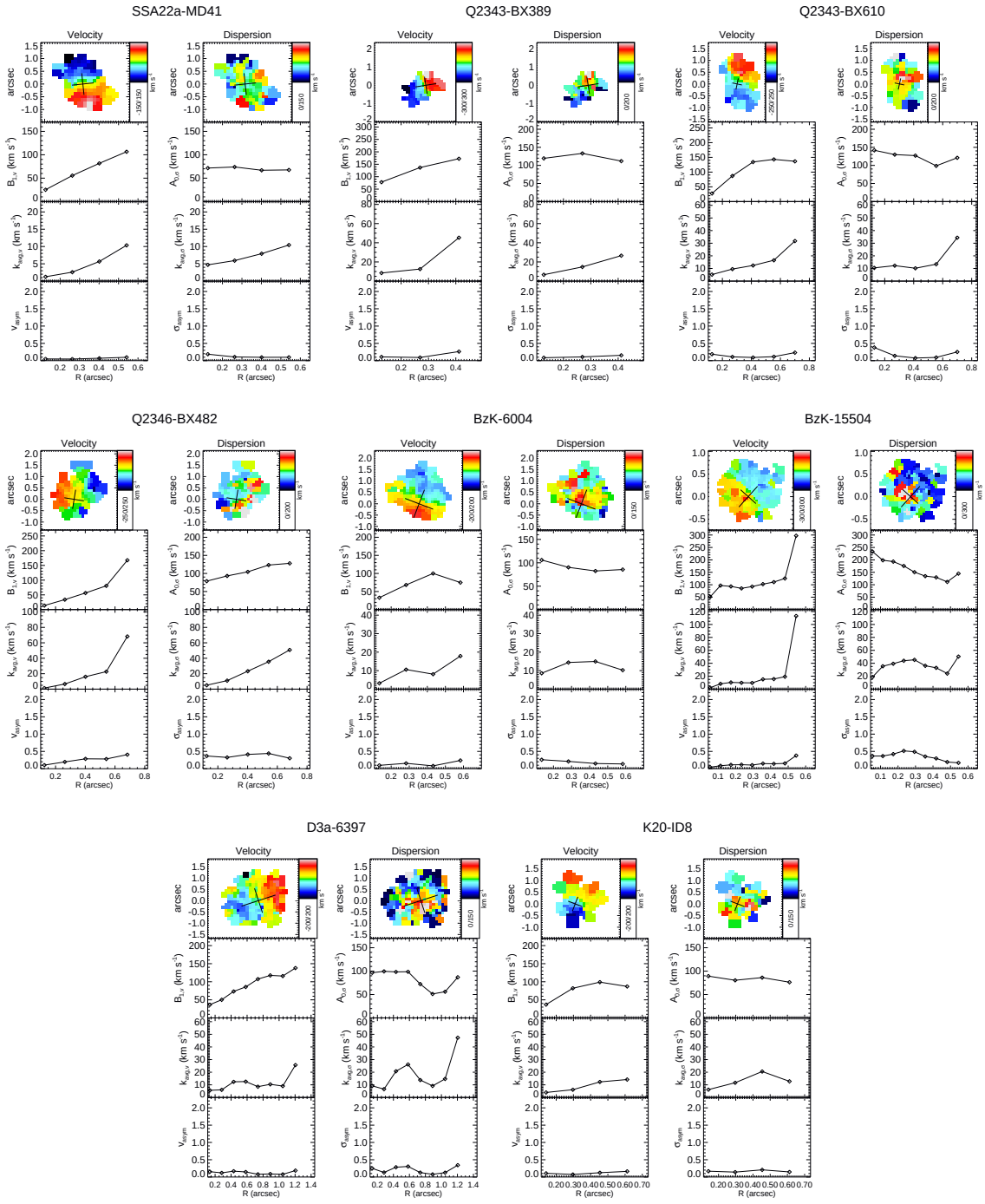

Figure 2.13: Kinemetry of SINS galaxies found to be disk-like.

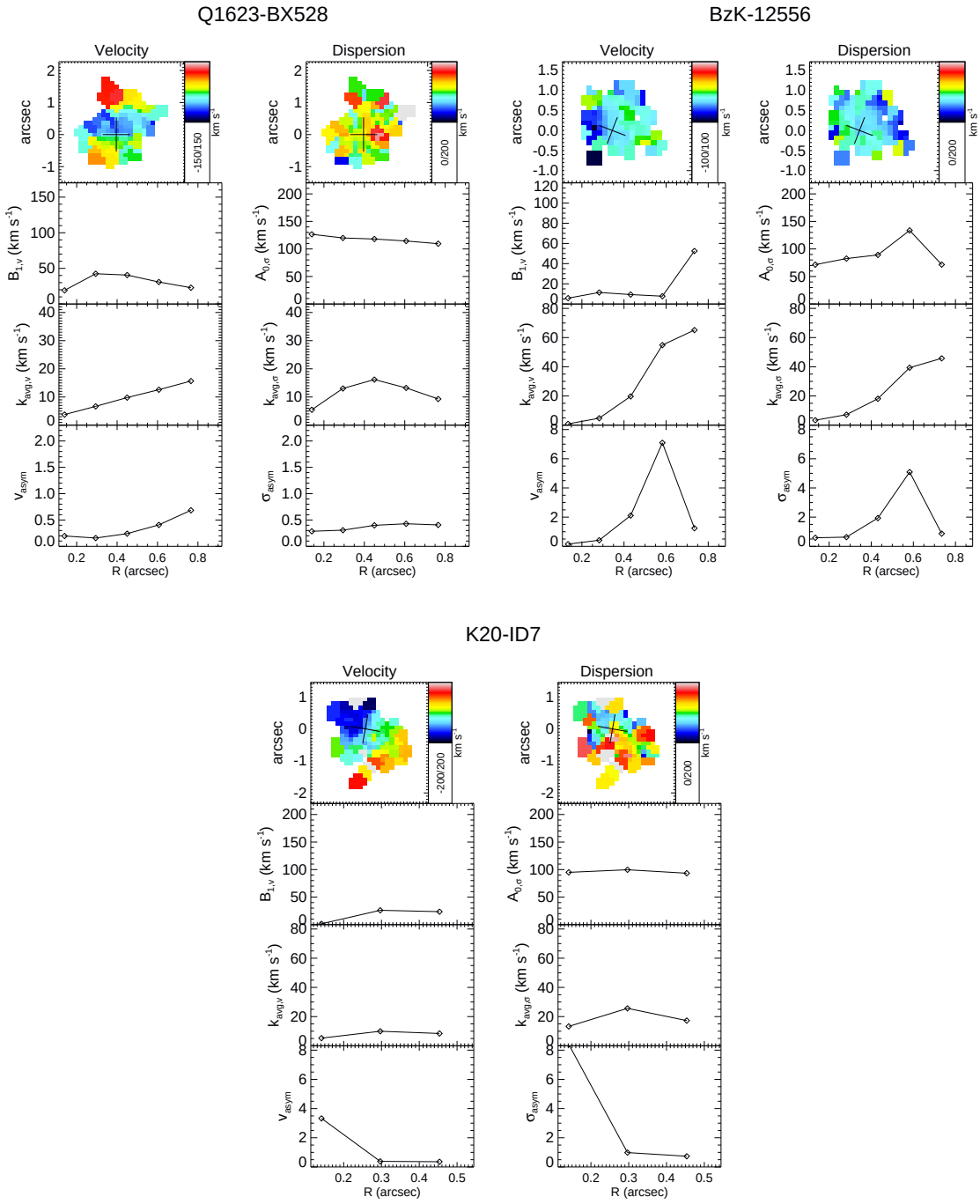

Figure 2.14: Kinemetry of SINS galaxies found to be merger-like.

Chapter 3

The SINS Survey: Broad Emission Lines in High-Redshift Star-Forming Galaxies

Abstract

High signal-to-noise, representative spectra of star-forming galaxies at $z \sim 2$, obtained via stacking, reveal a high-velocity component underneath the narrow Hα and [NII] emission lines. When modeled as a single Gaussian, this broad component has FWHM $\gtrsim 1500$ km s^{-1}; when modeled as broad wings on the Hα and [NII] features, it has FWHM $\gtrsim 500$ km s^{-1}. This feature is preferentially found in the more massive and more rapidly star-forming systems, which also tend to be older and larger galaxies. We interpret this emission as evidence of either powerful starburst-driven galactic winds or active supermassive black holes. If galactic winds are responsible for the broad emission, the observed luminosity and velocity of this gas imply mass outflow rates comparable to the star formation rate. On the other hand, if the broad line regions of active black holes account for the broad feature, the corresponding black holes masses are estimated to be an order of magnitude lower than those predicted by local scaling relations, suggesting a delayed assembly of supermassive black holes with respect to their host bulges.

3.1 Introduction

Observations of galaxies in the early Universe are a unique probe of matter assembly during its most active epoch; at $z \sim 2$, both the cosmic star formation rate and the luminous quasar space density are at their peaks (e.g. Fan et al. 2001; Chapman et al. 2005). Galaxies themselves undergo corresponding growth during this time, with the total stellar mass density in galaxies increasing from $\sim 15\%$ to $50-75\%$ its current value between $z \sim 3$ and $z \sim 1$

(e.g. Dickinson et al. 2003; Rudnick et al. 2003, 2006). Constraining the dynamical and baryonic processes driving this rapid evolution is therefore central to our understanding of galaxy formation and to informing cosmological simulations.

At the relevant epochs, key spectral diagnostic features are redshifted into the near-infrared. In recent years, a number of surveys have therefore begun to systematically probe high-redshift populations with near-infrared spectroscopy (e.g. Erb et al. 2006a,b,c; Swinbank et al. 2004; Takata et al. 2006; Kriek et al. 2008). Our recently completed SINS (Spectroscopic Imaging in the Near-infrared with SINFONI) survey has combined the resolving power of 8-10m class telescopes with high-resolution integral field spectrographs to study the detailed internal processes at work within massive, star-forming galaxies at $z \sim 2$ (Förster Schreiber et al. 2006, 2009; Genzel et al. 2006, 2008; Bouché et al. 2007; Shapiro et al. 2008; Cresci et al. 2009; see also related work by Puech et al. 2006; Swinbank et al. 2006; Wright et al. 2007; Law et al. 2007, 2009).

In this chapter, we combine the spectra of 47 galaxies detected in Hα emission to study the average spectral properties of star-forming galaxies at $z \sim 2$ (§3.2). In particular, we report the discovery of broad emission lines in these galaxies (§3.3) and interpret this high-velocity warm gas as arising either in large-scale galactic winds driven by the high star formation rates (SFR) in these galaxies or in the broad-line regions (BLR) surrounding active galactic nuclei (AGN). We explore the implications of both scenarios in §3.4 and conclude in §3.5.

Throughout this chapter, we assume a Λ-dominated cosmology with $H_0 = 70$ km s^{-1} Mpc^{-1}, $\Omega_{\rm m} = 0.3$, and $\Omega_\Lambda = 0.7$. For this cosmology, $1''$ corresponds to ≈ 8.2 kpc at $z = 2.2$.

3.2 Data and Analysis

In the context of the SINS program, 80 $z = 1-3$ systems were observed in emission lines in the infrared (rest-frame optical) with VLT/SINFONI (Eisenhauer et al. 2003; Bonnet et al. 2004) for an average of 3.5 hours per band and pixel scale on each target (Förster Schreiber et al. 2009). These galaxies were largely (62/80) taken from the (rest-frame) UV-selected samples of Erb et al. (2006b,c) and the (rest-frame) optically-selected samples of Abraham et al. (2004), Daddi et al. (2004b), Kong et al. (2006), Lilly et al. (2007), and Kurk et al. (in prep). From these magnitude- and color-defined samples, suitable SINS targets were culled, with the main selection criteria being a combination of target visibility during the observing runs, night sky line avoidance in the emission lines of interest, and an estimated integrated emission line flux $\gtrsim 5 \times 10^{-17}$ erg s^{-1} cm^{-2}, such that high quality data could be obtained in reasonable integration times. Of the 62 rest-frame UV/optically-selected galaxies chosen in this manner, 52 were well detected in Hα in our SINFONI observations.

Förster Schreiber et al. (2009) discuss the selection of this sample in detail and show that the SINS galaxies are representative of the $z \sim 2$ star-forming galaxy population, with some bias towards the more rapidly star-forming (and therefore more luminous in Hα emission) systems. They also note that the SINS sample (and some of the parent samples) selects

against known AGN and quasars, in the interest of studying the dynamic and evolutionary state of $z \sim 2$ star-forming galaxies. However, a small number of previously known AGN were in fact observed in the SINS program; in the UV/optically-selected part of the sample, there are 5 such systems, as originally identified with the UV/optical spectroscopy of the parent surveys. For further details about the SINS sample, observations, and data reduction, we refer interested readers to Förster Schreiber et al. (2009).

Here, we analyze our SINS observations of the galaxies that were UV/optically-identified and that are well-detected in Hα in individual spatial elements; this population (totalling 47 of 52 sources detected in Hα, including 4/5 of the previously known AGN) comprises the majority of the SINS sample. To study the average properties of these $z \sim 2$ star-forming galaxies, we generated stacked, high-signal-to-noise (S/N) spectra representative of the population as a whole.

From our integral field data, we first created a spatially-integrated one-dimensional spectrum for each galaxy by shifting each spectrum within the galaxy datacube by its measured (Hα) velocity and then collapsing the datacube into a single spatially-integrated spectrum. In this manner, the spatially-integrated spectrum contains no systematic velocity broadening (e.g. by large-scale rotation) on scales larger than the PSF (FWHM $\sim$ 4 kpc). Testing confirmed that this approach did not affect the properties of the broad Hα component (see below) but did improve the signal-to-noise (S/N) of the detection. This technique has the additional benefit of randomizing OH atmospheric emission lines in the Hα rest-frame and therefore effectively eliminating residuals from the OH line removal. The remaining residuals from this process were inspected and masked out by hand.

The 47 spatially-integrated spectra were then combined into a single spectrum (with equivalent integration time of 195 hours) by interpolating all spectra onto a common wavelength axis, converting their measured fluxes to luminosities using their luminosity distances, weighting each spectrum by the S/N of the Hα emission line, and averaging the resulting spectra. During this process, we do not correct for extinction (but see §3.4). Typical extinctions our sample galaxies have been measured to be $A_V \sim 1$ (Förster Schreiber et al. 2009; see also e.g. Daddi et al. 2004a; Erb et al. 2006c), which translates to an underestimation of our Hα luminosities by at most a factor of ~ 2.

The average spectrum for the SINS $z \sim 2$ star-forming galaxies is presented in the top panel of Figure 3.1. We also created average spectra of subsets of the SINS galaxy sample, in order to test the dependence of spectral properties on other known galaxy properties.

Our average spectra reveal a broad emission component underneath the bright narrow lines. We quantify this feature in each average spectrum by simultaneously fitting a combination of a constant continuum offset, narrow lines (Hα, [NII], [SII]) of identical kinematics (velocity and velocity dispersion), and a single broad component, whose kinematics are allowed to vary. All lines are assumed to be well-described by a single Gaussian; the validity of this assumption is confirmed by a reduced χ^2 of close to unity ($\chi^2_{dof} \sim 0.9-1.9$) for all fits (see Table 3.1). Our data can also be well fit with a combination of a constant continuum offset, narrow lines with shared kinematics, and broad forbidden and permitted lines with shared kinematics, with the [NII]/Hα ratio identical in the narrow and broad component.

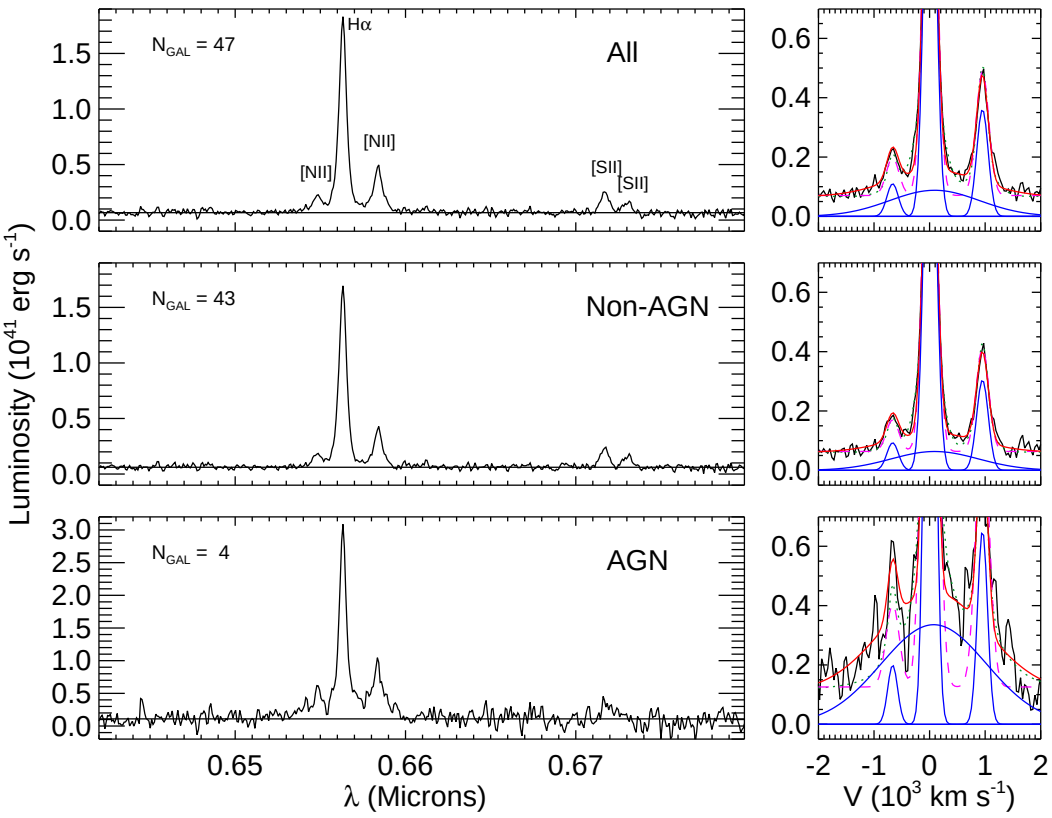

Figure 3.1: *Left*: Average spectrum of the 47 SINS galaxies (*top panel*), followed by the average spectrum of all non-active systems and that of all systems previously known to host AGN (*lower two panels*). *Right*: Zoomed view of the Hα and [NII] region, on a velocity scale, with the best-fitting combination of a constant continuum, narrow lines, and a broad component overplotted (*red*). The individual line components are also plotted (*blue*). For reference, also overplotted are the best fits derived by fitting both Hα and [NII] with only narrow lines (*dashed magenta*) and with a narrow and a broad component (*dotted green*).

Table 3.1: Results from Line Fitting

Subsample	Figure Reference	$L_{H\alpha,broad}$ (10^{41} erg s^{-1})	f_{broad} [a]	v_{off} [b] (km s^{-1})	FWHM$_{H\alpha,broad}$ (km s^{-1})	P_{false}	χ^2_{dof}	$\chi^2_{dof,n}$ [c]
All	1, top	$4.0^{+1.1}_{-1.0}$	$0.28^{+0.04}_{-0.08}$	18^{+79}_{-73}	1632^{+445}_{-301}	0.02	1.8	4.9
All, broad Hα and [N II] [d]	1, top	$5.9^{+1.0}_{-1.4}$	$0.42^{+0.08}_{-0.08}$	8^{+14}_{-3}	556^{+228}_{-87}	0.01	1.4	4.9
Non-AGN	1, center	$3.0^{+0.6}_{-0.4}$	$0.22^{+0.03}_{-0.02}$	19^{+82}_{-42}	1329^{+346}_{-139}	0.03	1.9	3.7
AGN	1, bottom	$8.2^{+0.7}_{-2.8}$	$0.36^{+0.03}_{-0.09}$	42^{+94}_{-29}	2863^{+669}_{-728}	0.007	0.9	3.0
$M_* < 2 \times 10^{10}\ M_\odot$	2, top	$2.2^{+0.4}_{-0.6}$	$0.21^{+0.03}_{-0.02}$	26^{+86}_{-30}	1051^{+149}_{-169}	0.11	0.9	1.3
$M_* = 2 - 7 \times 10^{10}\ M_\odot$	2, center	$2.9^{+0.6}_{-0.7}$	$0.22^{+0.06}_{-0.02}$	11^{+71}_{-70}	1425^{+443}_{-238}	0.05	1.4	2.0
$M_* > 7 \times 10^{10}\ M_\odot$	2, bottom	$6.7^{+2.9}_{-2.3}$	$0.31^{+0.04}_{-0.11}$	20^{+82}_{-42}	2183^{+392}_{-758}	0.03	1.3	3.6
Center	3, top	$5.1^{+2.8}_{-1.7}$ [e]	$0.24^{+0.13}_{-0.04}$	9^{+80}_{-27}	1564^{+601}_{-544}	0.08	1.3	1.9
Extended	3, bottom	$1.9^{+0.6}_{-0.5}$ [e]	$0.22^{+0.06}_{-0.02}$	10^{+69}_{-39}	1508^{+725}_{-244}	0.14	0.9	1.2

[a] Ratio of Hα luminosity in broad component to total Hα (narrow+broad) luminosity.
[b] Velocity offset of broad Hα feature from narrow Hα.
[c] Reduced χ^2 for a fit assuming only narrow emission lines.
[d] Most components of the fit (v_{off}, FWHM$_{H\alpha,broad}$), and f_{broad}) are constrained in the fit to be identical for the permitted and forbidden lines. The luminosity ($L_{H\alpha,broad}$) is quoted only for the broad component of the Hα line.
[e] Units are 10^{39} erg s^{-1} kpc^{-2}.

All lines are assumed to be well-described by this combination of two Gaussians (dotted green line in Figure 3.1; $\chi^2_{dof} = 1.4$), which has the same number of free parameters as the previous fit. In the limit of the S/N of our data, we cannot add additional free parameters to the fits, nor can we identify a preferred model. For clarity, we refer throughout to the former (single broad Gaussian under the Hα+[NII] complex) as "broad lines" and the latter (double Gaussians for both Hα and [NII]) as "broad wings." For simplicity and for comparison with the literature, we primarily quantify the observed high-velocity feature with a single broad Hα line in §3.3. However, we also discuss the implications of the broad wings scenario on the derived properties of the broad emission (§3.3) and on the interpretation of this emission (§3.4).

From these fits to the average spectra, we measure the fractional contribution of broad emission to the overall emission line flux, the kinematics of the broad component, and the line ratios of the narrow line components. The significance of these measurements are quantified in two ways. First, for each average spectrum, we re-created 100 spectra by randomly sampling (with replacement) and combining the individual contributing galaxy spectra. The properties of the broad component were measured in each of the resulting 100 average spectra, yielding confidence intervals for all derived quantities. Second, the probability of false positive detections P_{false} was tested by creating 1000 simulated spectra with the narrow line and observational properties (noise, spectral resolution) characteristic of each average spectrum. Comparing the derived broad components in these spectra to those in the real SINS spectra, we estimate the rate of spurious detections of broad components equal to or more prominent (in luminosity and FWHM) than those in the actual data. The results of this analysis for the different average spectra are presented in the following section.

3.3 Results

We find that the average SINS galaxy spectrum includes a significant amount of broad emission (top panel of Figure 3.1), with $\chi^2_{dof} = 4.9$ for a fit with only narrow lines (dashed magenta line in top right panel of Figure 3.1) and $\chi^2_{dof} = 1.8$ and 1.4 for fits including a broad Hα line and broad Hα and [NII] wings, respectively (red and dotted green lines in same panel; $P_{false} = 2\%$ and 1%). To ensure that this signature is not the result of the 4 known AGN included in this sample, we also create stacked spectra of the AGN and the rest of the sample. While the broad emission from the AGN host systems alone is quite substantial, a comparison of the average SINS spectrum and the average non-AGN spectrum illustrates that the broad emission in the average SINS spectrum is not dominated by that coming from the 4 AGN. These results are summarized in Table 3.1.

We test the dependence of the presence of broad emission on galaxy properties by dividing the sample into three stellar mass bins, using the results from the spectral energy distribution (SED) fitting of Förster Schreiber et al. (2009) for the 45 of our 47 targets for which sufficient broadband data exist. The average spectra for these three bins show an increasing presence of a broad component with stellar mass (Figure 3.2; $P_{false} = 11\%$, 5%, 3%

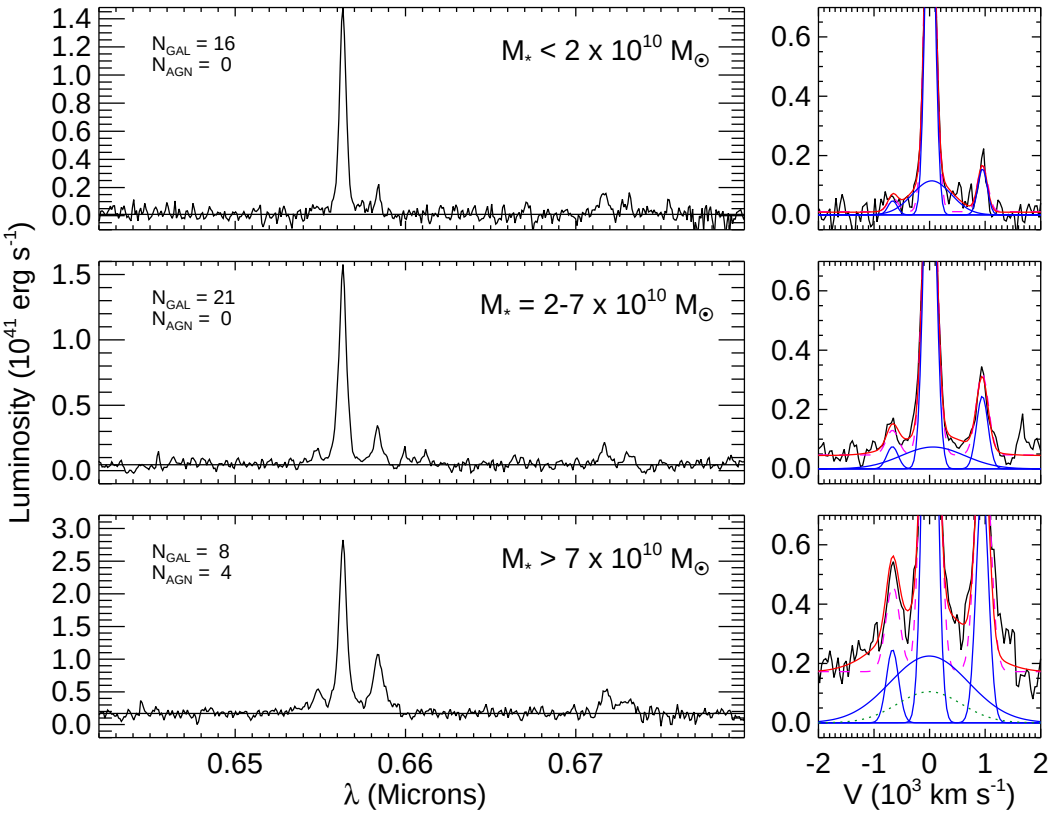

Figure 3.2: *Left*: Average spectrum of each mass bin. *Right:* Zoomed view of the Hα and [NII] region, on a velocity scale, with the best-fitting combination of a constant continuum, narrow lines, and a broad component overplotted (*red*). The individual line components are also plotted (*blue*). The best fit obtained with only narrow emission lines is plotted for comparison (*dashed magenta*). In the high mass bin, the best-fit broad line component to the average spectrum of the 3 non-active high mass galaxies is also overplotted (*dotted green*).

respectively). However, the spectrum of the highest mass bin is significantly affected by the contribution of the 4 previously known AGN in our sample, which all fall into this bin. The nuclear emission in these systems can bias the results of SED fitting towards larger masses, so we confirm their high masses with the dynamical mass measurements made by Cresci et al. (2009); in all cases, the dynamical masses of these galaxies are consistent with the stellar masses used here and remain among the highest in the SINS sample. Nevertheless, we confirm that a (weaker) broad component is also present in the non-active galaxies in this bin (green line in Figure 3.2), with $P_{false} = 9\%$.

Several other key properties of galaxies, including SFR, size, stellar age, and metallicity, have well established correlations with stellar mass in high-z galaxies (e.g. Noeske et al. 2007; Trujillo et al. 2006b; Erb et al. 2006b). Both the SFR-M_* relation and the mass-metallicity relation are apparent in Figure 3.2, via the increasing narrow Hα luminosity and increasing [NII]/Hα ratio with stellar mass, respectively. Since the [NII]/Hα ratio remains well below levels expected of shock heating or AGN activity, it is most likely tracing variations in metallicity (see below, as well as Buschkamp et al. in prep). To these established mass-dependent properties in high-z galaxies, we now add the presence and strength of a broad component.

With the spatially resolved data, we can also compare the integrated spectra from the central ($R < 3$ kpc) regions of high-z galaxies to those from extended ($R = 3 - 15$ kpc) regions, in order to determine what regions in these systems are generating broad emission. For this analysis, we use galaxies from the intermediate and high mass bins of Figure 3.2 in which the intensity distribution of the stellar continuum defines a clear center of the system (totalling 6 systems). The average spectra of the central and extended regions of these systems are shown in Figure 3.3, normalized to the spatial area over which the spectra were extracted.

In these spectra, a broad component is preferred by the best-fitting models; however, the significance of this result is low. The detection of broad emission in galaxy centers at $z \sim 2$ (with $P_{false} = 8\%$) is somewhat more robust than that in the extended regions ($P_{false} = 14\%$), in which the best fit broad component is very shallow. If real, the broad feature in the extended regions accounts for a comparable fraction of the total Hα luminosity to that in the central regions (Table 3.1). Tests of simulated galaxies indicate that such a broad line in the extended regions cannot be reproduced by a nuclear point-source of broad emission (i.e. AGN) broadened by the PSF.

In the spectra shown in Figure 3.3, we note that the average [NII]/Hα ratio is comparable in the central and extended regions, despite the difference in broad emission component, in support of the above interpretation of the [NII]/Hα feature as primarily reflecting the metallicity of these systems. However, this should not be interpreted as a lack of metallicity gradient in these galaxies, since the spectra shown here are averaged over a number of galaxies, in each of which the extended region is spatially integrated over a large range in radii. Detailed studies of metallicity gradients within and between individual SINS systems will be presented in Buschkamp et al. (in prep).

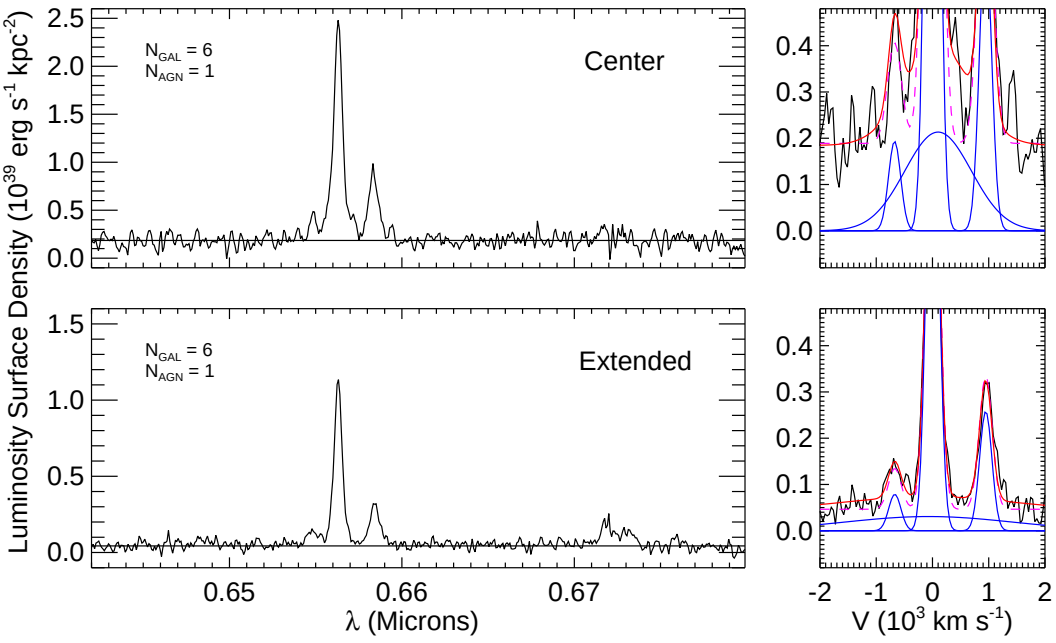

Figure 3.3: Average spectra, in luminosity surface density, of the central (*top panel*) and extended (*bottom panel*) regions of well-resolved SINS galaxies. Panels and colors are as in Figures 3.1 and 3.2.

3.4 Discussion

The low luminosity broad emission seen in our SINS galaxies can be interpreted in one of two ways: either as evidence of large-scale galactic outflows, presumably driven by the galaxies' very high star formation rates, or as a tracer of the broad-line regions surrounding AGN in these early galaxies. The current data do not allow us to robustly distinguish between these two scenarios empirically; in the following, we therefore examine both in detail.

3.4.1 Broad Emission from Starburst-Driven Winds

One possible explanation of the broad emission is a starburst-driven wind. This scenario is in keeping with the positive correlation between broad emission and stellar mass (and therefore star formation rate) seen in Figure 3.2 and with the possible broad emission from non-nuclear regions seen in Figure 3.3. Moreover, starburst-driven winds are expected to be ubiquitous in the rapidly star-forming populations common at high-redshift (e.g. Pettini et al. 2001; Shapley et al. 2003; Smail et al. 2003; Weiner et al. 2009) and are probably expelling mass from their host galaxies at rates comparable to the star formation rate (below; see also Martin 1999; Pettini et al. 2000; Martin 2003; Erb 2008; Weiner et al. 2009).

At low redshift, star-forming systems are known to drive galactic winds with observable signatures in the wings of the permitted and forbidden emission lines. In dwarf starburst galaxies, Westmoquette et al. (2007a) find that the broad wings of the emission lines can be modeled as a second Gaussian component with FWHM $\leq$ 300 km s^{-1}. In contrast, observations of the more massive and more rapidly star-forming IR-luminous galaxy population reveal higher FWHM in the broad wings (300$-$800 km s^{-1}; Arribas et al. 2001), whose line widths and f_{broad} are comparable to those observed in the SINS galaxies (550 km s^{-1}; see Table 3.1; Armus et al. 1989, 1990; Lehnert & Heckman 1996a).

Indeed, the relationship between wind speed and SFR (and the equivalent properties, galaxy mass and B-band magnitude) has been demonstrated by Rupke et al. (2005), Martin (2005), and Tremonti et al. (2007), respectively. In particular, Lehnert & Heckman (1996a) and Rupke et al. (2005) showed that systems with higher SFR have faster winds, whose velocities exceed $\sim$ 1000 km s^{-1} in ionized gas tracers. We recover similar trends and velocities with the three mass bins of the SINS data, as shown in Figure 3.4. Note, however, that this figure should not be directly compared with those in the works listed above, in which the wind speeds are probed with interstellar absorption features, whose velocities are typically lower than those of ionized emission line gas (e.g. Veilleux et al. 2005; Rupke et al. 2005). Nevertheless, the similarity between the properties of local winds and those of the broad wings seen in the SINS galaxies makes it plausible that this emission is due to the galactic winds that certainly exist in these systems.

These broad wings can be produced via several mechanisms, including turbulent mixing of the hot wind fluid and cool gas clumps at the base of the wind (Westmoquette et al. 2007a,b) or within a large-scale bubble along the galaxy minor axis (e.g. Armus et al. 1990; Arribas et al. 2001). In the idealized model of a wind plowing into a spherically symmetric

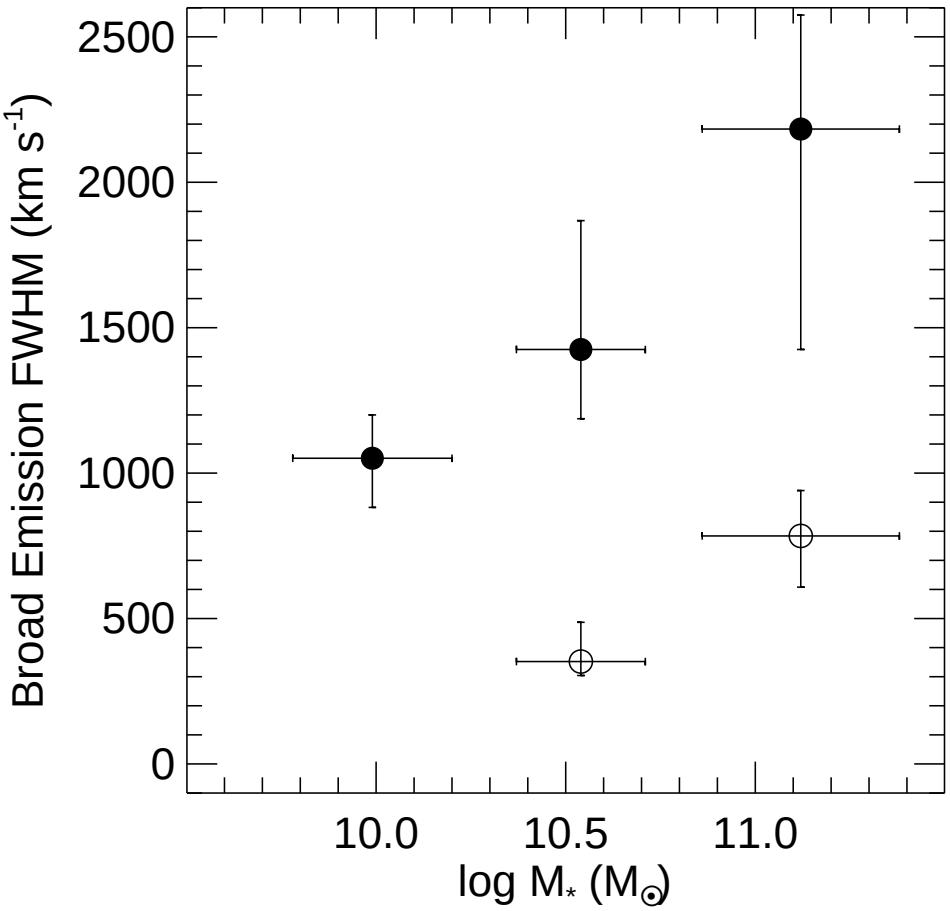

Figure 3.4: FWHM of the broad component in the SINS galaxies in the three stellar mass bins defined in Figure 3.2, as modeled by a single broad Hα line (*filled circles*) and by broad wings on both the Hα and [NII] lines (*open circles*). In the latter model, the low mass bin is not well constrained due to the low S/N of the [NII] feature (see Figure 3.2), resulting in a fit that strongly prefers a broad line for only the high S/N (Hα) line; we therefore omit this bin from the plot.

ambient medium, Heckman et al. (1993) provide analytic expressions for the velocity and Hα luminosity of the shocked gas as functions of the bolometric luminosity of the star-formation event, the duration of the event, and the ISM density. Converting the SFR (~ 100 M$_\odot$ yr^{-1}) of the SINS galaxies to a bolometric luminosity and accounting for the correspondingly denser ISM than in local spiral galaxies (by a factor of 10−30; Bouché et al. 2007), these relations predict a Hα luminosity of $0.7-10 \times 10^{42}$ erg s^{-1} generated from gas moving at $\sim 70-300$ km s^{-1}. These properties are broadly consistent with the high-velocity wings observed in the SINS galaxies.

However, our spectra can also be fit by a broad Hα line, and we therefore explore whether such a feature could likewise be generated in galactic winds. For simplicity, we assume that these winds are powered by supernova remnants (SNR), in local examples of which broad Hα (FWHM = 500−8000 km s^{-1}) is observed throughout the Sedov-Taylor expansion phase, the result of charge exchange of the electrons from slow neutral atoms to the fast post-shock protons (e.g. Chevalier & Raymond 1978; Smith et al. 1991; Heng & Sunyaev 2008). Although such broad Hα emission is not observed on galactic scales in local starbursting systems, we note that none of these systems are appropriate analogs to the star formation mode that dominates at $z \sim 2$. Only local ULIRGs have SFR comparable to that in the SINS galaxies, and the ionized gas emission in ULIRGs suffers significantly more extinction ($A_V = 5-1000$; Genzel et al. 1998) than in SINS galaxies ($A_V \sim 1$). We therefore briefly examine the possibility that galactic winds at $z \sim 2$ emit broad Hα lines via a superposition of SNR.

A simple test of this scenario is whether there are a sufficient number of SNR in the SINS galaxies to drive the observed broad Hα luminosity. Locally, SNR are observed to have broad Hα luminosities of $10^{30}-10^{34}$ erg s^{-1}, generated by change exchange as the shock encounters the ISM and therefore proportional to the square of the gas density. In the SINS galaxies, the high SFR (~ 100 M$_\odot$ yr^{-1}) and dense ISM (10−30 times denser than in local spiral galaxies) imply an increase in broad Hα luminosity per SNR by a factor of 100−1000, to $10^{32}-10^{37}$ erg s^{-1}. The SFR in the SINS galaxies yields ~ 1 supernova explosion per year, each of which will have an expected Sedov-Taylor lifetime of $\sim 10^4$ yr in the dense ISM, resulting in roughly 10^4 SNR radiating broad Hα at any given time in an average SINS galaxy, for a total broad Hα luminosity of $10^{36}-10^{41}$ erg s^{-1}. This number is lower than the observed broad Hα luminosity in the SINS galaxies by a factor of a few (see Table 3.1); however, real galactic winds penetrate much further through their host galaxies' ISM than do the sum of individual SNR, implying that additional broad Hα emission is expected from the interaction of the large-scale winds with the ambient medium. This effect brings the predictions into even closer agreement with the observations and thus makes this mechanism an energetically feasible explanation for the luminosity and FWHM of the broad emission in the SINS galaxies.

Regardless of whether the broad emission is a broad Hα line or broad wings on all emission lines, if the emission is in fact due to starburst-driven winds, it is worth examining what the fate of this high-velocity gas may be. The average SINS galaxy (top panel of Figure 3.1) has either broad wings in Hα and [NII] with velocity dispersions of ~ 250 km s^{-1}

or a broad Hα line with velocity dispersion $\sim$ 700 km s^{-1}. We can compare these values directly with the escape velocity $v_{esc} \approx 450$ km s^{-1} for a typical SINS galaxy ($\langle M_{dyn} \rangle = 8 \times 10^{10}$ M$_\odot$, $\langle R_{1/2} \rangle = 3.4$ kpc; Förster Schreiber et al. 2009). A significant fraction (7% or 55%, respectively) of the high-velocity gas has velocity exceeding the host galaxy's escape velocity; assuming that this gas is distributed throughout the star-forming disk, a non-negligible amount of it should be expected to escape the galaxy. Furthermore, if the surrounding dark matter halo has a flat rotation curve, this gas would also be expected to escape the halo into the intergalactic medium.

We can then estimate the mass outflow rate that would correspond to such superwinds. The escaping Hα-emitting gas is $\sim 3-17\%$ of the total Hα-emitting gas in the SINS galaxies (i.e. 30% of the emission is broad and 55% of the broad emission escapes). Assuming that the fraction of gas in the ionized phase is roughly the same in the galaxies' star-forming disks and in the outflows (compare $\sim 1\%$ in the Milky Way to $\sim 0.1-1\%$ in winds; Veilleux et al. 2005), this implies that $\sim 3-17\%$ of the galaxies' gas reservoirs are being expelled by the observed star-forming event. The dynamical times associated with these outflows can be approximated as the radius of the star formation event divided by the velocity of the flow; for the SINS galaxies, this yields dynamical times of ~ 10 Myr. The average SINS galaxy has a dynamical mass of 8×10^{10} M$_\odot$ and a gas fraction of 0.2–0.4 (e.g. Erb et al. 2006c; Bouché et al. 2007), yielding an expected outflow rate of 50–500 M$_\odot$ yr^{-1}. This is consistent with the results of Erb (2008), who argue that the observed $z \sim 2$ mass-metallicity relationship requires outflow rates slightly larger than the SFR (SFR = 1–800 M$_\odot$ yr^{-1} with median 72 M$_\odot$ yr^{-1} in the SINS sample; Förster Schreiber et al. 2009). If the broad emission we observe is due to galactic winds at $z \sim 2$, we thus find mass outflow rates consistent with the observed metallicity evolution of these galaxies.

3.4.2 Broad Emission from Active SMBHs

Another possible, and common, interpretation of broad emission lines are as signatures of nuclear activity. For our galaxies, this interpretation is supported by the strength of the broad Hα emission increasing with stellar mass (and therefore bulge mass and possibly black hole mass) seen in Figure 3.2, by the less luminous broad emission in the non-active systems (the driving mechanism being "turned off" or obscured; Figures 3.1 and 3.2), and by the more significant detection of broad emission in the centers of galaxies than in their non-nuclear regions. Moreover, studies of $z \sim 2$ star-forming galaxies in infrared and X-ray emission suggest that active nuclei may be a common feature of this population (Daddi et al. 2007b).

Early work in the local Universe has shown that broad Hα is by definition omnipresent in Type 1 AGN, in which the broad-line regions around the nuclei are unobscured. Moreover, the kinematics and sizes of these regions can be used to infer "virial" supermassive black hole (SMBH) masses, via calibrated relations between the observed AGN continuum luminosities at 5100 Å (L_{5100}) and the sizes of the BLR (Kaspi et al. 2000), which can then be used in combination with the width of the broad emission lines to estimate SMBH masses

(Vestergaard 2002). Greene & Ho (2005) have additionally related L_{5100} to the luminosity of the broad emission lines, making it possible to measure virial black hole masses using only a single broad line,

$$\mathrm{M_{BH}} = (2.0^{+0.4}_{-0.3}) \times 10^6 \left(\frac{L_{\mathrm{H}\alpha}}{10^{42}\ \mathrm{erg\ s^{-1}}}\right)^{0.55\pm0.02} \left(\frac{\mathrm{FWHM_{H}\alpha}}{10^3\ \mathrm{km\ s^{-1}}}\right)^{2.06\pm0.06} \mathrm{M_\odot}\ . \qquad (3.1)$$

Such virial black hole mass estimates have been verified against stellar and gas kinematic determinations of $\mathrm{M_{BH}}$ and found to be accurate to within a factor of ~ 3 (Onken et al. 2007; Hicks & Malkan 2008; Netzer 2009, but see also Marconi et al. 2008). As a result, they have been utilized in the high-z Universe to probe the masses of SMBHs in quasars (e.g. Willott et al. 2003; McLure & Dunlop 2004; Vestergaard 2004) and in the sub-mm-bright galaxy population (Alexander et al. 2008).

Additionally, the broad-line Hα luminosity can also be used to probe the accretion rate of SMBHs. Assuming the AGN continuum luminosity L_{5100} is roughly 1/10 the AGN bolometric luminosity L_{bol}, the accretion rate can be estimated by $\dot{\mathrm{M}}_{\mathrm{BH}} = L_{\mathrm{bol}}/(\eta c^2)$ (La Mura et al. 2007). Using a typical value of $\eta \sim 0.1$ and the calibrated relationship between $L_{\mathrm{H}\alpha}$ and L_{5100} (Greene & Ho 2005), we can then estimate $\dot{\mathrm{M}}_{\mathrm{BH}}$. Although approximate, this estimate of $\dot{\mathrm{M}}_{\mathrm{BH}}$ and the estimate of $\mathrm{M_{BH}}$ derived using equation 3.1 nevertheless allow us to study both the putative black hole masses in our SINS galaxies and their accretion rates using our measurements of the broad Hα features.

With this procedure, we derive for the average SINS spectrum (top row in Figure 3.1) a black hole mass of $\mathrm{M_{BH}} = 4^{+3}_{-2} \times 10^6\ \mathrm{M_\odot}$ with an Eddington ratio of ~ 0.2. Furthermore, we infer black hole masses of $\mathrm{M_{BH}} < 9 \times 10^5\ \mathrm{M_\odot}$, $\mathrm{M_{BH}} = 2^{+2}_{-1} \times 10^6\ \mathrm{M_\odot}$, and $\mathrm{M_{BH}} = 1^{+1}_{-0.5} \times 10^7\ \mathrm{M_\odot}$ in each of the three stellar mass bins, respectively. In the latter two bins, the Eddington ratios are estimated to be 0.3 and 0.4, respectively.

We note that the Hα luminosities used in these black hole mass estimates have not been corrected for extinction, and any such correction would increase the derived masses. However, broad emission lines associated with Type 1-1.5 AGN in local galaxies are consistent with no additional extinction along the line-of-sight to the BLRs (e.g. Rhee & Larkin 2000; Alonso-Herrero et al. 2003; Greene & Ho 2005). Likewise, at $z \sim 2$, Alexander et al. (2008) have used the Hα/Hβ broad-line Balmer decrement to measure only small amounts of nuclear extinction ($A_V \approx 1.2$) in their dust-rich sub-mm population. These authors postulate that the plentiful dust in the sub-mm galaxies obscures regions of star-formation and not the BLRs. In the SINS galaxies, the average extinction in the star-forming regions is $A_{\mathrm{H}\alpha} \sim 0.8$; if the BLR is similarly obscured, correcting for this effect would yield an increase of at most a factor of 2 in broad Hα luminosity and, from equation 3.1, a factor ~ 1.5 in derived black hole mass. This suggests that it is unlikely that the black hole masses measured here suffer significantly from extinction.

It is then naturally interesting to compare the estimated black hole masses with large-scale galaxy properties. In the left panel of Figure 3.5, we find the expected trend that

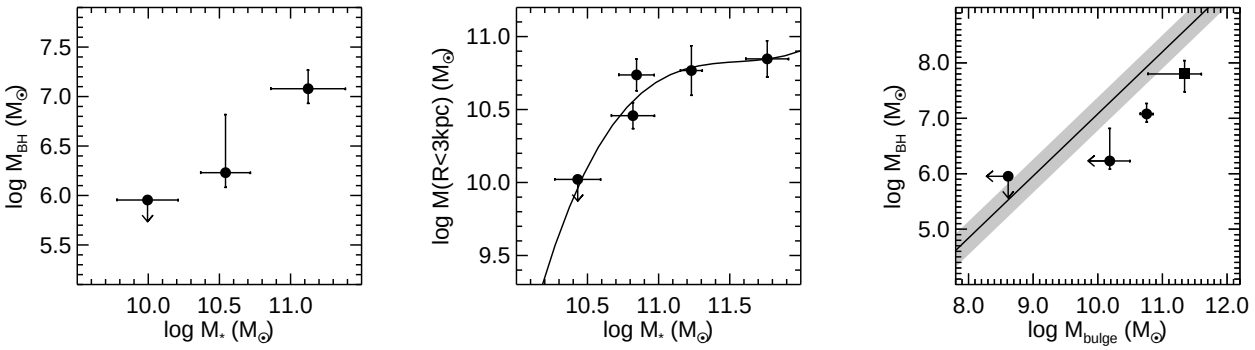

Figure 3.5: *Left*: Estimated black hole masses (derived with virial estimates from the broad Hα emission line) against average stellar mass (derived with SED modeling; Förster Schreiber et al. 2009) in each mass bin. *Center*: Relation between central mass concentration (dynamical mass within 3 kpc) and stellar mass for the five galaxies modeled in detail by Genzel et al. (2008), along with the best-fitting third-order polynomial. *Right*: Estimated black hole masses against estimated bulge masses (*circles;* M_{bulge} estimated from stellar masses shown in left panel and polynomial shown in center panel) for the three mass bins shown in Figure 3.2. Overplotted (*square*) is the average BH mass measured in $z \sim 2$ sub-mm galaxies by Alexander et al. (2008); for comparison with our central mass concentration (dynamical mass within 3 kpc), we adopt the stellar mass within ~ 4 kpc measured by Alexander et al. (2008) as the "bulge" mass, with the error bar extending to include all "bulge" masses estimated by those authors. The M_{BH}-M_{bulge} relation for the local Universe and its scatter are indicated with the solid line and shading (Häring & Rix 2004).

black holes of increasing mass are found in galaxies of increasing stellar mass, with black-hole-to-stellar mass ratios of $\sim 7 \times 10^{-5}$. For such black holes to be consistent with local scaling relations between black holes and bulges ($M_{BH}/M_{bulge} \sim 10^{-3}$), the bulge-to-total ratio B/T of these systems would need to be quite small ($\lesssim 0.07$). This is in marked contrast to results from detailed dynamical modeling of the five SINS galaxies with the highest-resolution observations (Genzel et al. 2008), which yield $B/T = 0.15-0.4$ (center panel of Figure 3.5). Parameterizing these results with a simple polynomial, we estimate "bulge" masses ($\sim$ dynamical mass within 3 kpc) for the three mass bins, albeit with large uncertainty. The resulting B/T for these mass bins are < 0.1, < 0.4, and 0.4, respectively. These bulge masses are then plotted against our measured black hole masses in the right panel of Figure 3.5.

Comparing to the local M_{BH}-M_{bulge} relation measured by Häring & Rix (2004), we find that our $z \sim 2$ galaxies lie significantly below the local relation, implying that black holes in the star-forming galaxies in the early Universe may have lagged significantly behind their host bulges in assembly. Genzel et al. (2008) have shown that $z \sim 2$ is, for many of these systems, an era of bulge formation via smooth but rapid secular processes, during which massive bulges are assembled from large star-forming clumps ($M \sim 10^8 - 10^9$ $M_\odot$) on timescales of $\lesssim 1$ Gyr. Elmegreen et al. (2008b) have demonstrated in simulations that, assuming each such clump contains a black hole of 10^{-3} of its total mass, these black holes would migrate to the galaxy center with their host clumps and form central SMBHs that are somewhat under-massive for the resulting bulges. The location of our $z \sim 2$ systems significantly below the local relation likewise suggests that the bulges in these galaxies form first, through rapid secular processes, with the assembly of the central SMBHs following later.

The timescale for this final SMBH growth can be estimated for the high mass bin, in which the galaxy bulges are probably largely in place at $z \sim 2$ (Genzel et al. 2008). Accretion onto the black hole at the current rate ($0.4\,\dot{M}_{Edd} \sim 5\times10^{-2}$ $M_\odot$ yr^{-1}) will bring these galaxies onto the local M_{BH}-M_{bulge} relation ($M_{BH} \sim 10^8$ $M_\odot$) in ~ 2 Gyr. Similarly, galaxies in the intermediate mass bin will acquire SMBHs with final masses $\sim 2 \times 10^7$ $M_\odot$ in $\lesssim 1$ Gyr. The evolutionary link between these final SMBHs at $z = 0$ ($M_{BH} \gtrsim 2 \times 10^7$ $M_\odot$) and their putative $z \sim 2$ host galaxies ($M_* > 10^{10}$ $M_\odot$) is supported by the similar space densities of these two populations ($\sim 3 \times 10^{-3}$ h_{70}^3 Mpc^{-3} and 2×10^{-3} h_{70}^3 Mpc^{-3}, respectively; McLure & Dunlop 2004; Daddi et al. 2004b, 2005; Reddy et al. 2005; Grazian et al. 2007). Moreover, the final black holes ($M_{BH} \gtrsim 2 \times 10^7$ $M_\odot$) are found at $z = 0$ in elliptical and bulge-dominated spiral galaxies (e.g. Tremaine et al. 2002; Marconi et al. 2004), consistent with the probable descendants of the $z \sim 2$ star-forming galaxy population (Genel et al. 2008; Conroy et al. 2008). This evidence thus confirm the plausibility of the rapid bulge formation seen at $z \sim 2$ in the SINS galaxies (Genzel et al. 2008) being followed by a few Gyr of rapid SMBH assembly, ultimately resulting in spheroids and bulges that obey the local M_{BH}-M_{bulge} relation.

Alexander et al. (2008) found similar delayed SMBH formation in the sub-mm galaxy population at $z \sim 2$ (see Figure 3.5), suggesting that the time lag between black holes and bulges may be a common phenomenon in rapidly forming galaxies at high redshift. However,

this trend is not universal; quasars and radio galaxies at similar redshifts are suspected to lie *above* local black hole scaling relations, with black holes that are over-massive for their host bulges by up to and exceeding an order of magnitude (e.g. Walter et al. 2004; Shields et al. 2006; McLure et al. 2006; Peng et al. 2006a; Maiolino et al. 2007, but see also Shields et al. 2003). These systems populate the highest mass end of the black hole mass function, with black hole masses of $> 10^8 - 10^9$ $M_\odot$ already in place at $z \sim 2$. It may therefore be that black holes in these different mass/activity regimes grow in very different circumstances and consequently relate to their bulges very differently. If this is the case, the challenge is then to locate the mechanism(s) that bring these varied high-redshift formation processes together into the black hole scaling relations observed at $z = 0$.

3.5 Conclusions

In stacked, average spectra of SINS $z \sim 2$ star-forming galaxies, we have detected broad emission underneath the much brighter narrow Hα and [NII] emission lines. This broad emission accounts for $\sim 30\%$ of the total Hα luminosity of these galaxies and can be parameterized equally well with a single broad Hα line ("broad line" of FWHM ~ 1500 km s^{-1}) and with a two Gaussian fit to both the permitted and forbidden lines ("broad wings" of FWHM ~ 550 km s^{-1}). The luminosity and FWHM of the broad component increases with increasing galaxy mass and therefore with SFR. This broad component is found both in known AGN and in stacked spectra of systems that have not been previously identified as AGN. There is some evidence that the broad emission is more luminous in galaxy centers, as opposed to in the outer regions, but the significance of these detections are low.

We cannot empirically determine whether this broad emission is due to high-velocity galactic winds and the associated shocks or to the BLR emission of AGN. In the former case, we find that simple scaling arguments show that the luminosity and FWHM of the broad emission can plausibly be accounted for via shocking of the ambient interstellar media from supernovae-driven galactic winds. These winds would then be ejecting matter from the host galaxy at rates slightly exceeding the star formation rate, in keeping with expectations from the metallicity evolution of these galaxies and with ultraviolet interstellar absorption-line studies at similar redshifts.

On the other hand, the broad emission may be generated in a BLR; in this case, we can estimate the black hole masses and luminosities necessary to fuel the observed emission for each of three galaxy mass bins. We find that the measured SMBH masses correlate with the host galaxy masses, as expected from local scaling relations, but that the SMBHs are significantly under-massive for their bulges when compared with local relations. While this result has large uncertainties, it is consistent with the emerging picture of galaxy assembly at $z \sim 2$, in which a gas-rich disk fragments into large (≥ 1 kpc) super-star-forming clumps that then migrate into the galaxy center on Gyr-timescales to form a nascent bulge. The bulge would then form first through this process and only later completely assemble its black

hole.

The obvious direction for future research is to determine the source of the broad Hα emission in high-redshift star-forming galaxies. This will most likely require detailed examination of individual galaxies. Among the diagnostics that will be useful for this task are comparisons with X-ray data and deep integrations in rest-frame UV/optical wavebands to spatially resolve e.g. UV interstellar absorption lines and broad Balmer emission.

Acknowledgments

We thank the ESO staff, especially those at Paranal Observatory, for their helpful and enthusiastic support during the many observing runs and several years over which the SINS project was carried out. We also acknowledge the SINFONI and PARSEC teams, whose hard work on the instrument and laser paved the way for the success of the SINS observations. This work has additionally benefited significantly from many enlightening conversations with colleagues, including Frédéric Bournaud, Mohan Ganeshalingam, Kevin Heng, Phil Hopkins, Chris McKee, Jeffrey Silverman, and Thea Steele.

Chapter 4

The Black Hole in NGC 3379: A Comparison of Gas and Stellar Dynamical Mass Measurements with HST and Integral-Field Data

Abstract

We combine *Hubble Space Telescope* spectroscopy and ground-based integral-field data from the SAURON and OASIS instruments to study the central black hole in the nearby elliptical galaxy NGC 3379. From these data, we obtain kinematics of both the stars and the nuclear gaseous component. Axisymmetric three-integral models of the stellar kinematics find a black hole of mass $1.4^{+2.6}_{-1.0} \times 10^8$ $M_\odot$ (3σ errors). These models also probe the velocity distribution in the immediate vicinity of the black hole and reveal a nearly isotropic velocity distribution throughout the galaxy and down to the black hole sphere of influence $R_{\rm BH}$. The morphology of the nuclear gas disk suggests that it is not in the equatorial plane; however the core of NGC 3379 is nearly spherical. Inclined thin-disk models of the gas find a nominal black hole of mass $(2.0 \pm 0.1) \times 10^8$ $M_\odot$ (3σ errors), but the model is a poor fit to the kinematics. The data are better fit by introducing a twist in the gas kinematics (with the black hole mass assumed to be 2.0×10^8 $M_\odot$), although the constraints on the nature and shape of this perturbation are insufficient for more detailed modeling. Given the apparent regularity of the gas disk's appearance, the presence of such strong non-circular motion indicates that caution must be used when measuring black hole masses with gas dynamical methods alone.

4.1 Introduction

In the study of galaxy formation and evolution, one of the more intriguing recent results is the so-called black hole - sigma (M_{BH}-σ) relation between the mass of a galaxy's central supermassive black hole (SMBH) and the large-scale velocity dispersion of the stars (e.g. Ferrarese & Merritt 2000; Gebhardt et al. 2000a). What is particularly remarkable is the tightness of this correlation, which spans three orders of magnitude in black hole mass and one in stellar velocity dispersion (but see Bender et al. 2005). The primary implication of the existence of the M_{BH}-σ relation is clear: over a large range of galaxy sizes, there must be a fundamental connection between the evolution of the very small central regions of an individual galaxy to that of the galaxy on much larger scales. This connection has yet to be completely understood; however, it is thought to reflect the SMBHs regulating the amount of gas and thus the rate of star formation in their host galaxies' spheroids (e.g. Silk & Rees 1998; Granato et al. 2004). Understanding SMBHs and their relation to their environments can therefore provide much insight into the formation and merger history of their host galaxies.

In practice, the M_{BH}-σ result is the product of nearly 40 measurements of SMBH masses in nearby galaxies using several distinct techniques (see e.g. Kormendy & Gebhardt 2001; Barth 2004, for reviews). By far the most reliable of these measurements is that of the SMBH in Milky Way, the relative proximity of which allows the orbits of individual stars in the vicinity of the black hole to be traced in great detail (Eckart & Genzel 1997; Genzel et al. 1997, 2000; Ghez et al. 1998, 2000). As to extragalactic BHs, the most accurate measurements are studies of H_2O maser emission in galaxy nuclei, which have been observed to follow nearly perfect Keplerian rotation around a central massive object (e.g. Miyoshi et al. 1995; Herrnstein et al. 2005). Although quite straightforward and precise, this method relies on a galaxy having detectable nuclear maser emission and therefore accounts for only a handful of the SMBH mass measurements. A similar method takes advantage of galaxies with nuclear ionized gas disks; assuming the gas is contained in a thin disk and is influenced solely by the combined gravitational potential of the galaxy and a central black hole, the kinematics of these disks can be used to estimate the mass of the black hole (e.g. Harms et al. 1994; Macchetto et al. 1997; van der Marel & van den Bosch 1998; Bertola et al. 1998; Barth et al. 2001). This technique has also recently been applied to the nuclear stellar disk in M31, which is unique in being sufficiently resolved for the stellar Keplerian motion to be measured (Bender et al. 2005). The most used technique for measuring SMBH mass, however, relies not on detecting Keplerian motion but rather on detailed models of the stellar dynamics. Over two-thirds of SMBH mass measurements are the results of long-slit stellar kinematic data, coupled with axisymmetric dynamical models (e.g. van der Marel et al. 1998; Cappellari et al. 2002; Gebhardt et al. 2003).

These gas dynamical and stellar dynamical methods, despite being responsible for nearly all black hole mass estimates, are often limited both by the necessary assumptions and by other factors such as spatial resolution of the observations and computational resources. Despite such uncertainties, measurements with these various techniques nevertheless result in a tight M_{BH}-σ correlation, and this is compelling evidence that the relationship is genuine.

However, these methods are expected to suffer mainly from systematic effects, mostly influencing the slope of M_{BH}-σ, which in turn affects extrapolations of the relation to higher and lower mass systems. To investigate the accuracy of current methods, black hole mass estimates for a number of objects, using multiple methods for each system, are required.

Several such tests have been conducted. Cappellari et al. (2002) and Verdoes Kleijn et al. (2002) have constructed both gas dynamical models and axisymmetric stellar dynamical models for individual galaxies. In both cases, the traditional thin-disk gas model requires a significantly (7 times and 30 times, respectively) smaller black hole than that needed in the stellar model, and the high stellar dynamical estimate is strongly excluded by the gas kinematics. Also in both cases, the gas and stellar measurements bracket the black hole mass predicted by the M_{BH}-σ relation. To reconcile these results, potential sources of error in the gas and stellar models were examined, including non-gravitational motion in the nuclear gas disks, deviations from axisymmetry, and data quality. The limitations of the data and of the assumptions in these studies require that further tests on a number of other galaxies be performed.

The nearby elliptical (E1) galaxy NGC 3379 (M105) is an ideal candidate for such a test. NGC 3379 has been classified as a "core" galaxy, in that the slope of its surface brightness profile is less positive in the central regions than in the rest of the galaxy (core radius of R_c=1.″98, Lauer et al. 2005), and Faber et al. (1997) have suggested that such a surface brightness distribution can be generated through mergers that result in a central binary SMBH system. Gebhardt et al. (2000b) have noted that the central two arcseconds (100 pc, at an assumed distance of 10.28 Mpc from Tonry et al. 2001) contain a well-defined dust disk, presumably linked to ionized gas and rotating around this SMBH (see also Pastoriza et al. 2000). Additionally, extensive stellar kinematic data out to 90″ (4.5 kpc) suggest that NGC 3379 has a very regular dynamical structure and may therefore be suitable for axisymmetric stellar dynamical models (Statler & Smecker-Hane 1999; Gebhardt et al. 2000b; Emsellem et al. 2004). From the stellar velocity dispersion measured in these data (201 km s^{-1}, Cappellari et al. 2006) and the M_{BH}-σ equation given by Tremaine et al. (2002), NGC 3379 is expected to harbor a SMBH of mass 1.4×10^8 $M_\odot$; such a black hole has a sphere of influence of radius $R_{BH} \approx 0.''29$ (15 pc). It should therefore be possible, with data of sufficient spatial resolution, to construct both gas dynamical models and stellar dynamical models for this galaxy and generate two independent estimates of the mass of the central SMBH.

Because of the proximity, brightness, and apparent normalcy of NGC 3379, this galaxy has already been the subject of many studies. While there are no previous gas dynamical models of the central regions of NGC 3379, Gebhardt et al. (2000b) have constructed axisymmetric stellar dynamical models, using a combination of ground-based long-slit data along four position angles and an FOS spectrum. Their best-fitting model required a black hole of $1^{+1.0}_{-0.4} \times 10^8$ $M_\odot$ (1σ errors, Gebhardt et al. 2000b), consistent with the predictions of the M_{BH}-σ relation.

In this chapter, we study both the gas and stellar kinematics to generate two independent measurements of the mass of the SMBH of NGC 3379 and to investigate the structure of

the stars and gas in its vicinity. We use the SAURON and OASIS ground-based integral-field units (IFUs) to obtain stellar kinematics in two spatial dimensions (§4.2), and we use *Hubble Space Telescope* (*HST*) data to examine the surface brightness and kinematics of the central gas disk in detail (§4.3). In §§4.4 and 4.5, the axisymmetric stellar dynamical model is presented, and the results are described. Likewise, the gas dynamical model and results are discussed in §§4.6 and 4.7, respectively. We then compare these results (§4.8) to gain quantitative insight into the robustness of black hole mass estimation techniques and summarize our conclusions in §4.9.

4.2 Observations: Ground-Based IFUs

4.2.1 SAURON Spectroscopy

To study both the stellar and gas kinematics of NGC 3379, two complementary sets of integral-field data, from the SAURON and OASIS instruments, were obtained. NGC 3379 is a part of the SAURON survey of nearby early-type galaxies and bulges (de Zeeuw et al. 2002) and, as such, was observed out to $\sim 1R_e$ using the SAURON IFU (Bacon et al. 2001) at the 4.2-m William Herschel Telescope in February 1999. The galaxy was observed in eight exposures, divided between three pointings, each including the galaxy center. Within pointings, individual exposures were spatially dithered in order to avoid systematic effects. Characteristics of the SAURON instrument and details of the observations are given in Table 4.1.

The reduction process and reduced SAURON datacube were presented in Emsellem et al. (2004). Briefly, the data were reduced using the XSauron software and reduction process, developed at the CRAL-Observatoire and described in Bacon et al. (2001). The steps included bias and dark subtraction, extraction of the spectra using a fitted mask model, wavelength calibration, low-frequency flat-fielding, cosmic-ray removal, homogenization of the spectral resolution over the field, sky subtraction, and flux calibration. All eight exposures were then merged into a single datacube and truncated to a common wavelength range. During this process, the data were spatially resampled on to a common spatial scale of $0\farcs8 \times 0\farcs8$, resulting in a field-of-view of approximately $45'' \times 70''$. To increase the signal-to-noise (S/N) ratio to sufficient levels for accurate determination of the kinematics, the datacube was spatially binned using the Voronoi 2D-binning scheme developed by Cappellari & Copin (2003). A minimum S/N of 60 per spectral element was imposed; in practice, however, many of the spectra have a much higher S/N ($\mathrm{S/N_{max}} \approx 560$), and over one quarter of the spectral elements remain unbinned.

Since we are interested in the details of the central regions of NGC 3379, a precise measurement of the PSF of the observations is necessary. This was accomplished by comparing the reconstructed SAURON intensity distribution to the *HST*/WFPC2/F555W data (see §4.3.1), the filter that best matches the SAURON spectral range. The WFPC2 data were convolved with a PSF, which was modeled as the sum of two concentric circular Gaussians,

Table 4.1: Specifications of SAURON and OASIS instruments and observations

	SAURON	OASIS
Field of view	$33'' \times 41''$	$8'' \times 10''$
Aperture size	$0''.94$	$0''.27$
Final spatial sampling	$0''.8$	$0''.2$
Spectral range	4810 - 5300 Å	4760 - 5558 Å
Spectral sampling	1.1 Å/pixel	1.95 Å/pixel
Spectral resolution (FWHM)	4.2 Å	5.4 Å
Instrumental dispersion σ	108 km s^{-1}	135 km s^{-1}
Number of field lenses	1431	1009
Number of sky lenses	146	0
Number of pointings	3	1
Number of exposures	8	2
Time per exposure	1800 s	3600 s
Weight, FHWM of PSF Gaussian 1	0.71, $1''.60$	0.84, $0''.94$
Weight, FHWM of PSF Gaussian 2	0.29, $5''.22$	0.16, $4''.31$

Table 4.2: Specifications of the *HST*/STIS observations

	# Exp.	Avg. $t_{\rm Exp}$	Nominal Shift	Actual Shift
Top Slit	5	2600 s	$+0''.25$	$+0''.25$
Center Slit	5	2700 s	$0''.00$	$0''.00$
Bottom Slit	4	2550 s	$-0''.25$	$-0''.20$

and the difference between the resulting image and the SAURON data was minimized. The derived PSF parameters are listed in Table 4.1.

4.2.2 OASIS Spectroscopy

NGC 3379 is also included in the OASIS survey, which investigates the centers of the SAURON galaxies with a similar spectral range to SAURON but with higher spatial resolution (McDermid et al. 2004). OASIS integral-field observations of NGC 3379 were taken at the 3.6-m Canada-France-Hawaii Telescope in March 2001. One pointing of two exposures was obtained, with the exposures dithered to provide oversampling and to avoid systematic effects. The details of the OASIS instrumental characteristics and of the observations are given in Table 4.1.

The data were reduced using the publicly available XOasis software and reduction process, developed at the CRAL-Observatoire, described in Rousset (1992) and McDermid et al. (2006). The reduction process is nearly identical to that for the SAURON data with two notable exceptions: the lack of sky subtraction (as OASIS does not have dedicated sky lenslets) and the inclusion of a fringe correction. Since OASIS was pointed at the high-signal central regions of NGC 3379, the sky signal is so far below the galaxy signal as to be undetectable, and neglecting sky removal therefore has a negligible effect on the resulting reduced datacube. Inspection of a preliminary reduction of the OASIS data revealed that the EEV1 detector used in the observations suffered from the effects of fringing. In order to remove this effect, an average twilight spectrum was divided off from a twilight datacube, leaving only the residual fringe pattern in all three dimensions (two spatial and one spectral). The science datacubes were then divided by this fringe pattern. The two final science datacubes were merged into a single datacube, during which the exposures were spatially resampled on to a common spatial scale of $0\farcs2 \times 0\farcs2$, resulting in a field-of-view of approximately $8'' \times 10''$. The data were spatially binned to a minimum S/N of 100 per spectral resolution element to accommodate the sparser spectral sampling of OASIS. In the central regions, this resulted in a maximum of two spatial elements being combined; since the PSF was oversampled, this mild binning did not cause a loss of spatial information. The final OASIS datacube of NGC 3379 is presented in McDermid et al. (2006).

The PSF of the OASIS measurements of NGC 3379 was determined using the same procedure as used for the SAURON data, and the derived PSF parameters are listed in Table 4.1.

4.2.3 Stellar Kinematics

The SAURON and OASIS datacubes contain several absorption features, including Hβ, Mg b, and some Fe lines, as well as several emission lines, including Hβ, [OIII] $\lambda\lambda$4959,5007, and [NI] λ5200. To extract reliable stellar kinematics, we used the penalized pixel fitting (pPXF) method of Cappellari & Emsellem (2004), which allows the emission regions to be omitted from the fit and minimizes the effects of undersampling via penalization. An

optimal template is constructed from a stellar library and is then convolved with Gauss-Hermite expansions (van der Marel & Franx 1993; Gerhard 1993) out to six terms until differences between the convolved template and the observed galaxy spectra are minimized.

To estimate the error on the stellar kinematics, Monte Carlo simulations of the kinematic extraction were performed, following the prescriptions of Cappellari & Emsellem (2004). Spectra were simulated by adding noise, based on the residuals of the original extraction, to the galaxy spectra. During the Monte Carlo realizations, the pixel fitting was done without penalization, in order to obtain the unbiased scatter of the kinematics. One hundred realizations were used, and the 1σ errors on the kinematics were derived from the resulting distributions.

This method is similar to that used by Emsellem et al. (2004) on the SAURON datacube and by McDermid et al. (2006) on the OASIS datacube, but it differs in the details of the extraction. In those papers, optimal stellar templates are constructed from a selection of single-burst stellar population models by Vazdekis (1999) and additional strong Mg b stellar spectra from the Jones (1997) library. The Jones spectra were used to attempt to compensate for possible Mg b over-abundance and thus to alleviate potential template mismatch. Both Emsellem et al. (2004) and McDermid et al. (2006) then simultaneously fit the optimal template and the Gauss-Hermite moments out to four terms for each bin.

Preliminary tests revealed that the possibility for template mismatch could be further reduced through the use of the larger MILES (Mid-resolution INT Library of Empirical Spectra) library of 998 individual stellar spectra, kindly provided pre-publication by Sánchez-Blázquez et al. (2006). This library has several advantages over the combined Vazdekis and Jones library, the most notable being greater coverage and sampling of stellar atmospheric parameters such as metallicity. This variety of abundances and larger number of stars in the library allows for a more precise determination of the optimal template, which for NGC 3379 is composed of 16 of the 998 spectra. We quantify the improvement in the optimal template through the RMS scatter of the residuals from a pPXF fit to a high S/N SAURON spectrum of this galaxy; the use of the MILES library instead of the Vazdekis and Jones library reduces this scatter from ~ 0.55 to ~ 0.20. Emsellem et al. (2004) show that the maximum systematic error in the higher Gauss-Hermite moments from template mismatch scales almost linearly with the RMS scatter (see their Figure B3). This implies that the MILES library decreases the maximum systematic errors by a factor of ~ 3, to less than 0.02.

Using the MILES optimal template, the kinematics in each bin were extracted out to six Gauss-Hermite terms for both the SAURON and OASIS data. For maximum consistency between these two data sets, the OASIS spectra were truncated to the same spectral region as the SAURON spectra (roughly from Hβ to Mg b) for the kinematic extraction. This was desirable because of the number of additional Fe features included in the OASIS spectral range, which render those data particularly sensitive to potential inabilities of the template library to reproduce the exact abundance ratios of this galaxy (see also Barth et al. 2002). The results of this extraction are consistent with the kinematics presented in Emsellem et al. (2004) and McDermid et al. (2006), with the exception that the measurements of the even moments presented here are slighly lower, a testament to the decreased effect of template

mismatch through the use of the more extensive stellar library.

A comparison of the SAURON and OASIS kinematics obtained with this method revealed nearly perfect agreement between all moments except the velocity dispersion, in which the OASIS data were approximately 5 km s^{-1} higher than the SAURON data. Given the excellent consistency in the higher moments, this deviation is most likely not an effect of template mismatch but rather of a systematic error in the reduction process. The most probable source of error is the homogenization of the spectral resolution across the field, a step that involves convolution with a Gaussian. To correct for this offset, we measure the circularly averaged velocity dispersion profiles between 3″and 4″, outside the influence of the PSFs. Since the systematic uncertainties in the homogenization are similar for both data sets, we adjust both sets to the midpoint of these radial profiles (in practice, ± 2.5 km s^{-1}) and implement the correction in quadrature to the entire dispersion field. This correction, used only for the velocity dispersion, mimics the nature of the problem as an error in the Gaussian convolution during the resolution homogenization.

The resulting SAURON and OASIS kinematics are shown and compared in Figure 4.1. (The full SAURON field is shown in §4.5.) Long-slit stellar kinematics for this galaxy have been measured by Statler & Smecker-Hane (1999), Gebhardt et al. (2000b), Halliday et al. (2001), and Samurović & Danziger (2005), all of whom extracted their LOSVD out to h_4. Figure 4.1 also presents the comparison of the SAURON and OASIS major axis kinematics to those long-slit measurements along the same axis. Overall, the kinematics agree quite well with each other and with the literature.

This qualitative agreement is reassuring; however, these kinematics will be used in detailed stellar dynamical modeling, which requires that they are completely consistent and are free of systematic effects. We therefore must establish that the somewhat ad hoc correction to the velocity dispersion measurements (as determined using data between 3″and 4″) produces consistent velocity dispersions throughout the field. At small radii, however, the OASIS dispersions are expected to be noticeably higher, since the narrower OASIS PSF allows the data to better resolve the rising central velocity dispersion (Figure 4.1). Since we have detailed measurements of the SAURON and OASIS PSFs, we can test the effectiveness of the dispersion correction by convolving the OASIS velocity dispersions up to the SAURON PSF and then comparing them to the observed SAURON velocity dispersions. To accomplish this, we convolve the flux-weighted true moments ($\mu_1 = v$ and $\mu_2^2 = v^2 + \sigma^2$) and then subtract the convolved true moments in quadrature to find the convolved dispersion (see Emsellem et al. 1994 for a more complete discussion of this method). The results of this comparison are shown in Figure 4.2 and indicate that the two data sets are in good agreement. Edge effects from the convolution are visible as slight rises in velocity dispersion at the boundaries of the OASIS field, but, most important for the determination of the SMBH mass, the central dispersion values are consistent. This agreement, as well as the agreement with the literature shown in Figure 4.1, suggests that the steps taken here to mitigate potential effects of template mismatch have been largely successful and have produced kinematics that adequately describe this galaxy.

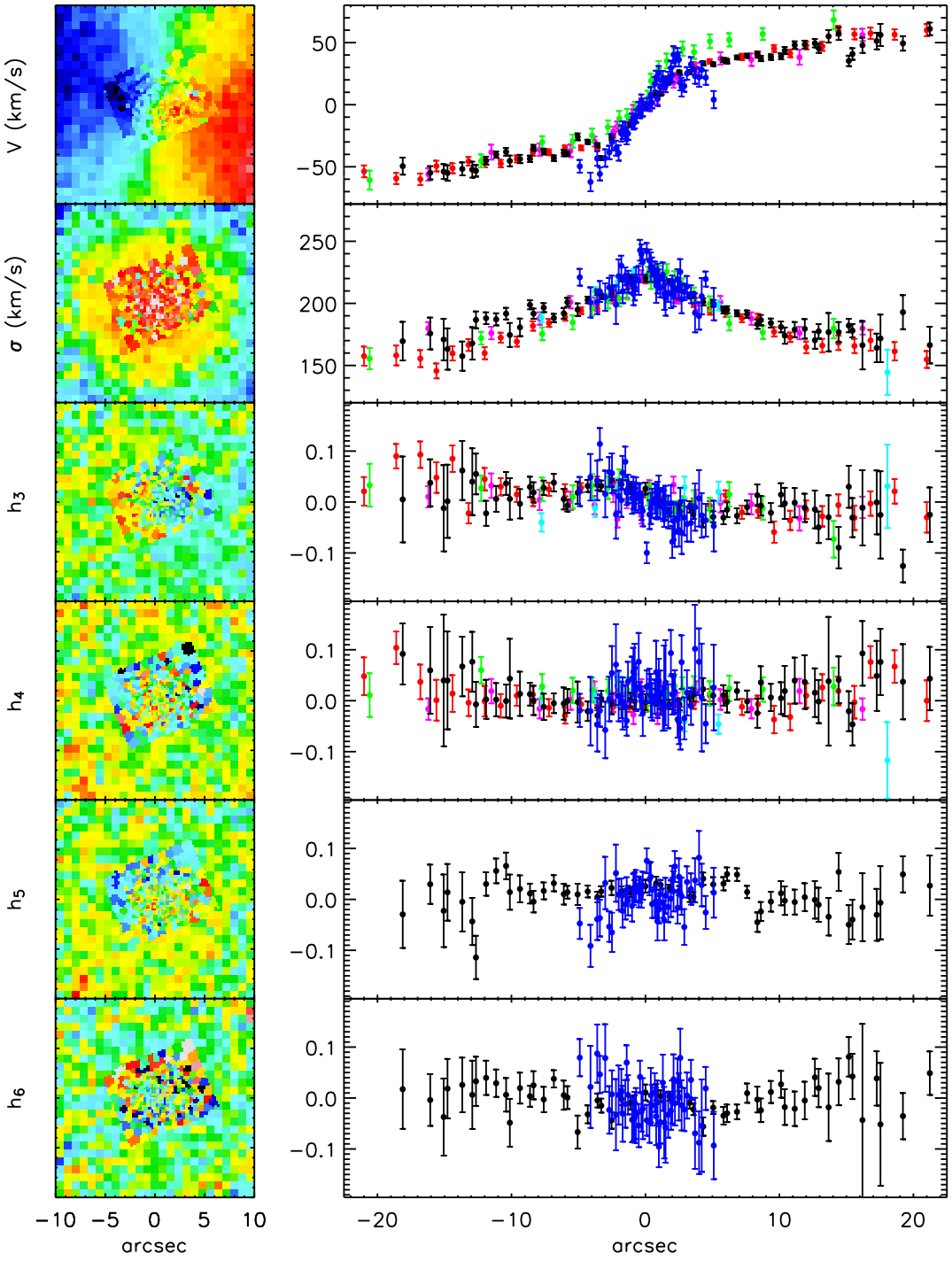

Figure 4.1: First six Gauss-Hermite moments of the LOSVD in NGC 3379. Left panels show the inner 10″ of the SAURON field, with the OASIS field overlaid. In these plots, north is up and east is to the left. Right panels show the LOSVD moments as seen through a 1″ slit placed along the galaxy's major axis (PA=70°) as observed with SAURON (*black*) and OASIS (*blue*). Red, magenta, cyan, and green points indicate the long-slit major axis data of Statler & Smecker-Hane (1999), Gebhardt et al. (2000b), Halliday et al. (2001), and Samurović & Danziger (2005) respectively. The small OASIS PSF allows the data to probe the central rise in velocity dispersion with more detail than previous measurements or the SAURON data.

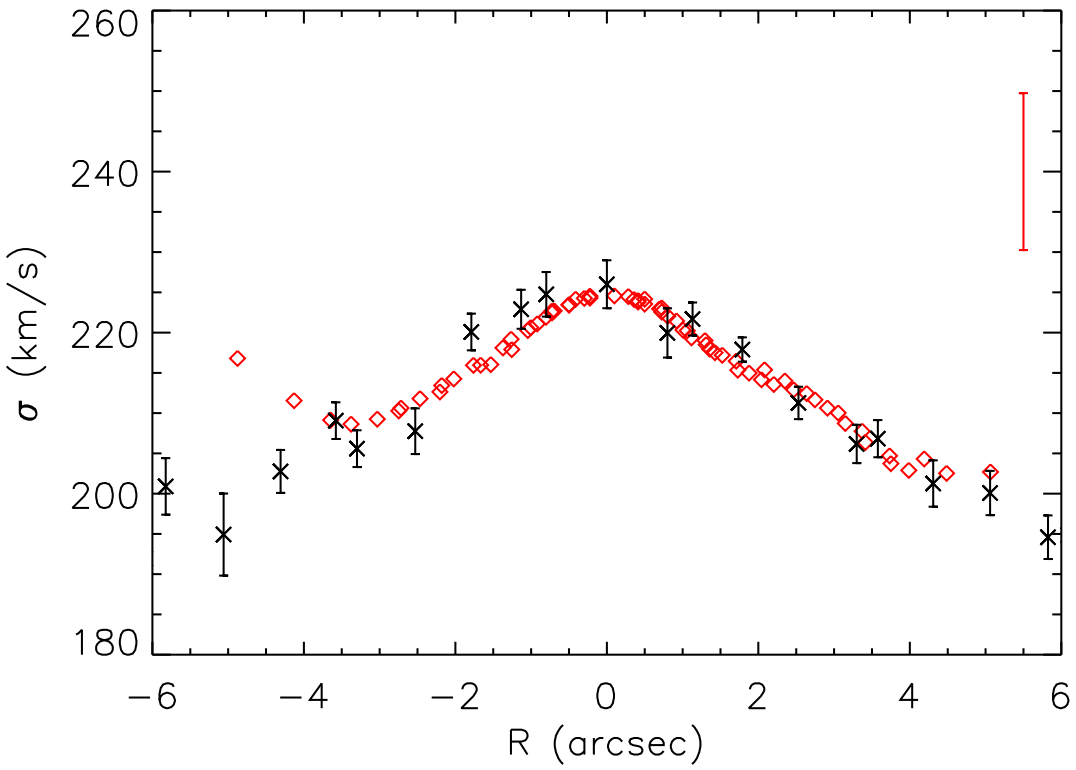

Figure 4.2: OASIS stellar velocity dispersions (*red diamonds*) are convolved up to the PSF of the SAURON observations and compared to the SAURON dispersion measurements (*black crosses*), both shown as extracted from slits along the major axis. The bar in the upper right corner gives the mean error of the unsmoothed OASIS data. The convolved OASIS values are given for all the original bins and therefore show strong point-to-point correlations. In general, this convolution brings the two data sets into agreement.

4.2.4 Gas Kinematics

In the region of the nuclear gas disk, the SAURON and OASIS datacubes show strong emission features, which can be used to measure the ionized gas kinematics in the galaxy center. In the SAURON field, however, the 0.″8 pixels probe the $\sim 2''$-diameter disk only marginally. Sarzi et al. (2006) present the ionized gas kinematics derived from the SAURON datacube, in which the disk's rotation is visible in only the central few pixels. We therefore make use of the OASIS datacube, with 0.″2 pixels, to obtain well-sampled spatially complete gas kinematics of this disk.

The gas kinematics in the OASIS datacube are measured following the method of Sarzi et al. (2006), which McDermid et al. (2006) have implemented on the OASIS sample. In this method, the pixel fitting is rerun with the stellar kinematics held fixed at the values determined above. Rather than excluding spectral regions around the emission lines, however, the emission lines are included in the template library as a series of Gaussians (one per line). The velocity and broadening of the emission lines are determined entirely from the [OIII] emission and then imposed on the other emission features. The amplitudes of all lines are then derived via an optimal (non-negative) linear combination of stellar spectra and emission line templates.

To remove spurious detections, we conservatively require an amplitude-to-noise ratio of 5 before an emission line is considered real (see McDermid et al. 2006, for a full discussion of sensitivity limits). The resulting gas kinematics of sufficient significance are shown in Figure 4.3. In these data, the shape and orientation of the nuclear gas disk are visible, as is the lack of ionized gas outside this disk.

The OASIS data are limited, however, by the seeing, which smears emission from the central $2''$of the galaxy over $\sim 4''$. Thus, although the spatial resolution of the OASIS instrument is sufficient to probe the sphere of influence of a hypothesized central black hole, the PSF smoothes these effects, such that any Keplerian rise in velocities is undetectable. While extremely useful for studying the complete velocity field of the gas disk, the OASIS data alone are insufficient for a gas dynamical model to measure the black hole mass in this galaxy.

4.3 Observations: HST

4.3.1 WFPC2 Imaging

To further investigate the central gas disk in NGC 3379, spatially-resolved photometric and spectroscopic data were obtained with *HST*, program 8589. The central region of the galaxy was imaged using the Wide Field Planetary Camera 2 (WFPC2), with the galactic nucleus placed on the higher-resolution PC chip (0.″0455/pixel). Data were obtained through the F658N filter in order to observe the Hα and [NII] emission in the central gas disk. With a spectral range from $\sim$ 6575-6605 Å, this passband includes all the Hα emission and most of the [NII] emission at this redshift ($\sim$ 900 km s^{-1}).

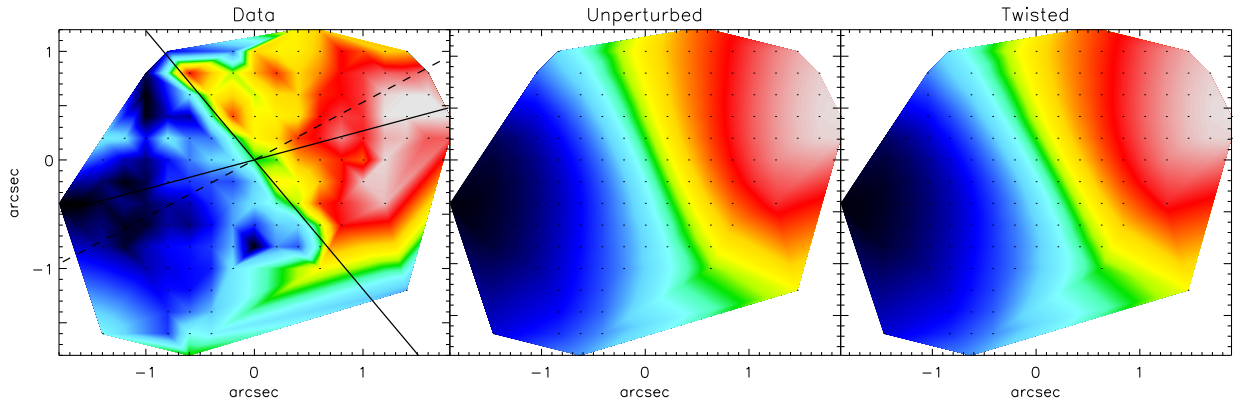

Figure 4.3: OASIS observed gas velocities (*left*) with the kinematic major and minor axes traced by solid black lines and the photometric major axis indicated with the dashed line (north up, east to the left). The unperturbed model (*center*) was constructed with the data symmetrized around the kinematic major axis, since a determination of M/L depends strongly on the peak velocities along the major axis. The twisted model (*right*) is only a marginally better fit to the data, since most of the features of the twist are smeared out by the OASIS PSF. However, qualitative analysis of the data strongly favors some type of perturbed model, as the kinematic major and minor axes are not orthogonal. The data shown in the left panel have been interpolated between pixels to clarify the kinematic axes and for ease of comparison with the model; the original kinematics are presented without interpolation in McDermid et al. (2006).

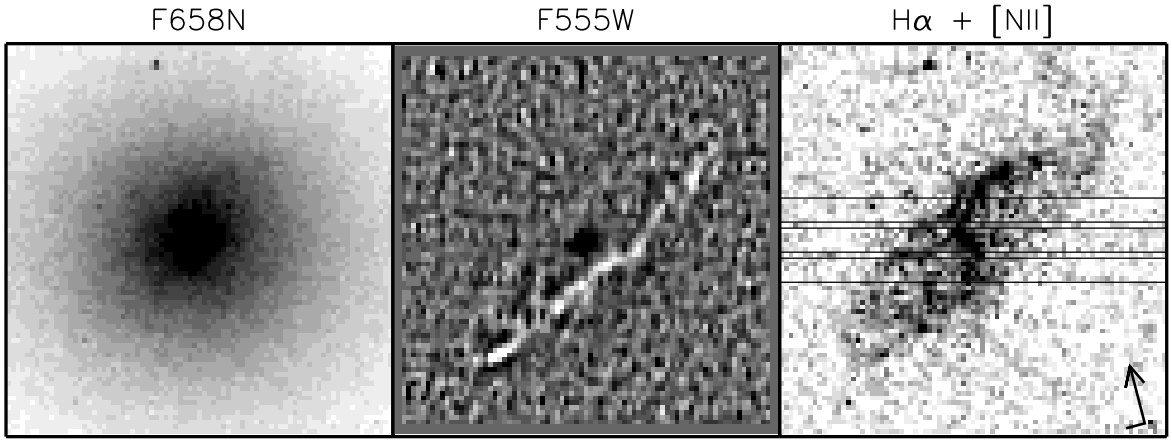

Figure 4.4: *HST*/WFPC2 images of the center of NGC 3379. The Hα narrow band continuum emission is shown at left, the dust ring (*center*) is detected in an unsharp-masked *V*-band image, and the Hα+[NII] image (*right*) was generated by the subtraction of the Hα image by an "*R*"-band continuum image (see text). The nominal location of the three STIS slits is shown in the right panel, with the position angle of the images indicated by the arrow on the lower right.

The F658N image was taken as a sequence of two individual exposures, each of length 1200 seconds. The images were processed in the *HST* data pipeline and were subsequently combined and cosmic-ray rejected.

In addition to these data, Gebhardt et al. (2000b) obtained F555W (*V*-band) and F814W (*I*-band) images of the nucleus of NGC 3379. In both of these images, the galaxy was also centered on the PC detector. Gebhardt et al. (2000b) present the deconvolved F555W image, with the galaxy's spheroidal light distribution subtracted, to reveal a central dust disk seen in absorption (see also Lauer et al. 2005). This disk corresponds in orientation and inclination with the gas emission in Hα, as shown in Figure 4.4.

To generate an image of the gas disk without stellar emission, we scale a broadband image and subtract it from the F658N data. In the absence of any *HST R*-band data, we simulate data from this passband by scaling the F555W and F814W images and averaging the two. This method yields a more accurate representation of the continuum emission and dust absorption present in the F658N image than can be achieved with either the *V*-band or *I*-band image alone. The resulting "*R*-band" image was subtracted from the F658N data to produce a map of only the Hα+[NII] emission (Figure 4.4).

The resulting Hα+[NII] image reveals a well-defined disk of emission around the galaxy center. The regularity of this disk allows for a simple and precise measurement of its photometric position angle and inclination. We fit an ellipse by eye to the outline of the disk in this image and measured the position angle to be PA = 118°. If the disk is assumed to be thin and intrinsically circular, then the inclination implied by this fit is $i_{\rm disk} = 70° \pm 8°$, where the error bar includes the inclination of the dust disk associated with the gas and an ellipse fit to the OASIS gas data.

Cappellari et al. (2006) have used the F814W WFPC2 image of NGC 3379, in addition to wide-field ground-based photometry taken in the same filter at the 1.3m McGraw-Hill telescope at the MDM observatory on Kitt Peak, to construct a Multi-Gaussian Expansion (MGE) parameterization of the surface brightness of this galaxy (Emsellem et al. 1994; Cappellari 2002). Their deconvolved MGE model was regularized to require that the axial ratio of the flattest Gaussian be as large as possible and was corrected for extinction. The resulting best-fitting MGE, a sum of 13 Gaussian components, is presented in their Figure 3, and the calibrated parameters, corrected for extinction and converted to a stellar surface density in solar units, are given in their Table B1. In Figure 4.5, we show the MGE fit to the surface brightness along several position angles, as well as the residuals of this fit. We adopt this parameterization to describe the stellar surface density distribution in this galaxy.

4.3.2 STIS Spectroscopy

Long-slit spectra of the central gas disk in NGC 3379 were obtained with the *HST* Space Telescope Imaging Spectrograph (STIS), through a 0.″2 slit and through the G750M filter with the grating tilted to provide a spectral range 6300 - 6860 Å. With this set-up, these data included the Hα and both [NII] emission lines in this galaxy, at a spectral resolution of 0.554 Å/pixel and a spatial sampling of 0.″051/pixel.

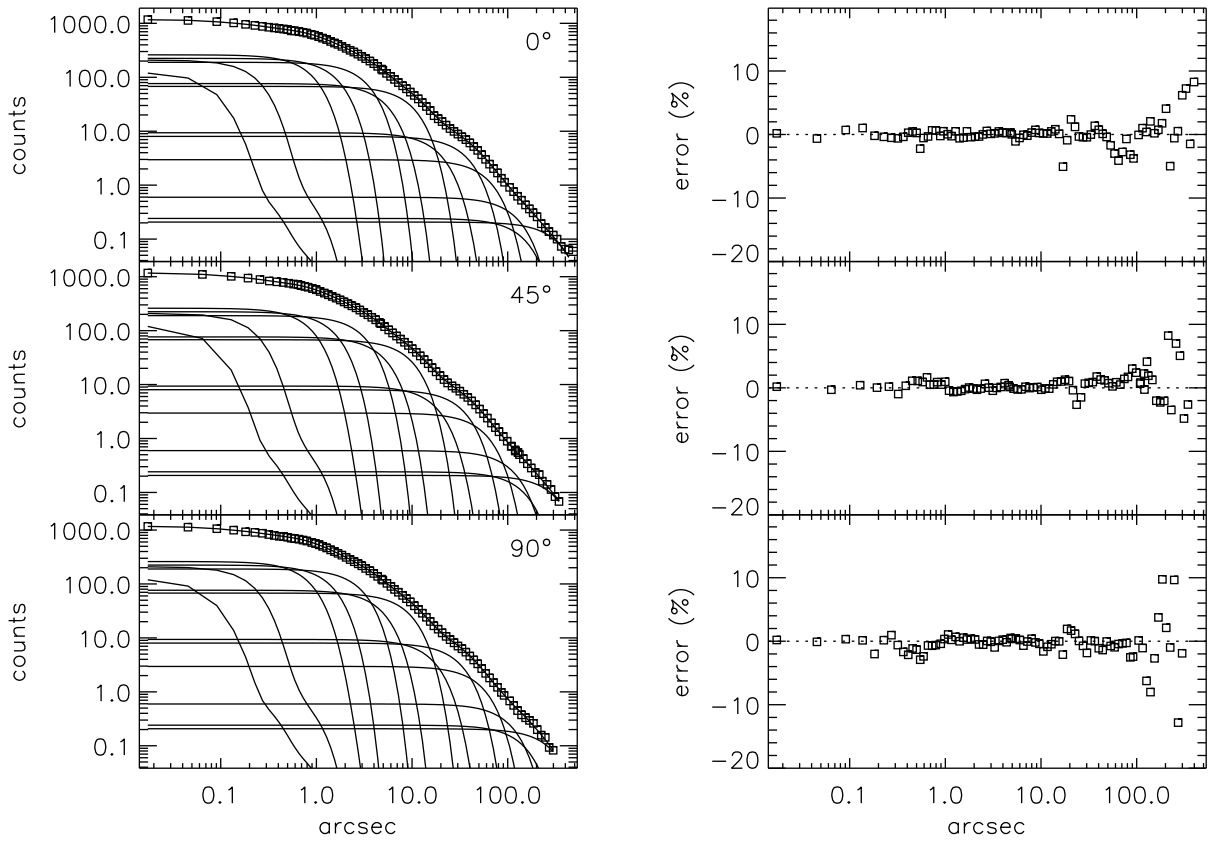

Figure 4.5: MGE fit to the data along three position angles (*left*), with percentage error (*right*). All individual Gaussian components are shown, as well their sum, which fits the surface brightness data (*boxes*) over four orders of magnitude in radius. This model was generated from combined *HST*/WFPC2 data and ground-based wide-field MDM imaging and was presented in Cappellari et al. (2006). The strong "core" signature can be seen inwards of $\sim 2''$.

Target acquisition and peak-up procedures were performed to center the STIS slit on the galaxy's nucleus. Spectroscopic images were then obtained at each of three locations: at the galaxy center and with a nominal offset $\pm 0\farcs25$ perpendicular to the slit, with a resulting gap of $0\farcs05$ between slits. Due to the scheduling of the observations, there was no observability at the requested position angle along the major axis of the gas disk; consequently, the observations were taken at a PA = -104.7°, approximately 40° offset from the major axis. This slit positioning and location is shown in Figure 4.4, and we designate the "top," "center," and "bottom" slits according to their location in this figure.

Data were acquired in five exposures on the top and center slits and four on the bottom slit. Observation details are presented in Table 4.2. Individual exposures were spatially dithered along the slit in order to avoid systematic effects. The images were processed by the *HST* data processing pipeline, including wavelength calibration, after which they were combined and cosmic-ray rejected. The resulting STIS data for all three slits are shown in Figure 4.6.

We use the STIS data themselves to measure the actual positions of the slits by collapsing the spectra over the spectral range and comparing that light profile to light profiles extracted from the acquisition image taken during the peak-up procedure. These latter profiles were extracted from the acquisition image by averaging the flux of pixels (and fractions of pixels) covered by synthetic $0\farcs2$ STIS slits. The best-fitting slit positions were determined using a χ^2 minimization of the ratio between the light profile measured from the slits and that measured from the acquisition image. For the top and center slit, the nominal offset is indeed the actual offset, to within a fraction of a STIS pixel. For the bottom slit, the actual offset is $-0\farcs20$, which deviates from the nominal offset of this slit by $\sim$1 STIS pixel. These results are summarized in Table 4.2.

4.3.3 Gas Kinematics

The gas kinematics in NGC 3379 were extracted for each individual row of all three STIS slits. As would be expected from the WFPC2 Hα+[NII] image, the emission signal drops off dramatically at the boundaries of the gas disk; therefore, all rows with detectable signal were used. This results in gas kinematics being obtained for roughly the inner two arcseconds of the galaxy.

To measure the kinematics, we first removed the stellar background emission by fitting a linear continuum to 6475 - 6525 Å and 6625 - 6675 Å. Over this spectral range, a straight line is a good approximation to the continuum shape. The Hα and the [NII] λ6584 lines were then fit separately by single Gaussians. The [NII] λ6548 emission was not used, as it has low signal in all rows and is not detectable at larger radii (see Figure 4.6). No other emission lines were detected. The higher [NII] λ6584 signal than Hα and the lack of other significant emission lines are consistent with the classification of NGC 3379 as a LINER galaxy.

Figure 4.7 shows the derived [NII] λ6584 and Hα kinematics, set to a systemic velocity of zero. Over most of the disk, the two lines share roughly the same velocity distribution, although for over half the data points, their differences are higher than the formal errors. The

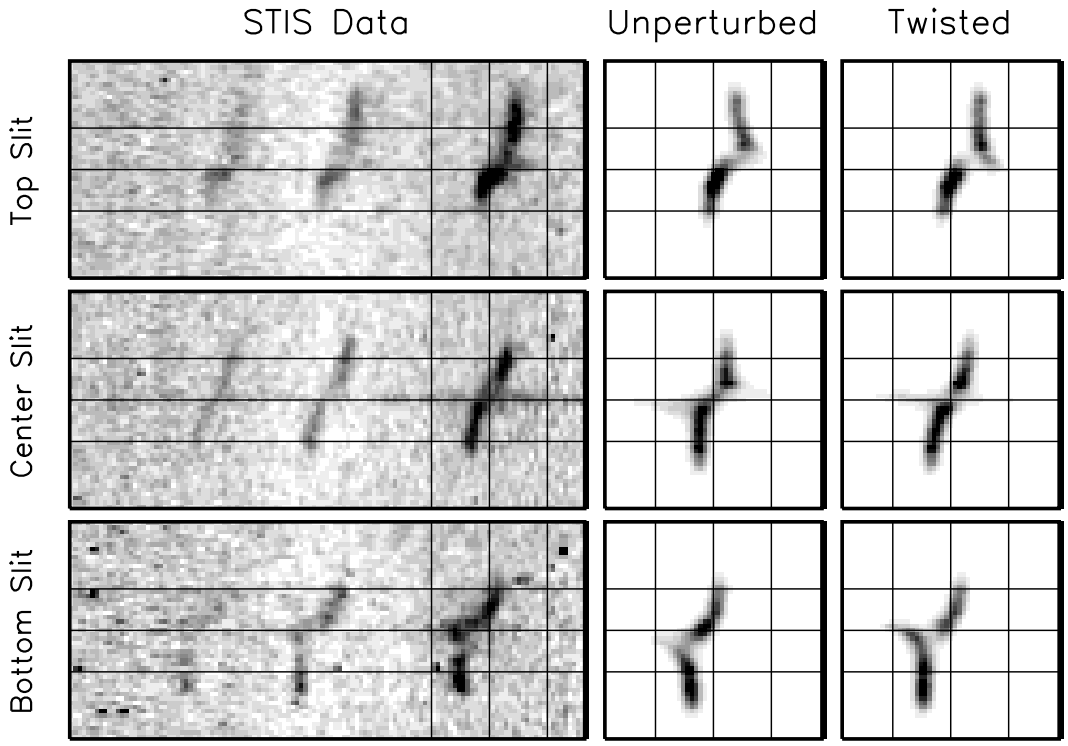

Figure 4.6: STIS longslit observations for all three slits (*left*), unperturbed model (*center*), and a twisted model (*right*). Lines have been added to guide the eye. In all images, wavelength is on the horizontal axis and distance on the vertical axis, with the galaxy center along the middle horizontal line. In the STIS data, the emission lines from left to right are [NII] λ6548, Hα, and [NII] λ6584. The main differences between the two models are the spatial positions of the peak velocity in the top and bottom slits, the shape of the spatial variation in velocity, and the ability to reproduce intensity variations across the slits. See text for further discussion of the models.

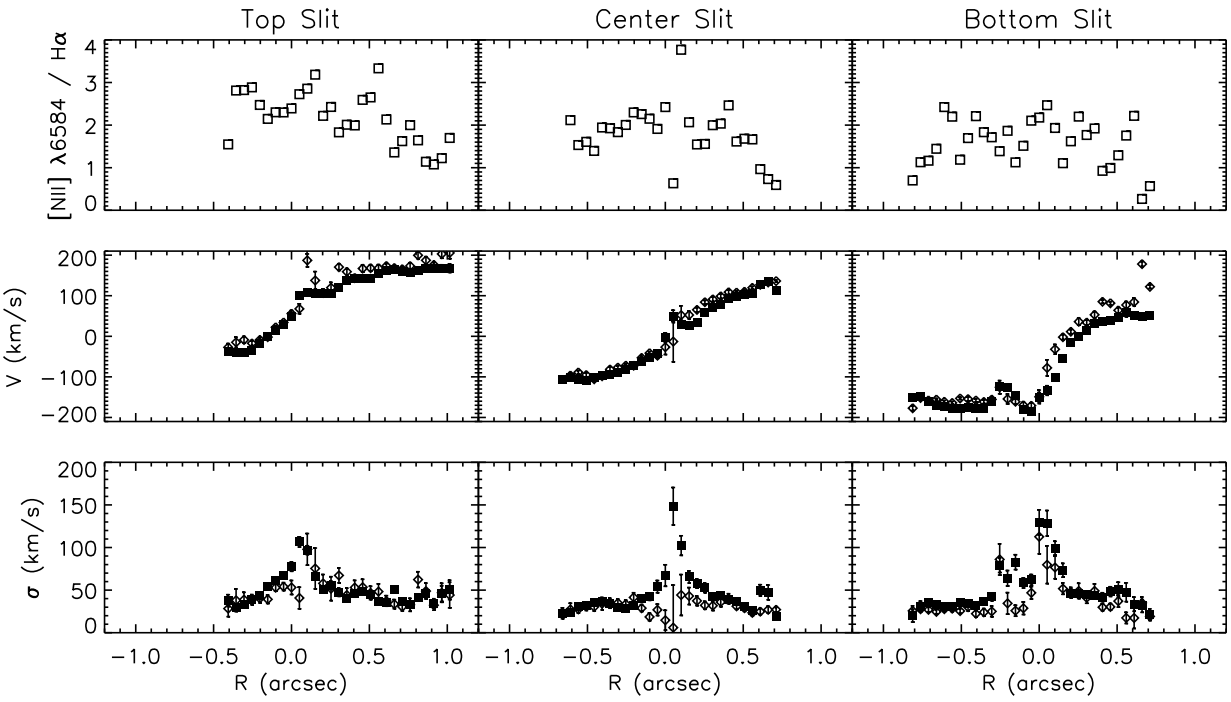

Figure 4.7: Results of kinematic extraction for the [NII] λ6584 (*closed squares*) and Hα (*open diamonds*) emission lines, for all three slits. Shown here are the ratio of [NII] λ6584 emission line flux to Hα emission line flux (*top row*), and the extracted velocities (*middle row*) and velocity dispersions (*bottom row*).

Hα velocity dispersion, in particular, is consistently lower than that of [NII]. A kinematic extraction that links the velocity and/or dispersion of the [NII] component of this disk to that of Hα component would therefore introduce a bias in the kinematics. We consequently restrict our kinematic measurements to those of the highest signal line, [NII] λ6584.

4.3.4 Stellar Kinematics

Using the pPXF method, we attempted to measure the central stellar kinematics using the STIS data, after careful masking of the emission features. However, the kinematic extraction has to rely mainly on the Hα absorption feature, which is almost completely filled with gas emission. For this reason, the accuracy on these measurements is modest and very sensitive to systematic effects, making the error bars significant ($\pm$40 km s^{-1} in the velocity dispersion).

Gebhardt et al. (2000b) also obtained *HST* stellar kinematics in the center of NGC 3379 with an FOS pointing, from which they measured $v = 0 \pm 14$ km s^{-1}, $\sigma = 289 \pm 13$ km s^{-1}, $h_3 = 0.11 \pm 0.04$, and $h_4 = 0.04 \pm 0.04$. They note the skewness of the LOSVD and attribute the non-zero h_3 value to the combined effects of miscentering of the aperture during the peak-up procedure and significant dust absorption in the central regions of the galaxy. Interpreting these kinematics is therefore a somewhat complicated process.

The STIS and FOS stellar kinematics are not inconsistent with the SAURON and OASIS measurements described in §4.2.3; however, the large errors in the STIS kinematics and the effects of dust in the FOS kinematics limit their usefulness in stellar dynamical modeling. Thus while the STIS emission line kinematics are critical for our gas dynamical modeling in §4.6, the absorption line kinematics add few constraints, and much uncertainty, to the stellar models, and we do not include them in those models.

4.4 Stellar Dynamical Modeling: Method

4.4.1 Axisymmetric Model Construction

To model the orbital structure of NGC 3379 and obtain a stellar dynamical black hole mass estimate, we construct general stationary axisymmetric models of the stellar component of the galaxy. These three-integral models are based on the Schwarzschild (1979, 1982) orbital superposition method, further developed by Richstone & Tremaine (1988), Rix et al. (1997), and van der Marel et al. (1998). This technique has been widely used to generate axisymmetric models of galaxies to determine galaxies' SMBH mass, mass-to-light (M/L) ratio, and orbital distribution and is thoroughly described in the literature by the aforementioned authors as well as by other groups (e.g. Gebhardt et al. 2003; Thomas et al. 2004; Valluri et al. 2004; Cappellari et al. 2006).

We use the implementation of Cappellari et al. (2006), with which they modeled a subsample of the SAURON early-type galaxies. This method proceeds in four steps. First,

the MGE parameterization is analytically deprojected and converted to a stellar potential, using an assumed shape (axisymmetry) and a constant stellar M/L ratio. In the second step, a representative orbit library is constructed by integrating a large number of orbits in this potential. Orbits are sampled evenly across observable space, such that their starting points are also varied over the three integrals of motion (energy E, angular momentum L_z, and non-classic third integral I_3). This grid covers >99% of the total luminous mass of the galaxy, with the radii sampled logarithmically from $0.01''$to $400''$. During the third step, these orbits are integrated and projected into the plane of observables, namely the x' and y' locations on the sky and the line-of-sight velocity distribution. This is done taking into account convolution with the PSF and aperture binning. The final step consists of using non-negative least-squares (NNLS, Lawson & Hanson 1974) fitting to determine the set of weights for each orbit such that the sum of the orbits in a given bin best reproduces the observed kinematics and stellar density in that bin.

This model implementation has been tested by Krajnović et al. (2005), who used it on SAURON observations to measure the inclination, M/L ratio, and integral space structure of NGC 2974. They evaluated the robustness of this method in recovering input parameters with a constructed two-integral (E and L_z) test galaxy. While they found that the model effectively recovers mass-to-light ratio and orbital structure, they note that the determination of their test galaxy's inclination is potentially degenerate, in that the differences between models of various inclinations are small with respect to realistic observational error estimates.

4.4.2 Application to NGC 3379

In the case of NGC 3379, the SAURON data consist of 1603 bins and the OASIS data of 344 bins. Prior to modeling, anomalous bins are flagged to be omitted from symmetrization and fitting. In practice, two SAURON bins (with a foreground star) and one OASIS bin (with a bad pixel in the middle of the Mg b feature) are omitted. With 6 LOSVD moments and the intrinsic and projected mass at each bin, there are thus 15552 observables. These data are then symmetrized using the mirror-(anti-)symmetry of the kinematic field and averaging the kinematic values from four symmetric points around the major and minor axes. Due to the irregular shape and distribution of the Voronoi bins, there are sometimes no bins at one of the symmetric positions; in this case, the value of the position is interpolated from surrounding bins. During this process, the error bars remain unchanged, since the number of data points has not been altered. The full, symmetrized SAURON and OASIS fields are presented with the model results in the following section.

As in Cappellari et al. (2006), the Schwarzschild model uses an orbit library constructed with 21 energies, and 8 angular and 7 radial values at each energy. We employ a 'dithering' method, which combines a large number of orbits ($6^3 = 216$) with different but adjacent initial conditions to allow the model to reproduce the observed (smooth) distributions. The final galaxy model is thus made with 21 x (8-1) x 7 x 2 x 6^3 = 444,528 different orbits, divided into 2058 groups of 216 orbits before the NNLS fitting. (The (8-1) accounts for duplication of angular values when symmetries are considered, and the additional factor of

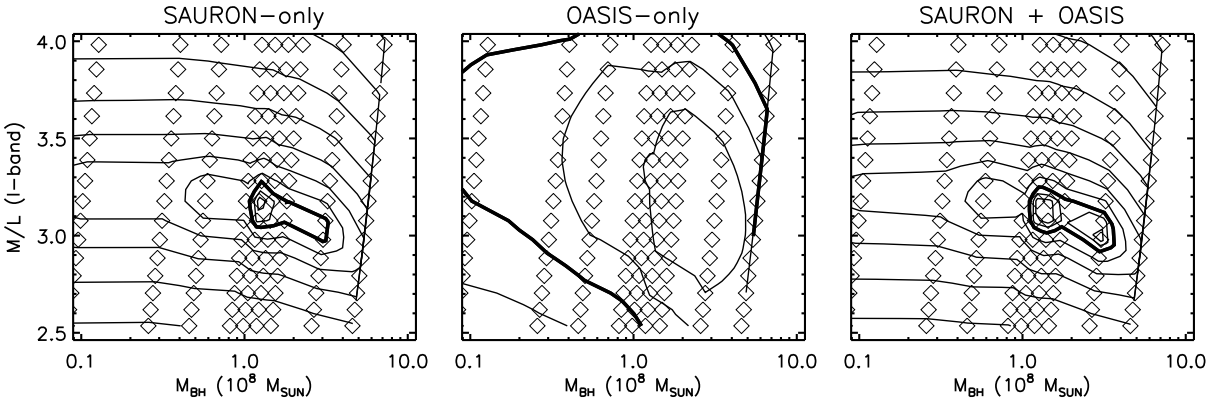

Figure 4.8: χ^2 contours for the SAURON-only models (*left*), OASIS-only models (*middle*), and the models using the full, combined data set (*right*). M/L is measured in solar units. Diamonds indicate locations where models were constructed. The thin lines are contours of integer values of the standard deviation, and thick contours indicate 3σ. Models at M_{BH}=0 were also constructed but are not shown here; in all cases, those models are excluded to at least 4σ.

2 accounts for positive and negative L_z.) We follow Verolme et al. (2002) in adopting a regularization parameter of $\Delta = 4$, which imposes smooth variation in integral space. Given recent concerns about the effects of regularization (e.g. Valluri et al. (2004); see §4.8.2 for a full discussion), we also generate a set of test models with no regularization ($\Delta = 1 \times 10^3$) to ensure that the derived black hole mass is not dependent on this parameter.

Each dynamical model requires three input parameters, namely the galaxy's inclination, the stellar M/L ratio, and the mass of the central SMBH. The values of these parameters are estimated by constructing models with various values for all three parameters and then determining which model best reproduces the stellar kinematics and mass distribution in the χ^2 sense. In the case of NGC 3379, several stellar dynamical models have already been constructed, some of which indicate that this galaxy is likely seen edge-on (Gebhardt et al. 2000b). However, the inclination of this galaxy has been the source of much debate, including suggestions that it is instead a face-on S0 (Capaccioli et al. 1991; Statler & Smecker-Hane 1999; see also §4.8.2). Subsequent models by Statler (2001), on the other hand, find that the most probable inclination is more moderate, at $i \approx 40°$. With the MGE surface brightness parameterization, we can set a lower limit on the inclination of $i = 35°$ from the deprojection of the narrowest Gaussian component. Following previous stellar dynamical results, we construct our primary set of models at $i = 88°$ (to avoid possible numerical artifacts at exactly 90°), but we supplement these with relatively face-on models at $i = 50°$ to test the effects of inclination on the black hole mass measurement. In both sets of models, we vary the M/L ratio and M_{BH} to fit the combined SAURON and OASIS data sets and investigate the internal structure of NGC 3379.

4.5 Stellar Dynamical Modeling: Results

4.5.1 Best-Fitting Models

The χ^2 results from the edge-on stellar dynamical model are shown in the right panel of Figure 4.8, with the best-fitting model being described by a black hole of mass $1.4^{+2.6}_{-0.2} \times 10^8$ $M_\odot$ and with $M/L = 3.08 \pm 0.2$ $M_\odot/L_\odot$ (errors are 3σ). The model predictions for the SAURON and OASIS kinematic fields are compared to the data in Figures 4.9 and 4.10 respectively; in general, these models do a very satisfactory job of reproducing the observations.

As a test of the effect of data resolution and spatial coverage on model results, we also ran models with the SAURON and OASIS data sets individually and show the resulting χ^2 contour plots in Figure 4.8. (We call these models the SAURON-only model, which fits the SAURON data and merely predicts the OASIS kinematics, and the OASIS-only model, which fits only the OASIS data and predicts the SAURON kinematics.) Both of these supplementary models have a best-fitting black hole mass and M/L consistent with the model constructed using the combined data sets.

While it is clear that the wide-field SAURON data play the dominant role in constrain-

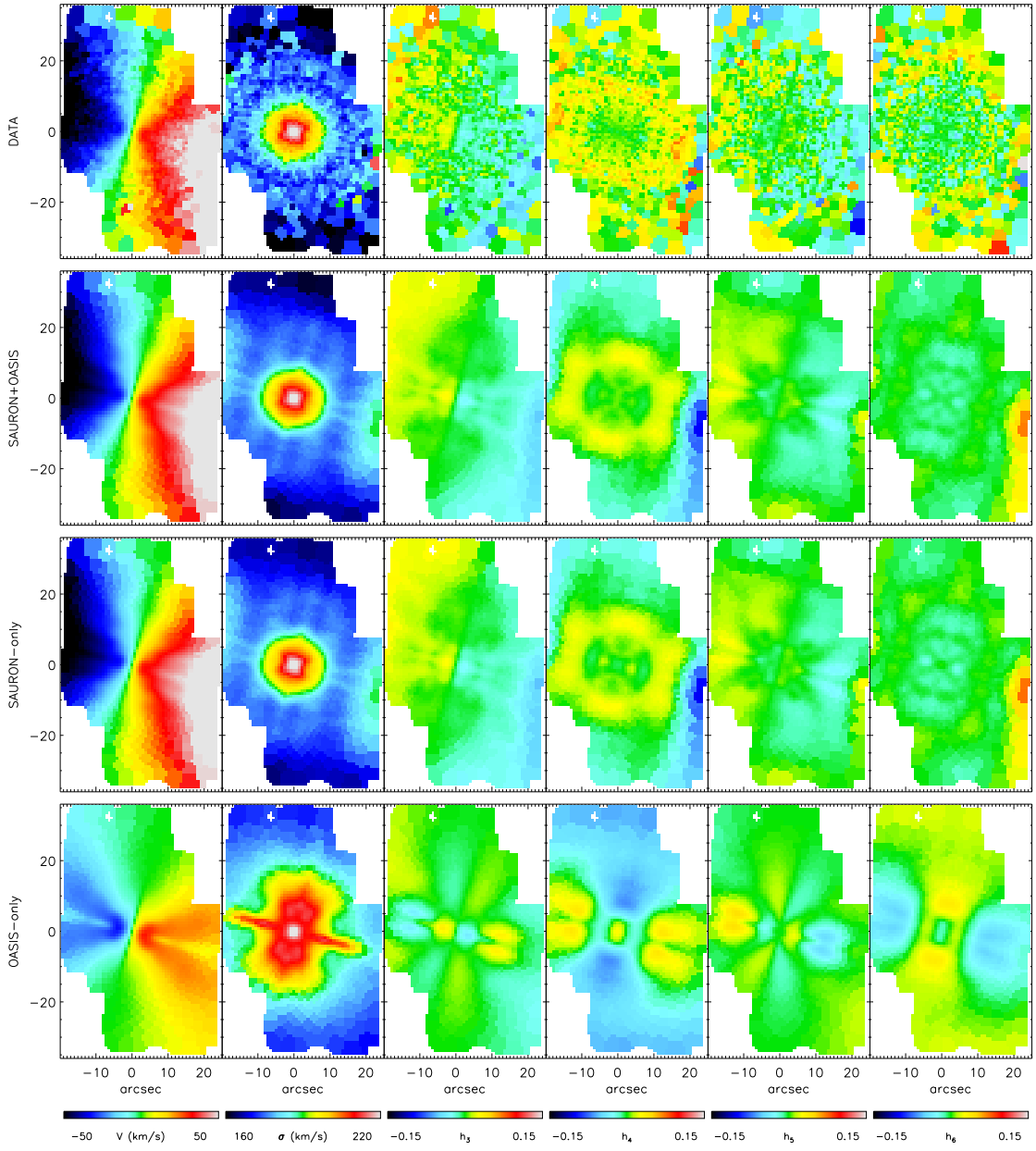

Figure 4.9: *From top to bottom:* The SAURON symmetrized kinematic data, the best-fitting model with both the SAURON and OASIS data fitted, the model that best fits only the SAURON data, and the predictions for the SAURON field from the model that best fits only the OASIS data. The model that uses only the SAURON data differs little from the model using the combined data set. The model that uses the OASIS data set suffers greatly from the lack of constraints outside 5″and consequently generates an unphysical orbital structure. (Note that the high velocity region at $x \sim 0''$, $y \sim -20''$ in the data is a foreground star and is masked during the modeling.)

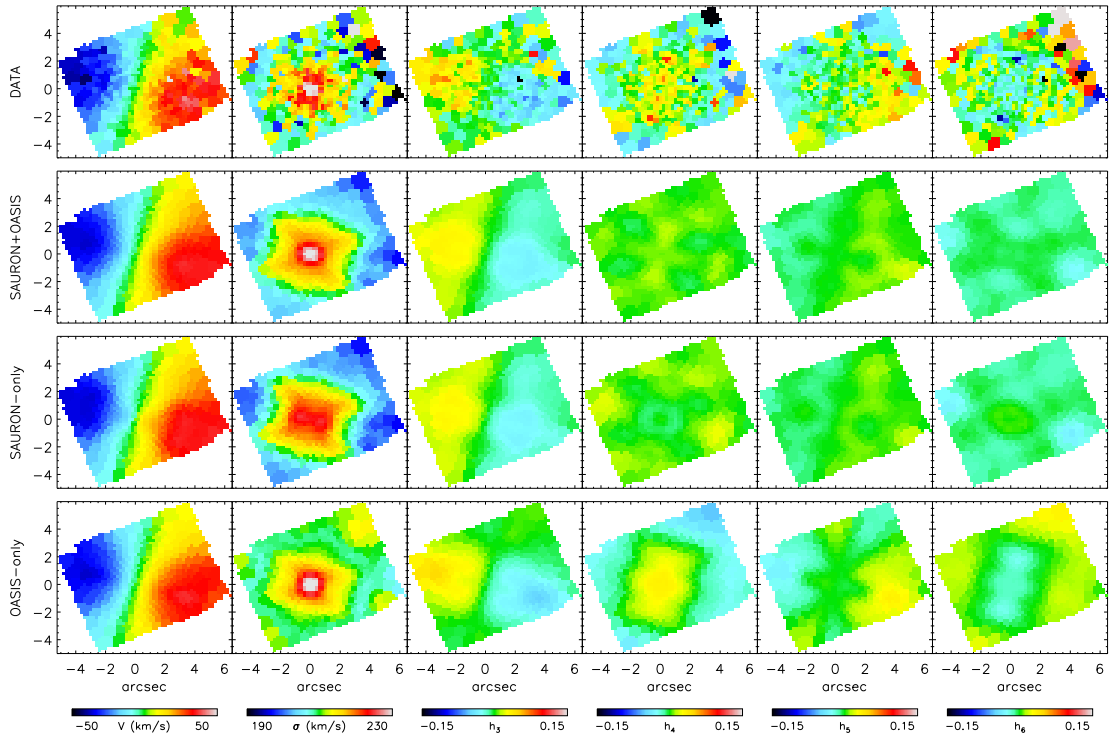

Figure 4.10: Analogous to Figure 4.9, except here the third row from the top is a prediction of the OASIS kinematics from the model fitting only SAURON data, and the bottom row is the fit to the OASIS kinematics from the model fitting only OASIS data. The model fitting only the SAURON data clearly underpredicts the central velocity dispersion, due to the lack of high resolution kinematics in the vicinity of the black hole. The model fitting only the OASIS data, on the other hand, has such freedom with the orbital structure that it reproduces nearly all the features in the fields, including some of the noise. Note that contour levels on the velocity dispersion have been rescaled from Figure 4.9 to aid the eye.

ing the stellar M/L, it is rather remarkable that these data are also able to constrain the black hole mass so well, given that the sphere of influence $R_{\rm BH} \sim 0\farcs29$ is well below the resolution and seeing limit of the SAURON observations. This black hole mass measurement must therefore be due to minute differences in the model predictions for the center-most spatial element. This is apparent in Figure 4.11, which shows the model velocity dispersions for different in black hole masses; the central regions of SAURON field display almost no detectable difference in velocity dispersion for extremely large variations in black hole mass (and likewise for other moments of the velocity distribution). This ability of the SAURON data to discriminate between such similar models speaks to the high quality of the data ($S/N_{\rm center} \approx 560$), but care must be taken when further interpreting these results. Figure 4.10 shows that the best-fitting SAURON-only model drastically underpredicts the central velocity dispersion observed in the higher resolution OASIS data. Thus, while the SAURON-only model is able to constrain the black hole mass, the lower spatial resolution of these data, and their correspondingly poor sampling of the black hole's sphere of influence, render them incapable of correctly measuring the central orbit structure. This is even more clearly seen in Figure 4.12; the higher resolution OASIS data, even in a model without a black hole, require a more physical (centrally-peaked) velocity dispersion distribution than that predicted for the OASIS field by the SAURON-only model. This test is a simple example of both the strengths and limitations of using data of insufficient resolution to study the central regions of galaxies; with high-quality data it may be possible to obtain accurate black hole masses, but it would be inadvisable to use those results in a more detailed discussion of the stellar dynamics in the galaxy center.

The OASIS data, on the other hand, have higher spatial resolution than the SAURON data but also have dramatically lower spatial coverage. The ability of the OASIS data to resolve the black hole's sphere of influence in two dimensions ensures that varying black hole masses will have noticeable effects on the predicted stellar kinematics. At first, it is therefore a bit surprising that the χ^2 contours for the OASIS-only models (Figure 4.8) are so broad and that the OASIS data alone are incapable of measuring the black hole mass with much significance. Figure 4.9 immediately resolves this issue; the lack of spatial coverage in the OASIS data gives the model complete freedom to vary the orbital distribution throughout the galaxy, since it is constrained only in the central few arcseconds. The predictions for the SAURON (wide-field) data from the OASIS-only models are utterly unrealistic, since models with so much freedom in the galaxy's orbital structure can not be depended upon to accurately extrapolate to large scales. However, when the SAURON data are included as constraints on the large-scale structure of the galaxy, the OASIS data are a powerful probe of the black hole mass. As shown in two dimensions in Figure 4.12 and along the major axis with errors in Figure 4.13, inspection alone is sufficient to locate the best-fitting model when the combined SAURON and OASIS data sets are used. This suggests that the best-fitting model from the combined data sets also provides an accurate representation of the stellar orbit structure in the central regions of the galaxy. To test this hypothesis, this best-fitting model was used to predict the higher spatial resolution STIS and FOS stellar kinematics, and these predictions were completely consistent with those measurements. The ability of

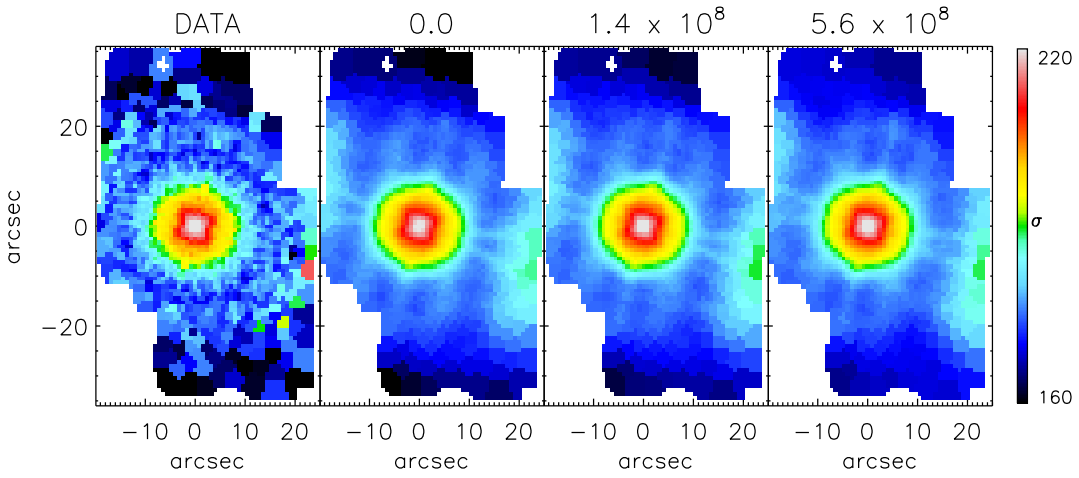

Figure 4.11: Velocity dispersions (in km s^{-1}) as observed in the SAURON field (*left*) and as modeled with varying black hole masses (indicated above each model, measured in $M_\odot$). Due to the small sphere of influence of any SMBH (on the scale of a SAURON pixel in all cases), differences between the various models occur only in central pixel and are nearly undetectable. The models shown here are for the SAURON+OASIS data set; however, the results for the SAURON datacube from the SAURON-only model are virtually identical. In both cases, the dispersion of the central pixel alone is sufficient to constrain the black hole mass.

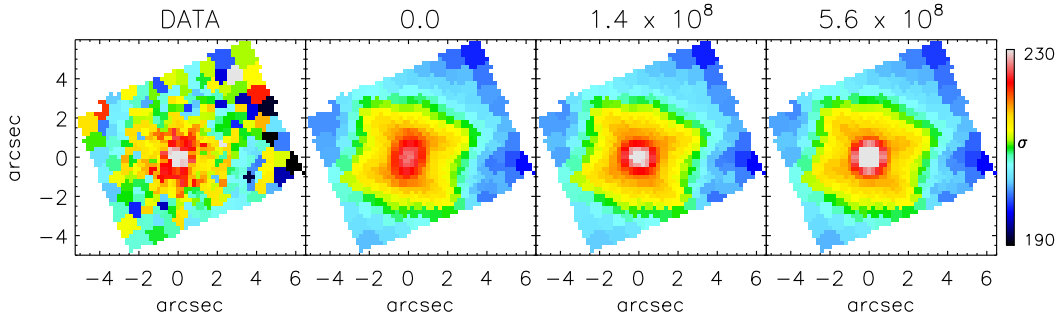

Figure 4.12: As in Figure 4.11, but for the OASIS field instead. The high resolution OASIS data probe the black hole's sphere of influence and thus provide significant leverage in measuring the mass of the SMBH. The black hole mass is constrained almost entirely by the velocity dispersion (displayed here); this is demonstrated explicitly in Figure 4.13. The models shown reflect the SAURON+OASIS model; as is clear in Figure 4.9, the OASIS-only model is unable to properly constrain the orbital structure and is therefore useless in this sort of comparison.

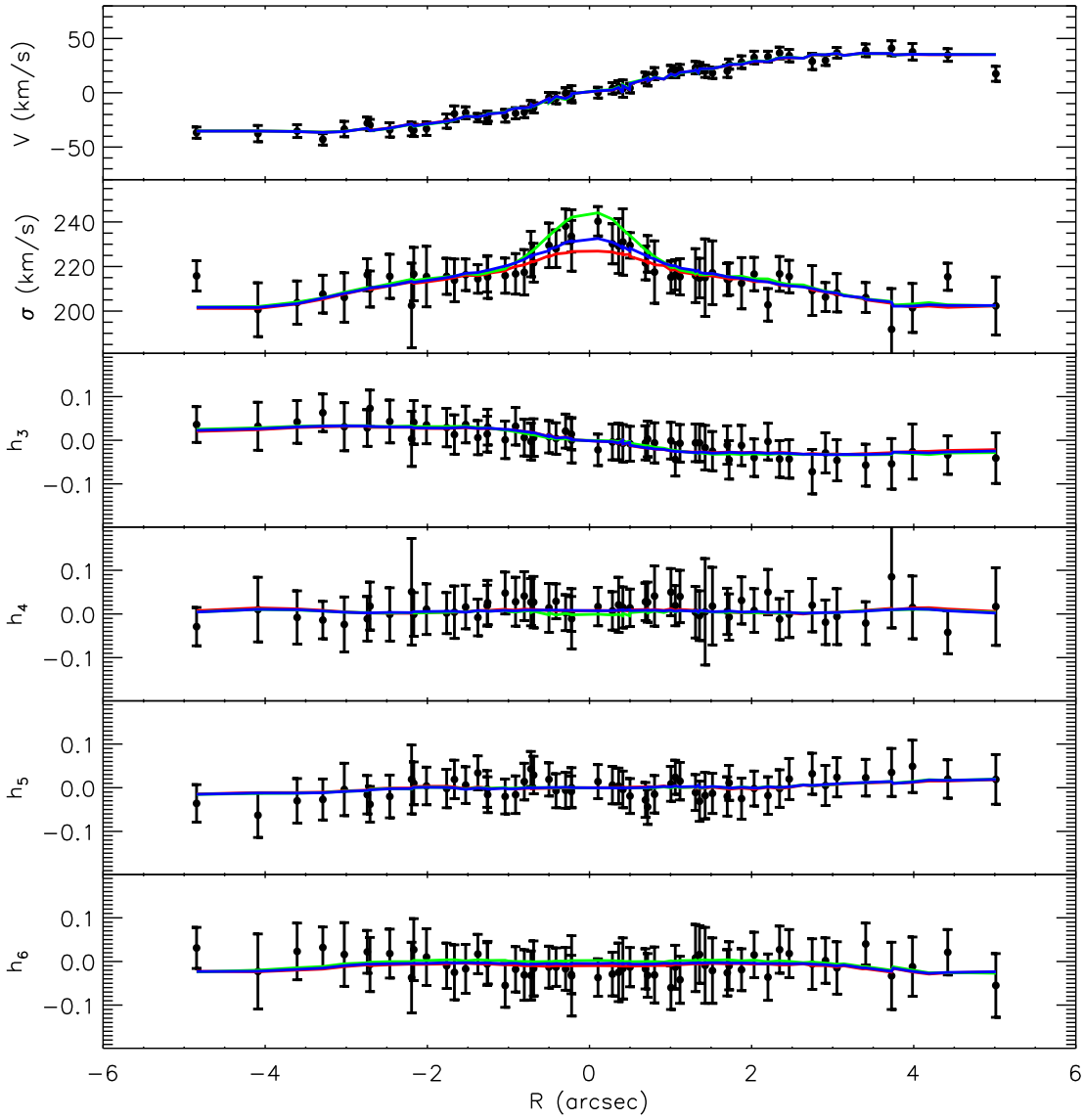

Figure 4.13: OASIS kinematics along the major axis, compared to models of several SMBH masses: 0 (*red*), 1.4×10^8 $M_\odot$ (*blue*), 5.6×10^8 $M_\odot$ (*green*). The velocity dispersions clearly provide the main constraint in measuring the black hole mass. The models shown reflect the SAURON+OASIS model. The model fits all the data points well within the error bars. This is because the plotted kinematics having been bi-symmetrized for input into the Schwarzschild model (see §4.4.2). This reduces the scatter between adjacent points, but the error bars remain unaltered, since the number of data points is unchanged. The unsymmetrized data are shown in Figure 4.1.

the OASIS data to resolve the black hole sphere of influence therefore provides sufficient constraints on the central stellar orbit structure that the predicted stellar dynamics from this model can be extrapolated to much smaller scales.

Neither the results from the SAURON-only model nor those of the OASIS-only model are unexpected; similar results were seen by Copin et al. (2004) in their models of NGC 3377 using SAURON and OASIS data for that galaxy. They found, as here, that the wide-field SAURON data are critical in constraining M/L; however, unlike this study, they also found that the SAURON data alone were unable to provide useful limits on the SMBH mass in NGC 3377. This difference is likely due to the combined effects of a slightly lower S/N in their SAURON data and worse seeing during those observations, which conspire to render the NGC 3377 SAURON data not quite sensitive enough to tiny differences in the predicted central velocity dispersions for varying black hole masses. Their results with the OASIS data, on the other hand, are identical to those here; taken alone, their OASIS data were able to exclude the no-black hole scenario to high significance but otherwise provided few constraints. They conclude that only the combined data set, with both high resolution data and wide-field data, is capable of determining both M/L and M_{BH}, as also seen here in Figures 4.9 and 4.10.

Gebhardt et al. (2003) and Krajnović et al. (2005) have also tested the effects of spatial resolution and coverage, respectively. Gebhardt et al. (2003) measured the black hole masses in 12 nearby elliptical galaxies with stellar dynamical models, using combined *HST* and ground-based data and also using ground-based data alone. They found that the ground-based data yield a black hole mass consistent with that from the combined data set, but at a reduced significance. Their high-resolution *HST* data were needed to probe the spheres of influence of the black holes, which mimics the need for OASIS seen here. They also note that models using *HST* data alone were unable to constrain the LOSVD at large scales, as seen here with the OASIS-only model. To study the effect of spatial coverage in more detail, Krajnović et al. (2005) constructed a series of models of a two-integral test galaxy with simulated SAURON data out to 1 and 2 R_e. Their results indicated that the orbital structure was recovered well by both models. As the SAURON data of NGC 3379 extends to roughly 1 R_e ($= 42''$, Cappellari et al. (2006)), the tests of Gebhardt et al. (2003) and Krajnović et al. (2005) illustrate that these wide-field data are both necessary and sufficient to measure the orbital structure of NGC 3379 on large scales. When combined with the OASIS data, which resolves the black hole's sphere of influence, the model can reliably measure the galaxy's orbital structure on both small and large scales.

Since there has been significant recent debate concerning the effects of regularization on black hole mass measurements, we generated a set of models for the SAURON+OASIS data set without smoothing in integral space ($\Delta = 1 \times 10^3$). The results are completely consistent with those of the $\Delta = 4$ models; there is perfect agreement on the black hole mass, mass-to-light ratio, and velocity distribution (presented in the following section). The uncertainties on these measurements are similar for the $\Delta = 4$ and $\Delta = 1 \times 10^3$ models, with those of the non-regularized models being slightly smaller. This simple test thus demonstrates that including moderate regularization of $\Delta = 4$ in the models is not driving the results and

consequently does not impact our conclusions (see also §4.8.2 for further discussion).

As a final test of the robustness of these results, we examined the effects of our assumed inclination on the measured black hole mass. In addition to the edge-on models presented above, we generated a series of models near the minimum possible inclination. Deprojection of the MGE model places a strict minimum of 35° on the inclination; however, inclinations of less than $\sim 45°$ require that the axial ratio of many of the Gaussian components be smaller than 0.2, implying that the galaxy is a thin disk. We therefore adopt a test inclination of i=50°, and the results are shown in Figure 4.14. Although the edge-on configuration is formally a better fit to the data, the tests of Krajnović et al. (2005) indicate that inclination determinations may be degenerate, and we restrict our interpretation of this result to noting that the assumed inclination plays a role in the measured black hole mass at the 50% level. Similar levels of dependence has been previously observed by e.g. Gebhardt et al. (2000b) for this galaxy and Verolme et al. (2002) for M32. Because of the potential degeneracy in the determination of inclinations, we cannot claim a definitive measurement of the inclination of NGC 3379, and we therefore marginalize over the two tested inclinations in our error estimates. This constrains the black hole mass to $1.4^{+0.3}_{-0.8} \times 10^8$ $M_\odot$ (1σ), or $1.4^{+2.6}_{-1.0} \times 10^8$ $M_\odot$ (3σ). For our analysis of the model results, we use the best-fitting model, which has i=88°, M/L=3.08, and M_{BH}=1.4×10^8 $M_\odot$.

4.5.2 Stellar Dynamics Near the SMBH

The inclusion of the OASIS high-resolution two-dimensional data in the stellar dynamical models provides us with the unique opportunity of probing the stellar velocity distribution in three dimensions in the vicinity of the central SMBH. By measuring the kinematics of the solution set of orbits, we can study the full three-dimensional motions of stars. In particular, we examine the velocity ellipsoid, the shape of which has been linked to the steepness of the central surface brightness profile (i.e. "cusp" or "core") and the nature of the central SMBH (i.e. single object or binary system, see Quinlan & Hernquist 1997; Gebhardt et al. 2003).

Figure 4.15 shows the ratio of the radial velocity dispersion σ_r of the stars to the their tangential velocity dispersion (σ_t, defined as $\sigma_t^2 = (\sigma_\phi^2 + \sigma_\theta^2)/2$) over all observed radii. Note that σ_ϕ includes only random, and not ordered, motion such that an isotropic distribution is characterized by $\sigma_r = \sigma_t$. In NGC 3379, the anisotropy profile shows a mild radial anisotropy throughout most of the galaxy. Within R_c, down to the limit of our spatial resolution, the distribution is consistent with isotropy.

However, in other core galaxies, the velocity distribution within R_c has been observed to be tangentially biased (Gebhardt et al. 2003), and this correlation has been hypothesized to be the fossil remnant of a binary black hole in the galaxy center. In this picture, during the merger of two large galaxies with SMBHs, the black holes fall to the center of the potential well through dynamical friction and form a binary. Stars with radial orbits then pass close to this binary and are ejected at much higher velocities, allowing the binary to lose energy and shrink in size. This process both reduces the number of stars in the center-most regions of the galaxy, creating a lower-density "core," and preferentially removes stars on radial orbits,

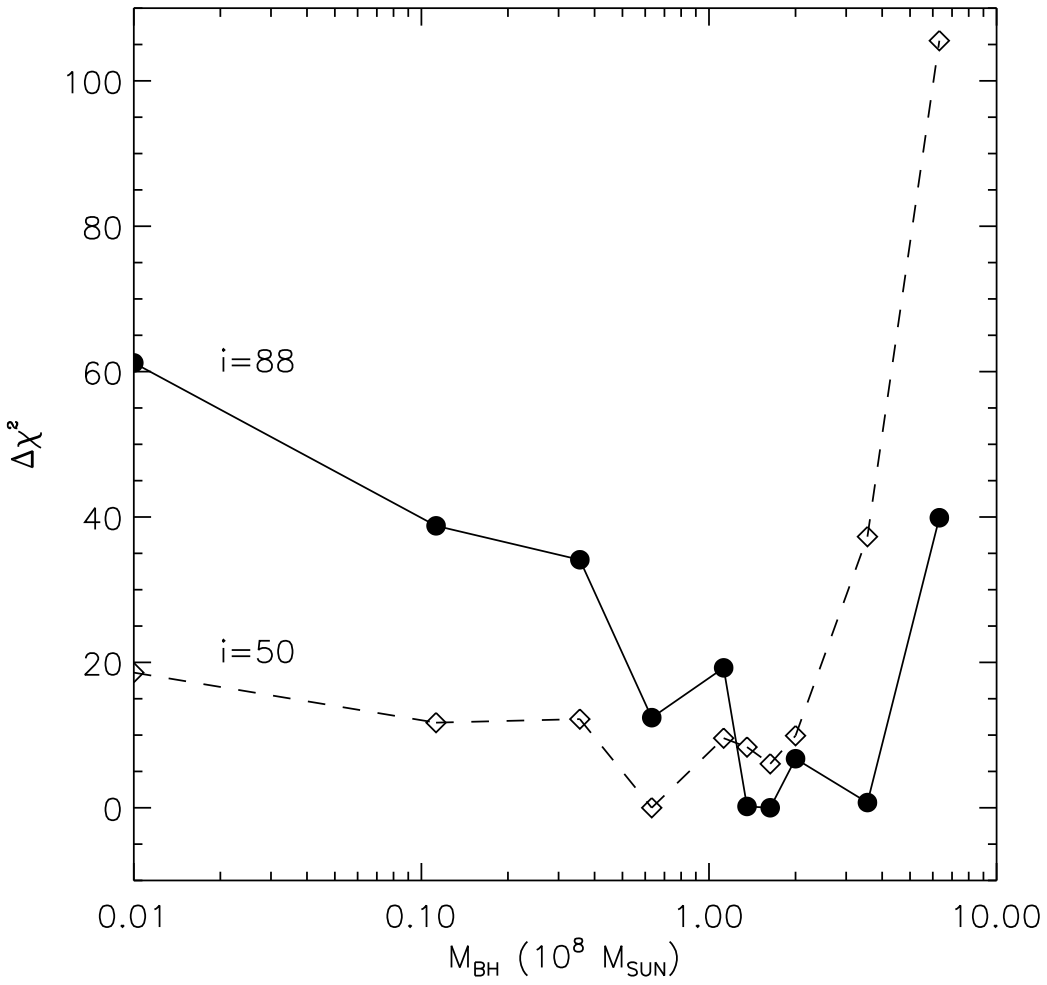

Figure 4.14: χ^2 as a function of black hole mass, marginalized over M/L, for the two tested inclinations. 10^6 $M_\odot$ has been added to the no-black hole model in order to include it on the log scale. The derived best-fitting black hole masses vary by 50% between the two inclinations.

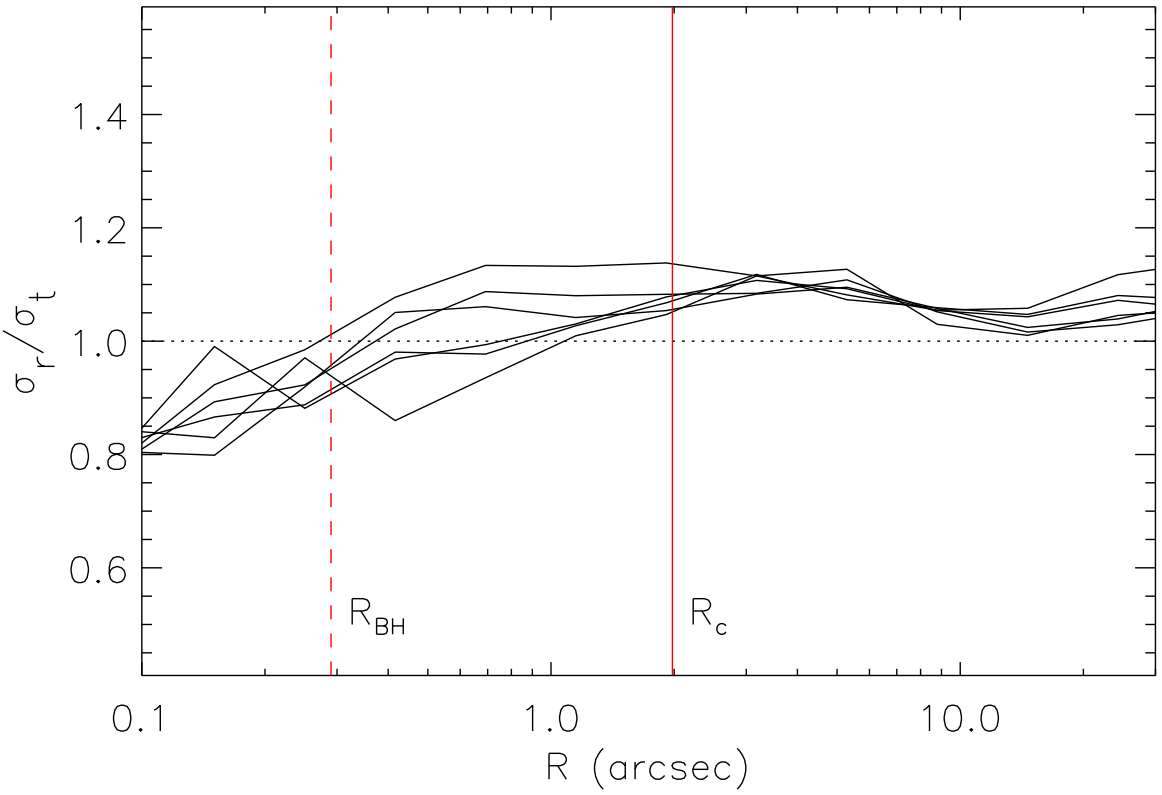

Figure 4.15: Velocity anisotropy of NGC 3379 as a function of radius along the angular sectors sampled in the Schwarzschild model. The dashed line marks $R_{\rm BH}$ (=0.″29) and the solid line marks R_c (=1.″98). The galaxy is characterized by mild radial anisotropy, tending towards isotropy within R_c. (The trends shown here are also seen in the model with $\Delta = 1 \times 10^3$ and in the model at i=50°.)

creating a strong tangential bias in the velocity ellipsoid (Quinlan & Hernquist 1997).

In detailed models of such systems, Milosavljević & Merritt (2001) have indeed shown that the formation and evolution of a hard black hole binary in a galaxy center is accompanied by a change in the surface brightness profile from power-law to core and by a central tangential anisotropy whose spatial extent increases with time from $R_{\rm BH}$ to R_c (see their Figures 7 and 16). As NGC 3379 has a very strong core in its surface brightness distribution, the results shown in Figure 4.15 make this galaxy not obviously explained by these simulations. This discrepancy may be due to multiple merger events during the galaxy's history, which would then make it difficult to directly compare the details of the simulations and the observations (Milosavljević & Merritt 2001).

4.6 Gas Dynamical Modeling: Method

4.6.1 Basics

To model the gas kinematics in the central gas disk of NGC 3379 and thus measure the mass of the central SMBH, we assume that a thin disk in circular motion is a reasonable description of the system. This method has been commonly used to model nuclear gas disks (e.g. Macchetto et al. 1997; van der Marel & van den Bosch 1998; Bertola et al. 1998; Barth et al. 2001), and it has been described extensively by those authors.

In the case of NGC 3379, Figure 4.4 shows the gas disk major axis to be at PA $\sim 118°$, approximately 45° away from the rotation axis of the stars, a configuration that is seemingly inconsistent with the gas being on stable circular orbits. However, both the MGE surface brightness parameterization and previous dynamical models (e.g. Statler 2001; Gebhardt et al. 2000b) suggest that NGC 3379 is intrinsically quite round, especially in the central regions, where the projected axial ratio $q' > 0.9$. In such a nearly spherical potential, there are no strongly preferred axes and therefore hardly any torques on a gas disk, regardless of its orientation. Consequently, the disk in NGC 3379 is likely to be stable on a timescale much longer than its rotation period, allowing the gas to settle into circular orbits in a thin disk.

To model this disk, we can therefore use the thin-disk method of the aforementioned authors. Briefly, from that assumption, it follows that the gas disk is rotating solely under the combined gravitational influence of the black hole and of a stellar potential. The velocity contribution from the enclosed stellar mass is determined by using the MGE surface brightness model in combination with a constant I-band stellar mass-to-light ratio. The resulting disk velocity field is then projected on to the plane of the sky by assuming an inclination $i_{\rm disk}$ of the disk. The projected line-of-sight velocities of the disk are therefore parameterized by only three variables: M_{BH}, the stellar M/L, and $i_{\rm disk}$.

This ideal velocity field is then made more physical by accounting for gas velocity dispersions and for surface brightness variations across the field. Since the mechanism responsible for the gas velocity dispersions is not understood, we fold a simple parameterization for the

dispersions into the model (§4.6.2). The resulting velocity field is then weighted by the Hα surface brightness, using the Hα+[NII] WFPC2 image (§4.6.3).

We simulate observations of the disk through the STIS instrument to achieve the best possible match to the data. Three slits are placed on the velocity field, with their locations described by a position angle relative to the major axis of the gas disk and by a spatial position relative to the galaxy center. There are thus six parameters in our model: M_{BH}, M/L, disk inclination, position angle of the slits, and x- and y-coordinates of the slit positions. To measure the black hole mass in NGC 3379, we constrain these parameters as best as possible and then construct models with varying values of these parameters and find the best match to the data in the χ^2 sense.

In practice, we used the procedures of Cappellari et al. (2002), which account for the finite STIS pixel size, instrumental broadening, and the STIS PSF. A model PSF was constructed using the TinyTim software (Krist 1993) for a monochromatic source at 6600 Å. We then modified the method of Cappellari et al. (2002) to include the slit effect (the velocity shift induced by the non-zero width of the slit and its projection on to the STIS CCD) as in Barth et al. (2001), and also to use the WFPC2 Hα+[NII] image (rather than an analytic formula) as a description of the gas surface brightness. The result of the model calculation is a simulated STIS observation of the emission lines in NGC 3379, with the model emission lines having the same spatial and spectral dimensions as the STIS data. The kinematics of the model emission lines were extracted in exactly the same manner as was done on the actual STIS data, with single Gaussians being fit to the LOSVDs of individual rows.

4.6.2 Intrinsic Velocity Dispersion

The measured STIS ([NII] λ6584) kinematics shown in Figure 4.7 display significant velocity dispersions, which peak at over 100 km s^{-1} in all three slits. Preliminary models revealed that a black hole and instrumental effects were insufficient to account for such broadening in an unperturbed gas disk. This phenomenon has been observed previously in similar studies in a number of galaxies (e.g. Verdoes Kleijn et al. 2002). However, the responsible mechanism is currently not understood; the large line widths may result either from the non-gravitational motions of local turbulence, from a non-circular motion analogous to stellar asymmetric drift, or from unresolved rotation (e.g. van der Marel & van den Bosch 1998; Verdoes Kleijn et al. 2004).

In the case of the velocity dispersions being due to turbulence, the dispersions have minimal effects on the model, which consists of only gravitational and instrumental considerations. Under this assumption, we assign a constant (thermal) velocity dispersion of $\sigma = 20$ km s^{-1}, which corresponds to a temperature of $\sim 5 \times 10^4$ K.

Several authors (e.g. Barth et al. 2001) have constructed models with a similar methodology to that described here, both with and without an "asymmetric drift" term to account for the large dispersions. Barth et al. (2001) find that the addition of asymmetric drift provides a much more satisfactory fit to their observed dispersions (which peak at $\sim$ 150 km s^{-1}) and changes their best-fitting black hole mass by 12% (Barth et al. 2001). Since

our results include uncertainties much larger than this (§4.7), we do not include this term in our models, nor do we expect this omission to alter our results significantly.

In the case of NGC 3379, we find that the most satisfactory explanation of the high central dispersions is in fact that of unresolved rotation (see §4.7.3). In this case, a thermal velocity dispersion of $\sigma = 20$ km s^{-1} is sufficient to explain much of the observed velocity dispersion structure. However, due to the present limited understanding of gas velocity dispersions, a given model's ability (or lack thereof) to reproduce the observed velocity dispersions provides little insight into the accuracy of the model; for this reason, we do not include velocity dispersions when considering the goodness-of-fit of individual models.

4.6.3 Surface Brightness

Since the STIS data are of the Hα and [NII] λ6584 emission in the gas disk, a representation of the actual appearance of the gas disk at the Hα and [NII] wavelengths is required. The Hα+[NII] image (§4.3.1) is a good first approximation; however, this image includes the WFPC2 PSF. Since the surface brightness image (folded in with the model velocity field) will be passed through the simulated STIS optics, we ideally want an image of the gas disk without the influence of this PSF.

We created a model PSF for the F658N filter, generated at the pixel location of the galaxy center, using the TinyTim software (Krist 1993). Richardson-Lucy deconvolution was used to remove this PSF from the Hα+[NII] image. Due to the low signal and diffuse nature of the image, the deconvolution was stopped after 10 iterations; further iterations amplified the noise to an unacceptable level. The deconvolved Hα+[NII] image was then rotated to the same frame as the STIS data, using position angle information in the image headers. The center of the disk photometry is assumed to be spatially coincident with the location of the supermassive black hole (i.e., the center of the model velocity field).

While both the Hα+[NII] surface brightness and velocity dispersion play significant roles in the model, they contain little or no information about the possible presence of a central SMBH. Consequently, these quantities are omitted from the χ^2 calculation. To measure the black hole mass, we therefore computed χ^2 for each model by comparing only the extracted model velocities (measured as described in §4.6.1) with those of the data.

4.7 Gas Dynamical Modeling: Results

4.7.1 Unperturbed Models

Of the six parameters in the model (M_{BH}, M/L, i_{disk}, slit PA, and x- and y-locations of the slit), the values of four (i_{disk}, slit PA, and x- and y-locations of the slit) have been previously determined, from the WFPC2 photometry (§4.3.1), *HST* data headers, and STIS acquisition images (§4.3.2), respectively. Preliminary models indicated that the STIS gas kinematics are consistent with these values, so we do not fit for them. The STIS data provide

little leverage in determining M/L, given their incomplete spatial coverage of the gas disk. However, NGC 3379 has a well-measured M/L (3.08 $M_\odot/L_\odot$ in the *I*-band), both from the stellar dynamical model presented here as well as from other models (e.g. the Jeans model of Cappellari et al. 2006), and we adopt that value here. This leaves only one parameter, the black hole mass, that must remain free in the gas dynamical models. Models were therefore generated for a variety of black hole masses and compared to the data in the χ^2 sense.

Figure 4.16 presents results from those models, with a clear χ^2 minimum between 1×10^8 and 3×10^8 $M_\odot$. Models lacking a central black hole are strongly excluded, as are those with a black hole of mass greater than 3×10^8 $M_\odot$. The best-fitting model requires a black hole mass of $(2.0\pm0.1)\times10^8$ $M_\odot$ (3σ), and the emission lines corresponding to this fit are shown in Figure 4.6. The gas velocities and dispersions measured from these lines are compared to the STIS gas kinematics in Figure 4.17.

Despite the tight χ^2 minimum, a visual comparison of the best-fitting unperturbed model to the data is rather unconvincing. Most noticeable is the extreme overprediction of the velocity gradient at low radii in all three slits, which would seem to indicate a too-high black hole mass. Indeed, the velocity gradient of the model fails to match that of the data at nearly all radii. Furthermore, the model also slightly underpredicts the gas velocities at the edges of the disk (larger radii).

At the edges of the disk, the motion of the gas is mainly a reflection of the underlying stellar potential. A possible solution to the data-model mismatch may therefore be found in lifting the assumption of a constant M/L throughout the galaxy. In this case, a higher central M/L would increase gas velocities at the edges of the disk and simultaneously allow for a smaller black hole at the galaxy's center. Alternatively, the problem with the model may lie in the assumption of circular motion. In the data of both the top and bottom slits, the peak velocity occurs at a radius of nearly zero (see Figure 4.6). Given that the slit position angles are offset from the major axis of the gas disk, any model of purely circular motion will result in the peak velocities in the top and bottom slit occurring at non-zero radii. (This concept is elaborated on and illustrated in §4.7.3.) In the following sections, we draw on the combined constraints of the STIS and OASIS gas kinematics to test both of these possible solutions.

4.7.2 Fitting M/L

The gas velocities are most sensitive to stellar M/L variations outside the sphere of influence of the black hole, a region that is only marginally probed by STIS due to the large position angle offset of the slits (see Figure 4.4). The OASIS data, on the other hand, provide a more comprehensive view of the gas kinematics over the entirety of the gas disk. While stellar population studies suggest that there is no significant population gradient in the center of NGC 3379 (e.g. McDermid et al. 2006), for completeness we examine the possibility of a higher M/L in the central regions of this galaxy. To fit for the M/L, we use the OASIS gas data, which has complete coverage of the gas disk and consequently samples the gas velocities further from the black hole.

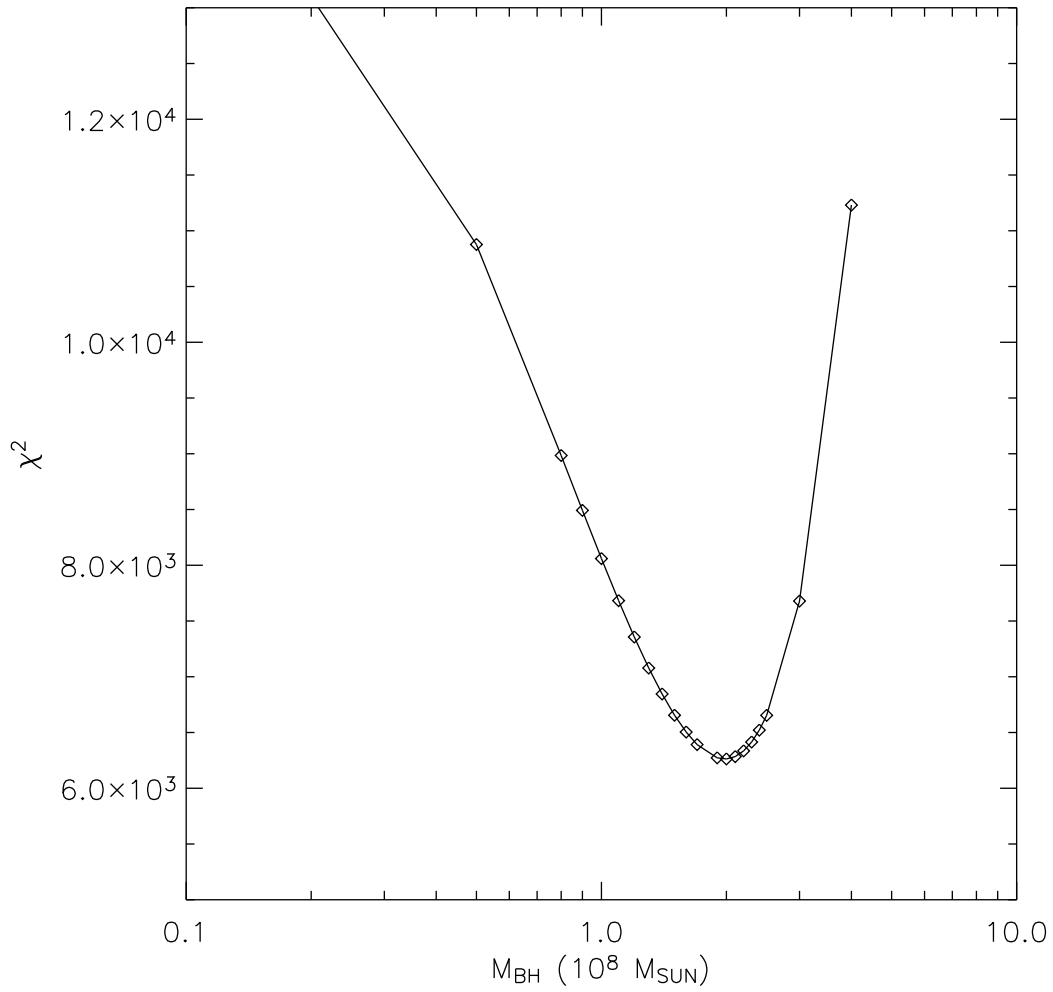

Figure 4.16: χ^2 as a function of black hole mass for the thin disk gas dynamical model. Points indicate individual models. With ~ 80 degrees of freedom, the reduced χ^2 for even the best-fitting model deviates significantly from unity. However, even this model is able to exclude the no-black hole scenario to over 6σ.

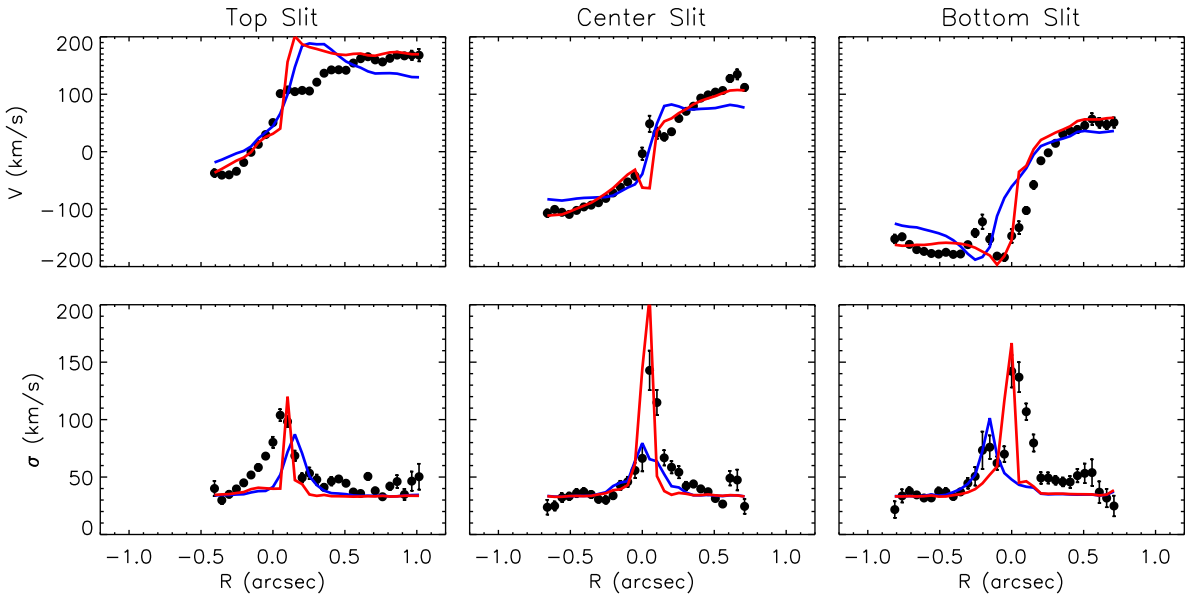

Figure 4.17: [NII] velocities and dispersions of the central gas disk, as measured along all three slits (*black*), as predicted by the unperturbed model (*blue*), and as predicted by the twisted model (*red*). One arcsecond at our assumed distance of 10.28 Mpc corresponds to 50 parsecs.

For consistency, the OASIS data are modeled as a series of slits, each of the same width as an OASIS pixel. The model is nearly identical to that used for the STIS data; the sole difference is the omission of the slit effect correction in the OASIS model, since spatial and spectral stages in the IFU observations are decoupled. Of the six free parameters, the disk inclination was measured from the WFPC2 photometry (as above), and the position angle of the "slits" and their x- and y-locations can be accurately found from the IFU data. OASIS provides the capability of measuring the kinematic PA rather than merely the photometric one found using the WFPC2 image. However, visual inspection of the data makes it immediately clear that the major and minor axes are not perpendicular (see Figure 4.3). Since the primary constraints on M/L come from the peak gas velocities at larger radii, we estimate the position angle of the gas disk from the major axis, despite the inconsistency with the minor axis. The resulting position angle is offset from the photometric position angle by $-13°$. The central x- and y-locations are taken as the center of the OASIS velocity field.

In principle, the remaining unknowns - M_{BH} and M/L - should both be varied in these models. In practice, however, the large PSF of OASIS renders the gas data insensitive to any velocity gradient in the vicinity of the black hole. This need of the gas dynamical models, namely to detect Keplerian motion around the black hole in order to measure its mass, contrasts with the less stringent requirements of the stellar dynamical models, in which OASIS measurements inside R_{BH} provide significant leverage on the central stellar orbital distribution and thus the black hole mass (as in §4.5). Thus, while varying the black hole mass has a strong effect on the OASIS stellar kinematic predictions, it has a negligible one on the OASIS gas velocity predictions. In the gas dynamical models of this data set, we therefore assume an M_{BH} of the unperturbed model's best-fitting value of 2.0×10^8 $M_\odot$ and vary only the I-band M/L.

The gas velocities and dispersions were extracted at each position along each slit, as described in §4.6.1, although the χ^2 parameter was computed from the velocities alone. Figure 4.18 shows how this parameter varies with the mass-to-light ratio, with a minimum at $M/L = 3.0 \pm 0.4$ (3σ errors). The model corresponding to this fit is shown in Figure 4.3. The OASIS data very clearly constrain the central M/L to be almost exactly the value found in the stellar dynamical modeling; there is no evidence for a significant M/L gradient in the center of NGC 3379.

4.7.3 Possible Non-Circular Motion

With a higher central M/L clearly ruled out, the only method of accounting for the data-model mismatch in the unperturbed model is with some form of non-circular motion. Unfortunately, there are numerous explanations for such motion (e.g. a bar, a spiral perturbation, a warp), and too few constraints on the type and shape of the perturbation. Using any such perturbation model to make a black hole mass estimate is not feasible given our limited knowledge of the system. However, it is possible to create a simple, though somewhat unphysical, model to determine whether the inclusion of non-circular motion can improve

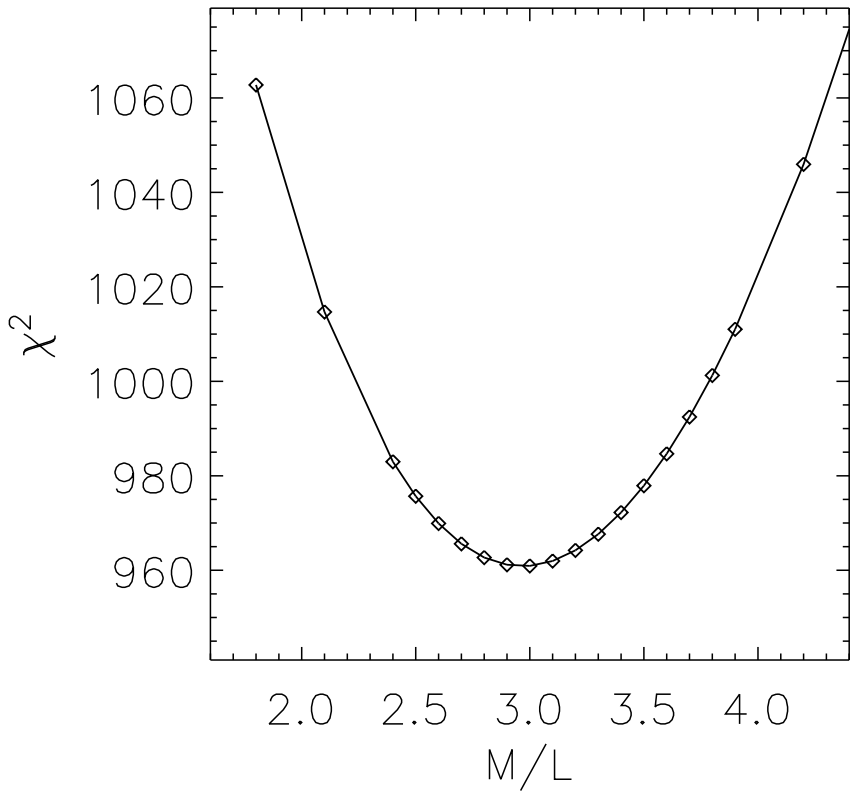

Figure 4.18: χ^2 as a function of M/L, as measured from the OASIS gas kinematics. Points indicate individual models. There are $\sim$ 150 degrees of freedom, making the $\chi^2_{\rm dof} \approx 6$ for the best-fitting model.

the model. For this experiment, we assume our best-fitting black hole mass of 2.0×10^8 $M_\odot$ and mass-to-light ratio of 3.08. (We note, however, that the following conclusions are unchanged when using the best-fitting stellar dynamical black hole mass of 1.4×10^8 $M_\odot$.)

Non-circular motion is introduced into the model described in §4.6 as a tilted ring model. In the original model, the gas velocity at every radius was determined by the underlying potential (black hole plus stellar potential) and the disk inclination. In the modified version, the underlying potential and inclination of the disk remain unchanged, but the position angle of the major axis at each radius is smoothly varied. When the disk is projected on to the plane of the sky, this imposed twist in the major axis is visible as a twist in the velocity field of the disk.

The shape and extent of this artificial twist is constrained by the regularity of the OASIS velocity field at large radii (Figure 4.3). The gas kinematics of the center STIS slit (Figure 4.7), on the other hand, require a significant deviation from the photometric major axis in the center of the disk. We therefore impose a twist of the form

$$\theta_{\rm offset} = A{\rm e}^{-r/B} + C,$$

where A gives the intensity of the twist, B gives its radial extent, and C allows for a position angle offset between the kinematic and photometric major axes, as seen in the OASIS data. Given the arbitrary nature of this model, a full χ^2 minimization was not performed over these parameters; instead they were varied by hand until the model reproduced most of the features in the STIS data. The final model was parameterized by A=2.4, B=0.″25, and C=-13° (see Figure 4.19).

The simulated STIS emission lines and LOSVD moments for this model are shown in Figure 4.6 and Figure 4.17 respectively. It is immediately apparent that many of the problematic features of the STIS gas velocities are reproduced quite well with this ad hoc model. This is reflected in the χ^2 for the STIS data against the twisted model, which is approximately half that of the best-fitting unperturbed model of §4.7.1. It is interesting to note that the gas velocity dispersions observed with STIS are generally predicted more accurately with this model, suggesting that the high dispersions are in fact unresolved rotation. However, the unphysical nature of this twist and the lack of understanding of these dispersions prevent this correspondence from leading to any strong conclusions.

As a consistency check, this twisted model was also applied to the OASIS gas model, and the results are presented in Figure 4.3. Although the blurring effects of the OASIS PSF remove most of the evidence of the twist, it is clear that the twisted model is an equally valid representation of the data, and indeed the χ^2 of the twisted model is slightly lower than that of the unperturbed one.

The velocity field and density structure corresponding to this twisted model are shown in Figure 4.19. It is encouraging that, although arbitrary, the model that matches the gas kinematics produces a spiral-like structure that is hinted at in the WFPC2 photometry (Figure 4.4). At the level of both the photometry and kinematics, this simple twisted model is an adequate representation of the gas disk in NGC 3379 and certainly a better representation than one restricted to perfect circular motion.

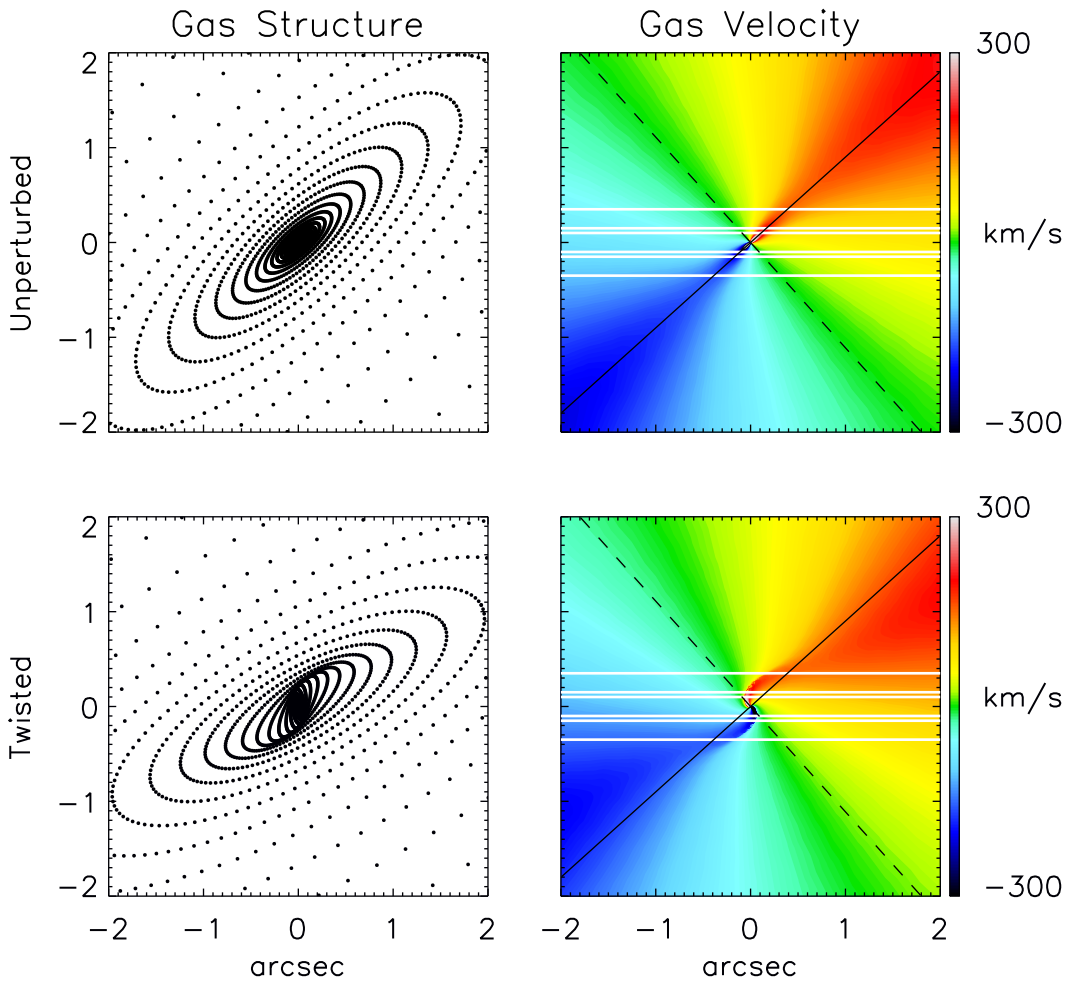

Figure 4.19: The gas structure (*left*), which loosely corresponds to density, and velocity field (*right*) in the unperturbed model (*top*) and in the twisted model (*bottom*), as projected on the plane of the sky. The photometric major and minor axes of the gas disk are indicated by the solid and dashed black lines respectively. It is evident that a non-twisted model requires that the peak velocity in the top and bottom STIS slits (*white*) must occur away from r'=0, whereas the twisted model permits the peak velocity to occur at r'=0. The latter scenario is in keeping with the observations (Figure 4.6). For clarity, these plots have been aligned with the same position angle as the WFPC2 images in Figure 4.4 such that the STIS slits are horizontal.

4.8 Discussion

4.8.1 The Black Hole in NGC 3379

Our stellar dynamical models, constructed using the combined SAURON+OASIS data set, yielded a black hole mass estimate of $1.4^{+2.6}_{-1.0} \times 10^8$ $M_\odot$ (3σ), or $1.4^{+0.3}_{-0.8} \times 10^8$ $M_\odot$ (1σ). This is similar to the black hole masses found previously in other stellar dynamical models. Using two-integral models and ground-based long-slit data, Magorrian et al. (1998) derived a black hole mass of $(3.9 \pm 0.4) \times 10^8$ $M_\odot$ (1σ). Gebhardt et al. (2000b) improved upon this method with the inclusion of *HST*/FOS data and three-integral models to measure a black hole mass of $1^{+1.0}_{-0.4} \times 10^8$ $M_\odot$ (1σ), completely consistent with the results derived here. Gebhardt et al. (2000b) attribute the smaller black hole in the three-integral model to a mild large-scale radial anisotropy predicted by their models (and seen here as well) that two-integral models are unable to reproduce. This very good agreement between the Gebhardt et al. (2000b) three-integral models and those presented here, in both black hole mass and in general trends in orbital anisotropy, is also a nice check of the robustness of black hole mass determination using different data sets and different model implementations.

However, all of these stellar dynamical models employ nearly identical methods of measuring black hole masses. A more objective comparison can be made using the results of completely different techniques. Unfortunately, our gas dynamical results are not conducive to strong conclusions. The unperturbed model, even at the best-fitting black hole mass of 2.0×10^8 $M_\odot$, is unable to reproduce most of the features of the observed data. The twisted model produces a much more satisfactory result, fitting both the perturbed velocity field and the density enhancements visible in the Hα+[NII] image. However, there are insufficient constraints on the true nature of this perturbation to generate a physical model and to perform a fit for the mass of the black hole. We therefore only conclude that the gas kinematics are consistent with the black hole mass measured in the stellar dynamical models.

We are also able to study the region around this black hole in great detail with the stellar dynamical results. Much of the galaxy is characterized by a mild radial anisotropy in the orbital structure, which becomes consistent with isotropy within R_c. This result is rather inconsistent with current simulations, which suggest that the galaxy's strong core signature should be accompanied by a tangential anisotropy within R_c. These surprising results have also been found in M87, a similarly round elliptical with a strong core, by Cappellari & McDermid (2005). Using integral-field data and three-integral models of M87, they measure a slightly radial velocity distribution across the galaxy and down to $0.5R_{\rm BH}$; within that radius, they marginally resolve a shift towards tangential anisotropy. Both M87 and NGC 3379 also have an R_c approximately three times larger than that predicted by the simulations of Milosavljević & Merritt (2001), suggesting that their formation histories include multiple merger events, which may be complicating this comparison of the data to single-merger simulations.

4.8.2 Reliability of Stellar Dynamical Models

The stellar models described here have two main sources of uncertainty: the data themselves and the model assumptions. As seen in §4.2.3, kinematic data are always subject to such systematic effects as template mismatch, in addition to statistical errors. In this sense, NGC 3379 is an ideal galaxy for stellar dynamical modeling, since the wealth of kinematic data available in the literature and in the SAURON and OASIS data sets provides a good consistency check on all kinematic measurements.

When modeling these data, we have implicitly assumed that NGC 3379 can be well-described as an axisymmetric system, and that the MGE parameterization's lower limit on inclination excludes face-on models. However, the true shape of NGC 3379 has been the subject of much speculation and, indeed, remains in doubt. On the basis of photometric and kinematic similarities of this galaxy to NGC 3115, Capaccioli et al. (1991) and Statler & Smecker-Hane (1999) have proposed that NGC 3379 is in fact a nearly face-on S0 galaxy. Statler (2001) modeled the shape and orientation of this galaxy using ground-based long-slit data and generally confirmed this result. Their best-fitting model is a nearly axisymmetric galaxy (T = 0.08) seen at moderate inclination ($i \approx 40^\circ$), although they were not able to completely exclude highly triaxial models.

From the SAURON stellar kinematic observations, we are able to place additional constraints on the shape of NGC 3379 and make a strong qualitative argument for axisymmetry. The integral field data have no minor axis rotation and have well-aligned kinematics and photometry, with a kinematic position angle of $72^\circ \pm 2^\circ$ (found with the kinemetry method of Krajnović et al. (2006) and a photometric position angle of $68^\circ \pm 2^\circ$ (from the MGE model). More generally, NGC 3379 shows significant rotation, and all similar galaxies in the SAURON survey have well-aligned kinematic and photometric axes and therefore likely do not deviate significantly from axisymmetry (Cappellari et al. 2005).

The combined results of Statler (2001) and the SAURON observations effectively rule out highly triaxial models, making the most probable description of NGC 3379 that of a nearly axisymmetric galaxy, seen at a moderate inclination. To test the effects of this possible configuration, we generated a series of models with i=50° and found that the best-fitting black hole mass differed from that of the edge-on models by 50%. While we include this effect in our final error estimations, we do not expect that the relaxation of our assumptions of axisymmetry and an 88° inclination will significantly affect our conclusions.

Finally, it has been suggested by e.g. Valluri et al. (2004) that there are fundamental problems with the reliability of three-integral dynamical modeling. They find black hole masses to be dependent on (extreme) variations of the regularization parameter Δ, which biases the orbital weights towards a smoothly-varying integral space. Verolme et al. (2002) explicitly tested the effects of varying Δ from 0.1 (high regularization) to ∞ (no regularization). They found that the optimal balance between fitting the observables and enforcing smoothness in integral space occurred at $\Delta = 4$. In our own tests of our implementation of the Schwarzschild method, we have likewise found that $\Delta = 4$ is most effective at recovering input parameters, including black hole masses. Cretton & Emsellem (2004) have

shown that it is the absence of regularization that leads to significant problems in black hole mass measurement, in that orbital weights vary rapidly (and unphysically) as a function of the integrals of motion. We have tested this explicitly for NGC 3379 by running a set of models without regularization and found no effect on our measured black hole mass or on the derived three-dimensional stellar velocity distribution. We therefore adopt a moderate regularization of $\Delta = 4$ in our models and do not expect this issue to affect our results.

However, perhaps the most convincing argument for the robustness of the stellar dynamical black hole mass determination is found in Figure 4.12, in which the best-fitting model is immediately evident through inspection of the OASIS data and models. This capability is unique to models with integral field data, as becomes clear in a comparison with the previous models of this galaxy by Gebhardt et al. (2000b). Using ground-based long-slit data plus an FOS spectrum, they were able to use χ^2 to differentiate between models with varying black hole masses. However, a visual comparison of the model with no black hole and that with a black hole of mass 1×10^8 $M_\odot$ shows almost no discernible difference between the two (see their Figure 11). The combined SAURON+OASIS integral-field data, on the other hand, provide such strong constraints on the orbital distribution that the models are unable to reproduce the data with anything other than a black hole of mass $\sim 1.4 \times 10^8$ $M_\odot$ (Figure 4.12).

4.8.3 Reliability of Gas Dynamical Models

The orientation of the nuclear gas disk in NGC 3379, which lies $\sim 45^\circ$ away from the rotation axis of the stars, has also played a role in discussions of the intrinsic shape of the galaxy. In order for this configuration to be completely stabilized, there must either be a small degree of triaxiality in the galaxy or NGC 3379 must be nearly face-on, such that the gas disk is in an orbit close to polar. In either case, as in the case of axisymmetry, Statler (2001) demonstrated that the disk must be decoupled from the main body of the galaxy (with possible origins from intergalactic HI, see e.g. Schneider 1989). However, the models of Statler (2001), as well as the MGE surface brightness parameterization of NGC 3379, reveal that the center of this galaxy is intrinsically quite round. There are thus no strong torques on the gas disk, making its orientation at least marginally stable. Nonetheless, given the position angle offset of this disk, it is perhaps unsurprising that the gas is not moving in perfect circular motion and that its distribution may in fact be (slowly) evolving.

Many elliptical galaxies are known to exhibit kinematic misalignments between the nuclear dust and stars, and it may be that the gas and dust disks in such objects are not generally settled into Keplerian orbits around a central black hole (e.g. van Dokkum & Franx 1995; Emsellem et al. 2003). However, even in the case of aligned stellar and gas kinematics, Verdoes Kleijn et al. (2002) were still unable to reconcile their gas and stellar dynamical measurements of the black hole mass in NGC 4335. In that case, as here, the nuclear gas appears regular, and yet its high central velocity dispersions are better described with the inclusion of non-circular motions in the model. Recent simulations have shown that spiral-like perturbations, whose unresolved rotation can cause such high velocity dispersions, can be

generated by a central black hole binary (Etherington & Maciejewski 2006); unfortunately, this scenario is not obviously consistent with our analysis of the stellar orbital structure. It therefore remains to be seen whether the "twisted" phenomenon observed in the gas disk of NGC 3379 is common in early-type galaxies and, if so, what causes this morphology.

Without the introduction of non-circular motion, inspection of the gas kinematics along the central slit of NGC 3379 suggests a smaller black hole mass. Slight deviations from circular motion in a gas disk may therefore cause Keplerian models to underestimate the mass of the central black hole. Indeed, in all of the existing comparisons of gas and stellar methods to date, the gas dynamical mass measurements are smaller than those derived from the stars. This may be indicative that thin disk, circular models are too simplistic to describe most gas distributions in the centers of elliptical galaxies, although the limited number of gas-star comparisons is not sufficient for drawing such strong conclusions.

4.9 Conclusions

As a nearby and seemingly normal elliptical galaxy, NGC 3379 seems, at face value, an ideal candidate for a comparison of stellar and gas dynamical black hole mass measurements. We have used the most extensive combined stellar data set available for this galaxy, with the most detailed two-dimensional probe (3×3 pixels in OASIS) into the region of influence of its black hole. From this data, we measured a black hole of mass $1.4^{+2.6}_{-1.0} \times 10^8$ $M_\odot$ (3σ), which agrees with results from previous stellar dynamical models based on longslit data and with the predictions of the M_{BH}-σ relation.

NGC 3379 also has what appears to be a regular central gas disk, which is photometrically well-defined and has clear rotation. Although it is not in the equatorial plane of the galaxy, the nearly spherical shape of the core allows the disk to be long-lived. This chapter presents the first detailed investigation into the kinematics of this disk, with the first dynamical model of it. However, despite the apparent regularity of the gas structure and kinematics, the disk in fact displays significant deviations from circular motion. Our nominal estimate of the black hole mass from the gas kinematics is $(2.0 \pm 0.1) \times 10^8$ $M_\odot$ (3σ), although the corresponding model fits the data quite poorly. Given the lack of constraints on the type and shape of the kinematic perturbation, it is not possible to properly model the true dynamics of the disk; our perturbed model provides a very satisfactory fit to the data but can only conclude that the disk is irregular and cannot provide an independent black hole mass measurement.

This chapter's comparison of black hole masses derived using both stellar and gas dynamical methods is one of a very small number of such comparisons; however, to date all of these have revealed limitations in the data and in the model assumptions that have complicated and biased the black hole mass measurements. There has yet to be a comparison of gas and stellar dynamical methods that shows the two methods to be in unequivocal agreement. Cappellari et al. (2002) and Verdoes Kleijn et al. (2002) both found that gas and stellar dynamical black hole mass estimates can differ on the order of factors of 10, and

in NGC 3379, the results are somewhat inconclusive. It is clear that in these three cases the black hole masses cannot be trusted to level of the formal errors, but rather that systematic effects in the models tend to dominate the uncertainties.

This should serve as a caution, since our present understanding of central SMBHs comes largely from black hole masses that have been measured using only a single method. In particular, all of the very low mass SMBHs have been measured using stellar dynamical techniques, while most of the very high mass SMBHs have been studied via the surrounding nuclear gas. While recent results have made it apparent that we have much to learn about galaxy evolution *from* M_{BH}-σ, the results presented here indicate that we still have much to learn *about* M_{BH}-σ as well.

Acknowledgments

It is a pleasure to thank the entire SAURON team for their efforts in carrying out the SAURON observations and data preparation, for many fruitful discussions, and for a careful reading of this chapter. We are grateful to Eric Emsellem and Pierre Ferruit for taking the OASIS observations and to the CFHT staff for their support of those observations. We also wish to thank Patricia Sánchez-Blázquez and Reynier Peletier for early access to their MILES stellar template library. Finally, I am grateful for the repeated hospitality of the Sterrewacht Leiden, as well as that of the CRAL-Observatoire and of the University of Texas at Austin.

Chapter 5

The SAURON Project - XV. Modes of Star Formation in Early-type Galaxies and the Evolution of the Red Sequence

Abstract

We combine SAURON integral field data of a representative sample of local early-type, red sequence galaxies with *Spitzer*/IRAC imaging in order to investigate the presence of trace star formation in these systems. With the *Spitzer* data, we identify galaxies hosting low-level star formation, as traced by PAH emission, with measured star formation rates that compare well to those estimated from other tracers. This star formation proceeds according to established scaling relations with molecular gas content, in surface density regimes characteristic of disk galaxies and circumnuclear starbursts. We find that star formation in early-type galaxies happens exclusively in fast-rotating systems and occurs in two distinct modes. In the first, star formation is a diffuse process, corresponding to widespread young stellar populations and high molecular gas content. The equal presence of co- and counter-rotating components in these systems strongly implies an external origin for the star-forming gas, and we argue that these star formation events may be the final stages of (mostly minor) mergers that build up the bulges of red sequence lenticulars. In the second mode of star formation, the process is concentrated into well-defined disk or ring morphologies, outside of which the host galaxies exhibit uniformly evolved stellar populations. This implies that these star formation events represent rejuvenations within previously quiescent stellar systems. Evidence for earlier star formation events similar to these in all fast rotating early-type galaxies suggests that this mode of star formation may be common to all such galaxies, with a duty cycle of roughly 1/10, and likely contributes to the embedded, co-rotating inner stellar disks ubiquitous in this population.

5.1 Introduction

Early-type (elliptical and lenticular) galaxies, as the most massive and most evolved components of the local Universe, are important test sites for our understanding of the growth of structure. In the past, these systems likely hosted much more powerful star formation and nuclear activity than is found in present day assembling systems ("downsizing"; e.g. Cowie et al. 1996; Kriek et al. 2007). However, these galaxies have long since ceased such activity and are now part of the "red sequence" in the optical color-magnitude space, so called because of the red colors produced by old stellar populations.

The lack of star formation in these galaxies has been attributed to various mechanisms, including gas exhaustion in the major mergers that supposedly give early-type systems their bulge-dominated morphologies, gas stripping as these typically more clustered galaxies encountered the cluster environment, and gas heating by AGN or by shock-heating as the accreting halos cross a mass threshold above which the gas shocks upon entry. Detailed studies of the gas content and of low-level star formation in early-type galaxies can therefore be a critical constraint on the relative importance of each of these mechanisms in regulating the interstellar media (ISM) and therefore star formation in these systems. Such data are a window into the mechanisms responsible for bringing early-type galaxies from the blue cloud onto the red sequence (e.g. Faber et al. 2007) and keeping them there.

Over the past several decades, increasingly sensitive probes of the ISM in early-type galaxies have shown that these systems contain detectable amounts of atomic hydrogen, cold dust, and ionized gas (see review by Schweizer 1987, also e.g. Sadler et al. 2000; Bressan et al. 2006; Temi et al. 2007; Kaneda et al. 2008b). More recently, Morganti et al. (2006) and Sarzi et al. (2006, hereafter Paper V) have shown that the majority of early-type galaxies in non-cluster environments contain atomic and ionized gas, with environment playing a critical role in the presence of an ISM. In some cases, the gas content in these systems is large, with $M_{HI} = 10^6{-}10^9$ $M_\odot$ and $M_{HII} = 10^2{-}10^5$ $M_\odot$ (Morganti et al. 2006; Paper V).

This abundance of gas naturally raises the question of whether these systems, some of which have up to the same amount of atomic hydrogen as the Milky Way, also sustain a molecular component and on-going star formation. Several surveys of CO emission in early-type galaxies have found substantial amounts of molecular gas in some systems (Lees et al. 1991; Young 2002; see also the compilation by Bettoni et al. 2003). More recently, millimeter interferometry has demonstrated that this gas is sometimes arranged in regularly rotating disks, whose size and orientation is consistent with that of the ionized gas and of the embedded stellar disks observed in this class of galaxies (Young et al. 2008). However, the trace amounts of star formation likely associated with these molecular reservoirs have historically been difficult to quantify and to disentangle from other gas excitation mechanisms.

In 2003, the launch of the *Spitzer Space Telescope* made possible sensitive observations of polycyclic aromatic hydrocarbons (PAHs) and of small hot dust grains, both ionized primarily by young stellar populations, in early-type galaxies. Nearly simultaneously, the launch of the *GALEX* satellite enabled similarly sensitive observations in the ultraviolet, in which the stellar photospheric signatures of these young stars can be probed directly. Data

from these satellites have revealed that star formation is occurring in a significant fraction of early-type galaxies (Yi et al. 2005; Young et al. 2009; Temi et al. 2009) and that this late-time star formation contributes 1−10% of the current stellar mass (Schawinski et al. 2007; Kaviraj et al. 2007).

The detection capabilities and spatial resolution available with these satellites now allows detailed comparisons within galaxies of star formation processes and other properties. With a suitable sample and extensive multi-wavelength data, it is then possible to study what governs star formation in early-type systems and to probe why some of these galaxies continue to regenerate their stellar populations while others truly are "red and dead."

In this chapter, we therefore present *Spitzer* data for our representative sample of early-type galaxies, the SAURON survey. In the context of this survey, these galaxies have all been observed with optical integral-field spectroscopy, which provides stellar kinematics and absorption line indices, as well as ionized gas fluxes and kinematics (§5.2). Such properties can be compared in detail with direct probes of star formation, as available in the mid-IR with *Spitzer*/IRAC (§5.3). We use these data to locate regions of on-going star formation in the SAURON galaxies and to probe the corresponding rates and efficiencies (§5.4). We then combine the SAURON, *Spitzer*, and auxiliary data sets to study the photometric and kinematic properties associated with star formation in early type galaxies (§5.5) and to probe the origins, evolution, and fate of these systems (§5.6). Finally, in §5.7, we summarize our conclusions about the continuing evolution of these red sequence galaxies.

5.2 The SAURON Survey

The SAURON survey is a study of the two-dimensional kinematic, stellar population, and gas properties of representative samples of early-type galaxies and bulges, using integral-field observations obtained with the SAURON instrument (Bacon et al. 2001, hereafter Paper I), mounted on the William Herschel Telescope in La Palma. The sample was selected to be evenly divided between morphological classes (E, S0, Sa) and environment (field, Virgo cluster), and to representatively cover the ellipticity versus absolute magnitude parameter space (de Zeeuw et al. 2002, hereafter Paper II). In the context of this program, 48 elliptical and lenticular galaxies and 24 spiral bulges were observed out to one effective radius. Here, we focus on the 48 early-type systems in the main SAURON survey, for which the stellar kinematics (Emsellem et al. 2004, hereafter Paper III), absorption line strengths (Kuntschner et al. 2006, hereafter Paper VI), and emission line fluxes and kinematics (Paper V) have been studied in detail. In these data, the pixel size is $0\farcs8$ and the median seeing FWHM is $1\farcs7$ (Paper III).

5.2.1 Survey Results: Stellar Kinematics

Analysis and comparison of the stellar kinematics maps of the SAURON sample has revealed that early-type galaxies are structurally quite complex. In particular, Emsellem

et al. (2007, hereafter Paper IX) showed that these systems naturally divide into two new categories: fast and slow rotators, as parametrized by their specific angular momentum within one effective radius, λ_R. Detailed analysis of the kinematics in these systems and dynamical modeling have revealed that the fast rotators, those systems with high λ_R, are uniformly characterized by significant embedded disk components and oblate axisymmetry, while the slow rotators, those systems with low λ_R, are fairly round and triaxial (Cappellari et al. 2007, hereafter Paper X; Krajnović et al. 2008, hereafter Paper XII; van den Bosch et al. in prep).

Within these systems, the stellar velocity maps also reveal a variety of kinematic substructures, most notably the kinematically decoupled components (KDCs, Paper XII). Moreover, McDermid et al. (2006, hereafter Paper VIII) have shown that the characteristics of the KDCs, where present, are linked to the rotational class of the host system. KDCs in fast rotators are all compact (<500 pc) and are generally composed of young (<5 Gyr) stars, while those in the slow rotators are universally large (>1 kpc) and much older (>8 Gyr; Paper VIII). It is thus apparent that the assembly and star formation processes involved in the creation of an early-type system are intimately linked with the resulting kinematic substructure.

5.2.2 Survey Results: Ionized Gas and Auxiliary Data

Additionally, the SAURON survey has located and spatially resolved likely regions of continuing evolution within early-type galaxies, where star formation appears to be on-going. From the SAURON maps, Paper V identified a subset of the sample in which the low emission-line [OIII]/Hβ ratios and settled gas systems can only be interpreted as sites of star formation activity. In these systems, the ionized gas is arranged in a regular, disk-like configuration, with low velocity dispersion (Paper V). Stellar population estimates (Paper VI; Kuntschner et al. 2010, hereafter Paper XVII) and *GALEX* UV imaging (Jeong et al. 2009, hereafter Paper XIII) have further revealed that these systems contain the young stellar populations that must exist in the presence of on-going star formation. Additional evidence for star formation in these galaxies comes from CO observations, which reveal the presence of molecular gas and show that, in some cases, this gas is organized into disks that are co-spatial and co-rotating with the ionized gas and the young stars (Combes et al. 2007; Young et al. 2008). However, it is important to note that despite this evidence for trace on-going star formation in this subset of the sample, wide field optical imaging of the SAURON galaxies continues to confirm that all the galaxies in this sample reside solidly on the red sequence in optical colors (Falcón-Barroso et al. in prep).

These star-forming galaxies in the SAURON sample are, however, the minority of the population, with the exact fraction depending on the tracer used (5/48: from [OIII]/Hβ emission line ratios, Paper V; 9/34: from UV emission, Paper XIII). The majority of the galaxies in the SAURON survey do contain measurable ionized gas, but these systems display emission line ratios inconsistent with on-going star formation (Paper V; Sarzi et al. 2010, hereafter Paper XVI). Many of these systems also contain extensive reservoirs of neutral

hydrogen ($M_{HI} = 10^6 - 10^9$ $M_\odot$), which in some cases is organized into large, regularly rotating structures (Morganti et al. 2006; Weijmans et al. 2008; Oosterloo et al. in prep). The presence of this neutral gas and its potential processing into stars is therefore complicated, and critical, to understand.

5.3 Spitzer Data

The obvious questions raised by these SAURON results are then: what are the origins of the large amounts of gas in some early-type galaxies, and what governs its conversion into stars? To address these questions, we must probe the star-forming structures in the SAURON galaxies in detail.

This requires a star formation tracer that is more direct than the [OIII]/Hβ ratio, which can be affected by AGN activity and metallicity gradients, and the presence of CO, which by itself is not evidence of on-going star formation. While both the ultraviolet and the mid-infrared, in which reprocessed UV light is emitted, are suitable for this task, the infrared telescope *Spitzer* yields spatial resolution $\sim$3 times better than that of the UV space telescope *GALEX* and comparable to that of SAURON. *Spitzer* observations, therefore, provide the unique opportunity to probe the star formation properties of the SAURON galaxies on the spatial scales of interesting stellar and ionized gas features, some of which lie below the *GALEX* spatial resolution.

To do this, we measure the mid-IR emission bands from polycyclic aromatic hydrocarbons (PAHs) in the SAURON galaxies. These large molecules, with sizes of few Å and containing up to a few hundred carbon atoms, are each stochastically heated by far UV photons, which excite high-energy vibrational modes that, as they decay, emit primarily in broad emission bands centered at 3.3μm, 6.2μm, 7.7μm, 8.6μm, 11.2μm, and 12.7μm. This emission is typically seen on the boundaries of HII regions, suggesting that late O and early B type stars provide the requisite UV photons and that harder radiation fields (e.g. within HII regions or from AGN) either destroy or chemically transform the molecules such that they no longer emit in these bands (e.g. Cesarsky et al. 1996). We therefore use these mid-IR emission bands, probed by *Spitzer*/IRAC broad-band images and supplemented where possible with *Spitzer*/IRS spectroscopy, to study the intensity and morphology of star formation in the SAURON galaxies.

5.3.1 Observations and Archival Data

For this study, we combine observations with data made publicly available through the Spitzer Science Center (SSC) archive, as originally acquired in the context of a number of different programs. These archival data cover a significant fraction of the SAURON sample. The remaining systems were observed in the context of Program 50630 (PI: G. van der Wolk) during Cycle 5, such that *Spitzer* data was obtained for the full SAURON sample of early-type galaxies.

Table 5.1: *Spitzer* Data for the SAURON Sample Galaxies

Galaxy	IRAC t_{exp} (sec)	IRS Spectral Range (μm)	$f_{3.6}$ (Jy)	$f_{8.0}$ (Jy)	Observers (PIs, Program IDs)
NGC 474	150	9.9 - 19.6	0.072	0.018	A. Zezas (20140)
NGC 524	150	–	0.283	0.098	G. van der Wolk (50630)
NGC 821	44	5.2 - 14.5	0.148	0.041	G. Fabbiano (20371); J. Bregman (03535)
NGC 1023	150	5.2 - 7.7	0.635	0.167	G. Fazio (00069)
NGC 2549	150	–	0.106	0.028	G. van der Wolk (50630)
NGC 2685	48	–	0.095†	0.050†	G. Rieke (40936)
NGC 2695	150	–	0.067	0.017	G. van der Wolk (50630)
NGC 2699	150	–	0.040	0.011	G. van der Wolk (50630)
NGC 2768	500	–	0.362	0.099	G. Fazio (30318)
NGC 2974	500	5.2 - 14.5	0.175†	0.062†	G. Fazio (30318); H. Kaneda (03619)
NGC 3032	480	–	0.038	0.110	S. Kannappan (30406)
NGC 3156	210	–	0.028	0.016	J. Surace (03403)
NGC 3377	150	5.2 - 14.5	0.219	0.058	G. Fazio (00069); J. Bregman (03535)
NGC 3379	60	5.2 - 14.5	0.604	0.150	G. Fazio (00069); J. Bregman (03535)
NGC 3384	500	–	0.298	0.088	G. Fazio (30318)
NGC 3414	150	–	0.142	0.044	G. van der Wolk (50630)
NGC 3489	60	5.2 - 7.7; 9.9 - 19.6	0.227†	0.104†	G. Fazio (00069); C. Leitherer (03674)
NGC 3608	500	5.2 - 14.5	0.145	0.035	G. Fazio (30318); J. Bregman (03535)
NGC 4150	150	5.2 - 7.7; 9.9 - 19.6	0.061†	0.054†	G. Fazio (00069); C. Leitherer (03674)
NGC 4262	150	–	0.086	0.022	G. van der Wolk (50630)
NGC 4270	150	9.9 - 19.6	0.040	0.011	A. Zezas (20140)
NGC 4278	60	5.2 - 14.5	0.282	0.087	G. Fazio (00069); E. Sturm (03237)
NGC 4374	60	5.2 - 14.5	0.770	0.204	G. Fazio (00069); G. Rieke (00082)
NGC 4382	150	5.2 - 14.5	0.880	0.243	A. Zezas (20140); A. Bressan (03419)
NGC 4387	150	–	0.038	0.010	G. van der Wolk (50630)
NGC 4458	500	–	0.039	0.010	G. Fazio (30318)
NGC 4459	60	9.9 - 19.6	0.294	0.156	P. Cote (03649); C. Leitherer (03674)

Continued on Next Page...

Table 5.1 – Continued

Galaxy	IRAC t_{exp} (sec)	IRS Spectral Range (μm)	$f_{3.6}$ (Jy)	$f_{8.0}$ (Jy)	Observers (PIs, Program IDs)
NGC 4473	60	5.2 - 14.5	0.255	0.066	P. Cote (03649); A. Bressan (03419)
NGC 4477	48	5.2 - 14.5	0.257	0.071	G. Rieke (40936)
NGC 4486	150	5.2 - 14.5	1.386	0.402	W. Forman (03228); G. Rieke (00082)
NGC 4526	60	5.2 - 7.7	0.492	0.286	G. Fazio (00069)
NGC 4546	150	–	0.227	0.063	G. van der Wolk (50630)
NGC 4550	150	5.2 - 14.5	0.056	0.019	G. van der Wolk (50630); A. Bressan (03419)
NGC 4552	240	5.2 - 14.5	0.401	0.104	R. Kennicutt (00159)
NGC 4564	44	5.2 - 14.5	0.125	0.032	G. Fabbiano (20371); A. Bressan (03419)
NGC 4570	60	5.2 - 14.5	0.129	0.033	P. Cote (03649); A. Bressan (03419)
NGC 4621	60*	5.2 - 14.5	0.419	0.110	P. Cote (03649); A. Bressan (03419)
NGC 4660	60	5.2 - 14.5	0.107	0.028	P. Cote (03649); A. Bressan (03419)
NGC 5198	150	–	0.056	0.014	G. van der Wolk (50630)
NGC 5308	150	–	0.065	0.016	G. van der Wolk (50630)
NGC 5813	60	5.2 - 14.5	0.248	0.060	G. Fazio (00069); J. Bregman (03535)
NGC 5831	210	5.2 - 14.5	0.097	0.026	J. Surace (03403); J. Bregman (03535)
NGC 5838	150	–	0.168	0.061	G. van der Wolk (50630)
NGC 5845	44	–	0.042	0.013	G. Fabbiano (20371)
NGC 5846	150	5.2 - 14.5	0.429	0.087	A. Zezas (20140); J. Bregman (03535)
NGC 5982	210		0.121	0.031	J. Surace (03403)
NGC 7332	150	5.2 - 14.5	0.086	0.024	G. van der Wolk (50630); R. Rampazzo (30256)
NGC 7457	500	–	0.098	0.027	G. Fazio (30318)

IRAC data noted with (*) are saturated in the 3.6μm band. Aperture photometry is given over the galaxy effective radius; note that for galaxies indicated with (†) non-stellar 8.0μm emission extends beyond R_e. In all cases, errors on the photometry are completely dominated by the assumed 3% systematic error in the IRAC photometric calibration (see text); consequently, we do not explicitly list this systematic error here.

When possible, the IRAC broad-band images are supplemented with archival IRS data, either with the optimal coverage of PAH emission bands achieved in observations with the SL module ($\lambda = 5.2-14.5\mu$m) or with coverage of the longer-wavelength PAH bands with the SH module ($\lambda = 9.9-19.6\mu$m). Table 5.1 describes the available data for each system.

5.3.2 Data Processing

To reduce the IRAC data, we began with the Basic Calibration Data (BCD), as generated in the *Spitzer* pipeline. Artifacts were removed from each exposure using the publicly available artifact mitigation code on the SSC website (courtesy of S. Carey). The exposures were processed and combined into final mosaics using MOPEX (v16.3.7) with pixel sizes of $1\farcs22$. These images were then sky subtracted in the standard way.

Aperture photometry was performed on all systems using three apertures: one of radius $14''$, for comparison with CO data obtained with a beam of this equivalent radius (in §5.4.2), another corresponding to the effective radius of the galaxy (R_e), and a third encompassing all of the 8.0μm non-stellar emission (see §5.3.3) for use in measuring the total star formation rate (SFR) in systems where the observed radius of star formation exceeds R_e. During this process, foreground and background objects and associated saturated pixels were masked out. (The two systems most affected by this are NGC 2974, with a bright foreground star to the southwest, and NGC 4150, with a z=0.52 QSO identified by Lira et al. 2000 to the southeast.) The SSC-recommended extended aperture corrections were applied in all cases for the relevant aperture sizes and wavebands (Reach et al. 2005; Cohen et al. 2007). Errors on the photometry were extracted from the same apertures on the uncertainty images, whose processing in the IRAC pipeline and post-processing was identical to that of the images. In cases where an image was saturated (see Table 5.1), the photometry was recorded as a lower limit. These errors and upper limits were combined in quadrature with the photometric error of IRAC of 3% (Reach et al. 2005).

For visual analysis of the mid-IR morphology of the SAURON galaxies, we also use the IRAC images directly. To re-scale the measured intensities in the images for extended sources, we multiply each image by the extended aperture correction appropriate for an infinite aperture (Reach et al. 2005, see also Gordon et al. 2008). In order to compare the 3.6μm images and the 8.0μm images for each galaxy (see §5.3.3), we then convolve the 3.6μm images with a kernel designed by Gordon et al. (2008) to transform their PSF to that of the 8.0μm images. In some cases, the convolution kernels altered the centering of the image by several tenths of a pixel; for these galaxies, the images were re-aligned using foreground stars for reference.

5.3.3 Tracing Star Formation

The presence of PAH emission in the resulting images and aperture photometry is best probed by the 8.0μm waveband, the spectral response function of which covers the strong

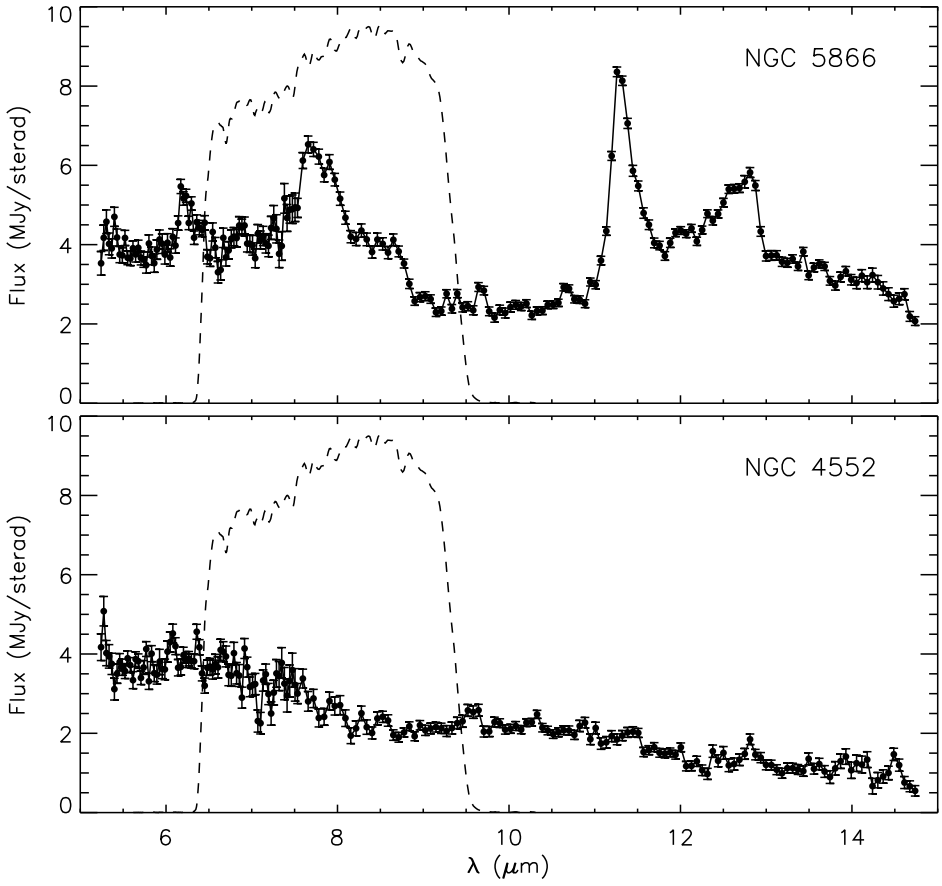

Figure 5.1: IRS spectra for an actively star-forming early-type galaxy (*top*) and a galaxy with no on-going star formation (*bottom*). The star-forming galaxy emits significantly in the main PAH bands at 6.2, 7.7, 8.6, 11.3, and 12.7μm, which are excited by the FUV photons associated primarily with massive young stars. In marked contrast, the quiescent galaxy's spectrum is featureless. The spectra shown here are for NGC 5866, a galaxy observed with SAURON but not in the context of the main sample, and NGC 4552, part of the SAURON sample. The spectra are taken from the SINGS survey (Kennicutt et al. 2003) data release. For reference, the IRAC 8.0μm filter response provided by the SSC is overplotted in dashed lines, with arbitrary normalization.

7.7μm and 8.6μm features (Figure 5.1). However, other emission processes can contribute to signal at 8.0μm, the most important of these being a non-negligible contribution from stars.

The stellar contribution to the 8.0μm band can be estimated using the flux in the 3.6μm band, both of which are dominated by the Rayleigh-Jeans tail of the stellar light, via the simple formula $f_{8.0,stellar} = X_{3.6} \times f_{3.6}$. However, predictions of $X_{3.6}$ from Bruzual & Charlot (2003) single stellar population (SSP) models (see Figure 5.2) and from Starburst99 continuous star formation models generated by Helou et al. (2004) reveal a wide range in this parameter depending on the age and metallicity of the stellar population (see also Calzetti et al. 2007). In late-type galaxies, for which a continuous star formation model is appropriate, Helou et al. (2004) find $X_{3.6} = 0.232$; however, this value has limited applicability to our early-type galaxies, which are not well described by a continuous star formation model. Wu et al. (2005) subsequently used images of quiescent galaxies to empirically estimate $X_{3.6} = 0.26$, although there is little reason to apply this number to systems with stellar populations that deviate from being uniformly very evolved.

Given the large range in ages and metallicities found in the SAURON galaxies (Paper XVII), it is preferable to directly measure $X_{3.6}$ in each of our sample galaxies, based on Bruzual & Charlot (2003) SSP models. We begin by computing SSP models that finely sample age and metallicity parameter space. For each galaxy, we then compare the observed stellar absorption line strengths (Hβ, Mg b, Fe5015) to those predicted by the SSP models and locate the best-fit model in the maximum likelihood sense. This model yields the predicted stellar spectral energy distribution in the mid-infrared, from which we measure $X_{3.6}$. (Tests with more recent SSP libraries that include an updated treatment of AGB stars found similar results to those quoted here.) The resulting range of $X_{3.6}$ for our sample galaxies is shown in the right panel of Figure 5.2, with a sample median of 0.264. We caution here that we find $X_{3.6}$ to differ significantly from 0.264 in some galaxies in our sample and especially in later-type systems (E/S0: Figure 5.2; Sa: Falcón-Barroso, private communication), so the conversions used here should not be blindly applied to other galaxies or HII regions. Using the derived values of $X_{3.6}$ for each galaxy, we estimate the non-stellar contribution to the 8.0μm flux via $f_{8.0,non-stellar} = f_{8.0} - X_{3.6}\ f_{3.6}$.

In galaxies where a significant amount of non-stellar 8.0μm emission is detected, we inspect the pipeline-processed pBCD (post Basic Calibration Data) IRS spectra, where available, to differentiate between emission dominated by PAH features (Figure 5.1) and emission dominated by strong non-thermal continuum emission powered by an AGN (see e.g. Bressan et al. 2007).

In cases where the 8.0μm non-stellar emission is due to PAH bands, the star formation rate needed to drive this PAH emission can be computed directly from $f_{8.0,non-stellar}$, using the relation from Wu et al. (2005),

$$\mathrm{SFR}\ (\mathrm{M}_\odot\ \mathrm{yr}^{-1}) = \frac{\nu L_\nu(8.0, non-stellar)}{1.39 \times 10^9\ L_\odot}, \tag{5.1}$$

These authors have calibrated this relation from the Yun et al. (2001) relation between SFR and radio continuum (based on the SFR-FIR and radio-FIR relations), with correlation coef-

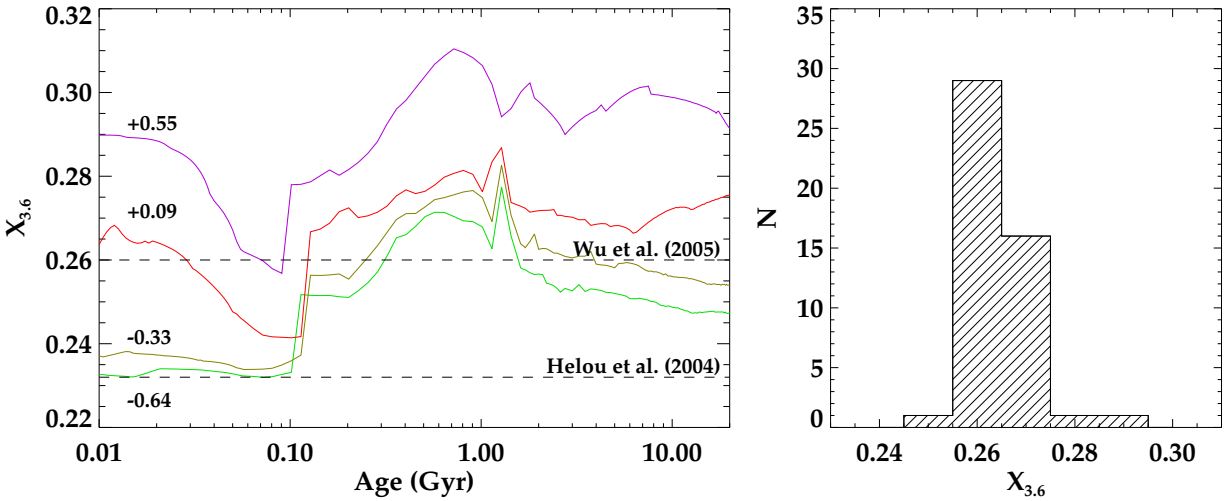

Figure 5.2: *Left*: Dependence of $X_{3.6}$ on a galaxy's age and metallicity, as predicted by Bruzual & Charlot (2003) SSP models. Four different metallicities, ranging from sub-solar (*green*) to super-solar (*magenta*), are plotted and labeled. The Starburst99 value found by Helou et al. (2004) and the empirical estimate by Wu et al. (2005) are overplotted with dashed lines. *Right:* Histogram of best-fit values of $X_{3.6}$ for the SAURON sample galaxies. See text for a description of the method.

ficient $\rho = 0.88$ between the 8.0μm and the radio continuum emission. Wu et al. (2005) have also calibrated the 8.0μm SFR estimator against the Kennicutt (1998) SFR-Hα conversion, which lowers the estimated SFR by $\sim$13%. The SFRs derived from equation 5.1 for the SAURON galaxies are typically several tenths of solar masses per year (Table 5.2), which is within the regime in which Wu et al. (2005) report a linear relation between SFR and 8.0μm flux. We note that non-linear relations between 8.0μm emission and SFR have been reported; however, this effect appears to be confined to galaxies with metallicities less than one third solar (Engelbracht et al. 2005; Calzetti et al. 2007) and likely does not apply to the metal-rich early-type galaxies discussed here.

The errors on our 8.0μm luminosities are derived in §5.3.2 and include the 3% IRAC photometric calibration. We then propagate the uncertainties in the relations between 8.0μm and radio luminosities (Wu et al. 2005) and SFR and radio luminosity (Yun et al. 2001) in order to estimate the total (statistical and systematic) error on our SFRs. The final error estimates derived in this way are listed in Table 5.2.

We measure SFRs for the 13 galaxies in our sample in which the 8.0μm non-stellar emission is significant (with respect to the statistical error bars) and is likely associated with star formation (as identified in §5.4.1 and shown in Figure 5.3*a*). For systems in which there is negligible 8.0μm non-stellar emission, we quote the r.m.s. errors on the non-detections as the upper limits in Table 5.2. For systems in which there is 8.0μm non-stellar emission that is likely not associated with star formation (as identified in §5.4.1 and shown in Figure 5.3*b*), we quote the derived SFRs from this emission as the upper limits. These latter upper limits are often contaminated by AGN emission or other processes (see §5.4.1) and are consequently less stringent limits on the SFRs in these systems.

As a final caveat to the SFRs measured here, it should be noted that there is some debate as to what radiation fields can drive PAH emission. In particular, Peeters et al. (2004) have suggested that PAHs may be better tracers of B stars than of the harder radiation fields found around O stars. Likewise, Calzetti et al. (2005) found evidence for a diffuse component of PAH emission unrelated to HII regions, suggesting that these molecules may be excited by UV photons in the general galactic radiation fields, possibly originating from B stars. Peeters et al. (2002) have also shown that post-AGB stars and planetary nebulae can produce radiation fields appropriate for PAH absorption and reprocessing. To differentiate between those systems in which the 8.0μm non-stellar emission is associated with young stellar populations and those in which it is not, in §5.4.1, we compare the *Spitzer* data with SAURON and auxiliary data to find compelling evidence for and against star formation in individual galaxies.

5.4 Star Formation in the SAURON Galaxies

Figures 5.10 and 5.11 present a detailed comparison of the SAURON stellar and ionized gas properties with the IRAC data. These data reveal a wide range in the mid-IR properties in the sample galaxies, from negligible 8.0μm non-stellar emission to highly-structured 8.0μm

Table 5.2: Observed SFRs and Related Properties for the SAURON Sample Galaxies

Galaxy	Rotator (Fast/Slow)	Type	R_e ($''$)	Distance (Mpc)	$X_{3.6}$	SFR ($M_\odot$ yr^{-1})	dSFR ($M_\odot$ yr^{-1})	R_{SF} ($''$)	M_{H_2} (10^8 $M_\odot$)
NGC 474	F	S0	28.0	26.06	0.264	0	0.0025	0	<0.26
NGC 524	F	S0	35.4	23.99	0.274	0.0971	0.0415	13	1.11
NGC 821	F	E6	31.3	24.10	0.261	0	0.0132	0	<0.39
NGC 1023	F	SB0	48.7	11.43	0.268	0	0.0012	0	<0.05
NGC 2549	F	S0	13.9	12.65	0.277	0	0.0008	0	<0.10
NGC 2685	F	SB0	23.6	11.86	0.258	0.0950	0.0406	50	0.12
NGC 2695	F	SAB0	18.7	32.36	0.261	0	0.0031	0	<0.87
NGC 2699	F	E	12.1	26.92	0.264	0	0.0039	0	<0.31
NGC 2768	F	E6	68.0	22.39	0.258	0	0.0265	0	0.74
NGC 2974	F	E4	28.3	21.48	0.271	0.1426	0.0610	70	<0.39
NGC 3032	F	SAB0	19.3	21.98	0.293	0.4017	0.1717	18	5.27
NGC 3156	F	S0	14.8	22.39	0.264	0.0349	0.0149	10	0.48
NGC 3377	F	E5-6	38.3	11.22	0.258	0	0.0012	0	<0.08
NGC 3379	F	E1	44.9	10.57	0.264	0	0.0036	0	<0.05
NGC 3384	F	SB0	28.5	11.59	0.271	0	0.0091	0	<0.12
NGC 3414	S	S0	32.0	25.23	0.258	0	0.0385	0	<0.14
NGC 3489	F	SAB0	21.5	12.08	0.271	0.0619	0.0265	38	0.15
NGC 3608	S	E2	33.6	22.91	0.264	0	0.0060	0	<0.33
NGC 4150	F	S0	15.9	13.74	0.271	0.0606	0.0259	16	0.59
NGC 4262	F	SB0	10.6	15.42	0.258	0	0.0004	0	<0.10
NGC 4270	F	S0	13.7	37.33	0.261	0	0.0053	0	<0.58
NGC 4278	F	E1-2	30.6	16.07	0.261	0	0.0294	0	<0.32
NGC 4374	S	E1	70.2	18.45	0.261	0	0.0124	0	<0.14
NGC 4382	F	S0	94.4	17.86	0.264	0	0.0298	0	<0.20
NGC 4387	F	E	11.0	17.95	0.261	0	0.0004	0	<0.21
NGC 4458	S	E0-1	19.9	16.37	0.252	0	0.0010	0	<0.17
NGC 4459	F	S0	41.0	16.07	0.264	0.1689	0.0722	12	1.68

Continued on Next Page...

Table 5.2 – Continued

Galaxy	Rotator (Fast/Slow)	Type	R_e ($''$)	Distance (Mpc)	$X_{3.6}$	SFR ($M_\odot$ yr^{-1})	dSFR ($M_\odot$ yr^{-1})	R_{SF} ($''$)	M_{H_2} (10^8 $M_\odot$)
NGC 4473	F	E5	26.8	15.28	0.264	0	0.0016	0	<0.10
NGC 4477	F	SB0	46.5	16.67	0.261	0.0088	0.0038	7	0.34
NGC 4486	S	E0-1	106.2	17.22	0.268	0	0.0761	0	<0.12
NGC 4526	F	SAB0	35.7	16.90	0.268	0.3700	0.1581	11	6.05
NGC 4546	F	SB0	22.0	14.06	0.261	0	0.0055	0	<0.08
NGC 4550	S	SB0	11.6	15.49	0.258	0.0084	0.0036	6	0.14
NGC 4552	S	E0-1	33.9	15.85	0.271	0	0.0041	0	<0.16
NGC 4564	F	E	19.3	15.85	0.268	0	0.0014	0	<0.20
NGC 4570	F	S0	12.8	17.06	0.261	0	0.0008	0	<0.24
NGC 4621	F	E5	46.0	14.93	0.261	0	0.0004	0	<0.15
NGC 4660	F	E	11.5	15.00	0.261	0	0.0002	0	<0.17
NGC 5198	S	E1-2	18.0	38.37	0.264	0	0.0028	0	<0.61
NGC 5308	F	S0	9.9	29.43	0.268	0	0.0032	0	<0.55
NGC 5813	S	E1-2	55.9	32.21	0.264	0	0.0202	0	<0.43
NGC 5831	S	E3	29.2	27.16	0.264	0	0.0005	0	<0.62
NGC 5838	F	S0	20.6	24.66	0.271	0.0819	0.0350	6	<0.38
NGC 5845	F	E	4.3	25.94	0.274	0.0062	0.0027	<3	<0.28
NGC 5846	S	E0-1	76.8	24.89	0.268	0	0.0624	0	<0.52
NGC 5982	S	E3	24.9	51.76	0.271	0	0.0152	0	<0.57
NGC 7332	F	S0	9.2	23.01	0.268	0	0.0022	0	<2.61
NGC 7457	F	S0	33.2	13.24	0.264	0	0.0016	0	<0.11

Rotator class is as derived in Paper IX. Hubble type is taken from NED. Distances and effective radii are taken from Falcón-Barroso et al. (in prep). SFRs are measured here, with upper limits indicated by SFR = 0 and the upper limit given in the error (dSFR) column. The spatial extent of the star formation activity R_{SF} and the ratio of the 8.0μm to 3.6μm stellar emission $X_{3.6}$ are derived in the text. Molecular gas masses are from Schinnerer & Scoville (2002), Combes et al. (2007), Young et al. (2008), Crocker et al. (2008), and Crocker et al. (in prep) and are adjusted to the distances assumed here.

non-stellar emission. Since many of the systems in the SAURON sample are unremarkable in their infrared properties, we present a single representative galaxy from this group in Figure 5.10. In Figure 5.11, we show all systems with marginal to significant infrared emission (also shown in Figure 5.3). Representative spectra from these two groups are shown in Figure 5.1.

5.4.1 Evidence for Star Formation in 8.0μm Emission

Of the 48 SAURON galaxies, roughly half (Figure 5.11, and reproduced in Figure 5.3) have 8.0μm non-stellar maps with significant power. Since this 8.0μm non-stellar emission can be powered by a variety of mechanisms, we combine the *Spitzer* data with SAURON and auxiliary data to differentiate between these emission processes. In our sample, we see evidence for several 8.0μm emission mechanisms; here we discuss the galaxies in each class in turn.

Clear Signatures of Star Formation

In 8 of the 48 SAURON galaxies, there is strong evidence that the 8.0μm non-stellar flux reflects PAH transitions excited by young stars. These systems are shown in the left and middle columns of Figure 5.3*a*; all eight display strong 8.0μm structures, and their spectra, where available, contain prominent PAH emission features. Furthermore, Figure 5.3*a* highlights the marked difference in spatial distribution between the 8.0μm and 3.6μm emission in these galaxies. This provides key evidence that the 8.0μm-emitting dust is not produced and excited by the stellar mass loss of an older FUV-bright population (e.g. the AGB stars responsible for the so-called "UV upturn," Bureau et al. in prep), since the spatial distribution of such populations is expected to closely follow that of the 3.6μm-emitting old stellar populations. The radial profiles in Figure 5.3*a* are also useful in quantifying the extent of the star formation $R_{\rm SF}$ (Table 5.2), which we define here as the radius at which $f_{8.0\mu m}/f_{3.6\mu m}$ decreases to <10% its peak height above $X_{3.6}$.

Additional evidence for young stellar populations in these galaxies comes from the SAURON integral field data, in which the PAH-emitting regions are found to be coincident with higher Hβ line strengths (Figures 5.4 and 5.11; see also Temi et al. 2009), indicative of the presence of younger stars (Paper VI; see §5.5 for details). These findings are also supported by auxiliary *GALEX* imaging, in which all five of the star-forming systems identified here that are included in that sample (NGC 2974, NGC 3032, NGC 4150, NGC 4459, NGC 4526) display blue $UV-V$ colors consistent with star formation at the same radii at which they exhibit non-stellar 8.0μm emission (Jeong et al. 2007; Paper XIII).

Observations of the interstellar media of these eight systems are also consistent with the presence of low-level star formation. In Paper V, ionized gas was detected in all of these systems, and some also display the low [OIII]/Hβ ratios that are associated with on-going star formation. Furthermore, the Hβ emission can be used to estimate the star formation rate via the Kennicutt (1998) SFR-Hα relation (Paper V). These estimates are compared to the PAH-derived SFRs in Figure 5.4 and are lower limits, since the extinction that likely accompanies

star formation in these regions cannot be quantified with only the narrow SAURON spectral range (Paper V; Temi et al. 2009). Indeed, the few direct literature measurements of Hα-derived SFRs for these systems (Gallagher et al. 1984; Young et al. 1996) are systematically higher than the Hβ estimates and more consistent with the PAH-derived SFRs (Figure 5.4). Temi et al. (2009) have also measured 24μm-derived SFRs for these eight galaxies. In the six galaxies with centrally-located and concentrated star-forming regions (excluding NGC 2685 and NGC 2974), the 24μm-derived SFRs are broadly consistent with, though slightly lower than, the PAH-derived SFRs (Figure 5.4).

Furthermore, the molecular content of the SAURON sample has been studied with single-dish CO observations (Combes et al. 2007), and six of the eight of the systems identified in the *Spitzer* data as hosting star formation are also detected in CO emission (Table 5.2). The two remaining galaxies are NGC 2685 and NGC 2974, in which the CO beam of Combes et al. (2007) only marginally overlaps the regions of star formation at high radii; the former has been detected with observations at larger radii by Schinnerer & Scoville (2002). Follow-up CO interferometry has revealed molecular disk-like structures in several of the star-forming galaxies (Young et al. 2008), whose spatial extents and morphologies are excellent matches to the structures seen in PAH emission. Combes et al. (2007) also compared their observed molecular gas masses to *IRAS* FIR fluxes and estimated SFRs. As a further test of the star formation origin of our observed PAH emission, we compare these FIR-derived SFRs to our PAH-derived SFRs in Figure 5.4 and find excellent agreement. This result is reassuring, if unsurprising, given that the PAH-derived SFRs are calibrated against the SFR-FIR relation (§5.3.3).

Finally, the atomic content of the interstellar media in the SAURON galaxies has also been observed for a subset of the full sample (Morganti et al. 2006; Weijmans et al. 2008). In the three star-forming galaxies in this subset (NGC 2685, NGC 2974, NGC 4150), HI is detected in the same regions as the PAH emission (and beyond). However, Morganti et al. (2006) also find significant HI reservoirs in early-type systems without star formation, so the link between this component of the ISM and star formation activity is, as with spiral and dwarf galaxies, less obvious.

Suggestive Signatures of Star Formation

In addition to the 8 galaxies with significant multi-wavelength evidence for on-going star formation, there are 5 (of 48) additional galaxies whose 8.0μm non-stellar emission is suggestive of star formation but whose SAURON and auxiliary data render these cases inconclusive. These systems (NGC 524, NGC 4477, NGC 4550, NGC 5838, NGC 5845) are shown in the right column of Figure 5.3*a*; as with the eight star-forming galaxies, these systems show prominent 8.0μm structures. Likewise, in four of these five galaxies, the radial profiles reveal clear differences in the spatial distributions of the old stars (as traced by 3.6μm) and the 8.0μm emission, which must therefore have a contribution not traceable to evolved stars. In these four systems, we can therefore measure $R_{\rm SF}$; in the remaining galaxy, we obtain only an upper limit.

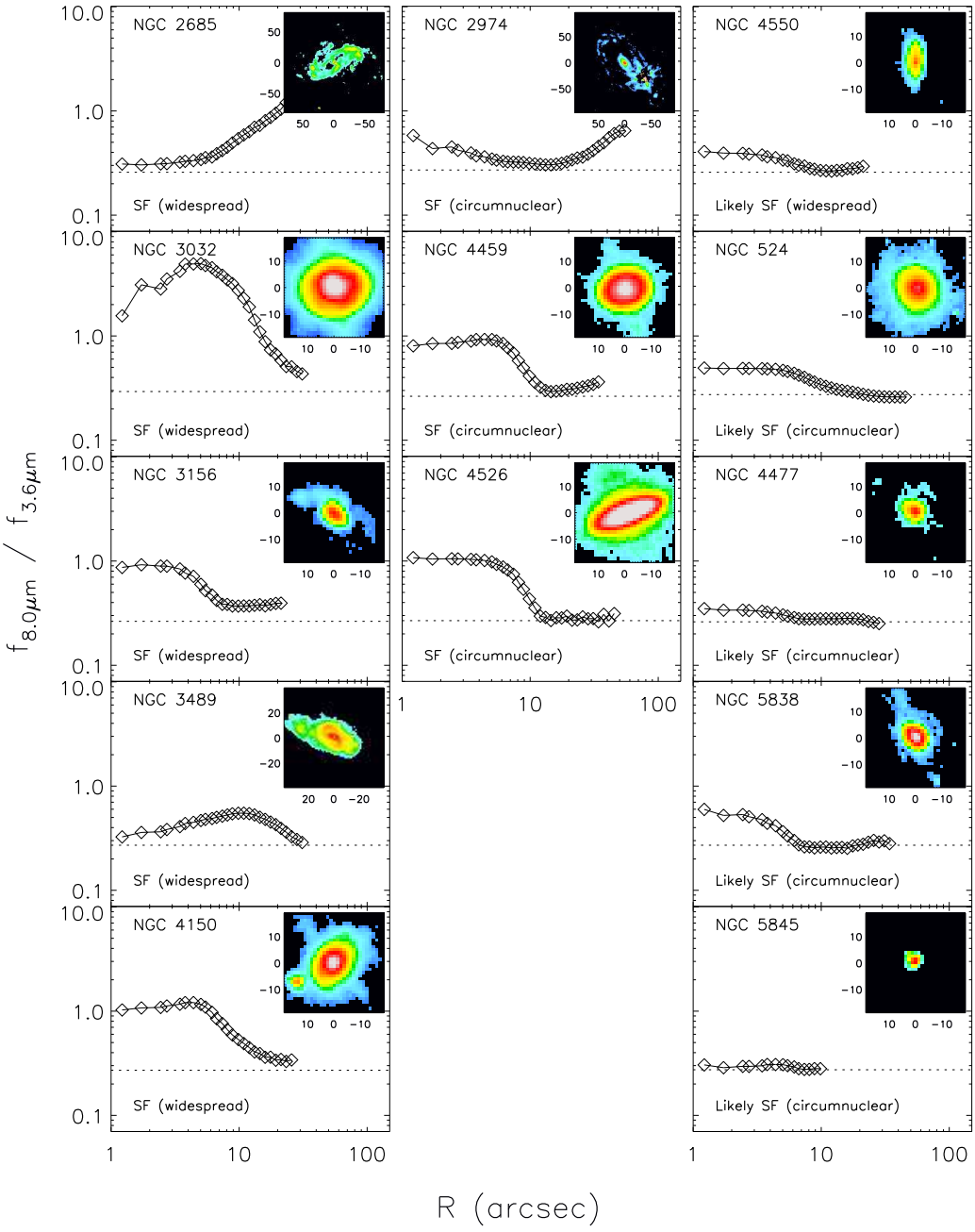

Figure 5.3: (*a*) Radial profiles of ratio of 8.0μm and 3.6μm fluxes and images of the 8.0μm non-stellar emission (*inset*) for clearly (*left and middle columns*) and possibly (*right column*) star-forming galaxies. The presence of star formation in each galaxy is indicated in its panel, along with the physical mechanism likely responsible for the 8.0μm non-stellar emission (see text in §5.4 and §5.5). Horizontal lines indicate the flux ratio expected of a purely stellar profile, $X_{3.6}$. Profiles were measured using the method of Muñoz-Mateos et al. (2009). Note that extended linear structures in these images (e.g. NGC 5838) are artifacts caused by high fluxes in galaxy centers (see Figure 5.11 for more detail).

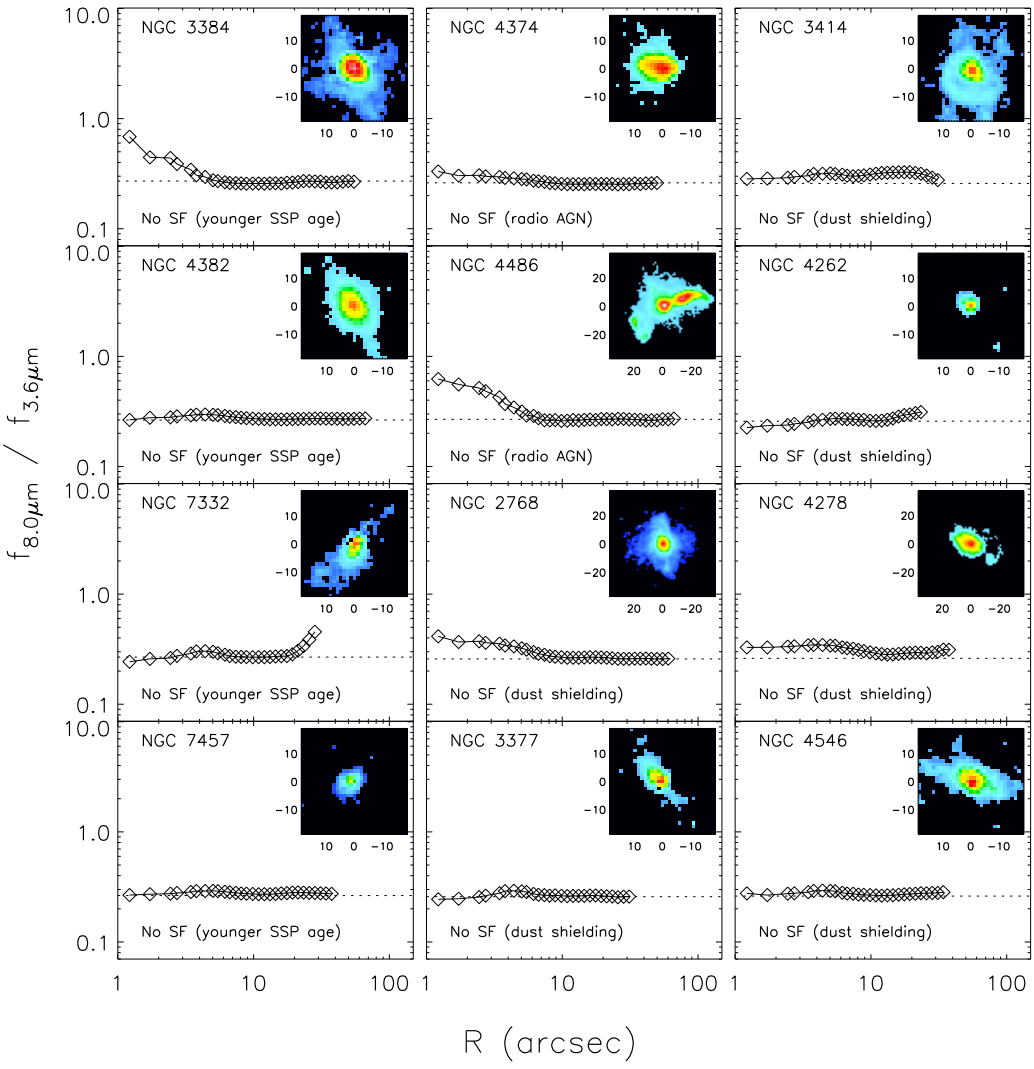

Figure 5.3: (*b*) Same as (*a*), for non-star-forming galaxies with 8.0μm non-stellar emission.

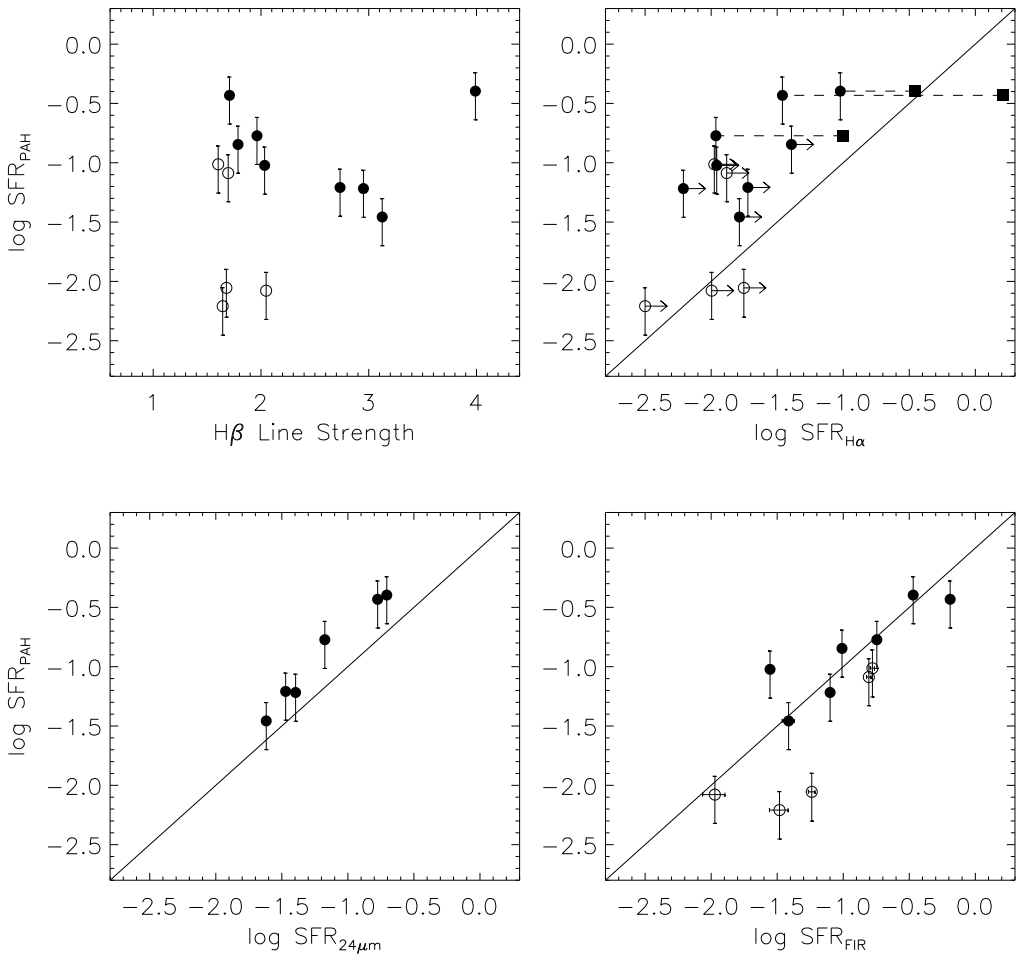

Figure 5.4: SFRs derived from PAH emission for the star-forming galaxies in our sample compared with other age and star formation indicators: Hβ absorption line strength, as measured from the SAURON data over an effective radius (*top left*); SFRs derived from Hα emission, as estimated from the SAURON Hβ emission and assuming no extinction (*top right*); SFRs derived from 24μm emission by Temi et al. (2009) for 6/13 of our star-forming galaxies (*bottom left*); and SFRs derived from FIR emission, estimated from the 60μm and 100μm *IRAS* fluxes collected from the NASA Extragalactic Database by Combes et al. (2007) for 12/13 of our star-forming galaxies (*bottom right*). Galaxies with clear signs of star formation are indicated with filled circles, while those with suggestive signs of star formation are indicated with open circles (see text for details). For three of our galaxies, direct Hα observations have been obtained (Gallagher et al. 1984; Young et al. 1996); those measurements, adjusted to the distances and SFR-Hα conversion assumed here (Kennicutt 1998), are plotted in the top right panel with squares. In all panels, SFR is given in $M_\odot$ yr^{-1}.

The regular morphologies of the 8.0μm non-stellar emission in these galaxies suggest an analogy to some of the star-forming galaxies in Figure 5.3*a*; however, the SFRs measured in these five systems are several times lower. This difference may explain why the signatures of star formation in these systems are less apparent in the SAURON data. In four of these five systems, the Hβ line strengths are very low (Figure 5.4) and so do not obviously point to a young stellar population (Paper VI). Likewise, the UV broad-band emission reveals bluer $UV - V$ colors in the 8.0μm-emitting regions in only the galaxy with slightly higher Hβ absorption (NGC 4550; Paper XIII).

The interstellar media of these systems similarly contribute to this complex picture. Although all five galaxies contain ionized gas, much of it is barely detected, and the [OIII]/Hβ emission-line ratios, where measurable, are neither low enough to be consistent with excitation only from star formation nor high enough to be consistent with other excitation mechanisms (Paper V). Nevertheless, the kinematics of the ionized gas are regular and are consistent with rotating disks, a picture that is also supported by prominent dust disks visible in unsharp-masked *HST*/WFPC2 V-band images (Paper V). In three of these systems (NGC 524, NGC 4477, NGC 4550), sensitive CO interferometry has identified molecular gas disks coincident with the dust (Crocker et al. 2009; Crocker et al. in prep), while the remaining two (NGC 5838, NGC 5845) were undetected with single-dish observations (Combes et al. 2007). Despite this absence, the FIR emission measured by (Combes et al. 2007) in all five systems produces SFR estimates broadly consistent with those from the PAHs. Temi et al. (2009) have observed two of these five galaxies (NGC 4477, NGC 5845) in 24μm emission and do not detect star formation; however, the PAH-derived SFRs of these two galaxies are the lowest in our sample by nearly an order of magnitude (Table 5.2; NGC 4550 has a similar SFR but was not observed by Temi et al. 2009), suggesting that they may have escaped detection at 24μm.

It is consequently difficult to assess whether the 8.0μm non-stellar emission in these systems represents on-going star formation. The analogy to some of the galaxies with evident star formation is highly suggestive, but the multi-wavelength data of these systems are somewhat contradictory and do not converge on this picture. On the one hand, the 8.0μm non-stellar emission in these systems may not be tracing star formation. On the other hand, however, it may be that the very small amounts of star formation measured in 8.0μm are not visible in other tracers, due to its low level and to the much more massive underlying old stellar populations.

Other Sources of 8.0μm Emission

In contrast to the two classes of galaxies discussed above, in which all or some of the evidence points to on-going or recently ceased star formation, there are 12 (of 48) additional systems in which 8.0μm emission is observed but cannot be easily linked to star formation activity. These galaxies are shown in Figure 5.3*b*.

In one of these systems, NGC 4486 (M87), the 8.0μm features are coincident with the well-known radio jet, seen prominently and ubiquitously in ultraviolet, optical, and infrared

imaging, and is thus almost certainly synchrotron emission (see also Perlman et al. 2007). Another, NGC 4374 (M84), is also a well-known radio galaxy, although in this case the 8.0μm emission is aligned with the dust filaments seen in the optical that are perpendicular to the radio jet. In at least these two cases, the 8.0μm non-stellar emission can be attributed to nuclear activity rather than to star formation.

In six systems (NGC 2768, NGC 3377, NGC 3414, NGC 4262, NGC 4278, NGC 4546), the 8.0μm non-stellar emission is patchy. Five of these galaxies have no detected molecular gas (Combes et al. 2007; Crocker et al. in prep), and the one system with detected CO emission (NGC 2768, Crocker et al. 2008) reveals little spatial overlap between this gas and the 8.0μm emission. Likewise, the stellar populations of these galaxies show no evidence of recent star formation and range from fairly to very evolved (8−12 Gyr; Paper XVII). As a group, therefore, these six 8.0μm emitters are unlikely to host star formation activity.

The 8.0μm emission in these galaxies does correlate loosely with optically observed asymmetric dust lanes seen in all of these galaxies in Paper V and therefore may be highlighting the densest regions of these structures. The IRS spectra for these systems, where available, reveal strong neutral PAH features at 11.3μm and only marginally detected ionized PAH 7.7μm emission, the latter of which is the primary PAH feature associated with star formation. The dominance of neutral PAHs has been observed in a number of early-type galaxies and attributed to softer interstellar radiation fields, as would be expected of older stellar populations in the absence of AGN (e.g. Kaneda et al. 2008a, but see also Bregman et al. 2008).

Paper XVI discusses the ionizing mechanisms in the SAURON galaxies in detail and, for these quiescent galaxies with 8.0μm non-stellar emission, compares the spatial distribution of this emission to the ionization of the galaxies, as parametrized by [OIII]/Hβ. In fact, the spatial coincidence between these two features is remarkable, in that regions of relatively lower [OIII]/Hβ are the regions where 8.0μm non-stellar emission is detected (see Figure 5.11). Within the hard radiation fields (seen as high [OIII]/Hβ) in these galaxies, there are embedded regions of softer radiation fields, in which lower [OIII]/Hβ and 8.0μm non-stellar emission is measured. The lower ionization in these regions may be due to the denser ISM found in these amorphous dust lanes, which absorbs some of the ionizing photons, partially shielding the gas from the hard ionization field. In this manner, PAH molecules could survive in these dusty regions and produce the observed emission. This mechanism may likewise shield the very small grains that produce 24μm emission, as detected in these galaxies by Temi et al. (2009). For details, we refer the reader to Paper XVI and do not further discuss this class of non-SF galaxies here.

In addition to the eight galaxies discussed above, four more have weak 8.0μm non-stellar emission detections. The IRAC images show the emission in these systems to be relatively weak, suggesting that perhaps this emission is associated with trace excitation of PAHs by B stars in these galaxies (NGC 3384, NGC 4382, NGC 7332, NGC 7457), which all have younger stellar populations.

5.4.2 Efficiency of Star Formation

For the 13 galaxies identified in §5.4.1 that are probably or potentially hosting star formation, we compare our measured SFRs to the molecular gas mass measurements of Schinnerer & Scoville (2002), Combes et al. (2007), Young et al. (2008), Crocker et al. (2008) and Crocker et al. (in prep) in order to probe the efficiency of star formation in the SAURON early-type galaxies. Our SFRs are measured over the star-forming regions, and we assume that all of the (mostly single-dish) CO emission originates in the same regions, as has been explicitly demonstrated for a subset of these galaxies with follow-up interferometry by Young et al. (2008). Defining our apertures in this way, we can directly compare with the results of Kennicutt (1998), in which the aperture size is determined by the extent of the Hα disk (for normal spiral galaxies) or of the central molecular disk (for starbursts). Our comparison to these data is shown in Figure 5.5; for reference, the results of more recent work by Bigiel et al. (2008) are also shown.

An earlier version of this plot has been presented by Combes et al. (2007), who compared their single-dish CO observations with the *IRAS* FIR luminosities discussed in §5.4.1. However, their single-dish data and the large *IRAS* beam did not allow them to constrain the size of the star-forming regions and to normalize their SFRs and H_2 luminosities to this aperture. As a result, their star formation and gas surface densities were artificially lowered by their much larger aperture sizes (R_{25}), which are revealed in the *Spitzer* data (and CO interferometry, e.g. Young et al. 2008) to only contain star formation activity in smaller, central regions.

Integrating over only the star-forming region, we find that early-type galaxies mainly inhabit the same regions of the plot as typical star-forming spiral galaxies (Figure 5.5). Interestingly, however, several of the galaxies fall closer to the circumnuclear starburst regime on these diagrams (filled circles), with gas surface densities approaching and exceeding 100 $M_\odot/pc^2$ (preferentially magenta). This implies that, whenever even trace amounts of star formation are present, the same physical processes that govern the rate and efficiency of star formation in late-type galaxies and starbursts are also at work in early-type galaxies.

5.5 Modes of Star Formation in Early-Type Galaxies

In the following sections, we compare the properties of the 13 galaxies in the SAURON survey that show signs of star formation in the infrared to those of the sample as a whole. Since the SAURON sample is representative of local elliptical and lenticular galaxies, this provides insight into how star formation is connected to the structure and evolution of early-type galaxies. From the comparisons in this section, two distinct modes of star formation in these galaxies emerge, and the properties of galaxies in these classes are observed to sample those of the early-type population in independent ways.

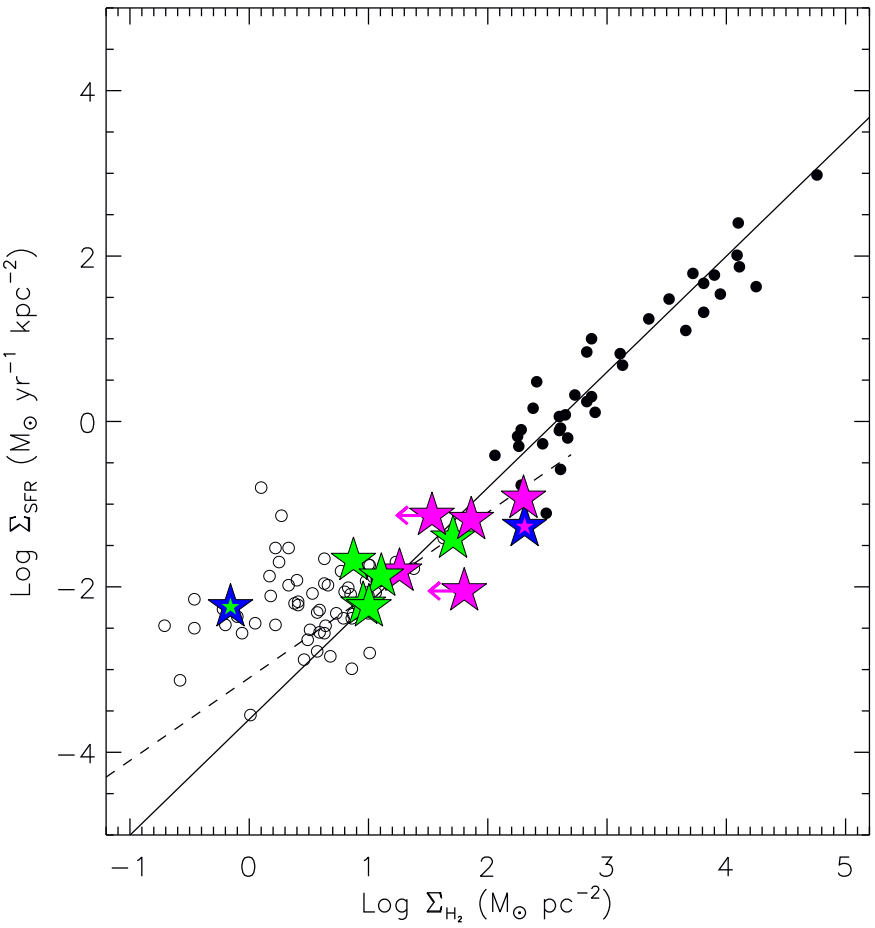

Figure 5.5: Schmidt-Kennicutt relation between gas and star formation densities (*solid line*), with data from Kennicutt (1998) overplotted (*open circles*: spiral galaxies, *filled circles*: circumnuclear starbursts). The recent analysis of Bigiel et al. (2008) and Leroy et al. (2008) with higher resolution data reveal a linear relation between these quantities (*dashed line*) in the spiral galaxy regime, although they note that a steepening of the relation probably occurs at higher molecular gas densities. The star formation rates for early-type galaxies measured in this work are combined with existing CO measurements and overplotted with stars, colored according to the mode of star formation as described in §5.5.2 (error bars on SFRs are smaller than the symbols). Only 12 of the 13 star-forming galaxies are shown here, since the outer regions of NGC 2974, in the vicinity of the star formation activity, have not been observed in CO emission.

5.5.1 Broadband Properties

By definition, the SAURON galaxies are drawn from a sample of local red sequence galaxies, whose very tight adherence to the optical red sequence is demonstrated by Falcón-Barroso et al. (in prep). For this reason, it is intriguing to find on-going or recent star formation in a number of these "red and dead" systems.

However, the $V-K$ colors used to define the optical red sequence are relatively insensitive to low mass fraction young stellar populations and can be strongly affected by dust. We therefore construct an infrared color-magnitude diagram (CMD), which has the advantage of being directly sensitive to star formation (Figure 5.6). In this CMD, star-forming galaxies have large 8.0μm fluxes and are therefore redder, although for clarity and comparison with optical CMDs, we reverse the color index such that redder objects (with higher SFR) are lower in the diagram.

To examine the extent to which our star-forming galaxies differ from quiescent systems in the infrared color-magnitude space, we compare the SAURON data to that from the SINGS galaxy sample (Kennicutt et al. 2003; Dale et al. 2005), in which galaxies with a wide range of properties were observed with *Spitzer*. From this comparison (Figure 5.6), it is evident that the star-forming SAURON galaxies have infrared colors spanning the full range observed in star-forming spiral galaxies, although the majority have colors intermediate between star-forming and quiescent galaxies. In the infrared CMD, the SAURON red sequence star-forming galaxies are thus readily distinguished from quiescent early-type systems (see also the UV CMD results of Yi et al. 2005; Kaviraj et al. 2007).

It is therefore instructive to study more fundamental properties of these star-forming galaxies than can be probed in a broadband CMD. In Figure 5.7, we plot the SAURON galaxies in the SFR-M_* parameter space, a more physical analog to the color-magnitude diagram. To accomplish this, we first estimate the stellar mass of the SAURON galaxies using the "observed virial" masses $M_{vir} = 5R_e\sigma_e^2/G$, where σ_e is the luminosity-weighted second velocity moment within 1 R_e (Cappellari et al. 2006, hereafter Paper IV; Paper IX). The factor 5 scales the dynamical mass within one effective radius to the total baryonic mass of the galaxy; Paper IV shows that this mass estimator contains an average dark matter contribution of $\sim 30\%$, although this percentage varies at the low and high mass extremes of the sample and depends strongly on the mass fraction of young stars in a galaxy (through the stellar population mass-to-light ratio). We therefore approximate $M_* \approx 0.7\ M_{vir}$, with the caveat that the stellar masses of individual galaxies may deviate from this estimate, and we plot these masses against the SFR measurements derived here (Table 5.2).

These results are compared to simulated galaxies generated by the Munich semi-analytic models (Croton et al. 2006; De Lucia & Blaizot 2007) for the Millennium simulation (Springel et al. 2005). For inclusion on this diagram, all simulated galaxies with no star formation are shifted to SFR = 10^{-3} $M_\odot$ yr^{-1}, with an imposed scatter of 0.2 dex. This reveals both a "red" sequence of zero star formation (left) and a "blue" sequence of the well-known SFR-M_* relation for star-forming galaxies (right). Additionally, the simulated broadband galaxy luminosities estimated in these models (including dust extinction) enable the SAURON selection

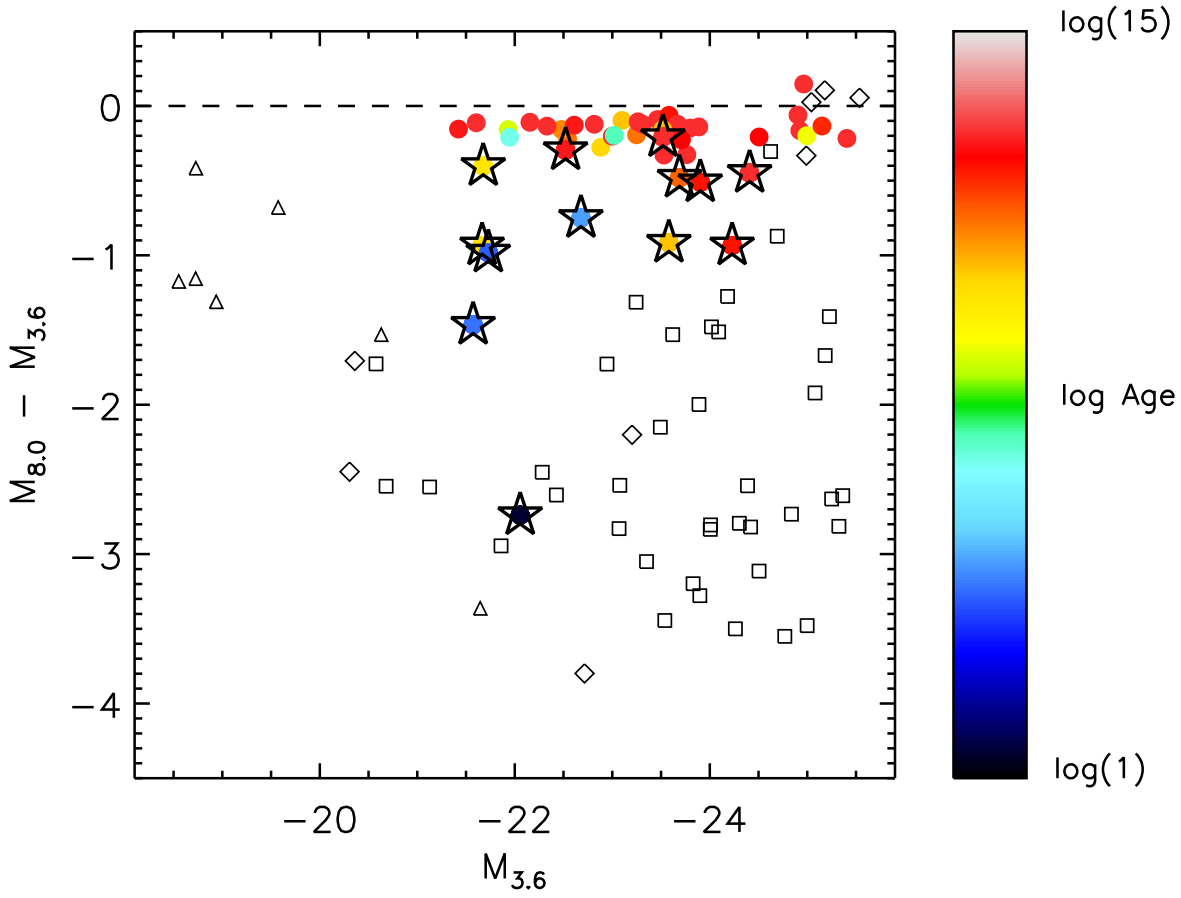

Figure 5.6: Infrared color-magnitude diagram for the SAURON galaxies, measured over apertures of one effective radius. Galaxies are indicated with points colored by their SSP ages (in Gyr; Paper XVII), such that younger stellar populations are blue. Galaxies with on-going star formation are indicated with stars. In the infrared bands, these systems are redder, since they appear more prominently in the redder 8.0μm (PAH) emission. In the optical bands, which probe stellar photospheric emission, star-forming populations are typically bluer. For straightforward comparison to optical CMDs, in which the (bluer) star-forming galaxies are lower on the vertical axis, the color index here is defined such that the (redder) star-forming galaxies are also lower on the vertical axis. For reference, the R_{25} colors and magnitudes of the SINGS galaxy sample are overplotted (E/S0: *diamond*, Sa-Sd: *square*, Sm-Im: *triangle*), although their slightly larger aperture R_{25} increases their luminosities (and thus decreases their magnitudes, moving them to the right) relative to the SAURON sample (photometry measured over R_e). An $M_{8.0} - M_{3.6}$ color of zero is indicated with the dashed line; the magnitudes quoted here are Vega magnitudes (zero-points given by the SSC), so this line corresponds roughly to the color of a purely stellar spectrum.

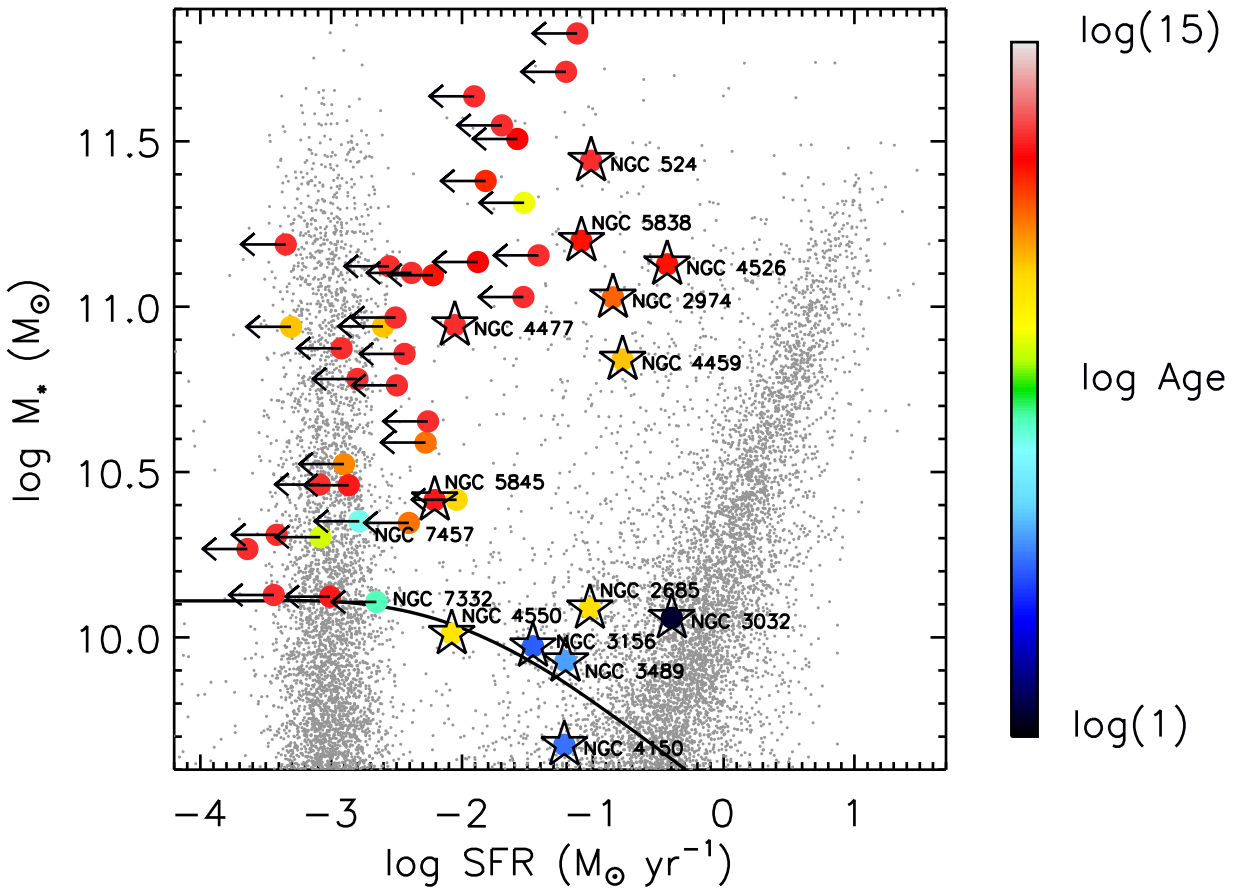

Figure 5.7: Relation of SFR and M_* for the Millennium Simulation at $z = 0$ (*grey dots*) and the SAURON early-type galaxies (*large, colored circles*). The SAURON galaxies are colored by their SSP age (in Gyr, measured over R_e), such that young stellar populations are blue, while older stellar populations are red. Those systems with evidence of star formation in the *Spitzer* images are indicated with stars; error bars are ∼1−2 times the size of the symbols and are omitted for clarity. The $M_B \leq -18$ selection criteria for the SAURON sample is evaluated in this parameter space using the simulated galaxies and plotted here with the black line.

criterion of B-band absolute magnitude ≤ -18 to be robustly identified in this parameter space (black line indicates the mass above which 90% of galaxies with a given SFR fulfill this criterion).

Figure 5.7 confirms the impression from the infrared CMD that nearly all of the SAURON star-forming galaxies fall in the "transition" region between actively star-forming and quiescent galaxies. The only exception to this may be NGC 3032, which lies on the cusp of the SFR-M_* relation and thus is consistent with a still actively star-forming galaxy. Before proceeding further, it is important to reiterate that the SAURON star-forming galaxies are detected as such in Figures 5.6 and 5.7 only due to the sensitivity of these parameter spaces to low-level star formation. All of these systems are traditional early-type galaxies, with red optical colors and bulge-dominated morphologies, which nevertheless do form stars at significant rates.

5.5.2 The Dynamics of Star Formation

With the SAURON data, it is possible to delve more deeply into the properties of early-type galaxies than can be accomplished with broadband data alone. Of particular interest are the stellar and gas kinematics associated with star formation in early-type galaxies.

Most apparent in the SAURON kinematic data is that all star-forming galaxies are so-called "fast rotators," with relatively high specific angular momenta (λ_R>0.1). The top left panel of Figure 5.8 illustrates that some of the star-forming galaxies are even among the most rapidly rotating galaxies in the sample. There is a single exception to this, NGC 4550. This galaxy is a pathological "slow rotator," in that it is composed of two rapidly counter-rotating disks (see stellar velocity maps in Figure 5.11), whose angular momenta largely cancel each other; however, in terms of general properties, it belongs in the fast rotator family (Paper IX; Paper X).

In Paper XII, fast rotators were shown to universally be composed of a large bulge and one or more stellar disks of varying thickness and spatial extent. Since, in many cases, these stellar disks rotate more rapidly and display different age and metallicity properties than their host galaxies (i.e. the bulges that dominate early-type systems), these structures may be connected to the more rapidly rotating gaseous component via recent star formation. In the top right panel of Figure 5.8, we compare the spatial extent of star formation detected here with the spatial extent of kinematically distinct structures (counter-rotating cores, embedded stellar disks, etc), if present, as measured in Paper XII.

It is apparent that in some cases (magenta stars), the kinematically distinct structure (or multiple component, MC) is directly related to the on-going star formation activity. In these galaxies, the MCs are embedded stellar disks whose kinematic position angle is identical to that of the main galaxy body and of the gas (bottom panels in Figure 5.8). These disks are also quite thin, as seen directly in edge-on systems (e.g. NGC 4526) or in optical images of the corresponding dust disks (e.g. NGC 4459). The star formation morphologies in these galaxies are highly regular; all star formation is confined to a disk that is spatially coincident with the ionized gas and dust disks, with variations in stellar populations, and with embedded

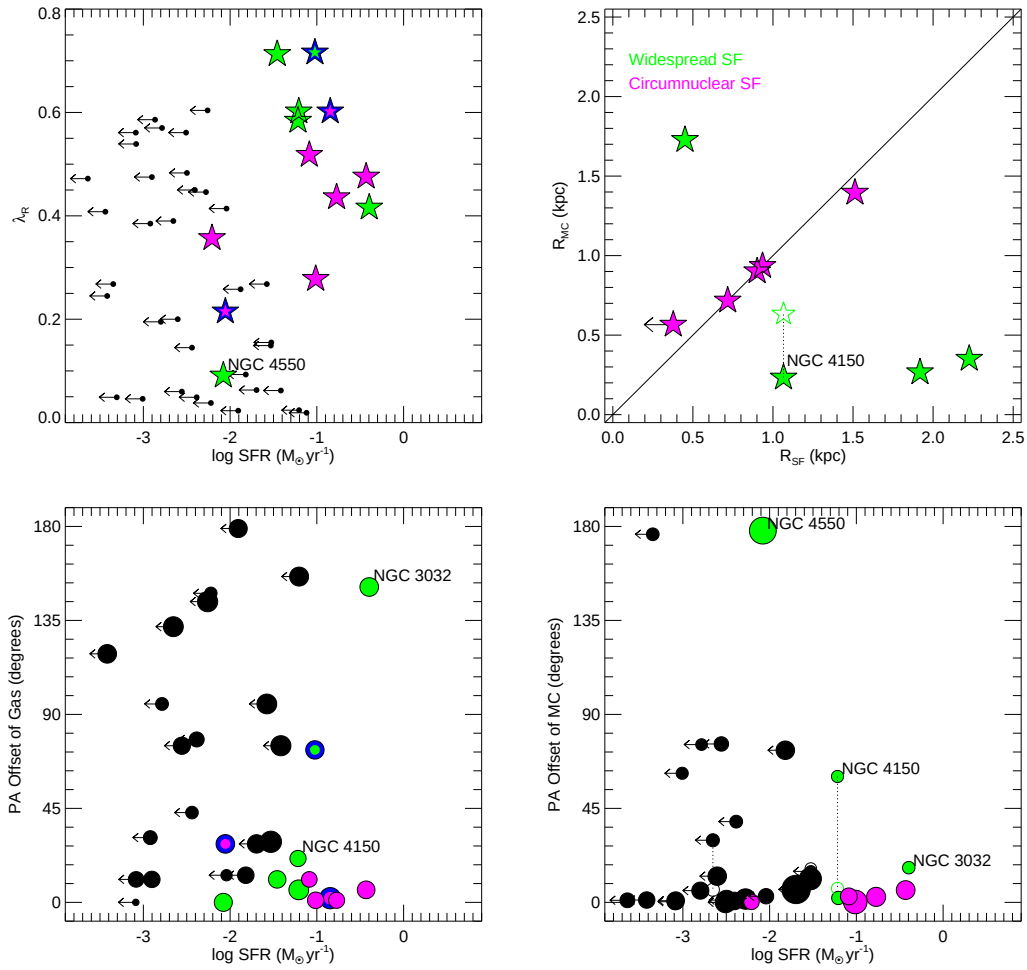

Figure 5.8: *Top left*: Comparison of (projected) specific angular momentum (Paper IX) with SFR in the SAURON galaxies. *Bottom left*: Comparison of position angle offset between the gas and stellar kinematic major axes (Paper V) with SFR, including the 12/13 star-forming galaxies with sufficient ionized gas to make this measurement. The sizes of the points correspond to the masses of ionized gas in the galaxies (Paper V). *Top right*: Comparison of the radial extent of distinct kinematic components $R_{\rm MC}$ (Paper XII) with radius of star formation activity $R_{\rm SF}$. *Bottom right*: Comparison of position angle offset between stellar kinematic components for galaxies with more than one component (from Paper XII). The sizes of the points indicate the sizes of the MCs (in kpc). In the latter two plots, the counter-rotating stellar disk in NGC 4550, which Paper XII notes is not detected in kinemetric analysis, is included, as is the marginally detected co-rotating MC in NGC 524. In galaxies with two MCs (= three kinematic components), the outer MC is indicated with an open symbol. In all plots, star-forming systems are indicated with colored symbols (*green*: widespread star-forming, *magenta*: circumnuclear star-forming, *blue outline*: outliers), with the specific locations of some galaxies noted (see text for discussion). Error bars on the SFRs of these galaxies are 1−2 times the sizes of the symbols.

stellar disks if present.

However, there are also star-forming galaxies in the sample with MCs whose extents are not obviously linked to the star formation activity (green stars in Figure 5.8). This disconnect is also apparent in the kinematic alignments in these galaxies; roughly half of these systems (3/5) contain counter-rotating stars, gas, or both. In many of these galaxies, the morphology of the star-forming region is markedly irregular (Figure 5.3) and extends at low levels to large radii, in keeping with the ubiquity of ionized gas, with the universally young stellar populations (§5.5.3), and with the lack of distinct stellar kinematic features associated with the (widespread) star formation.

We can therefore divide the star-forming galaxies into two distinct classes using the top right panel of Figure 5.8; we refer to those galaxies with signs of star formation out to large radii (green stars) as "widespread" star-forming galaxies and those galaxies in which the star formation is confined to a central disk morphology (magenta stars) as "circumnuclear" star-forming galaxies, in analogy to the two modes of star formation seen in late-type galaxies (Kennicutt 1998). Four additional star-forming galaxies are not included in this panel due to their lack of distinct kinematic structures in the SAURON data. The first, NGC 3156, shows PAH and ionized gas emission with slightly irregular morphologies out to large radii, has no kinematic structure associated with the star formation event, and contains universally young stellar populations. In all properties, this galaxy is therefore consistent with belonging to the widespread star-forming class (green), and we consider it a member of this group. The remaining three galaxies do not fit neatly into either category. Two of these three (NGC 2685, NGC 2974) contain large-scale rings of star formation and the third (NGC 4477) is highly disturbed by a strong bar. It is therefore not immediately obvious how these three galaxies (shown with blue outlines in Figure 5.8; inner color determined from discussion in §5.5.5) fit into the simple two-class division given above.

In the remainder of this section, we compare the properties of the five widespread star-forming galaxies (NGC 3032, NGC 3156, NGC 3489, NGC 4150, NGC 4550) to those of the five circumnuclear star-forming galaxies (NGC 524, NGC 4459, NGC 4526, NGC 5838, NGC 5845) in our sample and find these two classes to be fundamentally distinct, in more than the morphology and kinematics of their star formation events. We then describe the properties of the "outliers" (NGC 2685, NGC 2974, NGC 4477) and find each of these galaxies to be consistent with one of the two modes of star formation, when a more nuanced approach is taken.

It is worth noting, before moving on, that there is one deep similarity between all of the star-forming galaxies, namely that star formation is occurring in a thin disk or ring morphology. This is directly apparent in the one widespread star-forming galaxy with a dynamically relaxed interstellar medium (NGC 3032), in the circumnuclear star-forming galaxies (all of which contain thin dust disks), and in the two galaxies with star-forming rings. In the remainder of the widespread star-forming galaxies and in the third "outlier" galaxy (NGC 4477), the presence of a thin disk is implied by the rapid rotation velocities in the stars and by the low velocity dispersions in the ionized gas. Similar results have been found for star formation in the bulges of Sa galaxies in Peletier et al. (2007, hereafter

Paper XI). Together, this evidence suggests that a thin disk/ring morphology may be the most common mode of star formation in early-type galaxies and bulges.

5.5.3 Widespread Star-Forming Fast Rotators

In Figure 5.7, the widespread star-forming galaxies (NGC 3032, NGC 3156, NGC 3489, NGC 4150, NGC 4550) are seen to be those star-forming early-type galaxies with lower stellar masses. Given the comparable molecular content of all star-forming galaxies in our sample (see Table 5.2), the widespread star-forming galaxies are consequently also characterized by higher gas fractions and specific star formation rates. As a result, the current star formation event dominates the single stellar population (SSP) ages, which are measured to be young throughout these systems ($<$1$-$3 Gyr; Paper XVII). This is consistent with the location of the widespread star-forming galaxies in Figure 5.5; these systems have molecular gas and star formation surface densities similar to those found in late-type galaxies undergoing global star formation. That the star formation event is widespread is also apparent in its morphology and in the absence of stellar kinematic structures with spatial extents related to those of the star formation (by definition; see §5.5.2). Nevertheless, distinct stellar and gas kinematic structures do exist in these systems; galaxies in this class are evenly split between objects with counter-rotating stars, gas, or both (3/5) and those with purely co-rotating stellar and gaseous components (2/5).

Within this class, interesting trends in galaxy properties with SFR are found. In particular, galaxies with higher SFRs (e.g. NGC 3032; SFR = 0.4 $M_\odot$ yr^{-1}) have, unsurprisingly, more prominent signs of on-going star formation, including younger SSP ages, higher molecular gas masses, and lower [OIII]/Hβ ionized gas emission line ratios. Those widespread star-forming systems with lower SFRs (e.g. NGC 3156, NGC 3489, NGC 4150; SFR = 0.03$-$0.06 $M_\odot$ yr^{-1}) have SSP ages older by $\sim$1$-$2 Gyr, an order of magnitude less molecular gas, and high [OIII]/Hβ ratios that are inconsistent with significant on-going star formation (Paper XVI). Lower SFRs in a widespread star-forming galaxy also correlate with an increasingly irregular star formation and gas distribution, from a regular, disk-like morphology (NGC 3032) to disturbed ionized and molecular gas distributions (NGC 3489; Figure 5.11 and Crocker et al. in prep) to highly asymmetric molecular gas distributions (NGC 4550; Crocker et al. 2009). These increasingly irregular morphologies additionally correspond to more centralized star formation at lower SFR (compare NGC 3032, NGC 3156, and NGC 4550 in Figure 5.3*a*).

In the absence of a replenishing gas reservoir, widespread star-forming galaxies will experience declining SFRs, causing them to move to the left in Figure 5.7; the system with the most intense star formation (NGC 3032) will therefore be expected to eventually move towards the other widespread star-forming galaxies. Likewise, there is evidence that the widespread star-forming galaxies with lower SFRs previously had more intense star formation events that extended to larger radii, implying earlier positions to the right of their current location in Figure 5.7. In particular, the young SSP ages (1$-$3 Gyr in NGC 3156, NGC 3489, NGC 4150; $\sim$6 Gyr in NGC 4550; Paper XVII) found throughout these galaxies, beyond

the star-forming regions observed in PAH emission, indicate that star formation activity occurred out to larger radii in the past than in the present. Only in the galaxies' centers do the final traces of significant star formation, along with the youngest stellar populations, remain.

With this evidence for the movement of widespread star-forming galaxies towards lower SFR with time (to the left in Figure 5.7), along with the trends in galaxy properties with SFR, we can associate star formation events with the global production of young stars in rapidly rotating kinematic structures (Figures 5.8 and 5.11). Additionally, star formation in this class appears to cease in an "outside-in" manner that is coincident with a consumption, disruption, and/or heating of the molecular reservoir. It is interesting to note, however, that throughout this process, the last vestiges of star formation are still proceeding according to established SFR-H_2 scaling relations (Figure 5.5).

In §5.6.1 below, we analyze the mechanisms that may be responsible for creating the widespread star-forming galaxies described here and for governing the cessation of their star formation.

5.5.4 Circumnuclear Star-Forming Fast Rotators

The circumnuclear star-forming galaxies (NGC 524, NGC 4459, NGC 4526, NGC 5838, NGC 5845) appear to represent a completely different physical state than the widespread star-forming systems described above. In Figure 5.7, these galaxies are seen to be those star-forming systems with higher masses and therefore lower molecular gas fractions and specific star formation rates. Consequently, the current star formation events do not dominate the SSP ages, all of which are measured to be intermediate to old in the regions of star formation. Unlike in the widespread star-forming galaxies, these regions of star formation are spatially very distinct, with all of the star formation, younger SSP ages, ionized gas, molecular gas, dust, and stellar kinematic structures being spatially coincident in well-defined central disks (see the definition of this class in §5.5.2). Within these disks, the surface densities of star formation and molecular gas approach those seen in circumnuclear starbursts in late-type systems (Figure 5.5). Additionally, the stellar and gas kinematic structures universally co-rotate with one another and with the old stellar populations in the quiescent regions of the host galaxies.

Unlike in widespread star-forming galaxies, none of the galaxies in this class have migrated all the way to the SFR-M_* relation (Figure 5.7), likely because the star formation only occupies a small region of the galaxy. Within these circumnuclear star-forming systems, a range of properties is seen. In some systems (NGC 4459, NGC 4526), all star formation indicators (PAHs, CO, [OIII]/Hβ, UV, low ionized gas velocity dispersion), where available, paint a consistent picture of on-going star formation in the region of the central disk. In contrast, the presence of on-going star formation in other circumnuclear star-forming galaxies (NGC 524, NGC 5838, NGC 5845) is more tenuous. These galaxies have more tentative PAH detections (§5.4.1) and only marginally detected younger SSP ages and metallicity gradients. Nevertheless, the PAH emission remains spatially coincident with thin, regular dust

disks (Paper V) and with embedded stellar kinematic structures (Figure 5.8). These systems may have reached the end of their star formation epochs, since only one (NGC 524; Crocker et al. in prep) is detected in CO and the other tracers of star formation (PAH, [OIII]/Hβ) can be affected by a B star population that has not yet died. Nevertheless, as in widespread star-forming galaxies, even systems with trace amounts of molecular gas and PAH emission form their stars according to SFR-H_2 scaling relations (Figure 5.5).

In the following (§5.6.2), we speculate on the origins of gas responsible for this spatially distinct star formation event and on the mechanisms that spatially confine it into disks/rings.

5.5.5 Outliers

While the two classes described above neatly bring together two groups of early-type galaxies that have a large number of similar properties, several "outlier" galaxies in our sample (NGC 2685, NGC 2974, NGC 4477) resist such straightforward classification. Here, we discuss the characteristics of each of these unique systems in turn and relate them to the two main modes of star formation.

NGC 2685 is a prototypical polar ring galaxy, as is evident in a comparison of the morphology of the star-forming ring to the position angle of the galaxy and the stellar kinematics (Figure 5.11; see the molecular and atomic gas maps of Schinnerer & Scoville 2002; Morganti et al. 2006; but see also Józsa et al. 2009). This rare configuration is often attributed to the accretion of gas or a gas-rich satellite at a very specific orientation (see §5.6.1), but the relevant aspect for this discussion is that the resulting dynamics of the gas are unassociated with those of the stars, as in widespread star-forming galaxies. Moreover, NGC 2685 also resembles this class of star-forming galaxies in that it contains ubiquitous younger stellar populations (SSP age of 6 Gyr; Paper XVII) and ionized gas, the spatial distributions of which are unassociated with the current extent of the star formation event. In the following discussion, we therefore consider this system to be related to the widespread star-forming galaxies (see blue-green symbols in Figures 5.5 and 5.8); we elaborate on this relationship in §5.6.1.

NGC 2974 also contains a large-scale star-forming ring, detected in PAHs, broadband UV emission, and HI (Figure 5.3*a*; Jeong et al. 2007; Weijmans et al. 2008). In this system, the ring is morphologically and kinematically aligned with the stars (Figure 5.11; Weijmans et al. 2008). A probable interaction between this gas and a putative large-scale bar is responsible for generating the ring morphology (Krajnović et al. 2005; Jeong et al. 2007), suggesting that here, as with circumnuclear star-forming galaxies, there is a deep connection between stellar kinematic structures and the spatially distinct morphology of star formation. This galaxy resembles circumnuclear star-forming systems in other ways, including the co-rotation of the gas and the stars as well as the old SSP ages (11 Gyr; Paper XVII), and we consequently include NGC 2974 in our discussion of the circumnuclear star-forming galaxies in §5.6.2 (see blue-magenta symbol in Figure 5.8).

Finally, NGC 4477, though unremarkable in the morphology of its star-forming region (Figure 5.3*a*), is notable for being the most strongly barred of the star-forming galaxies in

our sample (see Figure 5.11), and the effects of this bar on the dynamics of the system are significant. The ionized gas kinematics are driven by the bar, producing a spiral inflow structure that creates a central star-forming disk kinematically aligned with the bar (Figure 5.11). The resulting strong misalignment between the stars and the ionized gas is another expected consequence of the bar, since the gas is confined to the bar's circular, non-intersecting orbits. In this sense, NGC 4477 resembles the circumnuclear star-forming galaxies in a fundamental way - the stars, ionized gas, and star formation activity are strongly related dynamically - despite more superficial differences. In addition, the stellar populations in NGC 4477, as with those in circumnuclear star-forming galaxies, are very evolved (SSP age of 11 Gyr; Paper XVII). This renders the detection of star formation in this galaxy slightly uncertain, although PAHs, molecular gas, dust, and age and metallicity gradients are detected in the central regions of this system (see Paper V; Paper XVII; Crocker et al. in prep). Given these similarities to circumnuclear star-forming galaxies, we discuss NGC 4477 alongside those galaxies in §5.6.2 (see blue-magenta symbols in Figures 5.5 and 5.8).

Despite being individually quite unique, these three "outlier" galaxies nevertheless each have important similarities to one of the two main modes of star formation. In the following sections, we speculate on these more nuanced connections and on the implications for the origin and evolution of the two main modes of star formation.

5.6 The Evolution of the Red Sequence

Our *Spitzer* data of the SAURON early-type galaxies make it possible to identify two different modes of star formation in these systems and to study the cessation of star formation in each regime. We cannot, however, make quantitative statements from these data about the origins of the star-forming gas or about the mechanisms responsible for the shut-down of the star formation. In this section, we nevertheless speculate on these topics, taking advantage of our multi-wavelength suite of data and the insights of §5.5, in order to probe the role of the widespread and circumnuclear modes of star formation in the evolution of fast rotator early-type galaxies. Afterwards, we briefly comment on slow rotators, none of which show any indication in our data for on-going or recent star formation; the formation and evolution of these systems are likely distinct from those of the fast rotators.

5.6.1 Widespread Star-Forming Fast Rotators

In §5.5, widespread star-forming galaxies were found to have an equal presence of co- and counter-rotating stellar and gaseous structures, a distribution of kinematic alignments that is strongly suggestive of an external origin for the star-forming gas (Paper V). Indeed, this has been explicitly demonstrated for two of the three systems with counter-rotating structures (NGC 3032: Young et al. 2008; NGC 4550: Crocker et al. 2009; see also Temi et al. 2009) and for the related "outlier" galaxy NGC 2685 by virtue of its polar ring (e.g. Schinnerer & Scoville 2002; Józsa et al. 2009). The widespread star-forming galaxies are

therefore more likely caused by the accretion of external gas than by secular evolution or rejuvenated star formation via internal mass loss (see also Sarzi et al. 2007). Given the high gas mass fractions and specific SFRs resulting from these accretion events, it is perhaps more correct to call such events gas-rich mergers, with the accreted system being either a galaxy or cold gas.

Furthermore, the majority of these mergers are likely minor mergers, since all of the widespread star-forming galaxies live in field or small group environments (with the possible exception of NGC 4150, which may be interacting with the outskirts of the Virgo cluster). It is difficult to justify invoking recent major mergers as the sole cause of the star formation in all six of these galaxies in our local (typical distance of a SAURON sample galaxy $\sim$20 Mpc) sample. While a major merger was likely responsible for one of these systems (NGC 4550; Crocker et al. 2009), the more frequent minor mergers (see e.g. theoretical results of Fakhouri & Ma 2008) are more logical causes for the star formation seen in most of the widespread star-forming galaxies. Similar conclusions have been reached by Kaviraj et al. (2009), who showed that the fraction of star-forming early-type galaxies, as detected in NUV, can be reproduced well by the rate of gas-rich minor mergers in cosmological simulations.

These minor mergers involve a large amount of gas that results in significant star formation throughout the system, bringing the remnants all the way to the SFR-M_* relation. The main progenitors of these mergers may have been quiescent early-type systems whose star formation has been rejuvenated; however, it is also possible that the main progenitors were spiral galaxies and that the minor merger is responsible for moving these galaxies off of the blue cloud, with the associated widespread star formation event representing the tail end of this process. Indeed, in the mass range of these galaxies, 60% of galaxies are late-type systems (from the mass functions of Bell et al. 2003 and Baldry et al. 2004), resulting in sufficient availability of such progenitors. Additionally, recent simulations have shown that S0-like galaxies can be produced by spiral galaxies subjected to single minor mergers (4:1 to 10:1; Bournaud et al. 2007b). The widespread star-forming galaxies, all morphologically classified as S0, are thus good candidates for the products of recent minor mergers.

In the wake of such (potentially formative) mergers, galaxies appear as widespread star-forming systems, which may in fact trace out the post-merger cessation of star formation in detail. Galaxies making this transition may initially resemble NGC 3032, the system that is forming stars very close to the SFR-M_* sequence and that is the youngest and most gas-rich galaxy in this class. As the molecular gas is depleted and/or disrupted, the star formation will cease first at large radii (§5.5.3). Indeed, the galaxies in which this is observed (NGC 3156, NGC 3489, NGC 4150) also have very high [OIII]/Hβ emission line ratios that Paper XVI associates with excitation by planetary nebulae in post-starburst galaxies. The residual star formation in these galaxies will fade to very low levels (as in NGC 4550) and eventually cease, after which the widespread star-forming galaxies are expected to migrate onto the sequence of quiescent galaxies in SFR-M_* space. This evolutionary process is somewhat modified in the polar ring galaxy NGC 2685, whose post-merger evolution (disruption of the gas and "outside-in" cessation of star formation) was halted by the special orientation of the interaction. The cessation of star formation in the resulting, rare polar ring feature

consequently may not follow a similar process to that in the other widespread star-forming galaxies, but the probable result, a quiescent lenticular galaxy, is the same.

When the star formation has ceased, galaxies will have intermediate SSP ages, with remnant B stars in the galaxies' centers that may produce marginal PAH detections (§5.4.1 and Figure 5.3*b*) and no corresponding molecular reservoir (Combes et al. 2007; Crocker et al. in prep). Candidate quiescent descendants of widespread star-forming galaxies may then be S0 systems with widespread intermediate SSP ages (5−10 Gyr), several of which have been identified in the SAURON sample in Paper XVII. Two of the youngest of these are NGC 7332 and NGC 7457 (SSP age of ∼3−5 Gyr; Paper XVII), both of which contain clearly disrupted interstellar media and very high [OIII]/Hβ emission line ratios. NGC 7332, in particular, is a likely descendant of an accretion event, caused by an interaction between this system and its companion gas-rich spiral galaxy. Atomic and ionized extra-planar gas structures connect these two galaxies and may be responsible for the central KDC visible in NGC 7332 (Falcón-Barroso et al. 2004; Morganti et al. 2006). However, the intermediate SSP ages in this galaxy and NGC 7457, along with the lack of detection of on-going star formation in the SAURON and *Spitzer* data, suggest that these systems are in fact quiescent relics, perhaps of widespread star-forming galaxies.

The cessation of star formation, which turns widespread star-forming galaxies into quiescent early-type systems, was shown in §5.5.3 to be coincident with the heating or exhaustion of the available molecular reservoir. Testing which of these processes is at work in widespread star-forming galaxies is not straightforward, but we can examine the state of the ISM to zeroth order in Figure 5.9, using H_2 masses measured by Schinnerer & Scoville (2002), Combes et al. (2007), Young et al. (2008), Crocker et al. (2008), and Crocker et al. (in prep) and HI masses compiled by Roberts et al. (1991) and measured by Morganti et al. (2006), all corrected to the distances assumed here. We find that the ratio of molecular to atomic gas declines steeply with SSP age; this decline reflects both a decreasing molecular component and a slightly increasing atomic component with age. However, this figure contains many upper limits and clearly requires more data, so we suffice to conclude that the observed phase of the ISM is not inconsistent with older systems having hotter interstellar media (more HI than H_2). Similarly, the data are also consistent with the end of star formation resulting from the gradual consumption of a finite reservoir of molecular gas (decreasing H_2 in the presence of constant HI).

The picture sketched in this section can thus be summarized as follows: A star-forming spiral galaxy or a quiescent lenticular galaxy undergoes a major or minor gas-rich merger, resulting in a bulge-dominated remnant. After the merger, the remaining gas settles into a plane, where it is gradually consumed or heated and therefore forms stars at ever decreasing rates. The star formation ceases in an "outside-in" manner, in which the star formation at large radii ends first, followed by that in the galaxy center. During this process, the galaxy is moving from the blue cloud, through the green valley, and eventually onto the red sequence. The residual star formation in this stage has created a young population that dominates the galaxy's stellar light and that rotates rapidly because of its (low velocity dispersion) gaseous origin. This process may therefore be connected to the production of the fastest rotating

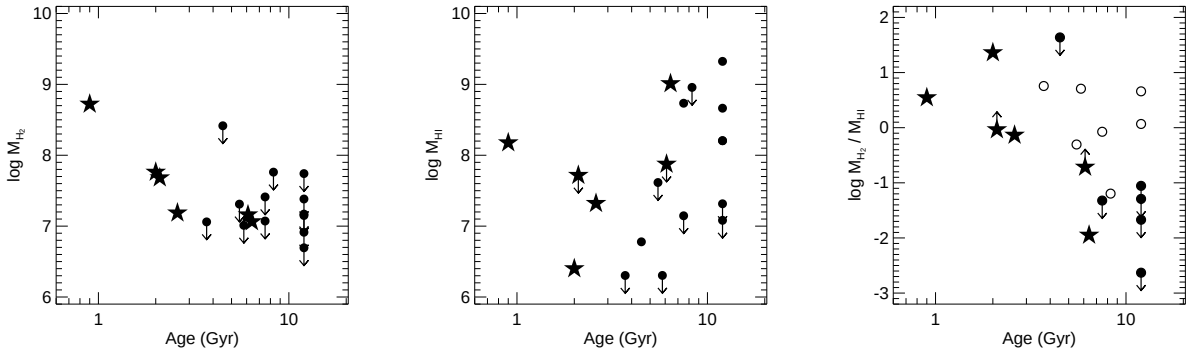

Figure 5.9: H_2 mass, HI mass, and the ratio of the two, as a function of SSP age measured over R_e (Paper XVII). The galaxies plotted are all SAURON systems classified as lenticular, excluding the circumnuclear star-forming star-forming galaxies where applicable. For the H_2/HI ratio, systems for which both the H_2 and HI masses are constrained only with upper limits are shown with open circles. In all plots, widespread star-forming galaxies are indicated with stars.

early-type galaxies.

5.6.2 Circumnuclear Star-Forming Fast Rotators

For the circumnuclear star-forming galaxies, in contrast, it is less straightforward to deduce the gas origins from the observations. Given the co-rotation of the gas and the stars in all circumnuclear star-forming systems (excepting NGC 4477, in which the gas kinematics are driven by the strong bar), a simple explanation would be that the gas originated within the galaxies, as a result of mass loss from evolved stellar populations. Temi et al. (2009) use a simple analytic calculation to demonstrate this scenario and show that the amount of gas generated by post-AGB stars is more than sufficient for late-time star formation in early-type galaxies (see also e.g. Ho 2009). Likewise, Paper XVI demonstrates that these stars dominate the ionized gas distribution and excitation in the SAURON sample, implying that the mass loss associated with this phase of stellar evolution plays a key role in regulating the ISM in early-type galaxies.

However, in one of the "outliers" associated with this class of galaxies (NGC 2974), the distribution of the star-forming gas in an outer ring is almost certainly caused by the interaction of accreted gas with a bar (Krajnović et al. 2005; Jeong et al. 2007). Some galaxies in the SAURON sample indeed show evidence of on-going gas accretion, in one of which (NGC 1023) the gas seems to be settling into co-rotation with the stars (Morganti et al. 2006); nevertheless, it remains unclear what the ultimate fate of this gas will be. With the available data, we therefore cannot rule out an external origin for the star-forming gas in at least some of the circumnuclear star-forming objects.

Although definite statements cannot be made about the origins of the gas in circumnuclear star-forming galaxies from the data presented here, their star formation can clearly be identified as a rejuvenation inside previously quiescent stellar systems. This is evident in the combination of the regular, confined star-forming structures with the presence of uniformly old stellar populations (SSP age $\gtrsim$10 Gyr; Paper XVII) outside of the star-forming regions in these galaxies. If the gas causing this rejuvenation has internal origins, the similar stellar mass loss rates in all galaxies imply that this mode of star formation may be common to the majority of fast rotators. Likewise, if the gas comes from wet minor mergers, it is expected to have been replenished at least once in the past 10 Gyr in these massive galaxies (Fakhouri & Ma 2008). In either case, all fast rotating galaxies would be equally eligible for such star formation events.

In this scenario, the only difference between those fast rotating galaxies with on-going circumnuclear star formation and those without is the amount of gas in the system. In the Toomre criterion for the stability of a system against star formation, the stability Q depends on the epicycle frequency, the sound speed of the gas, and the surface density of the gas. For the SAURON galaxies, we have explicitly tested that the epicycle frequency radial profiles show no systematic differences between galaxies with and without circumnuclear star formation. Consequently, gas of similar surface densities embedded in all of the fast rotators would result in similar Q values and thus similar star formation rates and morphologies.

The above results hint that this mode of star formation may be a transient and recurrent phenomenon in all fast rotators; it is therefore possible to estimate the duty cycle of this process. Since the SAURON sample is roughly complete for local early-type galaxies with stellar masses exceeding $\sim 10^{11}$ $M_\odot$, we restrict our estimate to this regime. One approximation of the duty cycle is simply the occurrence rate of on-going star formation in a central disk morphology; here, we observe this to be 2/9 for fast-rotating galaxies above our mass threshold (excluding the 3 circumnuclear star-forming galaxies that are below this mass threshold and the 2 circumnuclear star-forming galaxies that have only suggestive detections of on-going star formation). Another approximation comes from the lifetime of the star formation event relative to that of the system; the mean SSP age of $\sim$10 Gyr of massive galaxies and the gas exhaustion timescales in these galaxies of $\sim$1 Gyr (SFR $\sim$ several tenths of $M_\odot$ yr^{-1} and molecular reservoirs of several $\times$ 10^8 $M_\odot$) yield a duty cycle of 1/10.

In the $\sim$1/10 fast rotators in which the necessary gas (with sufficiently low mass fraction) is present, the star formation typically occurs in a well-defined central disk structure. This structure suggests a sharp radial limit exists in these galaxies. One natural explanation is via bar resonances, as are responsible for the large-scale ring galaxy NGC 2974 (Jeong et al. 2007), for the gas inflow in the strongly barred galaxy NGC 4477, and for the circumnuclear disks seen in the bulges of late-type galaxies (Kormendy & Kennicutt 2004). The role of bars in these systems is particular apparent in NGC 4477, in which the bar is driving a spiral structure in the gas and is funneling it towards the inner Lindblad resonance (ILR). Together with the lack of strong signatures of star formation (in SSP age or [OIII]/Hβ) in this galaxy, these observations suggest that this galaxy may be in an initial stage of circumnuclear star formation. The weaker bars detected in some of the other circumnuclear star-forming galaxies may have already driven the majority of the gas into the ILR and now function to maintain the observed radial limit. However, bars are not the only possible explanation for the radial limit of circumnuclear star formation events. An alternative explanation may be a balance between the background radiation within the galaxy and the cooling time, which decreases rapidly in the central regions, perhaps resulting in a sharply defined region in which the gas can cool and form stars.

When this star formation ceases, the descendant galaxies will likely not be readily identifiable via gradually increasing SSP ages, unlike as in the case of widespread star-forming galaxies. This is due to the difficulty inherent in detecting a low mass ratio, intermediate age population on top of a prominent background of stars with SSP ages $\gtrsim$10 Gyr; even in the circumnuclear star-forming systems with on-going star formation, the measured SSP ages are quite high (several Gyr to 10 Gyr) because of this effect. However, residuals from this process may in fact be visible via the resulting increased metallicity in the younger population; indeed, in Paper VI, more than half of the fast rotators are found to contain "Mg b disks," flattened, higher metallicity structures with similar spatial scales to that seen in PAH emission in circumnuclear star-forming galaxies (see also Paper XVII). Moreover, the stellar disks that ought to be created from secondary star formation events are also observed to be ubiquitous in fast rotators; Paper XII notes that the presence of these embedded, flattened and rapidly rotating structures is in fact what defines fast rotating early-type galaxies as a

population. This mode of recurrent and transient star formation may contribute to these components in all fast rotators.

The picture emerging here can thus be summarized as follows: A quiescent, fast rotating early-type galaxy acquires a new gas reservoir, either through internal stellar mass loss or through accretion of external gas. The gas settles into co-rotating orbits in the equitorial plane and forms stars, making the galaxy observable as a circumnuclear star-forming system. When the star formation ceases, over the course of $\sim$1 Gyr, the galaxy returns from being transiently star-forming back to passively evolving. The rekindled star formation from this event has replenished the galaxy's stellar disk, adding a younger, thinner, faster rotating, and more metal-rich (though low mass fraction) component to this structure. In this manner, the kinematically distinct stellar disks in fast rotators are maintained.

5.6.3 Slow Rotators

Much of the discussion so far in this chapter has focused on the evolution of fast rotator galaxies into and out of quiescent states. However, the SAURON sample of local early-type galaxies also contains a number of slow rotators, whose properties differ dramatically from those of the fast rotators. Of particular relevance to this discussion is the complete absence of star formation, as traced by PAH emission, in these systems. Instead, slow rotators can have significant X-ray halos of hot gas, unlike their rapidly rotating kin (Sarzi et al. 2007). These halos naturally explain the lack of star formation activity in the slow rotators, in which the ISM is simply too hot for gas to cool and condense.

The hot halos in slow rotators may be maintained by radio AGN, which are detected in some of the slow rotators both in the radio (Paper XVI) and in 8.0μm emission. Croton et al. (2006) have demonstrated that the presence of such AGN, operating in only the highest mass halos, is effective at replicating observed properties of red sequence galaxies in simulations. However, other mass-dependent "maintenance modes" not relying on AGN activity (e.g. Dekel & Birnboim 2006; Naab et al. 2007) can also reproduce the characteristics of this population and maintain hot halos.

Whatever the cause, it is likely that the slow rotators in the SAURON sample have been quiescent for much of their histories. These galaxies do not host on-going star formation, and their SSP ages are uniformly $\gtrsim$10 Gyr (Paper XVII). This is consistent with the cosmological (major and minor) mergers thought to be necessary to the formation of these objects (Naab et al. 2006; Burkert et al. 2008). This galaxy population is therefore distinct in that it does not appear to participate in the continuing dissipational evolution observed here in the fast rotators.

5.7 Conclusions

Using the synthesis of SAURON integral field spectroscopy and *Spitzer* mid-IR imaging, we have probed star formation processes in a representative sample of early-type galaxies.

We find compelling evidence for star formation in 8 of 48 early-type galaxies and potential evidence for star formation in an additional 5 of 48 systems. However, since the SAURON sample was designed to cover parameter space rather than to statistically sample it, the observed frequency of star formation in early-type galaxies should be used with caution, especially in the lower mass range where the SAURON sample is statistically incomplete.

Nevertheless, the representative nature of the SAURON sample does suggest that these results can be used to understand the properties of early-type galaxies as a population. With this sample and the associated auxiliary data, we find that star formation proceeds with the same surface densities and efficiencies as in spiral galaxies and circumnuclear starbursts. This suggests that the low-level star formation observed in early-type galaxies is essentially a scaled down version of similar processes in more vigorously star-forming galaxies. This analogy is also valid kinematically; we observe star formation to only be present in fast rotating early-type galaxies and to occur in flattened disk or ring morphologies.

Moreover, we find that star formation in these galaxies happens in one of two regimes: in the first, star formation is widespread and has no obvious link to stellar and gas kinematic substructures, while in the second, star formation is a spatially distinct process, often circumnuclear, whose extent corresponds well to that of the observed ionized gas, molecular gas, dust, and embedded stellar disks. Analysis of the galaxies in each regime and their relation to the early-type population as a whole indicates that these two classes in fact represent very different stages in the evolution of red sequence galaxies.

In widespread star-forming galaxies, the star formation events have relatively high mass fractions, perhaps due to the lower masses of these galaxies, causing them to dominate the galaxies' stellar light and kinematics. Together with the equal distribution of co- and counter-rotating kinematic structures in these systems that strongly indicates external origins for the gas, this suggests that widespread star-forming galaxies have recently undergone gas-rich minor mergers. Simulations show that such minor mergers are sufficient to transform star-forming spiral galaxies into red lenticular galaxies, and we suggest that the widespread star-forming galaxies are either in the final stages of such a transformation or represent a reinvigoration of star formation in previously quiescent lenticular galaxies. In either case, the eventual cessation of star formation in these galaxies is observed to occur in an "outside-in" manner as the molecular gas is heated or consumed and the galaxies become quiescent.

In contrast, circumnuclear star-forming galaxies are characterized by star formation with relatively low mass fractions, perhaps due to the higher masses of these galaxies. These galaxies are experiencing an epoch of renewed star formation, as evident in the evolved stellar populations outside the star-forming regions, from gas that was acquired either through internal stellar mass loss or very minor mergers. It is likely that this process, which has a duty cycle of $\sim$1/10 and can occur equally in all fast rotators, is important in reinforcing the embedded stellar disks that are found in this galaxy population. The circumnuclear star-forming star formation may therefore be a transient star formation event during the lives of all fast rotators, as they temporarily experience renewed star formation, resulting in additional thin, rapidly rotating, and metal-rich stellar disks.

A complete picture of early-type galaxies also includes the slow rotator population,

which shows no evidence for on-going or recent star formation in our data. In these systems, it is likely that a mass-dependent quenching mechanism, active only in these most massive galaxies, is continuously heating the interstellar media and preventing cooling and star formation. Consequently, the stars in these galaxies are uniformly old.

The scenarios of galaxy formation and evolution presented here will naturally need to be confirmed and refined. Future investigations with statistical samples will be crucial in probing the true nature of the two regimes of star formation proposed here, both of which are observed in only a handful of galaxies in our sample. Another avenue with great promise is augmenting the multi-wavelength coverage of the SAURON sample to include high resolution HI observations, in order to relate star formation processes to the morphology and kinematics of atomic gas reservoirs in these galaxies and thus further constrain the gas origins in both widespread star-forming and circumnuclear star-forming galaxies. Finally, extending the SSP modeling to allow multiple stellar populations can provide greater insight into the star formation histories of early-type galaxies. The results from these and similar studies will doubtlessly continue to improve our understanding of the formation and evolution of elliptical and lenticular galaxies.

Acknowledgments

We would like to thank Françoise Combes, Phil Hopkins, and Jacqueline van Gorkom for interesting discussions, and Martin Bureau, Alison Crocker, Nicholas Scott, and Lisa Young for providing access to their data pre-publication and for useful comments and suggestions. We also acknowledge the repeated hospitality of the Institute for Advanced Study, to which collaborative visits contributed greatly to the quality of this work, and support from Spitzer Research Award 1359449.

5.8 Appendix: Maps of Individual Galaxies

In this appendix, we display the full SAURON and *Spitzer* data for individual galaxies.

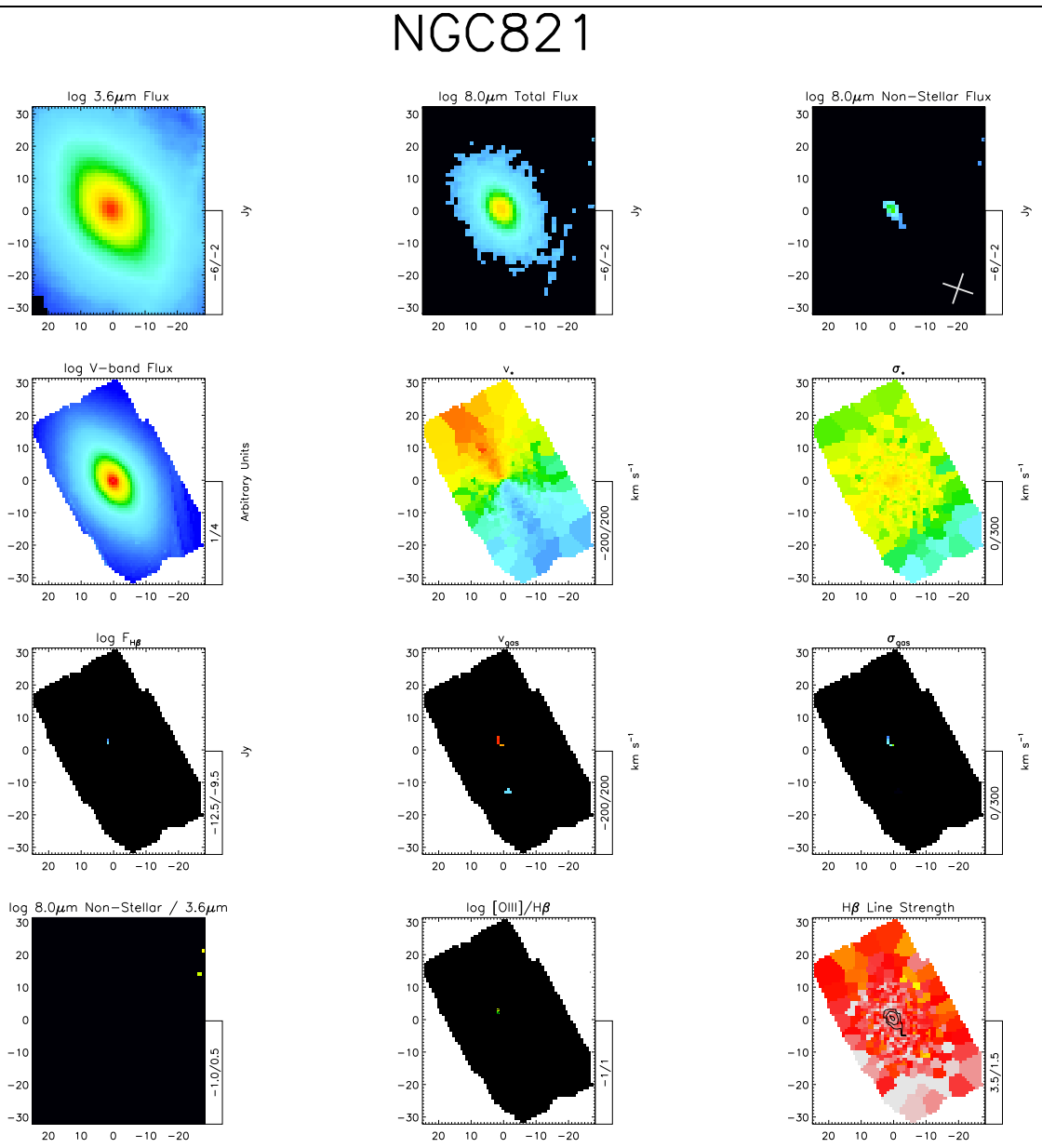

Figure 5.10: Comparison of SAURON maps and available *Spitzer* data for a representative galaxy with unremarkable infrared properties. *From left to right. Top row:* IRAC 3.6μm image, IRAC 8.0μm image, and IRAC 8.0μm image with stellar contribution removed (see text for details). The cross indicates the original axes of the IRAC CCD; high flux in a pixel (e.g. the galaxy center) can produce spurious structures along these axes. *Second row:* Broad-band image from SAURON integrated flux covering roughly the V-band, SAURON stellar velocity map, and SAURON stellar velocity dispersion map. *Third row:* SAURON Hβ emission line flux, SAURON ionized gas velocity map, and SAURON ionized gas velocity dispersion map (both of the latter derived from the typically stronger [OIII] emission). *Bottom row:* IRAC 8.0μm equivalent width (8.0μm non-stellar / 3.6μm) map, SAURON [OIII]/Hβ map, and SAURON Hβ line strength map (both of the latter with contours of the 8.0μm non-stellar map overplotted). In all maps, North is up and East to the left, and axes labels are in arcseconds.

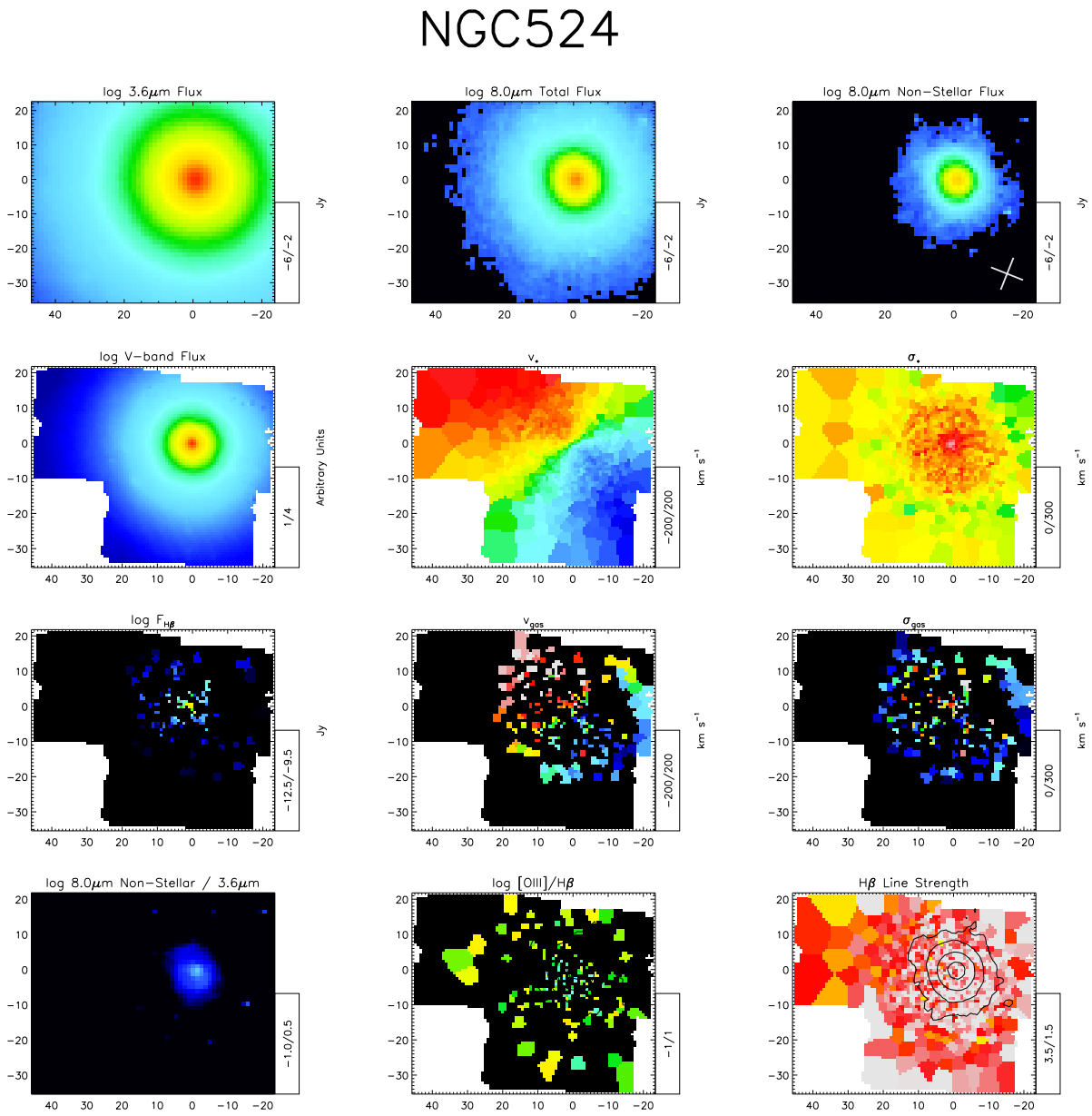

Figure 5.11: As with Figure 5.10, for all sample galaxies with significant infrared emission.

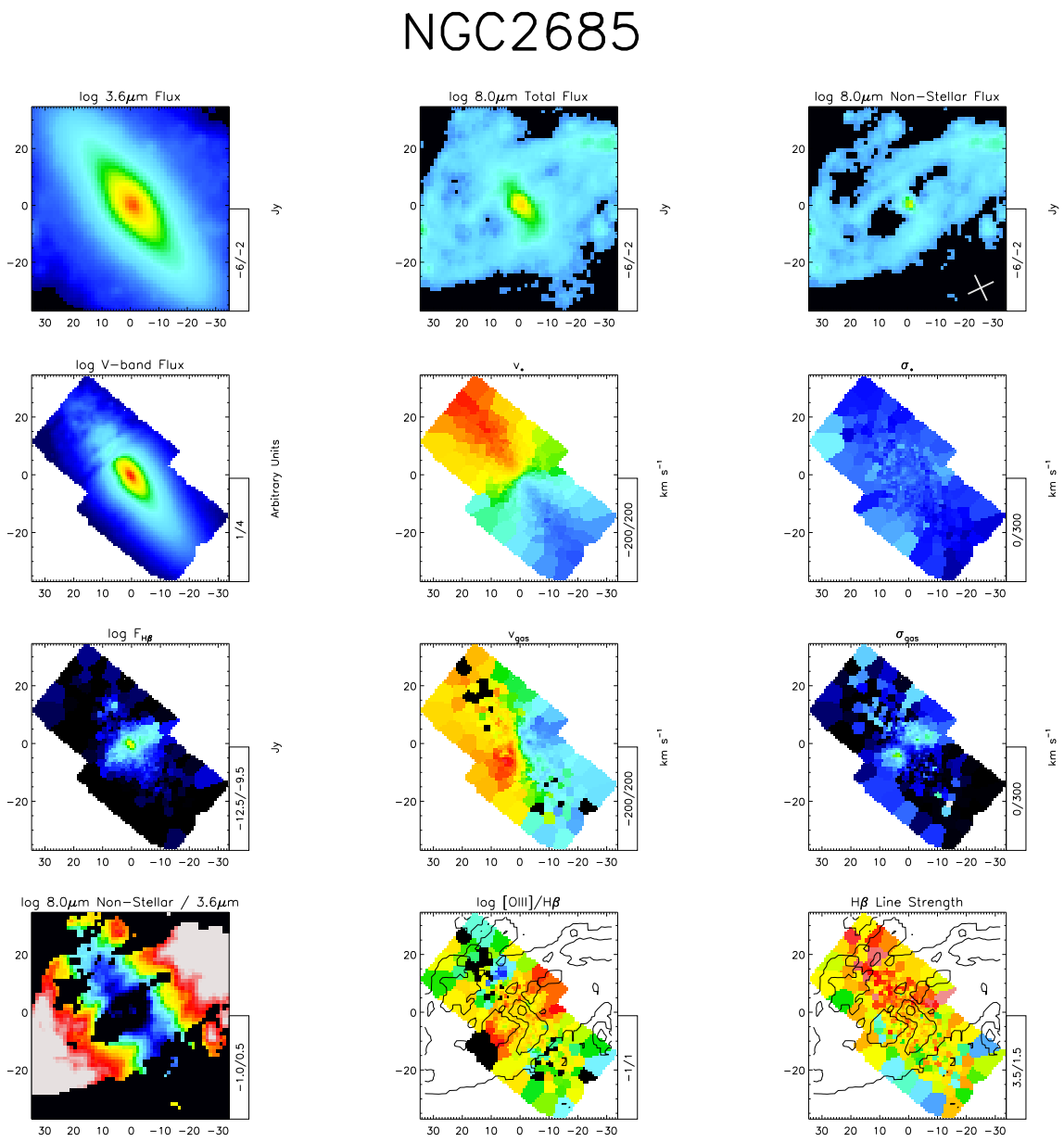

Figure 5.11: *continued*

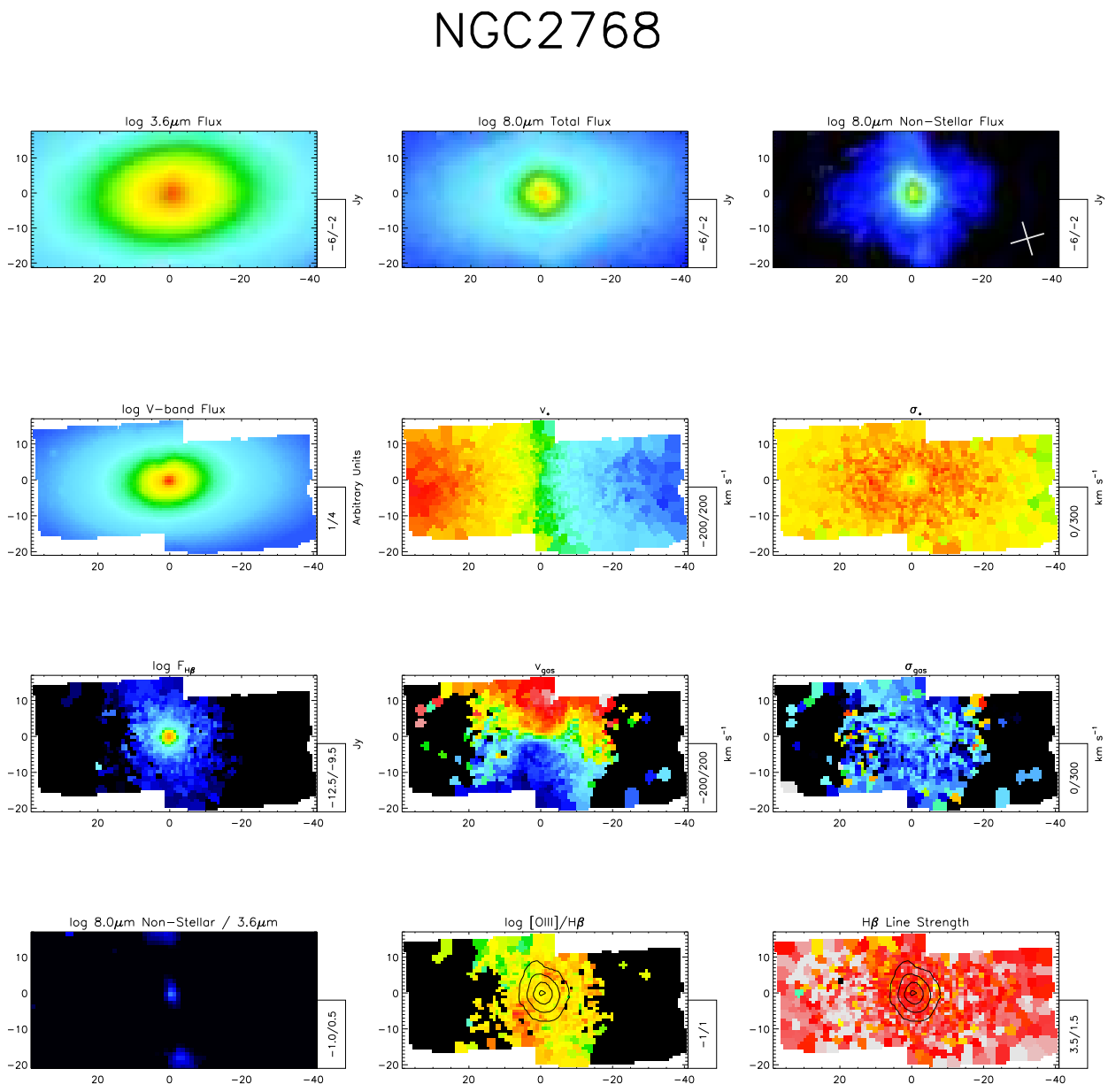

Figure 5.11: *continued*

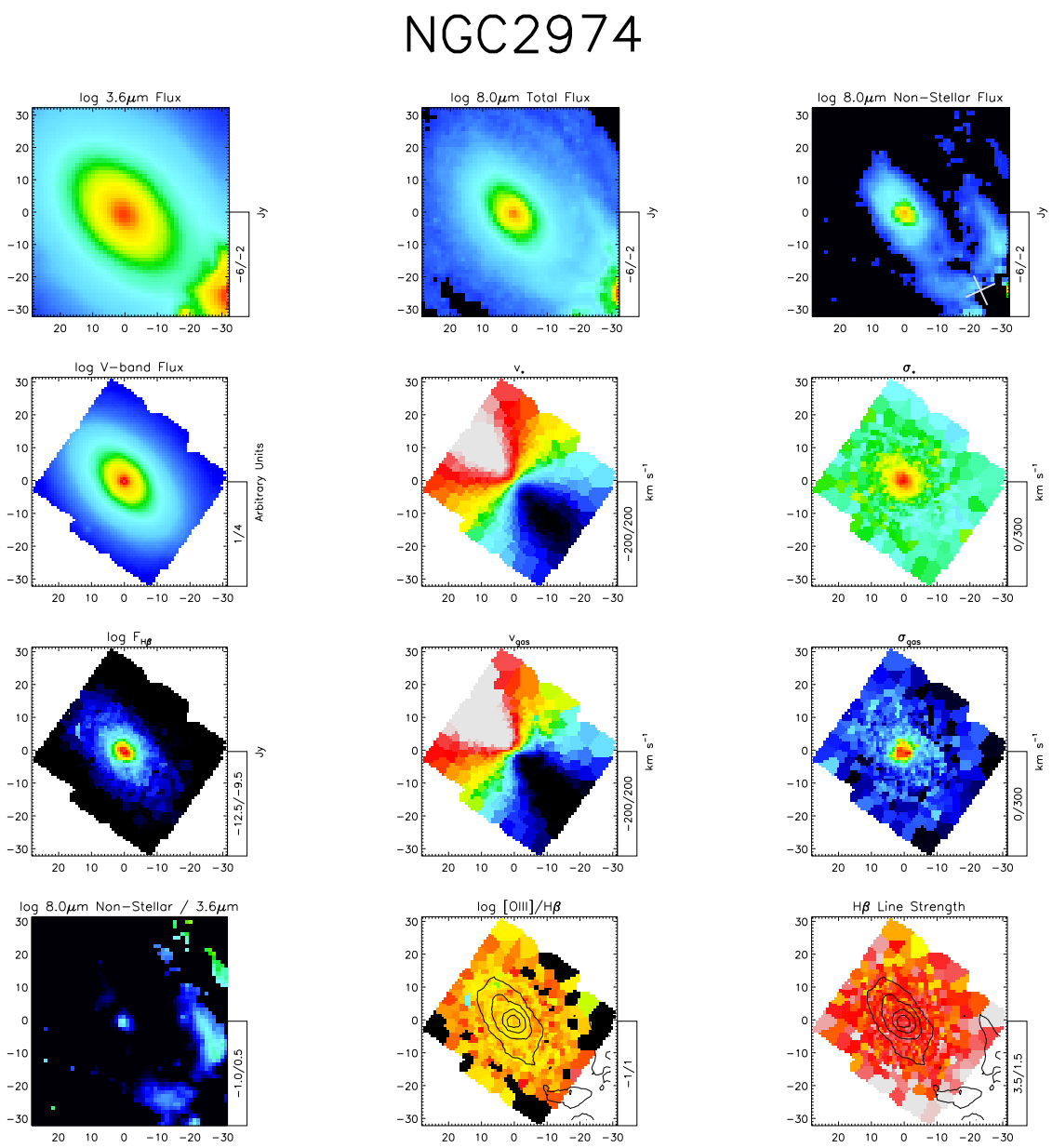

Figure 5.11: *continued* A foreground star is visible in the southwest corner of the *Spitzer* data.

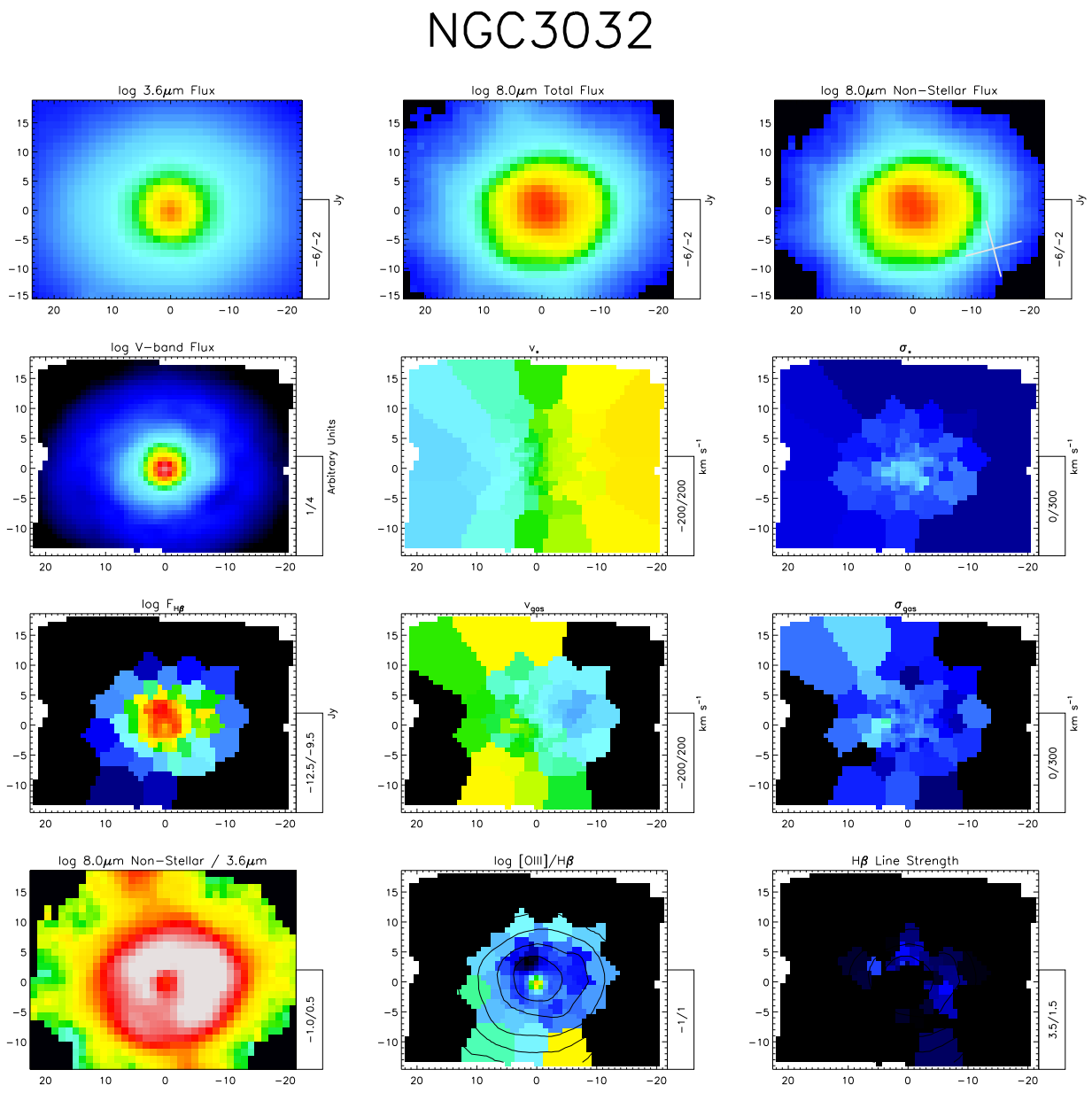

Figure 5.11: *continued.*

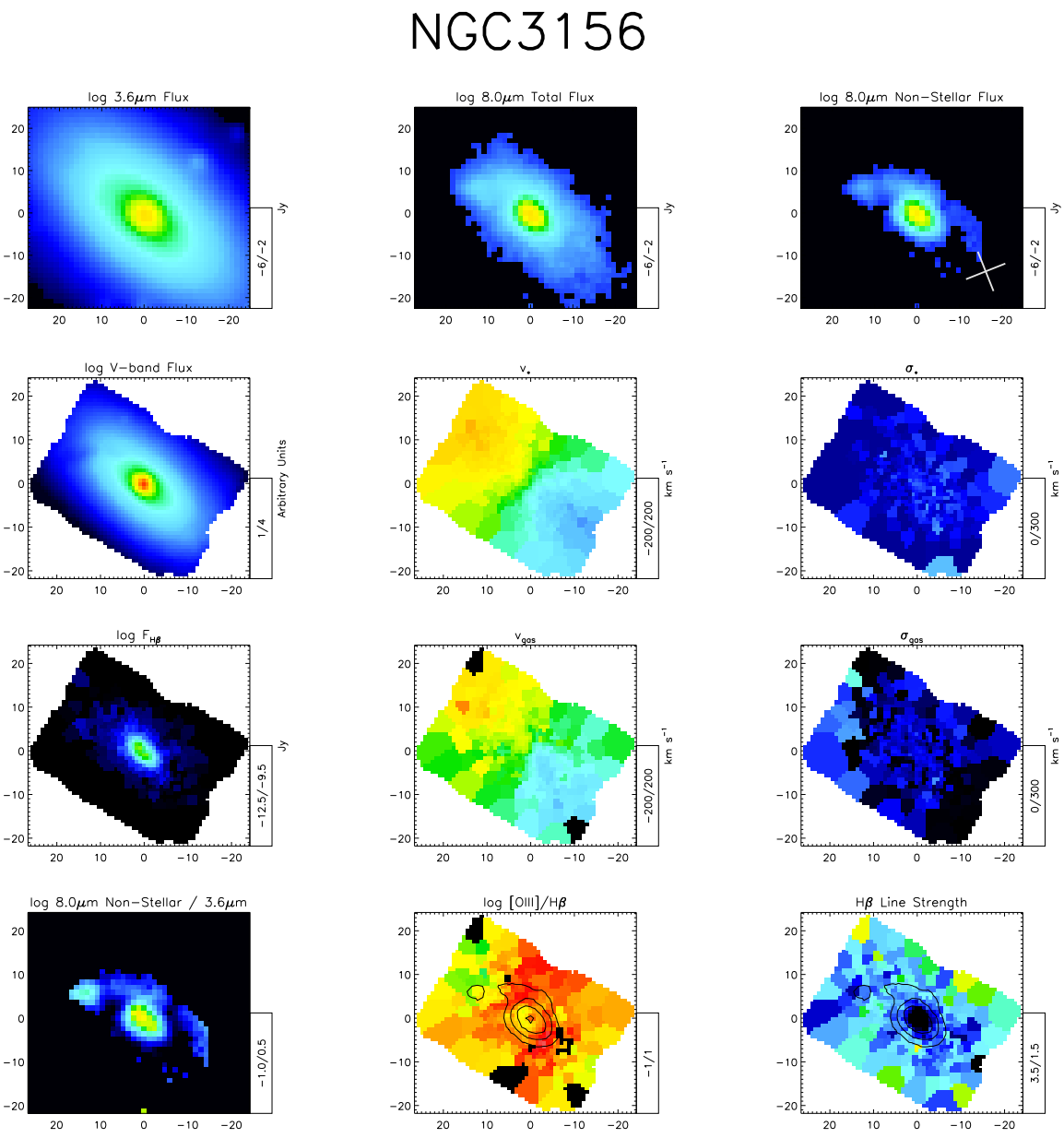

Figure 5.11: *continued*

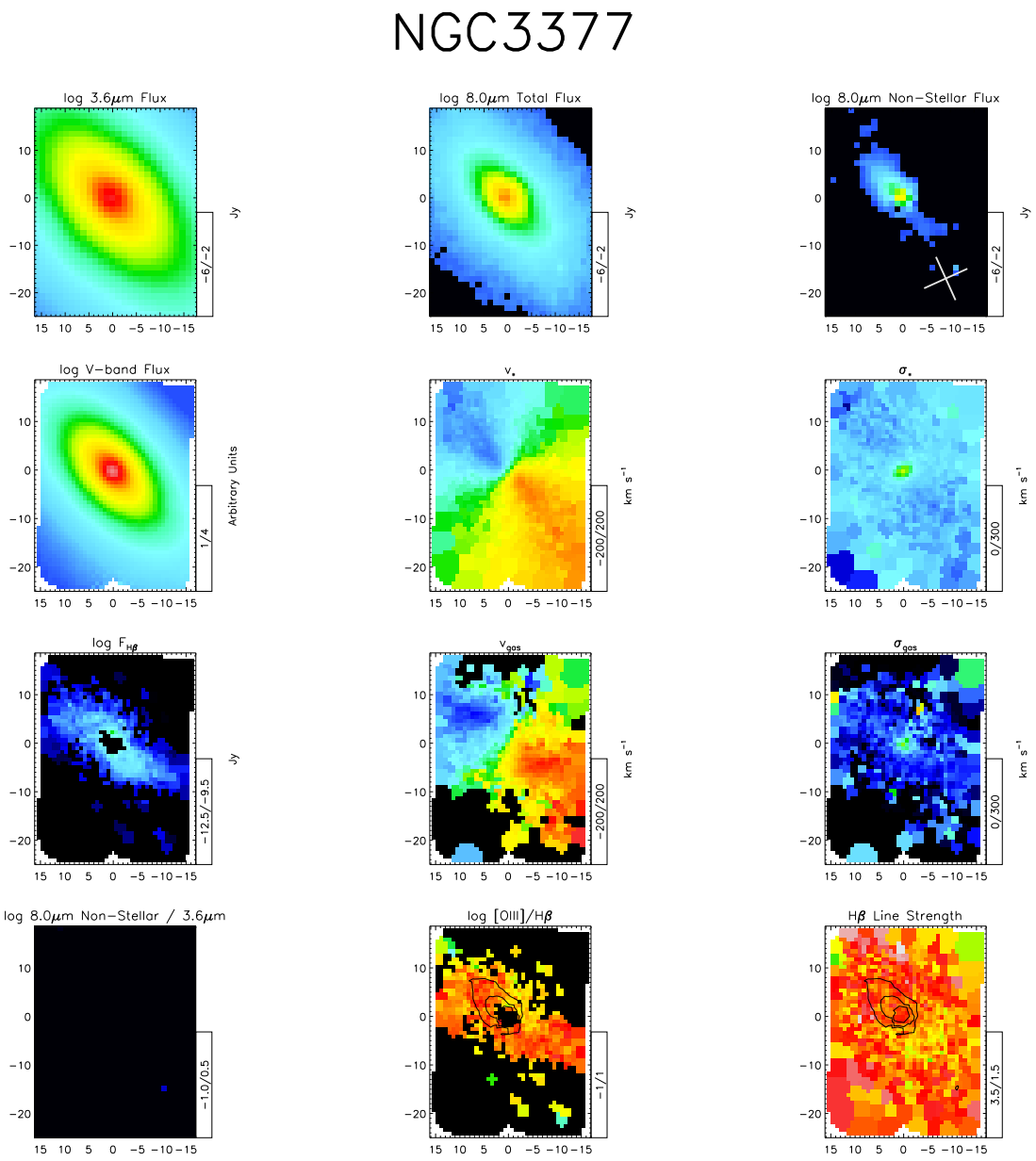

Figure 5.11: *continued*

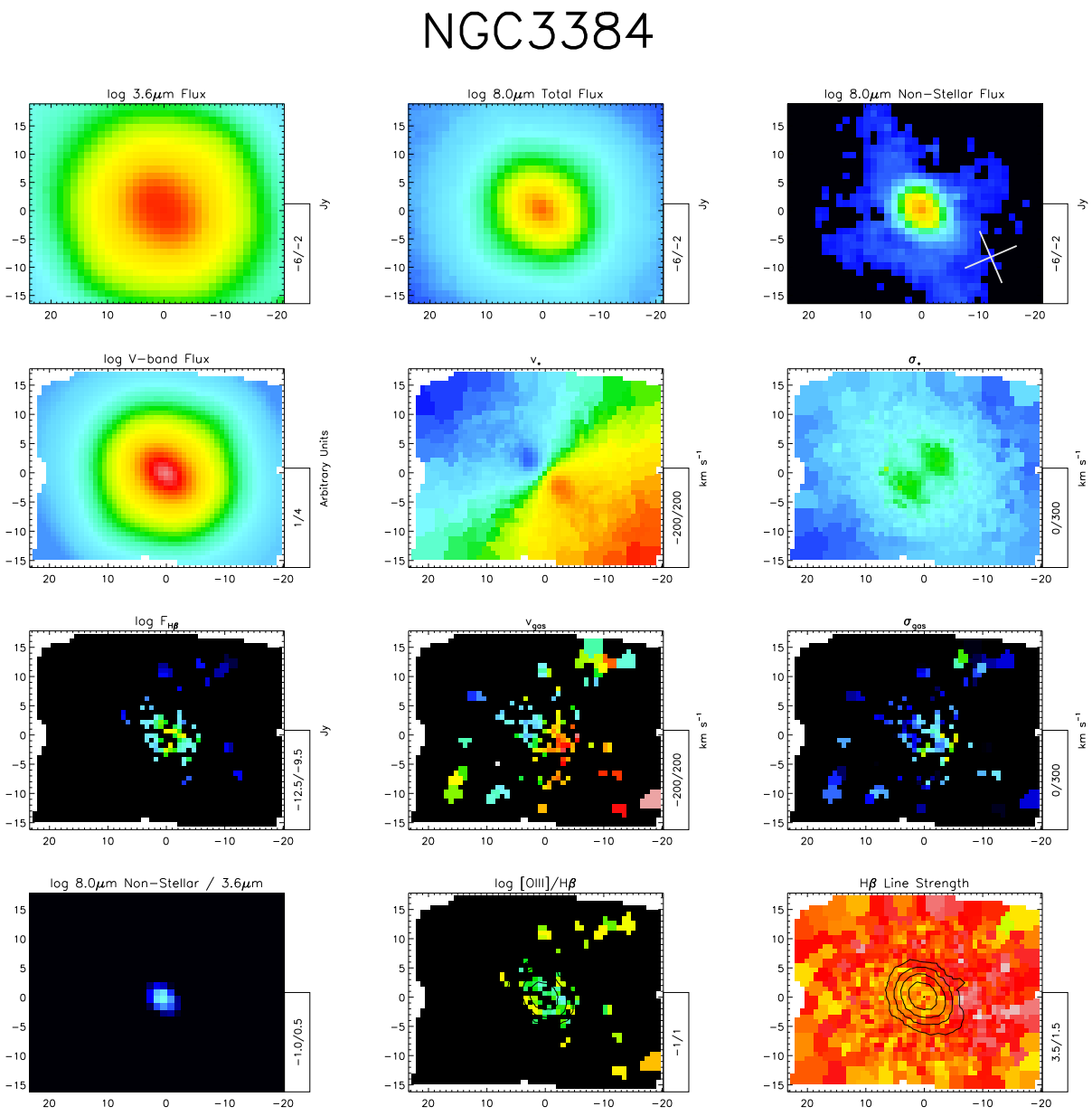

Figure 5.11: *continued*

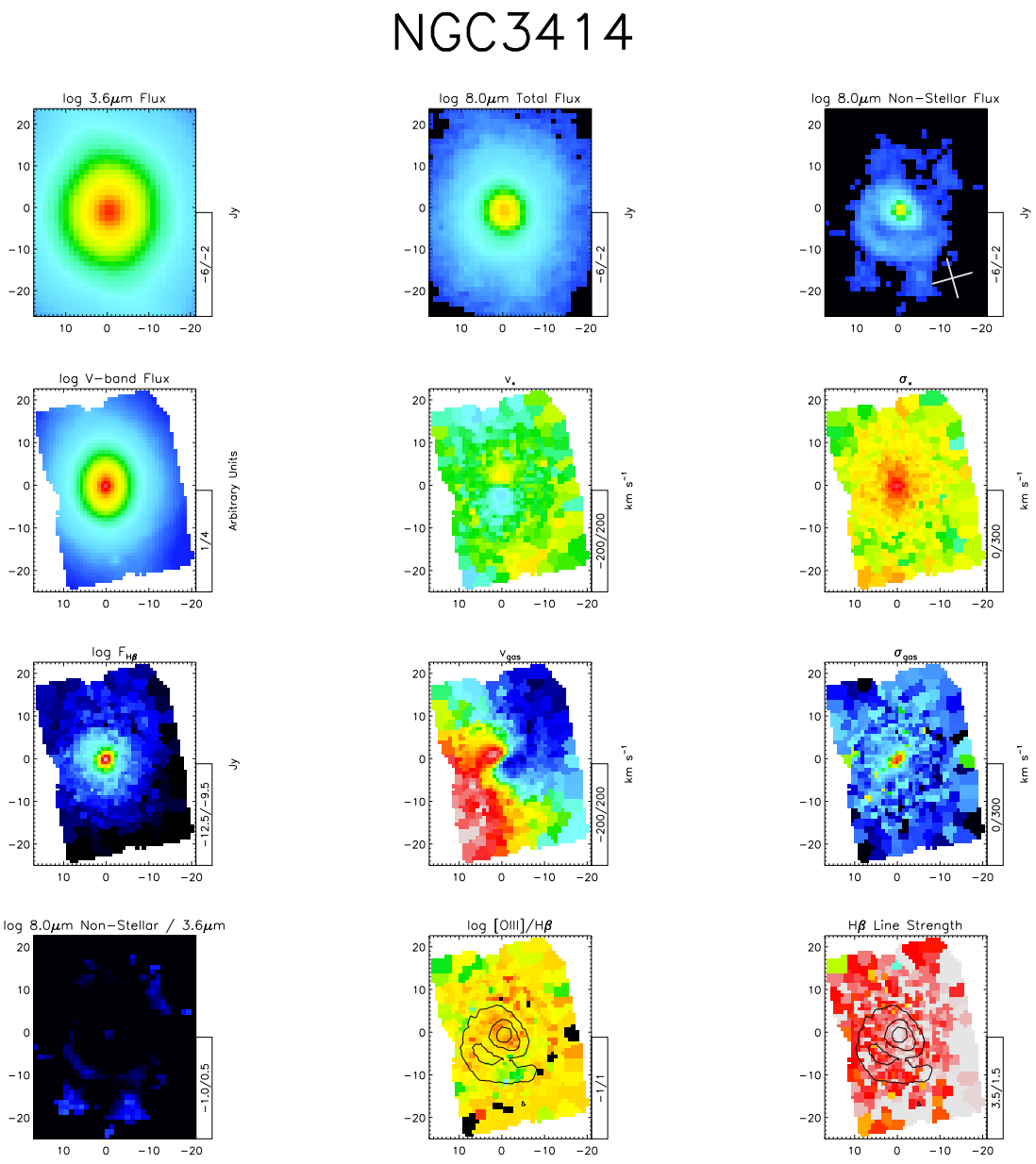

Figure 5.11: *continued*

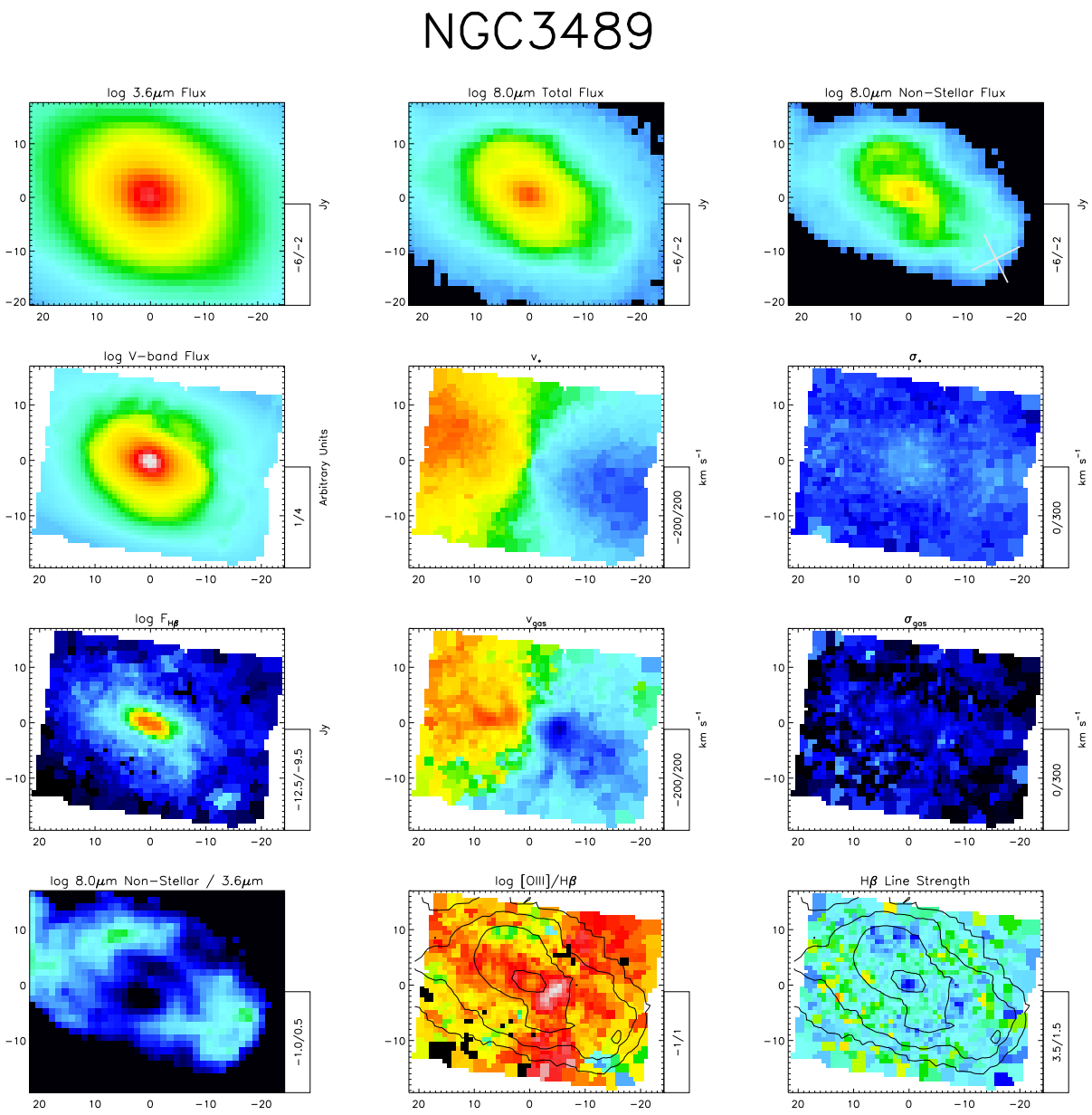

Figure 5.11: *continued*

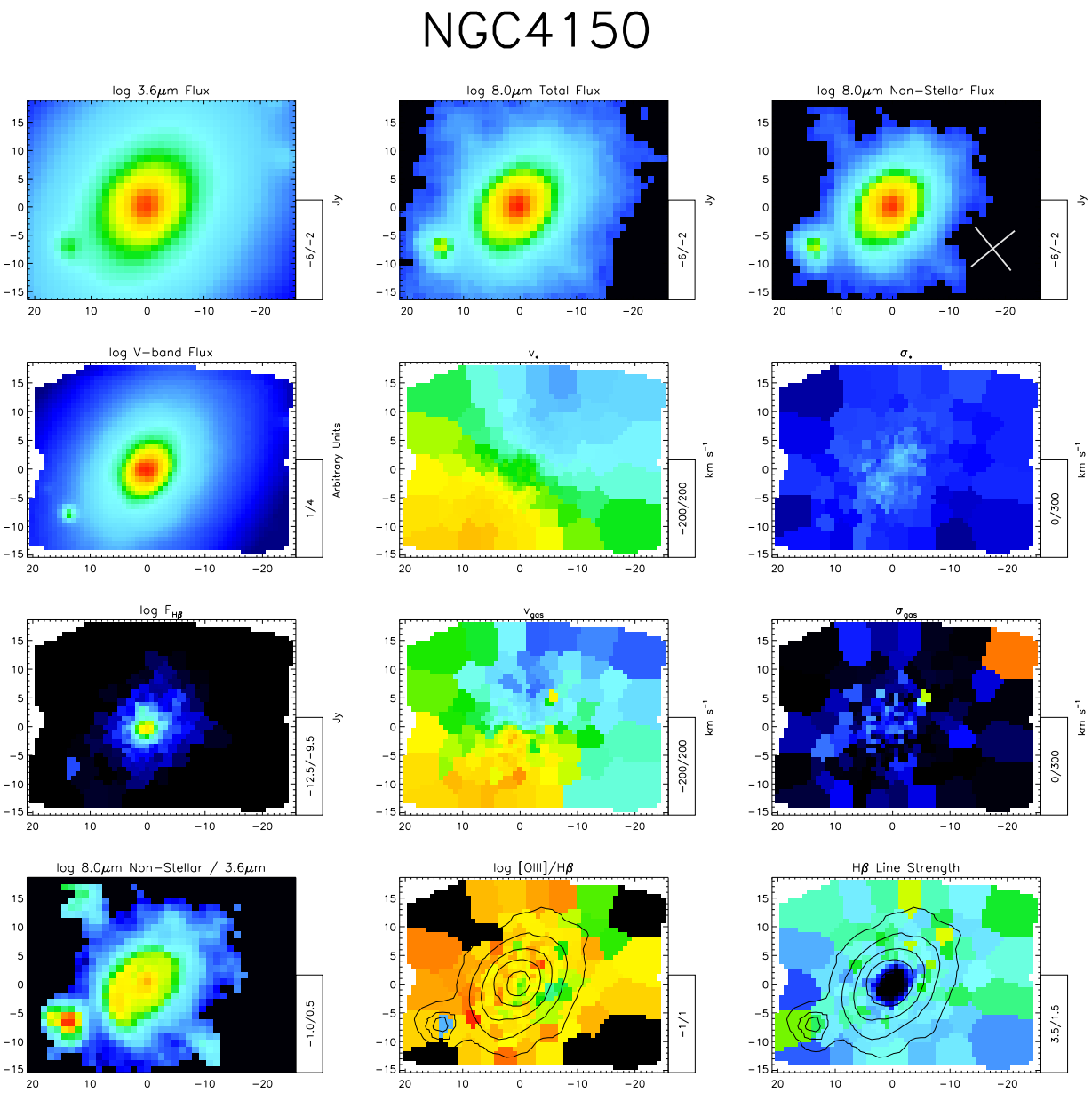

Figure 5.11: *continued* A quasar at z=0.52 (see Lira et al. 2000) is visible to the southeast of the galaxy.

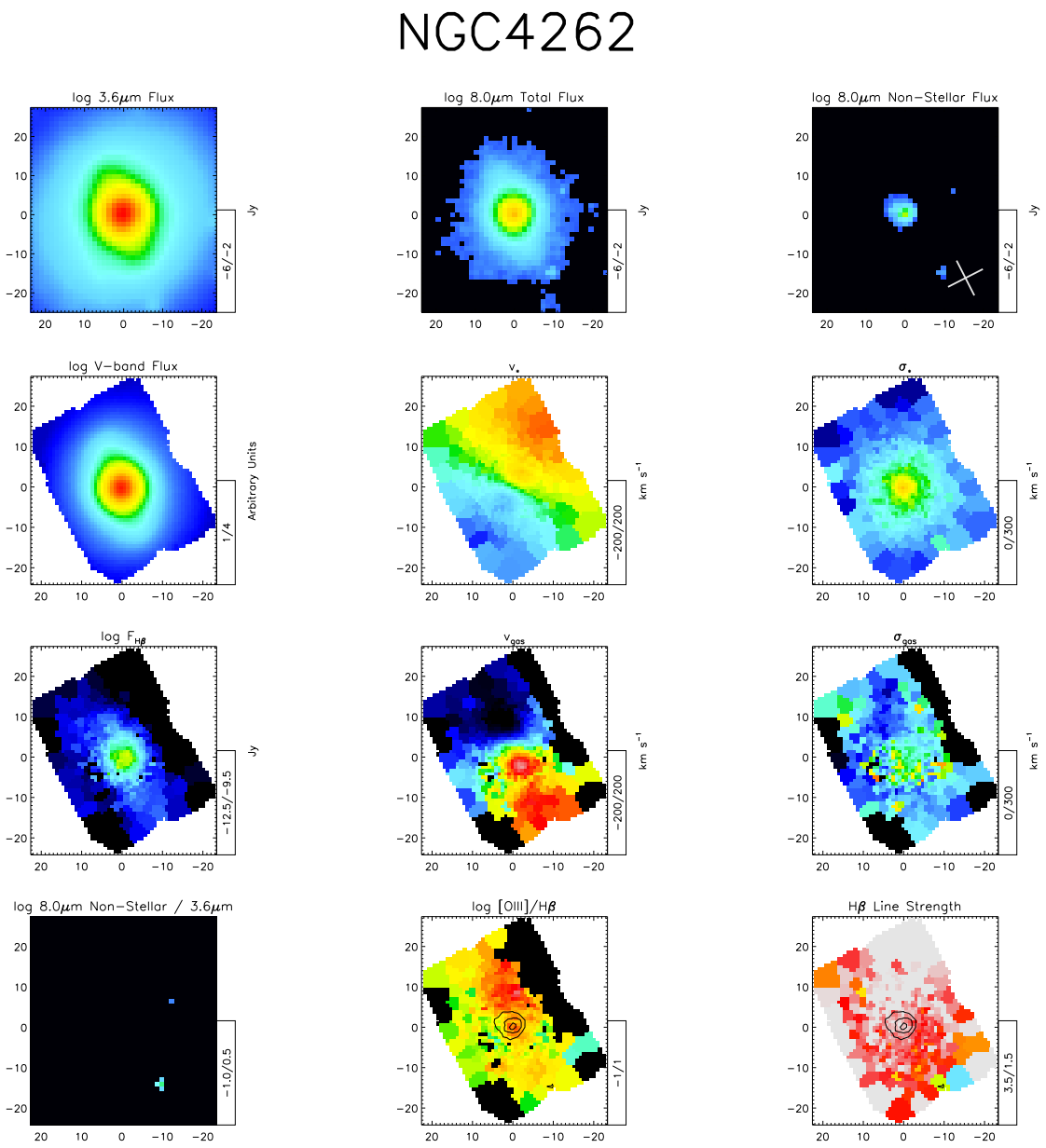

Figure 5.11: *continued.*

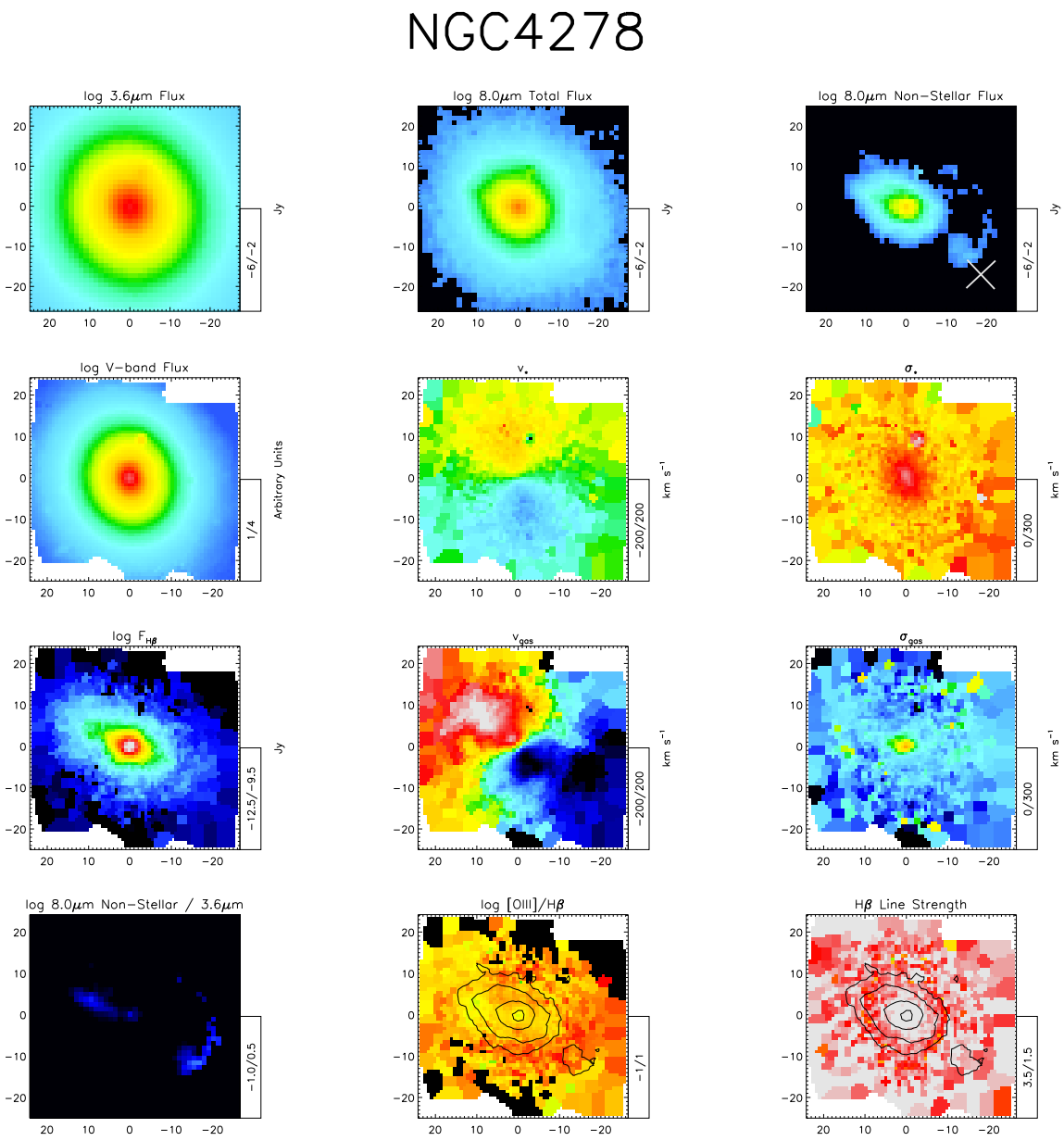

Figure 5.11: *continued*

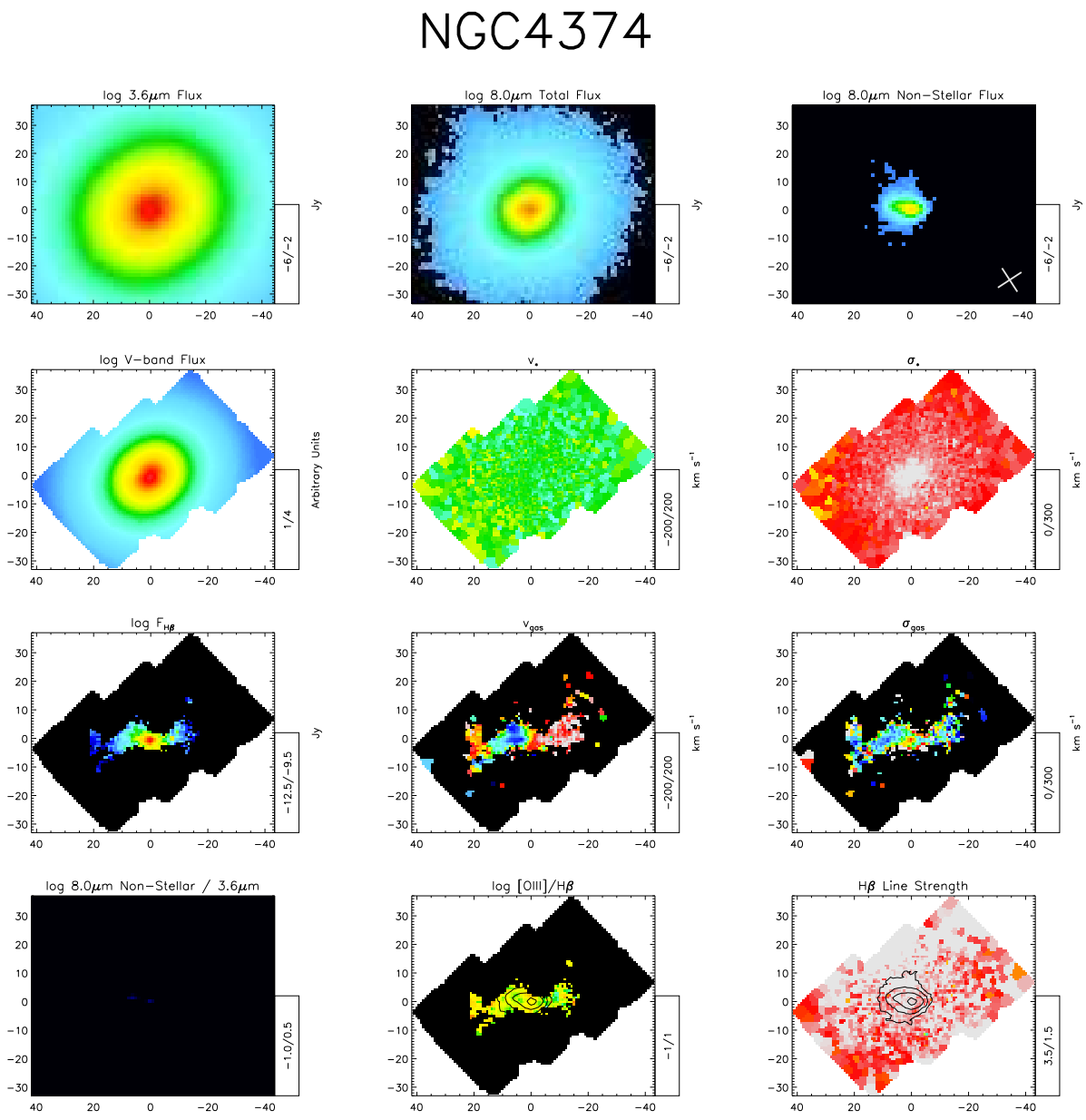

Figure 5.11: *continued*

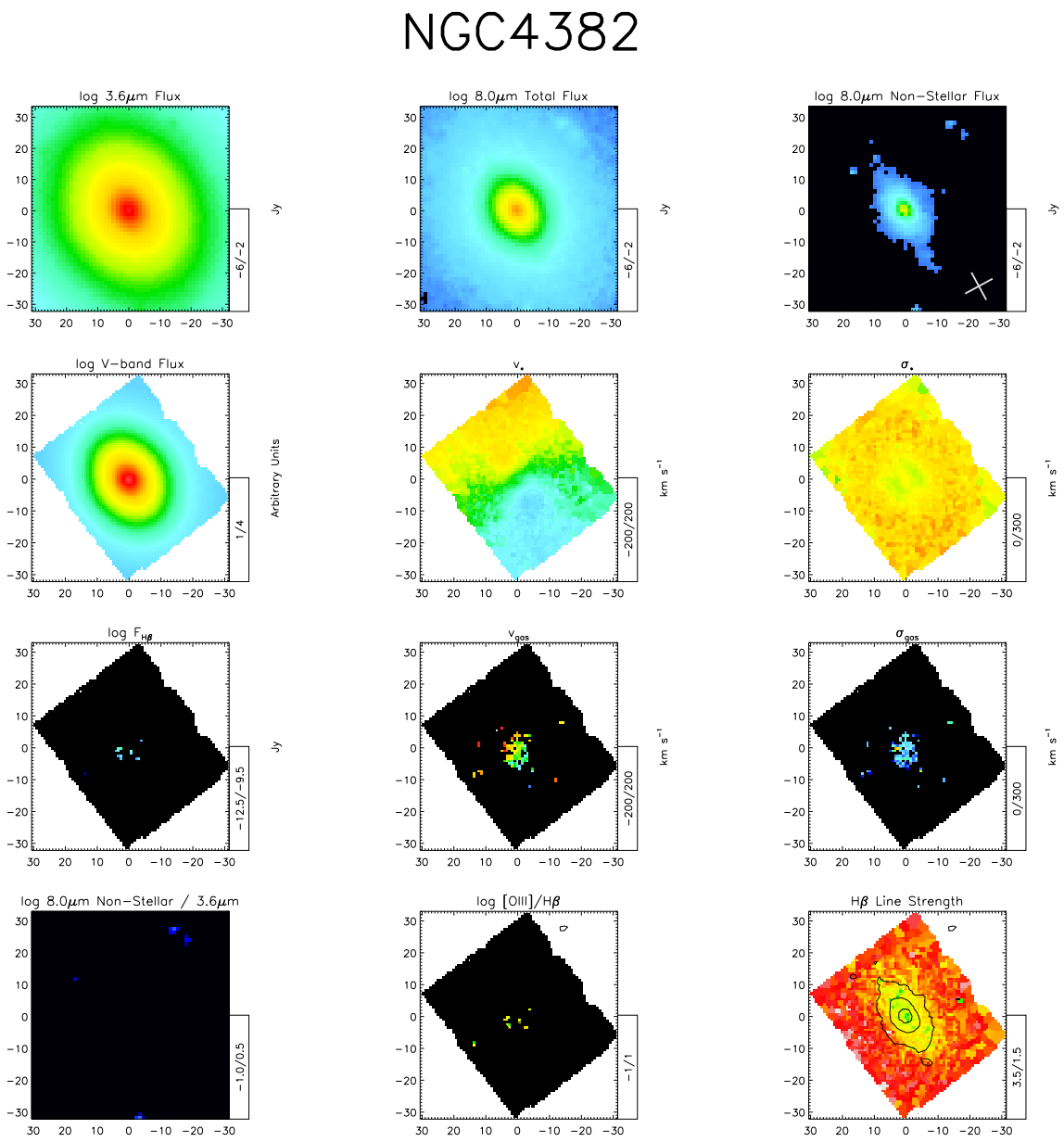

Figure 5.11: *continued*

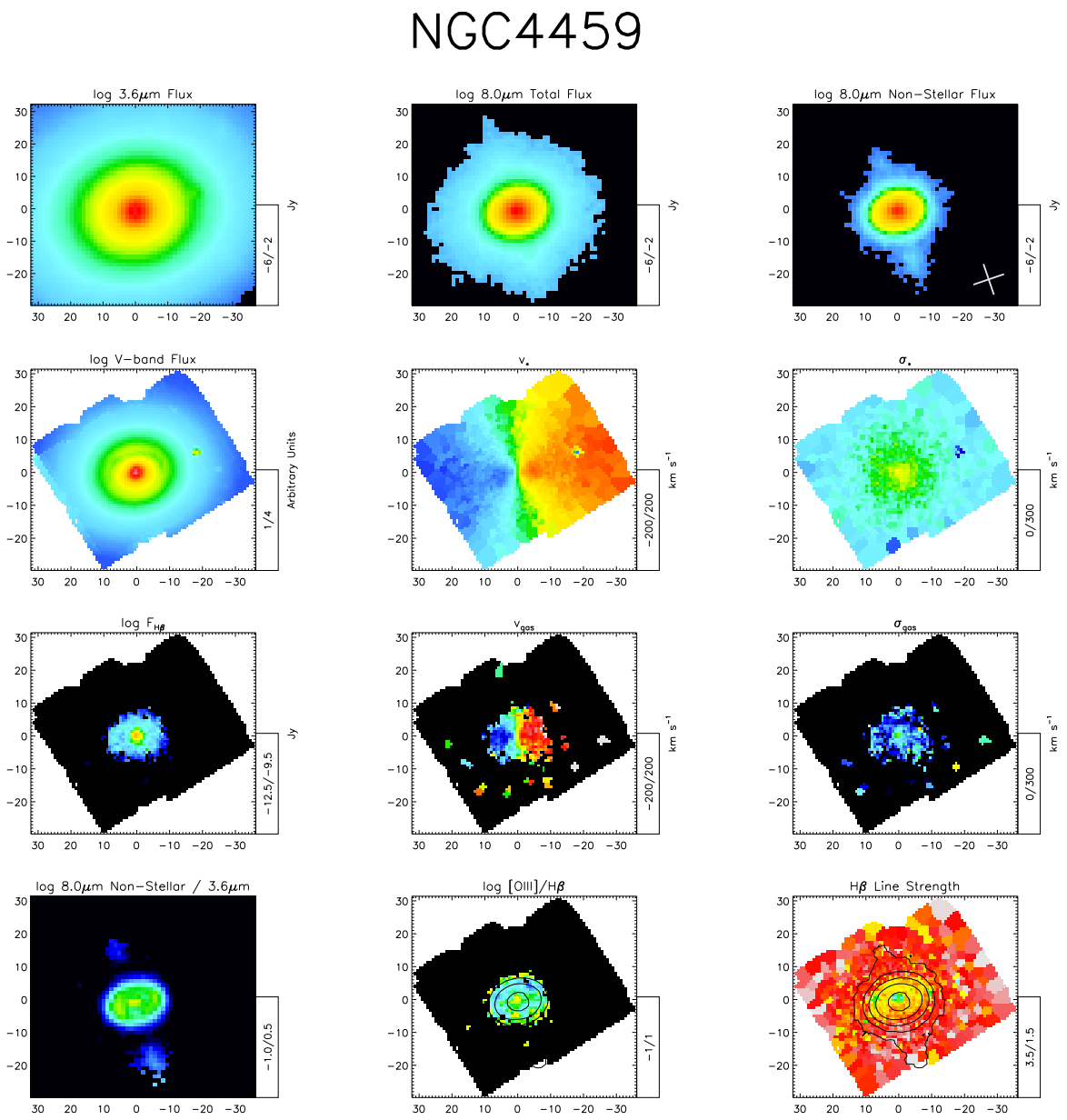

Figure 5.11: *continued*

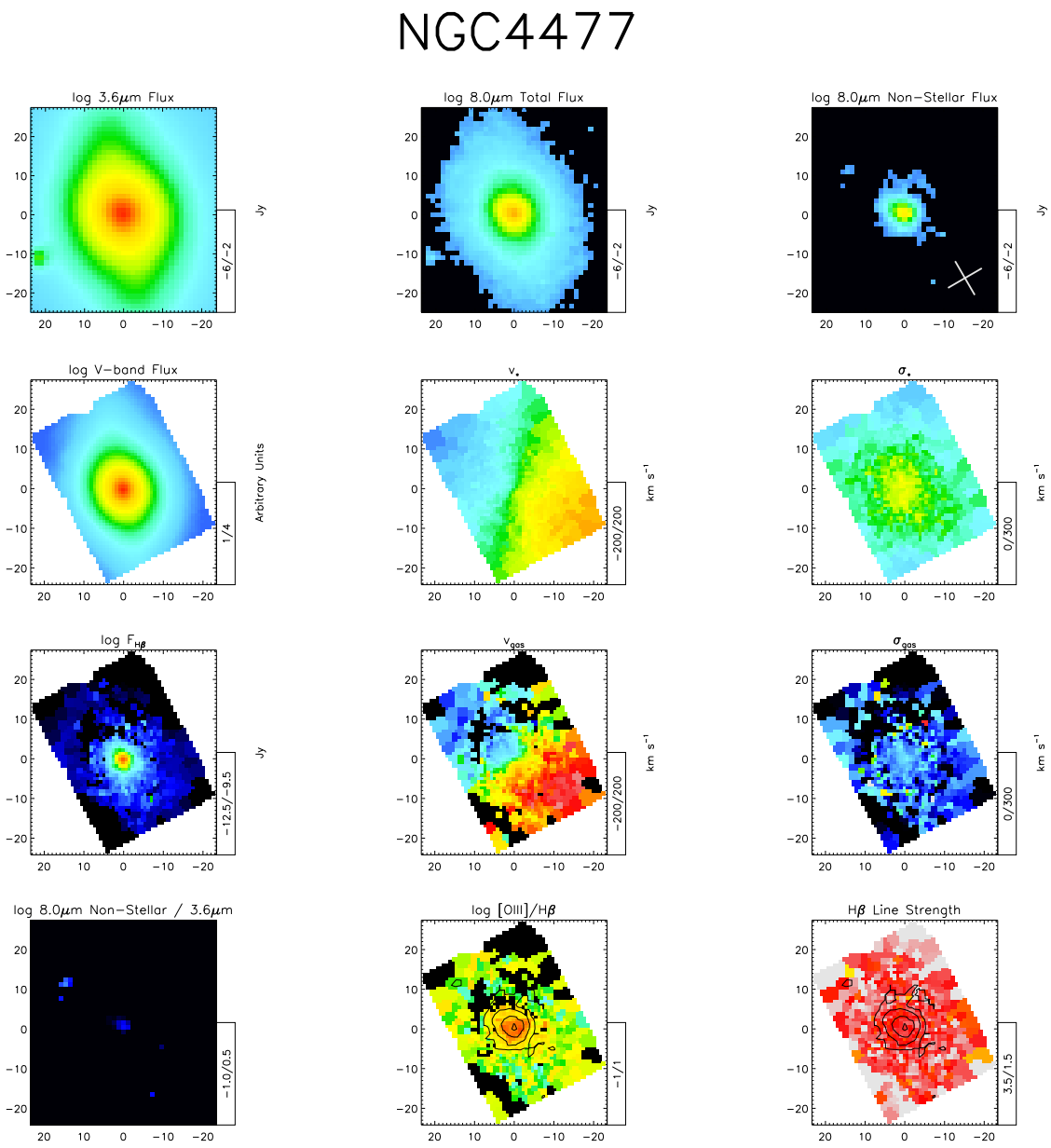

Figure 5.11: *continued*

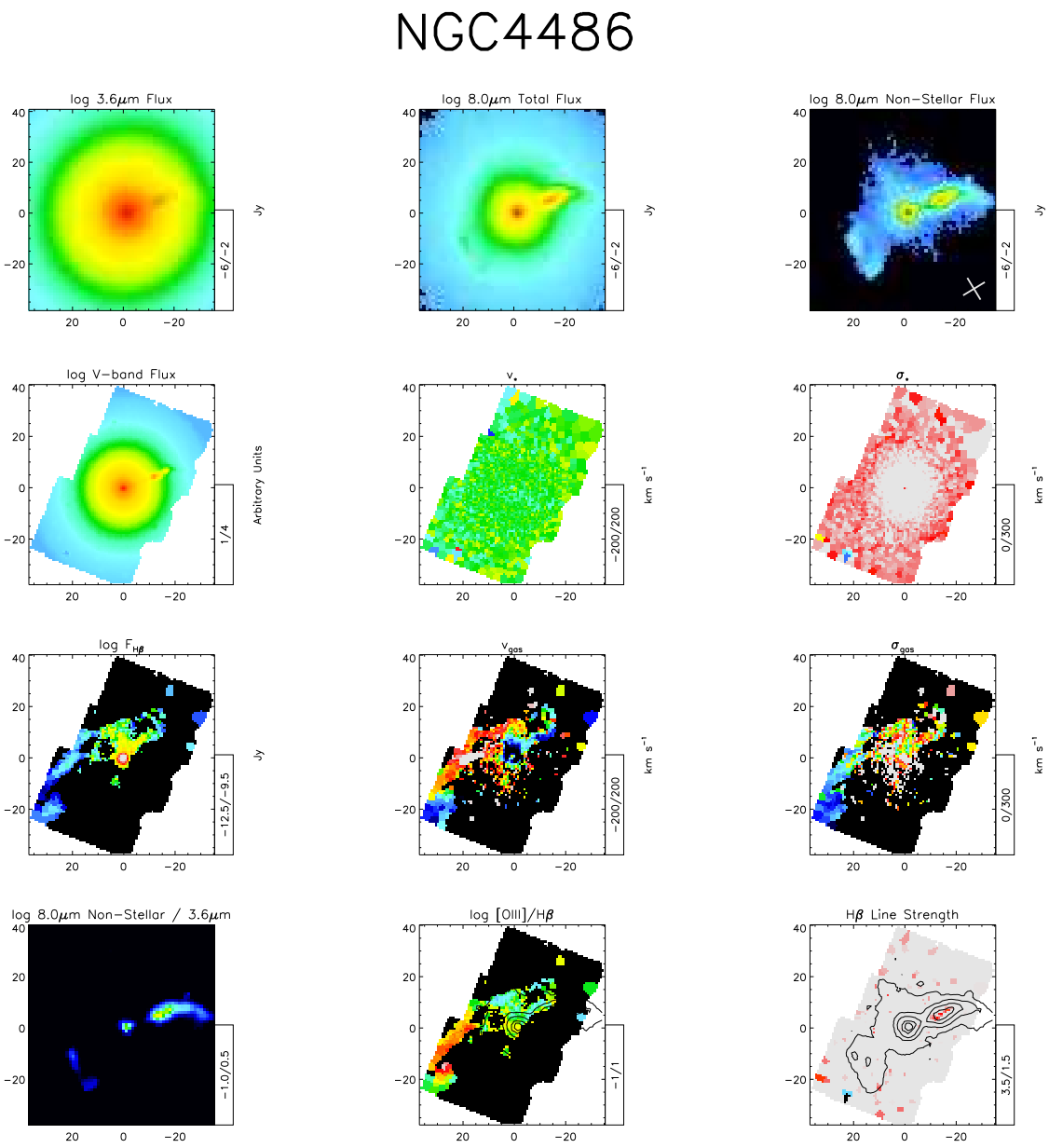

Figure 5.11: *continued*

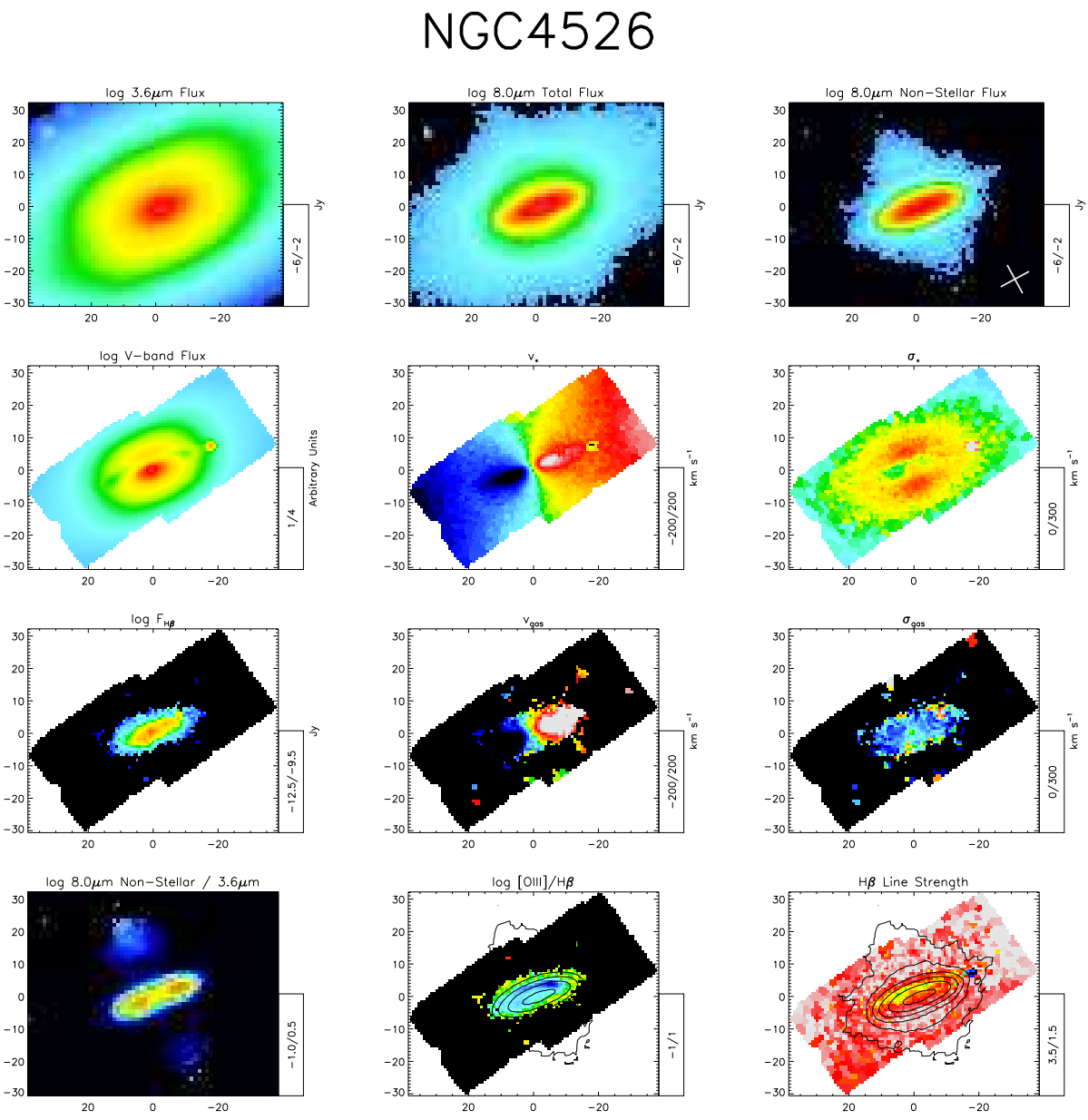

Figure 5.11: *continued*

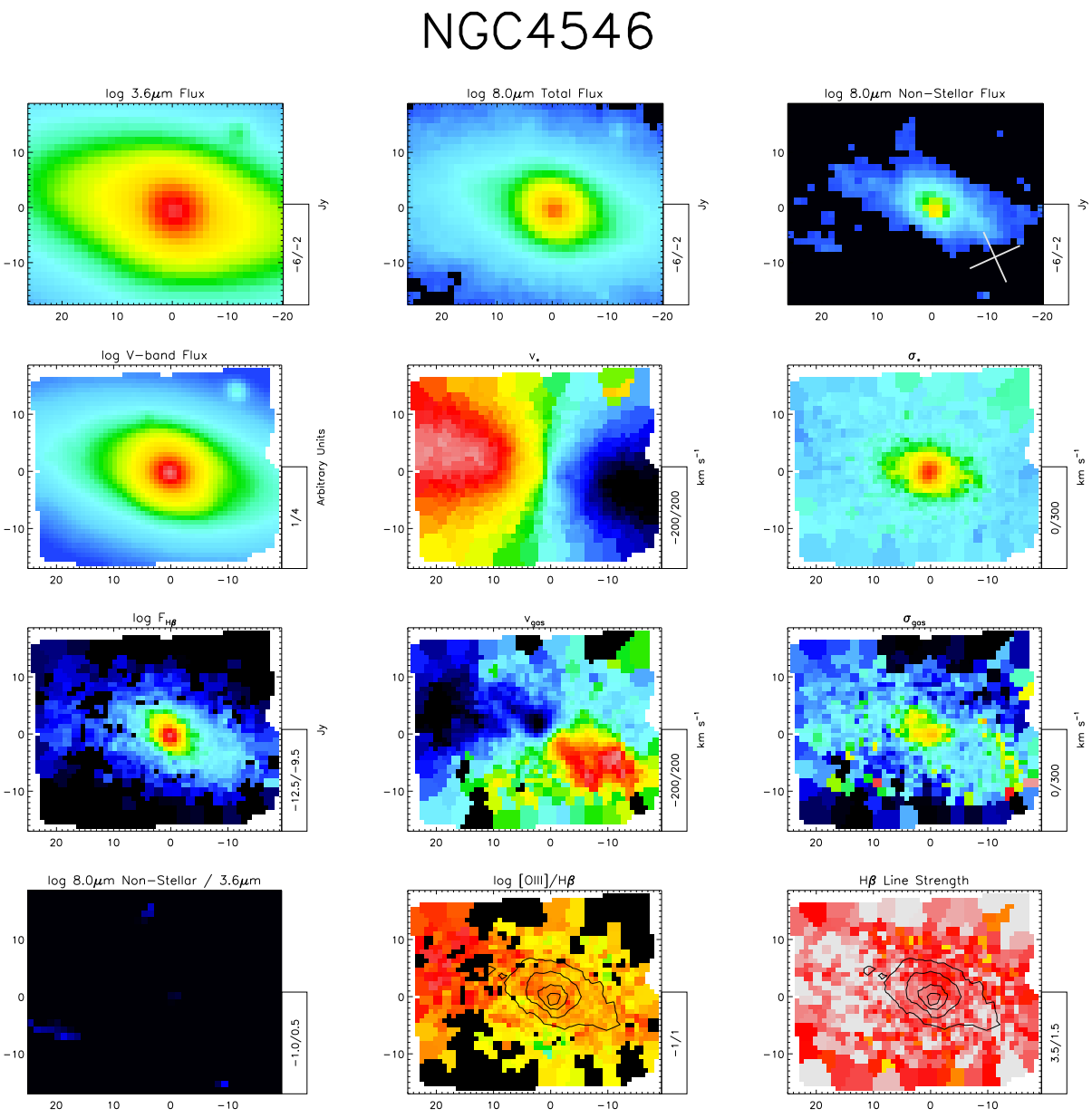

Figure 5.11: *continued*

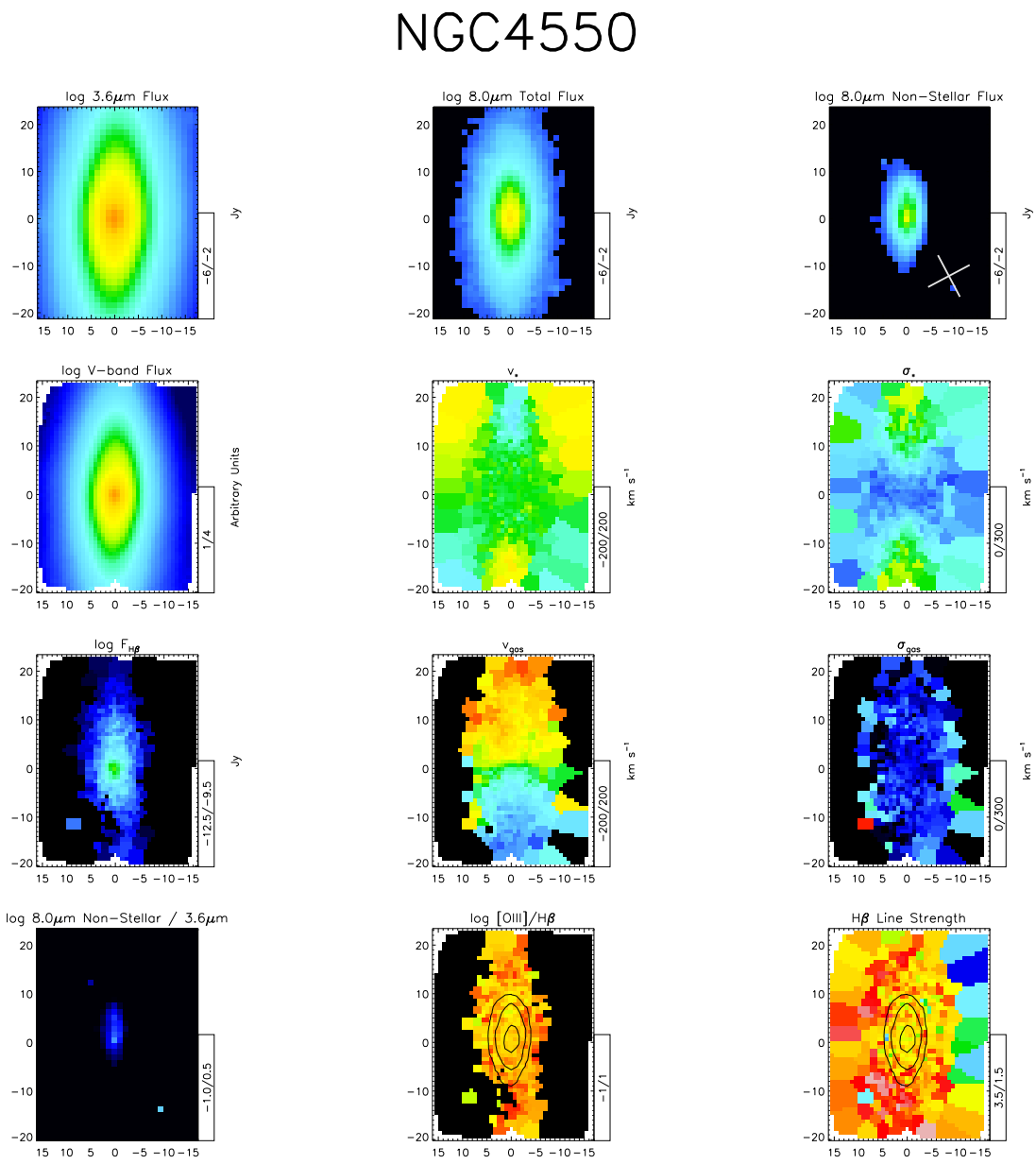

Figure 5.11: *continued*

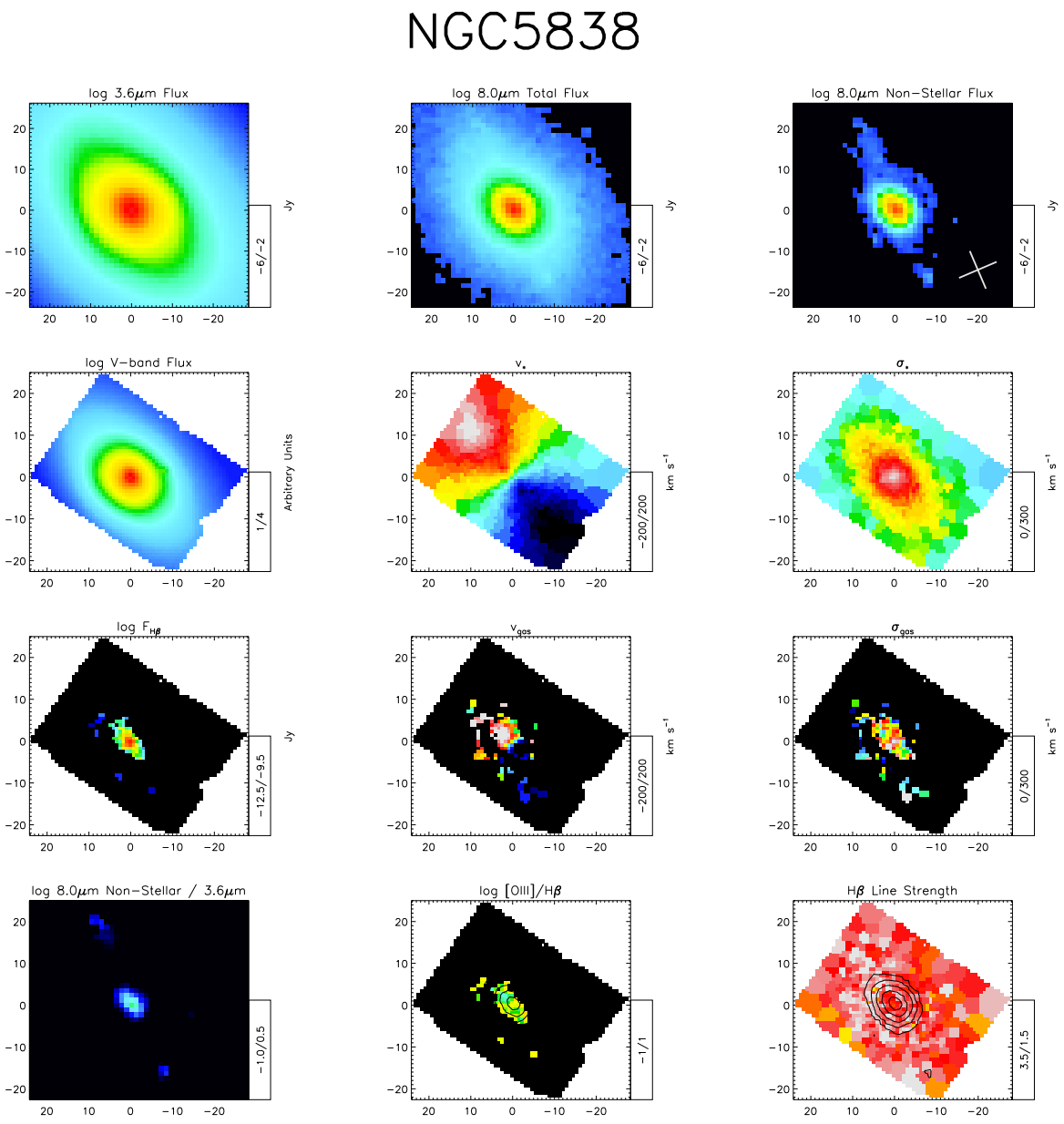

Figure 5.11: *continued*

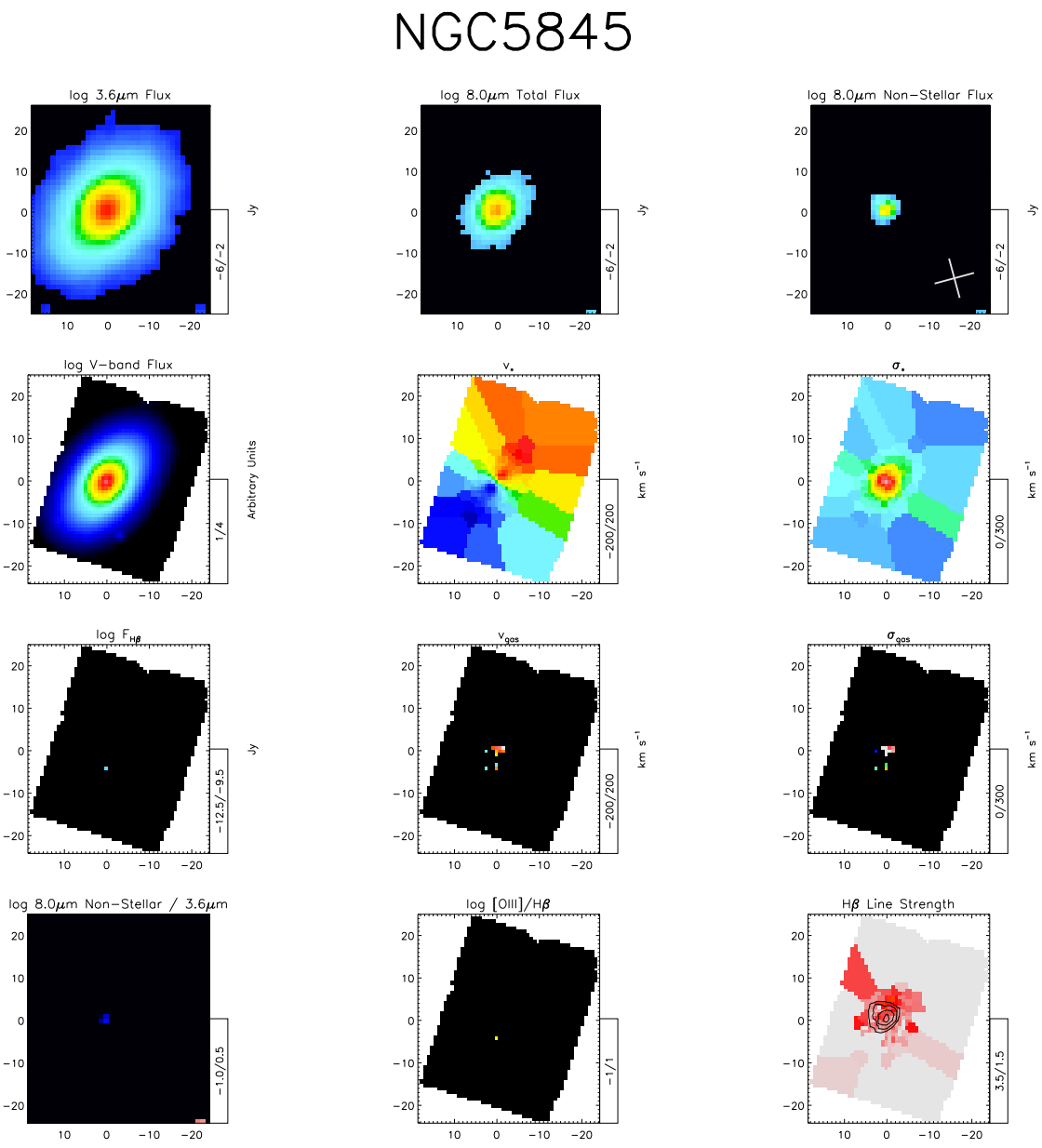

Figure 5.11: *continued*

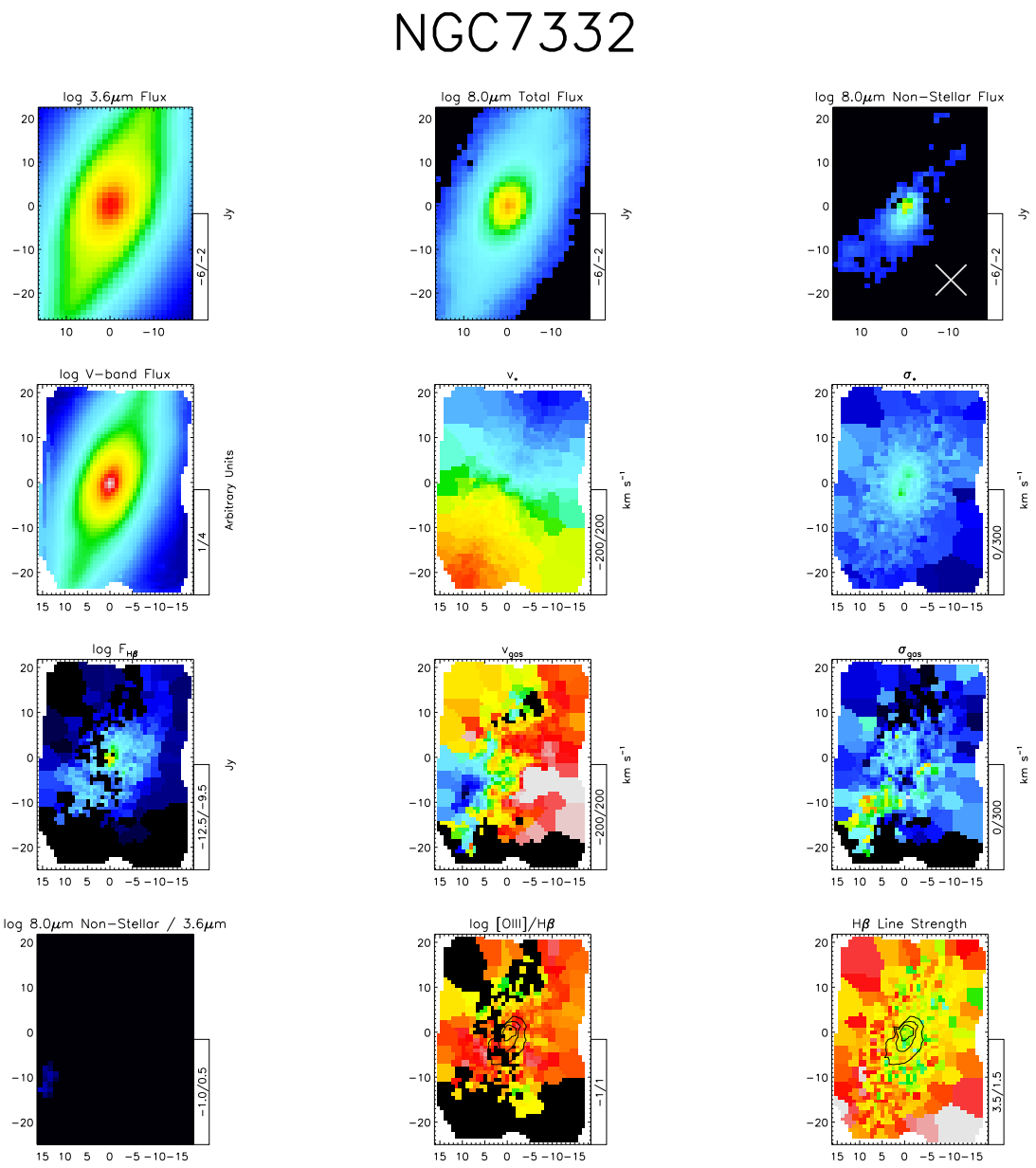

Figure 5.11: *continued*

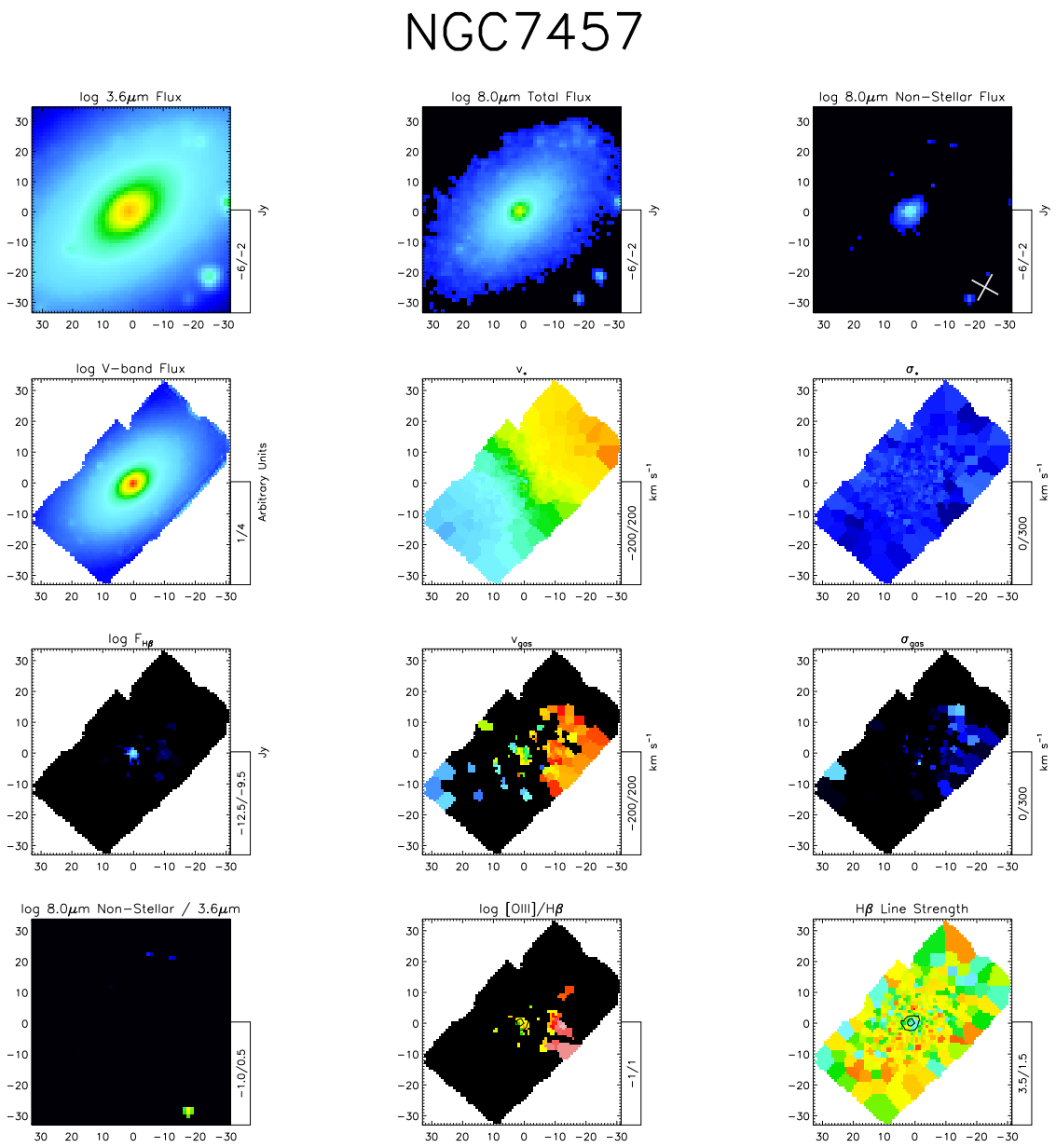

Figure 5.11: *continued*

Chapter 6

Star-Forming Galaxies at $z \sim 2$ and the Formation of the Metal-Rich Globular Cluster Population

Abstract

We examine whether the super star-forming clumps ($R \sim 1 - 3$ kpc; M $\sim 10^8 - 10^{9.5}$ $M_\odot$) now known to be a key component of star-forming galaxies at $z \sim 2$ could be the formation sites of the locally observed old globular cluster population. We find that the stellar populations of these super star-forming clumps are excellent matches to those of local metal-rich globular clusters. Moreover, this globular cluster population is known to be associated with the bulges / thick disks of galaxies, and we show that its spatial distribution and kinematics are consistent with the current understanding of the assembly of bulges and thick disks from super star-forming clumps at high redshift. Finally, with the assumption that star formation in these clumps proceeds as a scaled-up version of local star formation in molecular clouds, this formation scenario reproduces the observed numbers and mass spectra of metal-rich globular clusters. The resulting link between the turbulent and clumpy disks observed in high-redshift galaxies and a local globular cluster population provides a plausible co-evolutionary scenario for several of the major components of a galaxy: the bulge, the thick disk, and one of the globular cluster populations.

6.1 Introduction

The Universe at $z \sim 2$ is now known to be an important epoch in galaxy formation, during which the cosmic star formation rate density peaks as galaxies undergo rapid growth (e.g. Rudnick et al. 2003). Much of this activity occurs in massive, rapidly star-forming galaxies ($M_* \sim 10^{10} - 10^{11}$ $M_\odot$, SFR $\sim 10 - 200$ $M_\odot$ yr^{-1}; Reddy et al. 2005) identified via

their rest-frame optical and near-infrared colors. Comparisons of the observed properties of this population (clustering, dynamical masses, SFRs) with dark matter halo properties in cosmological simulations imply that these galaxies will evolve into local bulge-dominated spiral, lenticular, and low-mass elliptical galaxies, increasing in halo mass by a factor of three between $z \sim 2$ and $z = 0$ (Conroy et al. 2008; Genel et al. 2008). For the majority of the population, this evolution will occur in a "smooth" fashion, via accretion and minor mergers, with an average of $0-1$ major mergers during this interval (Genel et al. 2008). This smooth yet rapid mass growth, coupled with the lack of subsequent disruption by major mergers, renders these galaxies a natural population in which important structures in local galaxies may be assembled and thus a critical population to study.

Detailed dynamical and morphological observations of this galaxy population have revealed that a substantial fraction is characterized by large ($\sim 5-10$ kpc), regularly rotating, thick disks ($h_z \sim 1$ kpc, $v/\sigma \sim 2-6$; Förster Schreiber et al. 2006, 2009; Cresci et al. 2009; Elmegreen & Elmegreen 2005; Elmegreen et al. 2009). These galaxies are each populated by $5-10$ super star-forming (super-SF) clumps ($R \sim 1-3$ kpc), which collectively account for $\sim 30\%$ of the total baryonic mass in each galaxy (Cowie et al. 1995; van den Bergh et al. 1996; Elmegreen & Elmegreen 2005; Genzel et al. 2008; Elmegreen et al. 2009). The masses of individual super-SF clumps are limited at the upper end by the "Toomre" mass, the characteristic scale of these marginally stable ($Q \sim 1$) rotating galaxies, $M_T \sim 2.5 \times 10^9$ $M_\odot$, and are believed to have typical masses $M \sim 10^9$ $M_\odot$ (Genzel et al. 2008; Elmegreen et al. 2009; Dekel et al. 2009a). Simulations suggest that these clumps form naturally in a gas-rich turbulent disk and that dynamical friction on the clumps from their surrounding disk will cause them to spiral in to the center of the host galaxy on timescales $\lesssim 1$ Gyr and form a nascent bulge (Noguchi 1999; Immeli et al. 2004; Bournaud et al. 2007a), leaving a fraction of their mass behind in a thin star-forming disk and a quiescent thick disk (Bournaud et al. 2009). Similar conclusions are reached from observations of galaxies in this "gas-rich clump-driven phase" (Genzel et al. 2008; Elmegreen et al. 2008a), which we will refer to here as $z \sim 2$ star-forming galaxies (z2SFGs).

Could this phase of galaxy evolution also be associated with the formation of globular clusters (GCs)? The high masses ($M_* \sim 10^4 - 10^6$ $M_\odot$) and densities ($\rho_{central} \sim 8 \times 10^3$ $M_\odot$ pc^{-3}) of GCs require exceptionally massive and/or dense giant molecular clouds (GMCs); the super-SF clumps found in z2SFGs are thus good candidates for this process. Indeed the average properties of the super-SF clumps ($R \sim 1-3$ kpc; $M \sim 10^9$ $M_\odot$) are very consistent with the predictions of Harris & Pudritz (1994) and McLaughlin & Pudritz (1996), who concluded that "super GMCs" in the early Universe ($R \sim 1$ kpc; $M \sim 10^9$ $M_\odot$) are likely formation sites for GCs (see §6.3 for a discussion of other proposed GC formation mechanisms). Subsequently, Elmegreen & Efremov (1997) showed that such super GMCs / super-SF clumps are naturally formed in an interstellar medium characterized by high turbulent velocities and gas surface densities. Likewise, Escala & Larson (2008) showed that gas-rich disk galaxies would have large Jeans masses and could create the requisite massive super GMCs. These authors mention in passing that such disks may correspond to the turbulent and gas-rich galaxies observed at high redshift.

In this chapter, we expand this idea and propose that the observed features of $z = 0$ GC populations can be explained by assuming they formed in super-SF clumps in z2SFGs. To test this hypothesis, we investigate whether z2SFGs can account for the three main characteristics of local GC systems:

- the stellar populations of GCs,
- the spatial distributions and kinematics of GC systems, and
- the numbers and mass spectra of GCs within galaxies.

Globular clusters are a bimodal population in metallicity; metal-poor GCs increase in number with galaxy mass, and metal-rich GCs with bulge mass. Detailed observations of the Milky Way GC population additionally show that metal-poor GCs are associated spatially and kinematically with the galaxy halo and metal-rich GCs with the bulge and thick disk. Comparing these properties to those of the super-SF clumps in z2SFGs (§6.2), we find that z2SFGs are plausible formation sites for metal-rich GCs. This connection between an observed galaxy population and a globular cluster population provides further insight into the formation of both metal-rich and metal-poor GCs (§6.3).

Throughout this letter, we assume a Λ-dominated cosmology with $H_0 = 70$ km s^{-1} Mpc^{-1}, $\Omega_{\rm m} = 0.3$, and $\Omega_\Lambda = 0.7$.

6.2 Comparison of Globular Clusters and $z \sim 2$ Star-Forming Galaxies

6.2.1 Stellar Populations

Stellar population ages, chemical abundances, and metallicities provide important constrains on the formation epoch, duration, and sites of GCs. The ages of globular clusters are measured via the location of their stars in color-magnitude diagrams (for Milky Way GCs) and by comparing stellar absorption line indices in their spectra to single stellar population models (for GCs in other galaxies). However, both methods are limited by current observational and theoretical understanding of evolved stellar populations and can thus only constrain absolute ages to within a few Gyr for the oldest populations (age $\gtrsim 10$ Gyr). Current estimates of the ages of GCs are $9 - 12$ Gyr in the Milky Way (e.g. De Angeli et al. 2005; Mendel et al. 2007) and 10 ± 2 Gyr in other galaxies (e.g. Puzia et al. 2006). Such ages are comparable to the look-back time at $z \sim 2$ of 10.2 Gyr but are consistent with formation redshifts $z \sim 1.5 - 4$.

The formation timescale for GCs is known, via their high observed α-enhancement ($[\alpha/{\rm Fe}] \sim 0.3$, compared to the solar $[\alpha/{\rm Fe}] \equiv 0$), to be rapid enough that Type Ia supernovae have not yet exploded and enriched the interstellar medium with Fe-peak elements ($0.7 - 1$ Gyr; Scannapieco & Bildsten 2005). GC formation must therefore occur during a relatively

brief epoch of high SFR and significant mass growth; this is indeed the case for the gas-rich clump-driven phase in z2SFGs, which has a duty cycle of $0.5 - 1$ Gyr (Genzel et al. 2006, 2008; Daddi et al. 2007a). The duration of this phase is limited by dynamical friction on the clumps, which causes them to lose angular momentum and migrate from the disk to the galaxy center (Noguchi 1999; Immeli et al. 2004; Bournaud et al. 2007a; Genzel et al. 2008), as well as by stellar feedback, which may disrupt the molecular component of individual clumps even earlier (Murray et al. 2010). The α-element enhancement from this short and powerful star formation event has been directly observed in z2SFGs and higher-redshift analogs to be $0.25 - 0.7$ dex (Pettini et al. 2002; Halliday et al. 2008; Quider et al. 2009), comparable to those of GCs.

Finally, the most stringent constraint on GC formation comes from the metallicities of these systems, which have a clearly bimodal distribution. In most galaxies, the peaks of this distribution are near [Fe/H] $= -1.5$ and -0.5 (solar [Fe/H] $\equiv 0$), with a slight dependence on the mass of the host galaxy (e.g. Brodie & Strader 2006; Peng et al. 2006c). In Figure 6.1, we compare this relationship to an average measurement of [Fe/H] in z2SFGs (Halliday et al. 2008). For additional reference, the approximate locations of the mass-metallicity relationships at several redshifts are indicated. The metal-poor GCs have metallicities far below those observed in z2SFGs and therefore almost certainly did not form during the gas-rich clump-driven phase observed in z2SFGs. In contrast, the metal-rich GCs overlap impressively with the galaxy masses and metallicities of z2SFGs.

This agreement of the look-back time, star formation duty cycle, and metallicity of z2SFGs with the ages, elemental abundances, and metallicities of metal-rich GCs suggests that this subpopulation of GCs could have been formed in z2SFGs.

6.2.2 Spatial Distribution and Kinematics

The formation scenario for GCs is also strongly constrained by their phase space distribution, which has been well measured only in the Milky Way. GC systems similar to that of the Galaxy have been observed in other local spiral galaxies (M31:Huchra et al. 1991; Barmby et al. 2000 and M81:Schroder et al. 2002) but have not yet been confirmed with large samples of GCs in lenticular and low-mass elliptical galaxies (Brodie & Strader 2006, but see e.g. Bridges et al. 1997; Kuntschner et al. 2002). In this section, we therefore must assume that the spatial distributions and dynamics of GC populations in the Milky Way are representative of those in bulge-dominated spiral, lenticular, and low-mass elliptical galaxies; this allows us to examine whether the metal-rich GCs in such local galaxies could have been produced in z2SFGs.

The Milky Way's metal-rich GC population is associated with both the bulge and the thick disk (Table 6.1). These GCs are centrally concentrated, with the majority of the population distributed spherically in the Galaxy center (i.e. de Vaucouleurs profile) and having bulge-like kinematics (Côté 1999). A subset ($\sim 1/3$) of the metal-rich GCs is found at larger radii (> 4 kpc) and is rotationally supported ($v/\sigma \gtrsim 1$; Côté 1999). Based on the similar kinematics and stellar populations of these "disk" GCs and old thick disk stars, Zinn

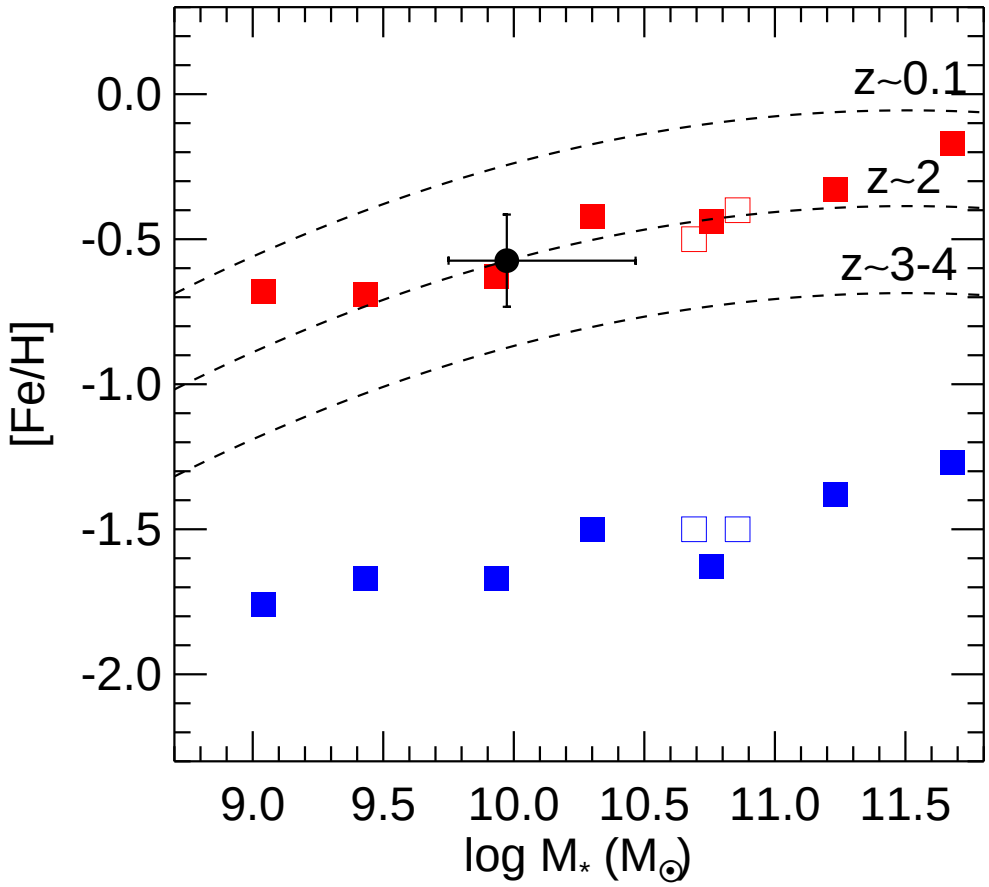

Figure 6.1: The observed relation between the host galaxy mass and the mean metallicities of the metal-rich (*filled red squares*) and metal-poor (*filled blue squares*) globular cluster populations for early-type Virgo Cluster galaxies (Peng et al. 2006c). The globular cluster populations of the Milky Way and M31 are also included (*open squares*). Halliday et al. (2008) have measured stellar [Fe/H] metallicities for a coadded average spectrum of z2SFGs (*black circle*); here we expand the horizontal error bar to include the average factor three mass growth between $z \sim 2$ and $z = 0$ (see §6.2.3). To compare with star-forming galaxies at other redshifts, the approximate locations of the galaxy mass-metallicity relationships are indicated (*dashed lines*). We use the $z \sim 2$ mass-metallicity relation of Erb et al. (2006a) and assume $[\alpha/\mathrm{Fe}] \sim 0.3$ (see text) to convert [O/H] to [Fe/H] (assuming $[\mathrm{O/H}] \approx [\mathrm{Z/H}] = [\mathrm{Fe/H}] + 0.94[\alpha/\mathrm{Fe}]$; Thomas et al. 2003). Erb et al. (2006a) and Mannucci et al. (2009) show that the $z \sim 0.1$ (SDSS) and $z \sim 3-4$ (for Lyman-break galaxies) relations are ~ 0.3 dex above and below that at $z \sim 2$, respectively, and the approximate locations of these relations are indicated.

(1985) proposed that these GCs were formed during a "transient, thick-disk phase." This prescient hypothesis virtually predicted modern observations of the gas-rich clump-driven phase in z2SFGs ($h_z \sim 1$ kpc; $v/\sigma \sim 2-6$).

The current understanding of this phase further elucidates the connection between the metal-rich GCs potentially formed in super-SF clumps, thick disks, and bulges. Dynamical friction causes the clumps (initially at $r \sim 5-10$ kpc) to migrate towards the center of their host z2SFGs to form a proto-bulge ($r \lesssim 3$ kpc; Genzel et al. 2008); during this process, the clumps presumably transport most of their newly-formed GCs with them, with a smaller fraction of the GCs being stripped off and remaining in the galaxy disk. This behavior has been seen in simulations by Elmegreen et al. (2008b), who populate each clump with a point mass of $\sim 10^5 - 10^6$ $M_\odot$ (used in their model to represent intermediate mass black holes) and find that most, but not all, of these point masses migrate to the galaxy center with their host clumps on short timescales ($t \lesssim 1$ Gyr). The final GC distribution and kinematics in fact mimic those of the stars, the majority of which are carried into the central few kpc, leaving behind a fraction of the mass in the (thick) disk (Bournaud et al. 2009). Those GCs that do migrate all the way to the galaxy center will interact with other GCs, other clumps, and the assembling bulge; this scattering will cause them to lose some of their rotational support, creating the low v/σ "bulge" GC population (Table 6.1). Some of these bulge GCs may be tidally disrupted and destroyed during this process, and some may sink to the galaxy center due to dynamical friction (see also §6.2.3). In contrast, the GCs that remained in the thick disk would not interact with other GCs or clumps and would therefore maintain the rotational support of the original clumpy thick disk ($v/\sigma \sim 2-3$ in thick-disk GCs; $v/\sigma \sim 2-6$ in z2SFGs).

The GC system that would result from a z2SFG would therefore be expected to have a primary component associated with the bulge and a less populous component associated with the thick disk, in excellent agreement with the observed properties of the metal-rich GC population. This scenario additionally explains why this GC population is associated with both the bulge and the thick disk.

6.2.3 Number and Mass Function

To evaluate whether super-SF clumps in z2SFGs can produce the number and mass distribution of the relevant (i.e. metal-rich) GC population, we employ a simple analytic model. We begin by estimating the number of metal-rich GCs expected in the $z = 0$ descendants of z2SFGs. In the local Universe, the parameter $T = N \ / \ (M_{gal}/10^9\ M_\odot)$ is used to express the number of GCs per 10^9 $M_\odot$ of galaxy stellar mass (Zepf & Ashman 1993; Rhode et al. 2005). Peng et al. (2008) have measured this quantity for a large range of galaxy masses in Virgo early-type galaxies; they find a nearly constant value of $T = 5$ for galaxies with $M_* = 0.02 - 2 \times 10^{11}$ $M_\odot$. At $z \sim 2$, the z2SFGs have stellar masses of $\sim 10^{10} - 10^{11}$ $M_\odot$ (e.g. Förster Schreiber et al. 2009). Assuming the factor three increase in halo mass expected between $z \sim 2$ and $z = 0$ (Conroy et al. 2008; Genel et al. 2008) includes a constant baryon fraction in the accreted material, this implies stellar masses at

Table 6.1: Distribution and Kinematics of Galactic Components and z2SFGs

	Profile	Extent (kpc)	v/σ
z2SFGs	Disk	$h_z \sim 1$	$2-6$
Thick Disk Stars	Disk	$h_z \sim 0.8-1.4$	$2-4$
MR (Disk) GCs	Disk	$h_z \sim 0.8-1.5$	$2-3$
Bulge Stars	de Vaucouleurs	$R_e \sim 1.2$	$1-1.5$
MR (Bulge) GCs	de Vaucouleurs	$R_e < 1.7$	$0.4-0.6$
Halo Stars	$R^{-3.5}$	$R < 40$	$0.2-0.8$
MP (Halo) GCs	$R^{-3.5}$	$R < 40$	$0.3-0.4$
Thin Disk Stars	Disk	$h_z \sim 0.3$	$6-12$

Comparison of metal-rich (MR) and metal-poor (MP) GC populations to components of the Milky Way and to z2SFGs (see definition in §6.1). Although the descendants of z2SFGs are likely more bulge-dominated than the Milky Way, the spatial and kinematic properties of GCs in these galaxies are not yet well constrained; here we assume the GC population of the Milky Way to be representative in order to evaluate the possible link with z2SFGs. Data are from Armandroff (1989), Côté (1999), Cresci et al. (2009), Elmegreen & Elmegreen (2006), Minniti (1995), and Zinn (1985).

$z = 0$ of $3 \times 10^{10} - 3 \times 10^{11}$ $M_\odot$ and thus $T = 5$ (or $\sim 150 - 1500$ GCs) is appropriate for this population. (Similar predictions of GC numbers are also obtained using the universal cluster formation efficiency of McLaughlin 1999.) In this galaxy mass range, $20 - 40\%$ of GCs are observed to be metal-rich (Peng et al. 2006b, 2008), implying that z2SFGs should produce roughly $30 - 600$ metal-rich GCs that persist to $z = 0$.

We now evaluate whether the super-SF clumps in z2SFGs can produce the requisite number of metal-rich GCs during the gas-rich clump-driven phase. Star formation within super-SF clumps has been explored analytically (Harris & Pudritz 1994; McLaughlin & Pudritz 1996) and has been observed for the GC-analogs, young massive clusters (YMCs), which form locally in gas-rich (e.g. LMC, M82) and high SF (e.g. the Antennae) environments (Elson & Fall 1985; Elmegreen & Efremov 1997; English & Freeman 2003; de Grijs et al. 2003; Wilson et al. 2003). These studies have concluded that star formation in super-SF regions plausibly proceeds in much the same fashion as in their less massive cousins, local GMCs; super-SF regions form gravitationally unstable structures with an efficiency of a few percent and with a power law mass spectrum of index $-2 < \alpha < -1.5$, the latter being a result of the turbulent cascade. The mass spectrum is limited at the high end, as in local GMCs, at $\sim 10^{-3}$ times the mass of the cloud, so super-SF clumps ($\sim 10^9$ $M_\odot$) form structures with masses up to 10^6 $M_\odot$ (i.e. YMCs, potential GCs), while local GMCs form structures with masses up to 10^3 $M_\odot$ (i.e. open clusters). At the low end of the mass spectrum, less is known about the limiting mass; here, we assume a similar scaling with cloud mass, such that the lower mass limit in local GMCs of 10^{-6} times the cloud mass (~ 1 $M_\odot$) applies also to super-SF clumps.

Combining this information with observations of super-SF clumps in z2SFGs, we predict the number and mass function of (metal-rich) GCs that can be produced. Letting each super-SF clump form stellar clusters according to the mass range and spectrum described above results in ~ 700 objects per clump with mass $10^4 - 10^6$ $M_\odot$, distributed with a power law of assumed slope $\alpha = 2$ (Figure 6.2). Fall & Zhang (2001) and Jordán et al. (2007) have shown that local GC mass spectra are not power laws but can instead be well-represented by "evolved" Schechter functions that flatten below a characteristic turn-over mass ($\sim 2 \times 10^5$ $M_\odot$), which they suggest results from the evaporation of lower mass GCs through two-body relaxation (see also McLaughlin & Fall 2008). At the high mass end (above a cutoff mass M_c), the distribution drops more steeply than a power law; this may be the result of higher mass GCs preferentially sinking to the galaxy center with their host super-SF clumps through dynamical friction (§6.2.2) or being destroyed by gravitational shock heating in the potential of the host galaxy (Fall & Zhang 2001; McLaughlin & Fall 2008). Jordán et al. (2007) show that the evolved and initial mass functions can be straightforwardly linked (their equations 4-7), with the exact shape of the final mass function dependent on only two parameters, a cutoff mass (M_c) and a cumulative mass loss per GC (Δ). Here, we adopt their values for M_c and Δ appropriate for galaxies with masses characteristic of z2SFG descendants. Integrating the resulting evolved GC mass function suggests that, of the initial ~ 700 GCs per clump, ~ 12 will survive from $z \sim 2$ to $z = 0$ (Figure 6.2). With $5 - 10$ clumps per galaxy, we therefore expect $3500 - 7000$ GCs to be created during a galaxy's

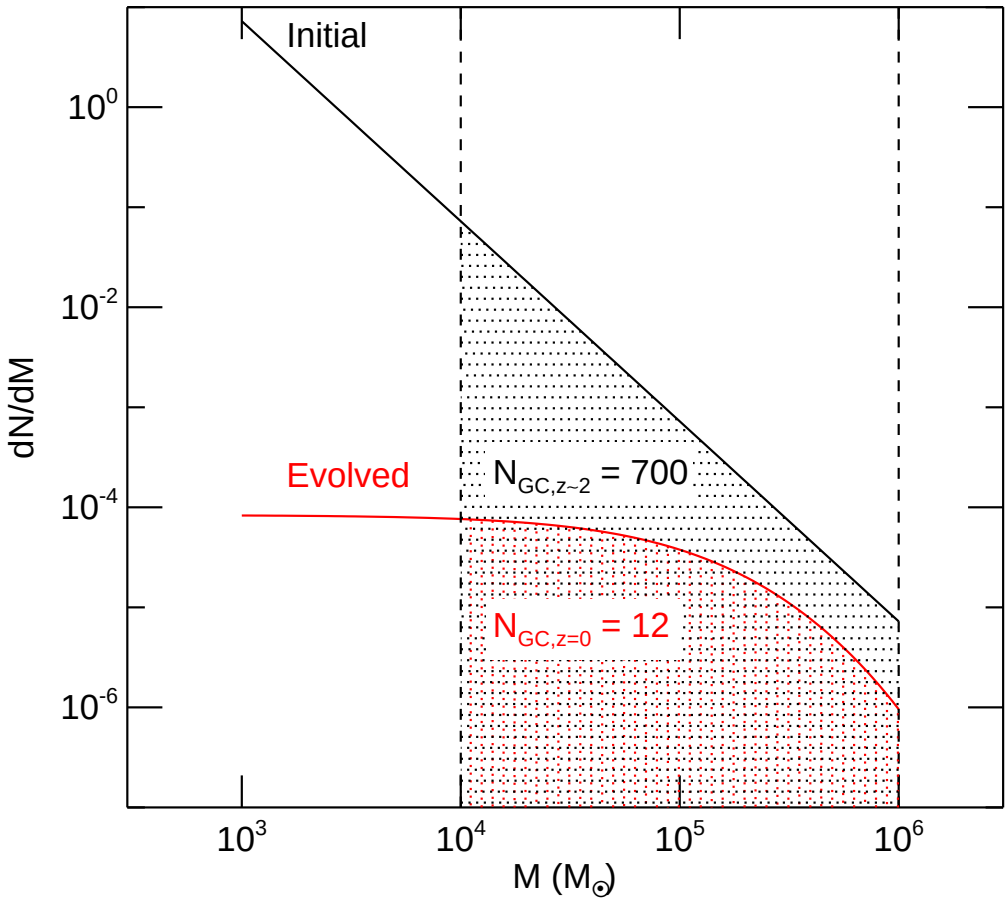

Figure 6.2: Predicted mass spectrum for structures formed in a z2SFG super-SF clump. The slope of the initial mass spectrum ($z \sim 2$; *black*) is observed to be common among all structures in the ISM (clouds, cores, open clusters, YMCs). The upper and lower limits are set by assuming that a molecular cloud forms structures with $10^{-6} - 10^{-3}$ of its mass, as observed in local GMCs, and the normalization is set such that $\sim 5\%$ of the original cloud mass will form stars, as observed locally (e.g. Wilson et al. 2003). The evolutionary model of Jordán et al. (2007) is applied to the initial mass spectrum and results in a preferential decrease of low-mass structures in the evolved mass spectrum ($z = 0$; *red*). Vertical dashed lines indicate the mass range in which bound structures are observed as GCs, and the shading and labels indicate the number of GCs produced per clump in this model.

gas-rich clump-driven phase, of which $\sim 60 - 120$ survive to $z = 0$.

This order-of-magnitude calculation shows that z2SFGs may plausibly produce metal-rich GCs whose numbers and mass spectra compare well with GCs observed in local bulge-dominated galaxies. Variations in our simple assumptions of super-SF clump masses and numbers would increase the scatter in the predicted number of metal-rich GCs ($60 - 120$) to more closely match the full range observed locally in likely z2SFG descendants ($30 - 600$).

6.3 Discussion and Conclusions

In the literature, two broad models of GC formation are discussed: 1) Each galaxy halo creates a single GC population of roughly uniform metallicity, with the second GC population being a product of hierarchical merging (metal-poor GCs accreted from dwarf galaxies: Côté et al. 1998; metal-rich GCs created during gas-rich mergers: Ashman & Zepf 1992). 2) Each galaxy halo has two distinct episodes of GC formation, with metal-poor GCs forming first during the collapse of the protogalactic cloud and metal-rich GCs in a subsequent phase of star formation ("in situ": Forbes et al. 1997). On the basis of the relation between galaxy luminosity (mass) and GC metallicity for both GC subpopulations (Figure 6.1), Strader et al. (2004) have argued that the "in situ" model is strongly preferred, since the accretion or creation of GCs during mergers would blur correlations between the properties of galaxies and their GCs.

Our hypothesis augments this model by providing a natural mechanism for the coincident formation of metal-rich GCs, bulges, and thick disks. In §6.2, we have shown that the stellar populations, spatial distribution, kinematics, numbers, and mass spectra of metal-rich GCs are all consistent with formation in super-SF clumps during the gas-rich clump-driven phase of a galaxy's evolution. The rapid ($\lesssim 1$ Gyr) migration of these clumps to the centers of their host galaxies, as caused by dynamical friction on the clumps, provides an effective means of transporting the majority of GCs to the vicinity of the proto-bulge formed from the coalescing clumps; this same mechanism also accounts for the thick-disk GCs, which, like the newly formed thick-disk stars, are stripped from their host clumps and left behind at large radii. This process has a built-in truncation mechanism: once a bulge has formed, it stabilizes the remaining disk against further fragmentation into large clumps (Bournaud et al. 2007a). Since the clumps are responsible for simultaneous GC, bulge, and thick disk formation, these must occur as a single, short ($\lesssim 1$ Gyr), and very significant event in the lifetime of a galaxy.

This scenario provides new insight into the process of galaxy assembly at high redshift. The formation of metal-rich GCs in the gas-rich clump-driven phase implies that the number of these GCs in a galaxy will be closely tied to the importance of this phase in the galaxy's history. Galaxies with a more dramatic gas-rich clump-driven phase will produce more metal-rich GCs, and the coalescing clumps will create larger bulges, resulting in the observed correlation between bulge mass and the number of metal-rich GCs (Peng et al. 2006b). The potential association of galaxies at the massive end of this correlation (e.g. M87) with

quiescent spheroids at $z \sim 2$ (e.g. Trujillo et al. 2006a; Tacconi et al. 2008) suggests that the populous metal-rich GC populations in these local giant ellipticals may result from a gas-rich clump-driven phase that was very dramatic and occurred prior to $z \sim 2$ during the galaxies' primary SF epochs or during a merger of two galaxies in the gas-rich clump-driven phase (see also e.g. Rhode & Zepf 2004). Conversely, the absence of significant metal-rich GC populations (and bulges) in late-type galaxies suggests that massive, migrating super-SF clumps did not play an important role in late-type galaxy formation.

Finally, the scenario proposed here also constrains metal-poor GC formation through the current understanding of the formation history of z2SFGs. Significant observational and theoretical evidence indicates that z2SFGs are assembled via the rapid and smooth transport of cold ($T < T_{vir}$) gas along filaments into the centers of halos (e.g. Genzel et al. 2006; Daddi et al. 2007a; Erb 2008; Dekel et al. 2009a). This inflow is almost certainly also present at the earlier epochs in which metal-poor GCs form. These GCs may thus be formed within small concentrations inside filaments or at the intersection of filaments inside the collapsing dark matter halo. This insight is essentially an update of the dissipational collapse model of Searle & Zinn (1978) and Harris & Pudritz (1994) with the detailed information now available at high redshift, and it provides a simple mechanism through which the formation of metal-poor GCs is linked to that of the halo.

Acknowledgments

We are grateful to the referee, Dean McLaughlin, whose comments significantly improved this chapter. We also wish to thank the SINS team, especially Andi Burkert, Ric Davies, Peter Johansson, Amiel Sternberg, and Linda Tacconi, for enlightening conversations and for comments on the manuscript. This chapter has benefitted from discussions with Harald Kuntschner, Chris McKee, Jeffrey Silverman, and Andrew Wetzel.

Chapter 7

Conclusions and Outlook

7.1 Synthesis of the Thesis

Since the individual conclusions of each of the preceding chapters were reviewed in Chapter 1 and described extensively in the bulk of this thesis, I summarize them here only briefly. Instead, I use the opportunity of this chapter to synthesize these results in light of our evolving understanding of galaxy evolution (in this section) and to discuss future work, and especially future facilities, that will provide additional insight into the incredibly complex process of galaxy assembly (in §7.2).

The formation of massive, bulge-dominated galaxies was first explained as a result of "monolithic collapse" of gas within dark matter halos (e.g. Hoyle 1953; Eggen et al. 1962). In this scenario, primordial gas in the early Universe fell towards the center of its host halo rapidly and isotropically, after which a dramatic burst of star formation produced a dense, roughly spherical galaxy supported by random motions. This remnant, observed today as an early-type galaxy, should have uniformly old stellar ages, all dating to the initial starburst. These stars should also be characterized by a strong α-element enhancement, since the short duration of the starburst ($t \lesssim 10^9$ yr; Pipino et al. 2008) would not have allowed sufficient time for the star-forming gas to be enriched by Type Ia supernovae.

For the same reason, this formation model also predicts that there should be a significant population of metal-poor stars, formed from the original primordial gas, in early-type galaxies. Observations, however, do not find such a stellar population; instead they indicate that many elliptical galaxies are quite metal-rich (e.g. Worthey et al. 1996). This difference between the monolithic collapse model and observations is hard to reconcile without invoking ad hoc scenarios involving pre-enrichment of the collapsing gas without a corresponding major star formation event.

Dramatic improvements in our understanding of cosmology provided the solution via a new model for bulge formation: early-type galaxies were assembled through "hierarchical merging," beginning as small systems in small dark matter halos and, as their host dark matter halos grew via accretion of nearby halos, merging with many other galaxies (e.g.

Frenk et al. 1988; Lacey & Cole 1993). The expected stellar populations from this model differ from those of the monolithic collapse model; the numerous merger-induced starbursts should produce stars with a range of ages, and the star-forming gas should have ample time to become enriched. The remnants should therefore be metal-rich and only slightly α-enhanced. Moreover, the strong gravitational torques on stellar orbits during mergers reshape the initial rotation-dominated disk galaxies into random motion-dominated elliptical systems and expel their remaining gas. This scenario has been very successful at explaining the shape, lack of gas, and stellar populations observed in early-type galaxies.

This cosmologically-motivated scenario is appealing because of its roots in our robust understanding of the evolution of dark matter structures. However, it is not without flaws. In this thesis, a binary major merger scenario was shown to be unable to reproduce the orbital structure of stars surrounding the supermassive black hole in the nearby elliptical galaxy NGC 3379 (Chapter 4). Additionally, as observations of the two-dimensional kinematics of early-type galaxies become available (as in the SAURON sample described in Chapter 5), detailed comparisons with numerical simulations indicate that the major merger scenario fails to reproduce the observed dynamical properties of both fast-rotator and slow-rotator early-type galaxies (Burkert et al. 2008; Jesseit et al. 2009). More generally, cosmological models of the growth of structure in the Universe find an insufficient number of major mergers to create all of the bulges and early-type galaxies observed today (e.g. Hopkins et al. 2009).

As a result, the potentially significant evolutionary effects of minor mergers have become a focus of recent attention. In this thesis, Chapter 5 argues from multi-wavelength and integral-field observations that minor mergers in the local Universe are playing an important role in the formation of low-mass early-type galaxies and shows that this claim is supported by numerical simulations of such mergers (Bournaud et al. 2007b). Similar conclusions have also been reached by other studies of the stellar and gas kinematic properties of bulge-dominated galaxies in the local Universe (e.g. Haynes et al. 2000). Extending these conclusions to a cosmological setting, Burkert et al. (2008) show that the integrated effects of the resulting multiple major and minor mergers over an extended amount of time are probably responsible for the properties observed in local early-type systems.

In this thesis, I take this suggestion one step further and incorporate our emerging understanding of galaxy assembly at high-redshift into the discussion. With recent detailed observations of galaxies at $z \sim 2$, we are now able to directly study the predecessors of local bulge-dominated galaxies *as they undergo their most important star formation event* (Conroy et al. 2008; Genel et al. 2008), but developments from such studies have yet to be assimilated into a general picture of galaxy evolution. Building on the discussion in Chapter 6, I use the remainder of the section to make a speculative attempt to do exactly this.

Perhaps the most fundamental insight from studies of $z \sim 2$ star-forming galaxies is that the strict differentiation between major mergers, minor mergers, and accretion, as is commonly made in the local Universe, is not appropriate. Detailed studies of individual star-forming galaxies at $z \sim 2$ suggest that their high star formation rates and undisturbed kinematics required the rapid but smooth accretion of external gas (Genzel et al. 2006); in Chapter 2, I quantitatively confirmed that these galaxies are rotation-dominated and

therefore fueled in this way. Ensemble studies of the $z \sim 2$ population have reached similar conclusions by noting that a galaxy's star formation rate depends primarily on its stellar mass and not, therefore, on transient merger/accretion events (Daddi et al. 2007a). Since this accretion occurs along filaments in the cosmic structure, it would naturally be expected that small concentrations of mass would develop within filaments, resulting in "clumpy accretion," as seen in simulations by Dekel et al. (2009b). Immediately, the lines between mergers and smooth accretion begin to blur; when the gas flow is smooth, the event is "accretion," and in the rare event of a sizable dark matter halo being part of this flow, the result is a "major merger."

The utility of such a shift in the conceptualization of galaxy growth becomes clear when probing the internal structure of the $z \sim 2$ star-forming galaxies. Several observational and theoretical studies of these systems have shown that their high gas fractions ($\sim 40\%$; Tacconi et al. 2010) result in large-scale fragmentation into clumps of $1/100 - 1/10$ the host galaxy's mass, in which the star formation rate is enhanced relative to the surrounding gas. These super-massive star-forming (super-SF) clumps are evolutionarily important entities, which dynamical friction causes to spiral in to the center of their host galaxies on short ($\lesssim$ 1 Gyr) timescales and merge (e.g. Bournaud et al. 2007a; Genzel et al. 2008). This "gas-rich clump-driven" phase in galaxy evolution can happen only once, before a significant central concentration of mass is established (Bournaud et al. 2007a), and is unique in that multiple encounters between large objects of similar masses are occurring *within* a gas-rich galaxy. This latter characteristic makes the assembly of sub-structures in a gas-rich galaxy analogous to the growth of galaxies with the gas-rich cosmic structure.

At $z \sim 2$, the evolution of the progenitors of local massive galaxies is thus dominated by a hybrid scenario, in which gas is continuously transported into and through galaxies in a smooth manner and yet substantial gas-rich mass concentrations are a part of this flow. I will refer to the super-SF clump motions and coalescence inside a $z \sim 2$ disk as "secular merging," since the clumps and their evolution are the result of secular processes, yet they collide in the galaxy center with clump-to-clump mass ratios characteristic of major and minor mergers. The importance of these encounters has been shown by Genzel et al. (2008) and Bournaud et al. (2007a), who demonstrated that bulges built in galaxy centers via secular merging are true classical bulges, as observed in bulge-dominated galaxies. Moreover, Bournaud et al. (2009) and Chapter 6 have respectively shown that remnants from this process are thick disks and metal-rich globular clusters; both of these sub-structures in local galaxies have traditionally been explained as the products of mergers. The long-standing puzzle of the assembly of supermassive black holes in early-type galaxies may also be able to be attributed to the formation and eventual merging of small black holes in super-SF clumps (Chapter 3; see also Elmegreen et al. 2008b).

These initial successes of the secular merging scenario are very encouraging and suggest that other properties of local early-type galaxies (SA, S0, and disky Es) could be explained through this formation scenario. Chapter 6 illustrated that the large amount of random motion (low v/σ) in the gas of $z \sim 2$ star-forming galaxies can naturally explain the similarly low v/σ ratios observed in the thick disk and bulge globular cluster populations. Taking

the comparison further, the rotational and random motions in old thick disks of local bulge-dominated galaxies are also quite similar to those of the disks in their potential $z \sim 2$ predecessors (compare data from Cappellari et al. 2007 and Förster Schreiber et al. 2006). Material in these $z \sim 2$ disks that was left behind during the clump coalescence could therefore plausibly evolve passively into the thick disks observed today. Likewise, the rotational and random motions in bulges are of similar magnitude to those of super-SF clumps in $z \sim 2$ star-forming galaxies and are consistent with a slight increase in random motions and decrease in rotation as the clumps undergo secular mergers.

Chapter 6 also noted that the stellar populations of $z \sim 2$ star-forming galaxies were consistent with being the formation sites of metal-rich globular clusters, whose stellar populations are similar to those of bulges and thick disks. By being able to account for the ages, metallicities, and chemical abundances of stars in metal-rich globular clusters, $z \sim 2$ star-forming galaxies therefore are also consistent with the average stellar population properties of bulges and thick disks. Moreover, this scenario can account for observed metallicity gradients in early-type galaxies. Since star formation will proceed more rapidly in the super-SF clumps than in the surrounding diffuse medium, more metals will be produced in the clumps and transported with them to the galaxy center, reproducing the observed decrease in metallicity with galaxy radius (see also Kuntschner et al. 2010). However, the age and duration of the star formation event is roughly the same throughout the galaxy, creating the constant stellar age and α-abundance with radius observed in evolved early-type galaxies (Kuntschner et al. 2010).

This emerging evidence that secular merging in $z \sim 2$ star-forming galaxies plays a significant role in shaping the local early-type descendants of these galaxies is only useful if their evolution from $z \sim 2$ (10 billion years ago) to the present is relatively unremarkable. For example, if all $z \sim 2$ star-forming galaxies were expected to undergo several secular merging phases and/or major mergers during this interval, the events at $z \sim 2$ could not be expected to have an important impact on the final state of the galaxy at $z = 0$. Fortunately, this is not the case. The gas-rich clump-driven phase is most likely a one-time event in a galaxy's life; once the super-SF clumps form a bulge, this bulge then stabilizes the galaxy against subsequent fragmentation into super-SF clumps (Bournaud et al. 2007a). Moreover, in the ~ 10 Gyr of the Universe's history following this phase, the descendants of $z \sim 2$ star-forming galaxies will grow primarily through smooth accretion, experiencing an average of $0 - 1$ major mergers (Genel et al. 2008). The rapid and dramatic evolution occurring in these galaxies during the gas-rich clump-driven phase at $z \sim 2$ should therefore be critical in shaping the properties of local bulge-dominated galaxies.

Indeed, as discussed briefly in Chapter 6 and in more detail above, the secular merging scenario is able to account for the presence, structure, kinematics, and stellar populations of bulge-dominated galaxies in a simple, though not yet fully explored, manner. This hybrid scenario is similar to monolithic collapse in that: 1) rapid gas inflow and collapse is probably responsible for the formation of the halo stellar populations and of the gas-rich star-forming disk, and 2) much of the relevant action takes place inside a single galaxy, without invoking collisions between galaxies. However, this scenario also resembles hierarchical merging in

that: 1) super-SF clumps with mass ratios characteristic of major and minor mergers collide with one another and with the forming bulge in the galaxy center, and 2) the main star formation event consists of a number of successive clump mergers rather than a single event. By combining monolithic collapse and hierarchical merging in this manner, secular merging explains observed galaxy properties while escaping the respective pitfalls of the two classical formation scenarios.

Secular merging also has the advantage of connecting elegantly with recent constraints on galaxy formation from the "fossil record" in the local Universe. These strongly point to multiple minor mergers being important in the formation of early-type galaxies; this process could be mimicked by the successive secular mergers of super-SF clumps in a $z \sim 2$ star-forming galaxy. Bringing together the evidence from the diverse chapters in this thesis, it seems plausible that "multiple minor mergers" are required to form observed local massive galaxies and that these "mergers" may in fact have been clump-clump encounters that occurred during the gas-rich clump-driven phase of galaxy evolution.

7.2 Future Progress

The scenario described above is a tantalizing step forward in our understanding of galaxy formation that clearly needs to be tested. Fortunately, there are a number of possibilities for doing so, and some exciting steps are beginning to be taken in this direction. At $z \sim 2$, it will be important to directly study the large quantities of gas involved in creating the gas-rich clump-driven phase. Using Ly-α emission, it should be possible to measure the quantity and dynamics of the (T $\sim 10^4$ K) gas involved in the smooth, rapid accretion driving star formation (see predictions for these observations by Goerdt et al. 2009). The gas involved in the star formation event itself is also becoming observationally accessible using high-sensitivity molecular gas observations (Tacconi et al. 2010), and systematic studies of the mass and dynamics of this gas phase, as well as its relation to other gas phases, will shed light on how star formation proceeds during the gas-rich clump-driven phase. The subsequent evolution of $z \sim 2$ galaxies into the local galaxy population is being explored in increasing detail with numerical simulations, which are beginning to resolve the formation of super-SF clumps and galaxy substructures (e.g. Dekel et al. 2009a). Finally, statistical surveys of the two-dimensional kinematic and stellar population properties of all early-type galaxies in the local Universe (e.g. Serra et al. 2009) will provide additional constraints and thus important anchors for galaxy formation scenarios.

The most dramatic progress in this area, however, is likely to come with exciting next-generation facilities that will be opening in the next few years (Table 7.1). Most immediate are new instruments in the millimeter regime: the Expanded Very Large Array (EVLA, currently beginning science) and the Atacama Large Millimeter Array (ALMA, under construction). These powerful facilities will enable us to expand to numerous high-redshift galaxies the pioneering study by Tacconi et al. (2010) of the mass, distribution, and kinematics of star-forming molecular gas in $z \sim 2$ galaxies. With these data, precise quantitative

Table 7.1: Notable Future Observing Facilities

Name	Wavelength	Science at $z \sim 2$	First Light Year	Partners
EVLA	radio/mm	star-forming gas	2009	NRAO
ALMA	mm	star-forming gas	2012	Multi-national
JWST	IR	ionized gas, stars	2014	NASA (lead)
EELT	optical/NIR	ionized gas, stars	2018	ESO
GSMTs	optical/NIR	ionized gas, stars	2018	US-based

statements about gas accretion and processing in these galaxies will be possible, and the effect of super-SF clumps on star formation will be easily probed.

Slightly further on the horizon are major advances in optical and infrared instrumentation, beginning with the James Webb Space Telescope (JWST, led by NASA and contracted to Northrop Grumman Aerospace Systems for construction). By reaching into the mid-infrared with high spatial resolution, this telescope will measure the detailed properties of the ionized gas and stellar components of $z \sim 2$ galaxies as well as probe galaxies at higher redshifts, reaching back to the formation of the first galaxies. The JWST will be complemented by several 30-meter class telescopes: the European Extremely Large Telescope (EELT, being developed by ESO), and one or more Giant Segmented Mirror Telescopes (GSMTs, currently being planned in the United States with international partners). The unprecedented spatial detail that will be available with these telescopes will, for the first time, resolve the super-SF clumps in $z \sim 2$ star-forming galaxies and determine the way in which stars and clusters of stars are formed in these unusual complexes. The giant leap in resolution that the EELT and GSMTs will provide will naturally also enable "discovery science" and raise unforeseen questions about galaxy assembly.

The discovery potential of these future facilities and research directions in the study of galaxy formation and evolution is substantial. As the fundamental building blocks of the Universe, galaxies are a reflection of both their cosmic context – the nature, evolution, and assembly history of the Universe – and of their components – the stars and planets that support life. As noted in the opening paragraphs of this thesis, our ultimate goal in the study of galaxies and in all astronomy is to fully understand our existence and therefore to have a more profound sense of our place in the Universe. The effort continues.

Bibliography

Abraham, R. G. et al. 2004, AJ, 127, 2455
Adelberger, K. L., Steidel, C. C., Shapley, A. E., Hunt, M. P., Erb, D. K., Reddy, N. A., & Pettini, M. 2004, ApJ, 607, 226
Alexander, D. M. et al. 2008, AJ, 135, 1968
Alonso-Herrero, A., Quillen, A. C., Rieke, G. H., Ivanov, V. D., & Efstathiou, A. 2003, AJ, 126, 81
Armandroff, T. E. 1989, AJ, 97, 375
Armus, L., Heckman, T. M., & Miley, G. K. 1989, ApJ, 347, 727
—. 1990, ApJ, 364, 471
Arribas, S. & Colina, L. 2003, ApJ, 591, 791
Arribas, S., Colina, L., & Clements, D. 2001, ApJ, 560, 160
Arribas, S. et al. 1998, in Presented at the Society of Photo-Optical Instrumentation Engineers (SPIE) Conference, Vol. 3355, Proc. SPIE Vol. 3355, p. 821-827, Optical Astronomical Instrumentation, Sandro D'Odorico; Ed., ed. S. D'Odorico, 821–827
Ashman, K. M. & Zepf, S. E. 1992, ApJ, 384, 50
Bacon, R. et al. 2001, MNRAS, 326, 23
Baldry, I. K., Glazebrook, K., Brinkmann, J., Ivezić, Ž., Lupton, R. H., Nichol, R. C., & Szalay, A. S. 2004, ApJ, 600, 681
Barmby, P., Huchra, J. P., Brodie, J. P., Forbes, D. A., Schroder, L. L., & Grillmair, C. J. 2000, AJ, 119, 727
Barnes, J. E. 2002, MNRAS, 333, 481
Barnes, J. E. & Hernquist, L. 1996, ApJ, 471, 115
Barth, A. J. 2004, in Coevolution of Black Holes and Galaxies, ed. L. C. Ho, 21–+
Barth, A. J., Ho, L. C., & Sargent, W. L. W. 2002, AJ, 124, 2607
Barth, A. J., Sarzi, M., Rix, H.-W., Ho, L. C., Filippenko, A. V., & Sargent, W. L. W. 2001, ApJ, 555, 685
Bell, E. F., McIntosh, D. H., Katz, N., & Weinberg, M. D. 2003, ApJS, 149, 289
Bender, R. et al. 2005, ApJ, 631, 280
Bertola, F., Cappellari, M., Funes, J. G., Corsini, E. M., Pizzella, A., & Vega Beltrán, J. C. 1998, ApJ, 509, L93
Bettoni, D., Galletta, G., & García-Burillo, S. 2003, A&A, 405, 5
Bigiel, F., Leroy, A., Walter, F., Brinks, E., de Blok, W. J. G., Madore, B., & Thornley,

M. D. 2008, AJ, 136, 2846
Birnboim, Y., Dekel, A., & Neistein, E. 2007, MNRAS, 380, 339
Blain, A. W., Smail, I., Ivison, R. J., Kneib, J.-P., & Frayer, D. T. 2002, Phys. Rep., 369, 111
Bonnet, H. et al. 2004, in Presented at the Society of Photo-Optical Instrumentation Engineers (SPIE) Conference, Vol. 5490, Advancements in Adaptive Optics. Edited by Domenico B. Calia, Brent L. Ellerbroek, and Roberto Ragazzoni. Proceedings of the SPIE, Volume 5490, pp. 130-138 (2004)., ed. D. Bonaccini Calia, B. L. Ellerbroek, & R. Ragazzoni, 130–138
Bouché, N. et al. 2007, ApJ, 671, 303
Bournaud, F., Elmegreen, B. G., & Elmegreen, D. M. 2007a, ApJ, 670, 237
Bournaud, F., Elmegreen, B. G., & Martig, M. 2009, ApJ, 707, L1
Bournaud, F., Jog, C. J., & Combes, F. 2007b, A&A, 476, 1179
Bouwens, R. J. & Illingworth, G. D. 2006, Nature, 443, 189
Bregman, J. D., Bregman, J. N., & Temi, P. 2008, in Astronomical Society of the Pacific Conference Series, Vol. 381, Infrared Diagnostics of Galaxy Evolution, ed. R.-R. Chary, H. I. Teplitz, & K. Sheth, 34–+
Bressan, A. et al. 2006, ApJ, 639, L55
Bressan, A. et al. 2007, in Astronomical Society of the Pacific Conference Series, Vol. 374, From Stars to Galaxies: Building the Pieces to Build Up the Universe, ed. A. Vallenari, R. Tantalo, L. Portinari, & A. Moretti, 333–+
Bridges, T. J., Ashman, K. M., Zepf, S. E., Carter, D., Hanes, D. A., Sharples, R. M., & Kavelaars, J. J. 1997, MNRAS, 284, 376
Brodie, J. P. & Strader, J. 2006, ARA&A, 44, 193
Bruzual, G. & Charlot, S. 2003, MNRAS, 344, 1000
Burkert, A., Naab, T., Johansson, P. H., & Jesseit, R. 2008, ApJ, 685, 897
Calzetti, D. et al. 2005, ApJ, 633, 871
—. 2007, ApJ, 666, 870
Capaccioli, M., Vietri, M., Held, E. V., & Lorenz, H. 1991, ApJ, 371, 535
Cappellari, M. 2002, MNRAS, 333, 400
Cappellari, M. & Copin, Y. 2003, MNRAS, 342, 345
Cappellari, M. & Emsellem, E. 2004, PASP, 116, 138
Cappellari, M. & McDermid, R. M. 2005, Classical and Quantum Gravity, 22, 347
Cappellari, M., Verolme, E. K., van der Marel, R. P., Kleijn, G. A. V., Illingworth, G. D., Franx, M., Carollo, C. M., & de Zeeuw, P. T. 2002, ApJ, 578, 787
Cappellari, M. et al. 2005, in Nearly Normal Galaxies in a LCDM Universe. A conference celebrating the 60th birthdays of George Blumenthal, Sandra Faber and Joel Primack. 2005. Santa Cruz: UC Santa Cruz
Cappellari, M. et al. 2006, MNRAS, 366, 1126
—. 2007, MNRAS, 379, 418
Cesarsky, D., Lequeux, J., Abergel, A., Perault, M., Palazzi, E., Madden, S., & Tran, D. 1996, A&A, 315, L309

Chapman, S. C., Blain, A. W., Smail, I., & Ivison, R. J. 2005, ApJ, 622, 772
Chemin, L. et al. 2006, MNRAS, 366, 812
Chevalier, R. A. & Raymond, J. C. 1978, ApJ, 225, L27
Cimatti, A. et al. 2004, Nature, 430, 184
Cohen, M. et al. 2007, MNRAS, 374, 979
Colina, L., Arribas, S., & Monreal-Ibero, A. 2005, ApJ, 621, 725
Combes, F., Young, L. M., & Bureau, M. 2007, MNRAS, 377, 1795
Conroy, C., Shapley, A. E., Tinker, J. L., Santos, M. R., & Lemson, G. 2008, ApJ, 679, 1192
Conselice, C. J. 2003, ApJS, 147, 1
Copin, Y., Cretton, N., & Emsellem, E. 2004, A&A, 415, 889
Côté, P. 1999, AJ, 118, 406
Côté, P., Marzke, R. O., & West, M. J. 1998, ApJ, 501, 554
Cowie, L. L., Hu, E. M., & Songaila, A. 1995, AJ, 110, 1576
Cowie, L. L., Songaila, A., Hu, E. M., & Cohen, J. G. 1996, AJ, 112, 839
Cresci, G., Davies, R. I., Baker, A. J., Mannucci, F., Lehnert, M. D., Totani, T., & Minowa, Y. 2006, A&A, 458, 385
Cresci, G. et al. 2009, ApJ, 697, 115
Cretton, N. & Emsellem, E. 2004, MNRAS, 347, L31
Crocker, A. F., Bureau, M., Young, L. M., & Combes, F. 2008, MNRAS, 386, 1811
Crocker, A. F., Jeong, H., Komugi, S., Combes, F., Bureau, M., Young, L. M., & Yi, S. 2009, MNRAS, 393, 1255
Croton, D. J. et al. 2006, MNRAS, 365, 11
Daddi, E., Cimatti, A., Renzini, A., Fontana, A., Mignoli, M., Pozzetti, L., Tozzi, P., & Zamorani, G. 2004a, ApJ, 617, 746
Daddi, E. et al. 2004b, ApJ, 600, L127
—. 2005, ApJ, 626, 680
—. 2007a, ApJ, 670, 156
—. 2007b, ApJ, 670, 173
Daigle, O., Carignan, C., Amram, P., Hernandez, O., Chemin, L., Balkowski, C., & Kennicutt, R. 2006, MNRAS, 367, 469
Dale, D. A. et al. 2005, ApJ, 633, 857
De Angeli, F., Piotto, G., Cassisi, S., Busso, G., Recio-Blanco, A., Salaris, M., Aparicio, A., & Rosenberg, A. 2005, AJ, 130, 116
de Grijs, R., Bastian, N., & Lamers, H. J. G. L. M. 2003, ApJ, 583, L17
De Lucia, G. & Blaizot, J. 2007, MNRAS, 375, 2
de Zeeuw, P. T. et al. 2002, MNRAS, 329, 513
Dekel, A. & Birnboim, Y. 2006, MNRAS, 368, 2
Dekel, A., Sari, R., & Ceverino, D. 2009a, ApJ, 703, 785
Dekel, A. et al. 2009b, Nature, 457, 451
Dickinson, M., Papovich, C., Ferguson, H. C., & Budavári, T. 2003, ApJ, 587, 25
Eckart, A. & Genzel, R. 1997, MNRAS, 284, 576
Eggen, O. J., Lynden-Bell, D., & Sandage, A. R. 1962, ApJ, 136, 748

Eisenhauer, F. et al. 2003, in Presented at the Society of Photo-Optical Instrumentation Engineers (SPIE) Conference, Vol. 4841, Instrument Design and Performance for Optical/Infrared Ground-based Telescopes. Edited by Iye, Masanori; Moorwood, Alan F. M. Proceedings of the SPIE, Volume 4841, pp. 1548-1561 (2003)., ed. M. Iye & A. F. M. Moorwood, 1548–1561
Elmegreen, B. G., Bournaud, F., & Elmegreen, D. M. 2008a, ApJ, 688, 67
—. 2008b, ApJ, 684, 829
Elmegreen, B. G. & Efremov, Y. N. 1997, ApJ, 480, 235
Elmegreen, B. G. & Elmegreen, D. M. 2005, ApJ, 627, 632
—. 2006, ApJ, 650, 644
Elmegreen, B. G., Elmegreen, D. M., Fernandez, M. X., & Lemonias, J. J. 2009, ApJ, 692, 12
Elson, R. A. W. & Fall, S. M. 1985, PASP, 97, 692
Emsellem, E., Goudfrooij, P., & Ferruit, P. 2003, MNRAS, 345, 1297
Emsellem, E., Monnet, G., & Bacon, R. 1994, A&A, 285, 723
Emsellem, E. et al. 2004, MNRAS, 352, 721
—. 2007, MNRAS, 379, 401
Engelbracht, C. W., Gordon, K. D., Rieke, G. H., Werner, M. W., Dale, D. A., & Latter, W. B. 2005, ApJ, 628, L29
English, J. & Freeman, K. C. 2003, AJ, 125, 1124
Erb, D. K. 2008, ApJ, 674, 151
Erb, D. K., Shapley, A. E., Pettini, M., Steidel, C. C., Reddy, N. A., & Adelberger, K. L. 2006a, ApJ, 644, 813
Erb, D. K., Shapley, A. E., Steidel, C. C., Pettini, M., Adelberger, K. L., Hunt, M. P., Moorwood, A. F. M., & Cuby, J.-G. 2003, ApJ, 591, 101
Erb, D. K., Steidel, C. C., Shapley, A. E., Pettini, M., Reddy, N. A., & Adelberger, K. L. 2006b, ApJ, 647, 128
—. 2006c, ApJ, 646, 107
Escala, A. & Larson, R. B. 2008, ApJ, 685, L31
Etherington, J. & Maciejewski, W. 2006, MNRAS, 367, 1003
Faber, S. M. et al. 1997, AJ, 114, 1771
—. 2007, ApJ, 665, 265
Fakhouri, O. & Ma, C.-P. 2008, MNRAS, 386, 577
Falcón-Barroso, J. et al. 2004, MNRAS, 350, 35
Fall, S. M. & Zhang, Q. 2001, ApJ, 561, 751
Fan, X. et al. 2001, AJ, 121, 54
Ferrarese, L. & Merritt, D. 2000, ApJ, 539, L9
Flores, H., Puech, M., Hammer, F., Garrido, O., & Hernandez, O. 2004, A&A, 420, L31
Fontana, A. et al. 2003, ApJ, 594, L9
—. 2004, A&A, 424, 23
Forbes, D. A., Brodie, J. P., & Grillmair, C. J. 1997, AJ, 113, 1652
Förster Schreiber, N. M. et al. 2006, ApJ, 645, 1062

—. 2009, ApJ, 706, 1364
Frenk, C. S., White, S. D. M., Davis, M., & Efstathiou, G. 1988, ApJ, 327, 507
Gallagher, III, J. S., Hunter, D. A., & Tutukov, A. V. 1984, ApJ, 284, 544
Gebhardt, K. et al. 2000a, ApJ, 539, L13
—. 2000b, ApJ, 543, L5
—. 2003, ApJ, 583, 92
Genel, S. et al. 2008, ApJ, 688, 789
Genzel, R., Baker, A. J., Tacconi, L. J., Lutz, D., Cox, P., Guilloteau, S., & Omont, A. 2003, ApJ, 584, 633
Genzel, R., Eckart, A., Ott, T., & Eisenhauer, F. 1997, MNRAS, 291, 219
Genzel, R., Pichon, C., Eckart, A., Gerhard, O. E., & Ott, T. 2000, MNRAS, 317, 348
Genzel, R. et al. 1998, ApJ, 498, 579
—. 2006, Nature, 442, 786
—. 2008, ApJ, 687, 59
Gerhard, O. E. 1993, MNRAS, 265, 213
Ghez, A. M., Klein, B. L., Morris, M., & Becklin, E. E. 1998, ApJ, 509, 678
Ghez, A. M., Morris, M., Becklin, E. E., Tanner, A., & Kremenek, T. 2000, Nature, 407, 349
Goerdt, T., Dekel, A., Sternberg, A., Ceverino, D., Teyssier, R., & Primack, J. R. 2009, ArXiv e-prints
Gonzalez Delgado, R. M. & Perez, E. 1996, MNRAS, 281, 1105
Gordon, K. D., Engelbracht, C. W., Rieke, G. H., Misselt, K. A., Smith, J., & Kennicutt, Jr., R. C. 2008, ApJ, 682, 336
Granato, G. L., De Zotti, G., Silva, L., Bressan, A., & Danese, L. 2004, ApJ, 600, 580
Grazian, A. et al. 2007, A&A, 465, 393
Greene, J. E. & Ho, L. C. 2005, ApJ, 630, 122
Halliday, C., Davies, R. L., Kuntschner, H., Birkinshaw, M., Bender, R., Saglia, R. P., & Baggley, G. 2001, MNRAS, 326, 473
Halliday, C. et al. 2008, A&A, 479, 417
Häring, N. & Rix, H.-W. 2004, ApJ, 604, L89
Harms, R. J. et al. 1994, ApJ, 435, L35
Harris, W. E. & Pudritz, R. E. 1994, ApJ, 429, 177
Haynes, M. P., Jore, K. P., Barrett, E. A., Broeils, A. H., & Murray, B. M. 2000, AJ, 120, 703
Heckman, T. M., Lehnert, M. D., & Armus, L. 1993, in Astrophysics and Space Science Library, Vol. 188, The Environment and Evolution of Galaxies, ed. J. M. Shull & H. A. Thronson, 455–+
Helou, G. et al. 2004, ApJS, 154, 253
Heng, K. & Sunyaev, R. A. 2008, A&A, 481, 117
Hernandez, O., Carignan, C., Amram, P., Chemin, L., & Daigle, O. 2005, MNRAS, 360, 1201
Hernandez, O., Gach, J.-L., Carignan, C., & Boulesteix, J. 2003, in Presented at the Society of Photo-Optical Instrumentation Engineers (SPIE) Conference, Vol. 4841, Instrument

Design and Performance for Optical/Infrared Ground-based Telescopes. Edited by Iye, Masanori; Moorwood, Alan F. M. Proceedings of the SPIE, Volume 4841, pp. 1472-1479 (2003)., ed. M. Iye & A. F. M. Moorwood, 1472–1479
Herrnstein, J. R., Moran, J. M., Greenhill, L. J., & Trotter, A. S. 2005, ApJ, 629, 719
Hicks, E. K. S. & Malkan, M. A. 2008, ApJS, 174, 31
Ho, L. C. 2009, ApJ, 699, 638
Hopkins, A. M. & Beacom, J. F. 2006, ApJ, 651, 142
Hopkins, P. F., Somerville, R. S., Hernquist, L., Cox, T. J., Robertson, B., & Li, Y. 2006, ApJ, 652, 864
Hopkins, P. F. et al. 2009, ArXiv e-prints
Hoyle, F. 1953, ApJ, 118, 513
Huchra, J. P., Brodie, J. P., & Kent, S. M. 1991, ApJ, 370, 495
Immeli, A., Samland, M., Gerhard, O., & Westera, P. 2004, A&A, 413, 547
Jeong, H., Bureau, M., Yi, S. K., Krajnović, D., & Davies, R. L. 2007, MNRAS, 376, 1021
Jeong, H. et al. 2009, MNRAS, 398, 2028
Jesseit, R., Cappellari, M., Naab, T., Emsellem, E., & Burkert, A. 2009, MNRAS, 397, 1202
Jesseit, R., Naab, T., Peletier, R. F., & Burkert, A. 2007, MNRAS, 376, 997
Jones, L. A. 1997, PhD thesis, University of North Carolina at Chapel Hill
Jordán, A. et al. 2007, ApJS, 171, 101
Józsa, G. I. G., Oosterloo, T. A., Morganti, R., Klein, U., & Erben, T. 2009, A&A, 494, 489
Kaneda, H., Onaka, T., Sakon, I., Kitayama, T., Okada, Y., & Suzuki, T. 2008a, ApJ, 684, 270
Kaneda, H., Suzuki, T., Onaka, T., Okada, Y., & Sakon, I. 2008b, PASJ, 60, 467
Kaspi, S., Smith, P. S., Netzer, H., Maoz, D., Jannuzi, B. T., & Giveon, U. 2000, ApJ, 533, 631
Kaviraj, S., Peirani, S., Khochfar, S., Silk, J., & Kay, S. 2009, MNRAS, 394, 1713
Kaviraj, S. et al. 2007, ApJS, 173, 619
Kennicutt, Jr., R. C. 1998, ApJ, 498, 541
Kennicutt, Jr., R. C. et al. 2003, PASP, 115, 928
Kong, X. et al. 2006, ApJ, 638, 72
Kormendy, J. & Gebhardt, K. 2001, in American Institute of Physics Conference Series, Vol. 586, 20th Texas Symposium on relativistic astrophysics, ed. J. C. Wheeler & H. Martel, 363–+
Kormendy, J. & Kennicutt, Jr., R. C. 2004, ARA&A, 42, 603
Krajnović, D., Cappellari, M., de Zeeuw, P. T., & Copin, Y. 2006, MNRAS, 366, 787
Krajnović, D., Cappellari, M., Emsellem, E., McDermid, R. M., & de Zeeuw, P. T. 2005, MNRAS, 357, 1113
Krajnović, D. et al. 2008, MNRAS, 390, 93
Kriek, M. et al. 2006, ApJ, 649, L71
—. 2007, ApJ, 669, 776
—. 2008, ApJ, 677, 219
Krist, J. 1993, in Astronomical Society of the Pacific Conference Series, Vol. 52, Astronomical

Data Analysis Software and Systems II, ed. R. J. Hanisch, R. J. V. Brissenden, & J. Barnes, 536–+
Kronberger, T., Kapferer, W., Schindler, S., & Ziegler, B. L. 2007, A&A, 473, 761
Kuntschner, H., Ziegler, B. L., Sharples, R. M., Worthey, G., & Fricke, K. J. 2002, A&A, 395, 761
Kuntschner, H. et al. 2006, MNRAS, 369, 497
—. 2010, MNRAS, submitted
La Mura, G., Popović, L. Č., Ciroi, S., Rafanelli, P., & Ilić, D. 2007, ApJ, 671, 104
Labbé, I. et al. 2005, ApJ, 624, L81
Lacey, C. & Cole, S. 1993, MNRAS, 262, 627
Lauer, T. R. et al. 2005, AJ, 129, 2138
Law, D. R., Steidel, C. C., & Erb, D. K. 2006, AJ, 131, 70
Law, D. R., Steidel, C. C., Erb, D. K., Larkin, J. E., Pettini, M., Shapley, A. E., & Wright, S. A. 2007, ApJ, 669, 929
—. 2009, ApJ, 697, 2057
Lawson, C. L. & Hanson, R. J. 1974, Solving least squares problems (Prentice-Hall)
Lees, J. F., Knapp, G. R., Rupen, M. P., & Phillips, T. G. 1991, ApJ, 379, 177
Lehnert, M. D. & Heckman, T. M. 1995, ApJS, 97, 89
—. 1996a, ApJ, 462, 651
—. 1996b, ApJ, 472, 546
Leroy, A. K., Walter, F., Brinks, E., Bigiel, F., de Blok, W. J. G., Madore, B., & Thornley, M. D. 2008, AJ, 136, 2782
Lilly, S. J. et al. 2007, ApJS, 172, 70
Lira, P., Lawrence, A., & Johnson, R. A. 2000, MNRAS, 319, 17
Lotz, J. M., Primack, J., & Madau, P. 2004, AJ, 128, 163
Macchetto, F., Marconi, A., Axon, D. J., Capetti, A., Sparks, W., & Crane, P. 1997, ApJ, 489, 579
Magorrian, J. et al. 1998, AJ, 115, 2285
Maiolino, R. et al. 2007, A&A, 472, L33
Mannucci, F. et al. 2009, MNRAS, 398, 1915
Marconi, A., Axon, D. J., Maiolino, R., Nagao, T., Pastorini, G., Pietrini, P., Robinson, A., & Torricelli, G. 2008, ApJ, 678, 693
Marconi, A., Risaliti, G., Gilli, R., Hunt, L. K., Maiolino, R., & Salvati, M. 2004, MNRAS, 351, 169
Martin, C. L. 1999, ApJ, 513, 156
Martin, C. L. 2003, in Revista Mexicana de Astronomia y Astrofisica Conference Series, Vol. 17, Revista Mexicana de Astronomia y Astrofisica Conference Series, ed. V. Avila-Reese, C. Firmani, C. S. Frenk, & C. Allen, 56–59
—. 2005, ApJ, 621, 227
McDermid, R. et al. 2004, Astronomische Nachrichten, 325, 100
McDermid, R. M. et al. 2006, MNRAS, 373, 906
McLaughlin, D. E. 1999, AJ, 117, 2398

McLaughlin, D. E. & Fall, S. M. 2008, ApJ, 679, 1272
McLaughlin, D. E. & Pudritz, R. E. 1996, ApJ, 457, 578
McLure, R. J. & Dunlop, J. S. 2004, MNRAS, 352, 1390
McLure, R. J., Jarvis, M. J., Targett, T. A., Dunlop, J. S., & Best, P. N. 2006, MNRAS, 368, 1395
Mendel, J. T., Proctor, R. N., & Forbes, D. A. 2007, MNRAS, 379, 1618
Mihos, J. C. & Hernquist, L. 1996, ApJ, 464, 641
Milosavljević, M. & Merritt, D. 2001, ApJ, 563, 34
Minniti, D. 1995, AJ, 109, 1663
Miyoshi, M., Moran, J., Herrnstein, J., Greenhill, L., Nakai, N., Diamond, P., & Inoue, M. 1995, Nature, 373, 127
Morganti, R. et al. 2006, MNRAS, 371, 157
Muñoz-Mateos, J. C. et al. 2009, ApJ, 703, 1569
Murray, N., Quataert, E., & Thompson, T. A. 2010, ApJ, 709, 191
Naab, T., Jesseit, R., & Burkert, A. 2006, MNRAS, 372, 839
Naab, T., Johansson, P. H., Ostriker, J. P., & Efstathiou, G. 2007, ApJ, 658, 710
Nesvadba, N. P. H. et al. 2007, ApJ, 657, 725
Netzer, H. 2009, ApJ, 695, 793
Noeske, K. G. et al. 2007, ApJ, 660, L43
Noguchi, M. 1999, ApJ, 514, 77
Onken, C. A. et al. 2007, ApJ, 670, 105
Papovich, C. et al. 2006, ApJ, 640, 92
Pastoriza, M. G., Winge, C., Ferrari, F., Macchetto, F. D., & Caon, N. 2000, ApJ, 529, 866
Peeters, E., Hony, S., Van Kerckhoven, C., Tielens, A. G. G. M., Allamandola, L. J., Hudgins, D. M., & Bauschlicher, C. W. 2002, A&A, 390, 1089
Peeters, E., Spoon, H. W. W., & Tielens, A. G. G. M. 2004, ApJ, 613, 986
Peletier, R. F. et al. 2007, MNRAS, 379, 445
Peng, C. Y., Impey, C. D., Rix, H.-W., Kochanek, C. S., Keeton, C. R., Falco, E. E., Lehár, J., & McLeod, B. A. 2006a, ApJ, 649, 616
Peng, E. W. et al. 2006b, ApJ, 639, 95
—. 2006c, ApJ, 639, 838
—. 2008, ApJ, 681, 197
Perlman, E. S. et al. 2007, ApJ, 663, 808
Pettini, M., Rix, S. A., Steidel, C. C., Adelberger, K. L., Hunt, M. P., & Shapley, A. E. 2002, ApJ, 569, 742
Pettini, M., Shapley, A. E., Steidel, C. C., Cuby, J.-G., Dickinson, M., Moorwood, A. F. M., Adelberger, K. L., & Giavalisco, M. 2001, ApJ, 554, 981
Pettini, M., Steidel, C. C., Adelberger, K. L., Dickinson, M., & Giavalisco, M. 2000, ApJ, 528, 96
Pipino, A., D'Ercole, A., & Matteucci, F. 2008, A&A, 484, 679
Puech, M., Hammer, F., Flores, H., Östlin, G., & Marquart, T. 2006, A&A, 455, 119
Puzia, T. H., Kissler-Patig, M., & Goudfrooij, P. 2006, ApJ, 648, 383

Quider, A. M., Pettini, M., Shapley, A. E., & Steidel, C. C. 2009, MNRAS, 398, 1263
Quinlan, G. D. & Hernquist, L. 1997, New Astronomy, 2, 533
Ravindranath, S. et al. 2004, ApJ, 604, L9
Reach, W. T. et al. 2005, PASP, 117, 978
Reddy, N. A., Erb, D. K., Steidel, C. C., Shapley, A. E., Adelberger, K. L., & Pettini, M. 2005, ApJ, 633, 748
Rhee, J. H. & Larkin, J. E. 2000, ApJ, 538, 98
Rhode, K. L. & Zepf, S. E. 2004, AJ, 127, 302
Rhode, K. L., Zepf, S. E., & Santos, M. R. 2005, ApJ, 630, L21
Richstone, D. O. & Tremaine, S. 1988, ApJ, 327, 82
Rix, H.-W., de Zeeuw, P. T., Cretton, N., van der Marel, R. P., & Carollo, C. M. 1997, ApJ, 488, 702
Roberts, M. S., Hogg, D. E., Bregman, J. N., Forman, W. R., & Jones, C. 1991, ApJS, 75, 751
Rousset, A. 1992, PhD thesis, PhD Thesis, Univ. J.Monnet de Saint-Etienne., (1992)
Rudnick, G. et al. 2003, ApJ, 599, 847
—. 2006, ApJ, 650, 624
Rupke, D. S., Veilleux, S., & Sanders, D. B. 2005, ApJS, 160, 115
Sadler, E. M., Oosterloo, T. A., Morganti, R., & Karakas, A. 2000, AJ, 119, 1180
Samurović, S. & Danziger, I. J. 2005, MNRAS, 363, 769
Sánchez-Blázquez, P. et al. 2006, MNRAS, 371, 703
Sarzi, M. et al. 2006, MNRAS, 366, 1151
—. 2007, New Astronomy Review, 51, 18
—. 2010, MNRAS, 402, 2187
Scannapieco, E. & Bildsten, L. 2005, ApJ, 629, L85
Schawinski, K., Thomas, D., Sarzi, M., Maraston, C., Kaviraj, S., Joo, S.-J., Yi, S. K., & Silk, J. 2007, MNRAS, 382, 1415
Schinnerer, E. & Scoville, N. 2002, ApJ, 577, L103
Schneider, S. E. 1989, ApJ, 343, 94
Schoenmakers, R. H. M., Franx, M., & de Zeeuw, P. T. 1997, MNRAS, 292, 349
Schroder, L. L., Brodie, J. P., Kissler-Patig, M., Huchra, J. P., & Phillips, A. C. 2002, AJ, 123, 2473
Schwarzschild, M. 1979, ApJ, 232, 236
—. 1982, ApJ, 263, 599
Schweizer, F. 1987, in IAU Symposium, Vol. 127, Structure and Dynamics of Elliptical Galaxies, ed. P. T. de Zeeuw, 109–122
Searle, L. & Zinn, R. 1978, ApJ, 225, 357
Serra, P. et al. 2009, in American Institute of Physics Conference Series, Vol. 1111, American Institute of Physics Conference Series, ed. G. Giobbi, A. Tornambe, G. Raimondo, M. Limongi, L. A. Antonelli, N. Menci, & E. Brocato, 111–114
Shapiro, K. L., Cappellari, M., de Zeeuw, T., McDermid, R. M., Gebhardt, K., van den Bosch, R. C. E., & Statler, T. S. 2006, MNRAS, 370, 559

Shapiro, K. L., Genzel, R., & Förster Schreiber, N. M. 2010a, MNRAS, 403, L36
Shapiro, K. L. et al. 2008, ApJ, 682, 231
—. 2009, ApJ, 701, 955
—. 2010b, MNRAS, 402, 2140
Shapley, A. E., Steidel, C. C., Pettini, M., & Adelberger, K. L. 2003, ApJ, 588, 65
Shields, G. A., Gebhardt, K., Salviander, S., Wills, B. J., Xie, B., Brotherton, M. S., Yuan, J., & Dietrich, M. 2003, ApJ, 583, 124
Shields, G. A., Menezes, K. L., Massart, C. A., & Vanden Bout, P. 2006, ApJ, 641, 683
Silk, J. & Rees, M. J. 1998, A&A, 331, L1
Silverman, J. D. et al. 2005, ApJ, 624, 630
Smail, I., Chapman, S. C., Ivison, R. J., Blain, A. W., Takata, T., Heckman, T. M., Dunlop, J. S., & Sekiguchi, K. 2003, MNRAS, 342, 1185
Smail, I., Ivison, R. J., Blain, A. W., & Kneib, J.-P. 2002, MNRAS, 331, 495
Smith, R. C., Kirshner, R. P., Blair, W. P., & Winkler, P. F. 1991, ApJ, 375, 652
Springel, V. et al. 2005, Nature, 435, 629
Statler, T. S. 2001, AJ, 121, 244
Statler, T. S. & Smecker-Hane, T. 1999, AJ, 117, 839
Steidel, C. C., Shapley, A. E., Pettini, M., Adelberger, K. L., Erb, D. K., Reddy, N. A., & Hunt, M. P. 2004, ApJ, 604, 534
Strader, J., Brodie, J. P., & Forbes, D. A. 2004, AJ, 127, 3431
Swinbank, A. M., Chapman, S. C., Smail, I., Lindner, C., Borys, C., Blain, A. W., Ivison, R. J., & Lewis, G. F. 2006, MNRAS, 371, 465
Swinbank, A. M., Smail, I., Chapman, S. C., Blain, A. W., Ivison, R. J., & Keel, W. C. 2004, ApJ, 617, 64
Tacconi, L. J., Genzel, R., Tecza, M., Gallimore, J. F., Downes, D., & Scoville, N. Z. 1999, ApJ, 524, 732
Tacconi, L. J. et al. 2006, ApJ, 640, 228
—. 2008, ApJ, 680, 246
—. 2010, Nature, 463, 781
Takata, T., Sekiguchi, K., Smail, I., Chapman, S. C., Geach, J. E., Swinbank, A. M., Blain, A., & Ivison, R. J. 2006, ApJ, 651, 713
Temi, P., Brighenti, F., & Mathews, W. G. 2007, ApJ, 660, 1215
—. 2009, ApJ, 695, 1
Thomas, D., Maraston, C., & Bender, R. 2003, MNRAS, 339, 897
Thomas, J., Saglia, R. P., Bender, R., Thomas, D., Gebhardt, K., Magorrian, J., & Richstone, D. 2004, MNRAS, 353, 391
Tonry, J. L., Dressler, A., Blakeslee, J. P., Ajhar, E. A., Fletcher, A. B., Luppino, G. A., Metzger, M. R., & Moore, C. B. 2001, ApJ, 546, 681
Tremaine, S. et al. 2002, ApJ, 574, 740
Tremonti, C. A., Moustakas, J., & Diamond-Stanic, A. M. 2007, ApJ, 663, L77
Trujillo, I. et al. 2006a, MNRAS, 373, L36
—. 2006b, ApJ, 650, 18

Valluri, M., Merritt, D., & Emsellem, E. 2004, ApJ, 602, 66
van den Bergh, S., Abraham, R. G., Ellis, R. S., Tanvir, N. R., Santiago, B. X., & Glazebrook, K. G. 1996, AJ, 112, 359
van der Kruit, P. C. & Allen, R. J. 1978, ARA&A, 16, 103
van der Marel, R. P., Cretton, N., de Zeeuw, P. T., & Rix, H.-W. 1998, ApJ, 493, 613
van der Marel, R. P. & Franx, M. 1993, ApJ, 407, 525
van der Marel, R. P. & van den Bosch, F. C. 1998, AJ, 116, 2220
van Dokkum, P. G. & Franx, M. 1995, AJ, 110, 2027
Vazdekis, A. 1999, ApJ, 513, 224
Veilleux, S., Cecil, G., & Bland-Hawthorn, J. 2005, ARA&A, 43, 769
Verdoes Kleijn, G. A., van der Marel, R. P., de Zeeuw, P. T., Noel-Storr, J., & Baum, S. A. 2002, AJ, 124, 2524
Verdoes Kleijn, G. A., van der Marel, R. P., & Noel-Storr, J. 2004, in Coevolution of Black Holes and Galaxies, ed. L. C. Ho
Verolme, E. K. et al. 2002, MNRAS, 335, 517
Vestergaard, M. 2002, ApJ, 571, 733
—. 2004, ApJ, 601, 676
Walter, F., Carilli, C., Bertoldi, F., Menten, K., Cox, P., Lo, K. Y., Fan, X., & Strauss, M. A. 2004, ApJ, 615, L17
Weijmans, A.-M., Krajnović, D., van de Ven, G., Oosterloo, T. A., Morganti, R., & de Zeeuw, P. T. 2008, MNRAS, 383, 1343
Weiner, B. J. et al. 2009, ApJ, 692, 187
Westmoquette, M. S., Exter, K. M., Smith, L. J., & Gallagher, J. S. 2007a, MNRAS, 381, 894
Westmoquette, M. S., Smith, L. J., Gallagher, III, J. S., O'Connell, R. W., Rosario, D. J., & de Grijs, R. 2007b, ApJ, 671, 358
Willott, C. J., McLure, R. J., & Jarvis, M. J. 2003, ApJ, 587, L15
Wilson, C. D., Scoville, N., Madden, S. C., & Charmandaris, V. 2003, ApJ, 599, 1049
Wong, T., Blitz, L., & Bosma, A. 2004, ApJ, 605, 183
Worthey, G., Dorman, B., & Jones, L. A. 1996, AJ, 112, 948
Wright, S. A. et al. 2007, ApJ, 658, 78
Wu, H., Cao, C., Hao, C.-N., Liu, F.-S., Wang, J.-L., Xia, X.-Y., Deng, Z.-G., & Young, C. K.-S. 2005, ApJ, 632, L79
Wuyts, S. et al. 2007, ApJ, 655, 51
Yi, S. K. et al. 2005, ApJ, 619, L111
Young, J. S., Allen, L., Kenney, J. D. P., Lesser, A., & Rownd, B. 1996, AJ, 112, 1903
Young, L. M. 2002, AJ, 124, 788
Young, L. M., Bendo, G. J., & Lucero, D. M. 2009, AJ, 137, 3053
Young, L. M., Bureau, M., & Cappellari, M. 2008, ApJ, 676, 317
Yun, M. S., Reddy, N. A., & Condon, J. J. 2001, ApJ, 554, 803
Zepf, S. E. & Ashman, K. M. 1993, MNRAS, 264, 611
Zinn, R. 1985, ApJ, 293, 424